A University of Sussex DPhil thesis

Available online via Sussex Research Online:

http://sro.sussex.ac.uk/

This thesis is protected by copyright which belongs to the author.

This thesis cannot be reproduced or quoted extensively from without first obtaining permission in writing from the Author

The content must not be changed in any way or sold commercially in any format or medium without the formal permission of the Author

When referring to this work, full bibliographic details including the author, title, awarding institution and date of the thesis must be given

Please visit Sussex Research Online for more information and further details

University of Sussex

The Role of Environment in Infrared Surveys: From Supernovae to Clusters

Matthew Thomson

Doctor of Philosophy

June 2010

Declaration

I hereby declare that this thesis has not been and will not be submitted in whole or in part to another University for the award of any other degree.

Signature:

Matthew Thomson

UNIVERSITY OF SUSSEX

Matthew Thomson, Doctor of Philosophy

The Role of Environment in Infrared Surveys: From Supernovae to Clusters

Summary

In this thesis we investigate several aspects of galaxy evolution. We begin by giving a brief introduction to the subject of galaxy evolution in the context of the Universe as we know it today. We discuss infrared surveys of galaxies as a tool for studying galaxy evolution. Initially, we are interested in the large scale environment of galaxies and identify clusters of galaxies at high redshift. We compare the mass and star-formation properties of galaxies in the cluster and field environments. To take this further we look to the AKARI all-sky survey and assess the potential of this survey for future studies. We calculate the completeness and reliability of the survey. Such wide surveys also allow for the possibility of studying rare and extreme phenomena. Such phenomena can push theories of galaxy evolution to their extremes and constrain these theories. We present the discovery of four such objects in the SWIRE survey. Finally, since environment plays a large role in the evolution of galaxies we extend this investigation to smaller scales. We investigate the progenitors of Type Ia Supernovae from a study of their host galaxies, which have implications for their use as standardisable candles.

Acknowledgements

There are many people that I would like to thank in helping me write this thesis. Firstly, I would like to thank my parents and family. Without their help and support I would not be in this position. I would also like to thank Sarah for her support throughout my PhD and especially in the final months. I would like to thank all those at the University of Sussex Astronomy Centre in providing a healthy and enjoyable working environment in which to conduct research and I would particularly like to thank my supervisor, Seb Oliver. I would also like to thank Duncan Farrah for his advice throughout. I would like to thank Isaac Roseboom, Eduardo Ganzalez-Solares, Dave Shupe, Jason Surace and Mattia Vaccari for the contributions they have made. I would also like to thank the AKARI FIS team for their hospitality and contributions. Finally, I would like to thank Ranga-Ram Chary and all at the *Spitzer* Science Center for giving me the wonderful opportunity to spend 6 months in California working with them.

Support for most of this work was provided by a Science and Technology Facilities Council Studentship, Grant Reference: PPA/S/S/2006/04466.

We thank Chris Conselice and Rychard Bouwens for the design and reduction of the small number of NICMOS observations that were used in this thesis to obtain host F160W magnitudes. We are also very grateful for the extensive telescope resources that were dedicated to the GOODS Legacy program and the contribution of various members in the analysis and reduction of those datasets. Partial support for this work was provided by NASA through the Spitzer Space Telescope Visiting Graduate Student Program, through a contract issued by the Jet Propulsion Laboratory, California Institute of Technology under a contract with NASA. This work is based in part on observations obtained with MegaPrime/MegaCam, a joint project of CFHT and CEA/DAPNIA, at the Canada-France-Hawaii Telescope (CFHT) which is operated by the National Research Council (NRC) of Canada, the Institut National des Science de l'Univers of the Centre National de la Recherche Scientifique (CNRS) of France, and the University of Hawaii. This work is based in part on data products produced at TERAPIX and the Canadian Astronomy Data Centre as part of the Canada-France-Hawaii Telescope Legacy Survey, a collaborative

project of NRC and CNRS.

This research has made use of the NASA/IPAC Extragalactic Database (NED) which is operated by the Jet Propulsion Laboratory, California Institute of Technology, under contract with the National Aeronautics and Space Administration.

This work is based in part on observations carried out with the IRAM 30m Telescope located on Pico Veleta in the Spanish Sierra Nevada. IRAM is supported by INSU/CNRS (France), MPG (Germany) and IGN (Spain).

This research has made use of the NASA/ IPAC Infrared Science Archive, which is operated by the Jet Propulsion Laboratory, California Institute of Technology, under contract with the National Aeronautics and Space Administration.

This work is based in part on observations made with the Spitzer Space Telescope, which is operated by the Jet Propulsion Laboratory, California Institute of Technology under a contract with NASA.

This work makes use of the *Spitzer* IRS which was a collaborative venture between Cornell University and Ball Aerospace Corporation funded by NASA through the Jet Propulsion Laboratory and Ames Research Center.

This research is based in part on observations with AKARI, a JAXA project with the participation of ESA.

Contents

List of Tables

List of Figures

Chapter 1

Introduction

1.1 The Universe in a Nutshell

The evolution of galaxies has been a subject of intense study ever since Hubble (1925) discovered that several spiral like objects, known as 'nebulae' at the time, were host to Cepheid variable stars with distances far beyond the reaches of our own galaxy. These nebulae were shown to be collections of billions of stars that we now refer to as galaxies. However, before we can discuss the evolution of these objects, and in particular the role that environment may play, we must explore how the Universe itself has evolved.

1.1.1 The Big Bang Model

In 1929 Hubble was able to measure both the distance (from Cepheid variable stars) and the velocity (from the redshift of the galaxy spectra) to many nearby galaxies. Hubble showed first that galaxies are in general moving away from us and furthermore that the recession velocity v is proportional to the distance, d (Hubble, 1929)

$$v = H_0 d \tag{1.1}$$

where the proportionality constant, H_0, is now known as the Hubble constant. This observation suggests that the Universe is expanding and that in the past it was very small. This discovery was the first piece of supporting evidence for the current consensus theory of cosmology, first proposed by Lemaître (1927), the Big Bang theory. In this theory, the Universe began with the explosion of a singularity 13.7 Gyrs ago. Since then the Universe has expanded and cooled allowing stars and galaxies to form into the Universe we see today. This theory has several pieces of supporting evidence, but perhaps the most important was the discovery of the Cosmic Microwave Background (CMB) by Penzias & Wilson (1965).

Wherever Penzias and Wilson pointed their microwave receiver, they found a constant background noise. This background noise can be explained in the Big Bang model. The early Universe was a hot (T > 3000K) plasma of ionised Hydrogen. The mean free path of a photon was small due to interactions with electrons (Thomson scattering). The photons were coupled to the baryonic matter and unable to travel freely. The Universe at this time was in thermal equilibrium with a black-body spectrum. As the Universe expanded, it cooled, until after ∼300,000 years the temperature was low enough for atoms to form. At this point there were no longer any free electrons and the photons decoupled from the baryonic matter. Photons were thus able to travel freely through the Universe. We see these photons now in the microwave band as the photon wavelength has been stretched due to the expansion of the Universe. This stretching of the wavelength of light as it travels through an expanding Universe is referred to as *cosmological redshift*. This redshift, z, is defined as

$$1 + z = \frac{\lambda_o}{\lambda_e} \tag{1.2}$$

where λ_o is the observed wavelength and λ_e is the emitted wavelength[1]. The COsmic Background Explorer (COBE; Mather, 1982; Gulkis et al., 1990) satellite was able to measure the CMB to a high degree of accuracy. COBE showed that the CMB has a perfect black-body spectrum which is (almost) homogeneous across the sky.

Prior to this discovery, Alexander Friedmann had mathematically described the expansion of the Universe under the assumption that it was *homogeneous* and *isotropic*. A homogeneous Universe is one that looks the same for all observers. An isotropic Universe is one that looks the same in all directions. Friedmann showed that such a Universe would satisfy the following equation

$$\left(\frac{\dot{a}}{a}\right)^2 = \frac{8\pi G}{3}\rho - \frac{kc^2}{a^2} \tag{1.3}$$

In this equation, a is the *scale factor* and is a parameter which quantifies the expansion rate of the Universe. It is a function of time, t, and $\dot{a}$ is the derivative of a with respect to t. G and c are Newton's gravitational constant and the speed of light in a vacuum respectively. ρ is the energy density of the Universe and k represents the *curvature* of the Universe. The curvature of the Universe refers to its geometry. A Universe in which $k = 0$ is spatially flat, following Euclidean geometry. Values of k greater than or less than 0 give closed, spherical geometry or open, hyperbolic geometry respectively. The left

[1]Strictly this redshift includes a contribution from both the cosmological redshift and any intrinsic velocity the emitting object has in the line of sight to the observer. However, since the cosmological redshift dominates for all but the nearest objects we use the two interchangeably.

hand side of the equation is often re-written as $H(t) = \left(\frac{\dot{a}}{a}\right)^2$, where $H(t)$ is the Hubble parameter. The constant in equation 1.1, H_0, is the Hubble parameter measured today, i.e. $H_0 = H(t = \text{now})$.

Given this equation to describe the expansion of the Universe one might ask what is its ultimate fate. Matter in the Universe slows the expansion due to its gravity. This leads to three regimes for the final fate of the Universe depending on how much matter there is in it. In the first, there is enough matter to slow the expansion and cause it to reverse, leading to the Universe collapsing. In the second there is enough matter to slow the expansion but not to reverse it, leading to a Universe that expands ever more slowly. Finally, a Universe which does not have enough matter to slow the expansion significantly and the Universe expands forever. According to Einstein's Theory of General Relativity, matter and energy in the Universe cause space-time to curve. So the three matter density regimes correspond to three possible values for the curvature k. $k < 0$ is a closed Universe which re-collapses. $k = 0$ is a flat Universe which expands ever more slowly. $k > 0$ is an open Universe, where the expansion continues forever. The critical density, ρ_c, is the energy density of the Universe required to make it flat and is given by

$$\rho_c = \frac{3H^2}{8\pi G} \tag{1.4}$$

The energy density of the universe is then given as a fraction of the critical density, such that

$$\Omega = \frac{\rho}{\rho_c} \tag{1.5}$$

Detailed measurements of the power spectrum of the CMB first from COBE and more recently from the Wilkinson Microwave Anisotropy Probe (WMAP; Bennett et al., 2003) have shown that Ω is very close to unity and that hence the Universe is spatially flat.

There are two major issues with this theory that must be addressed. These are referred to as the *flatness problem* and the *horizon problem*. The *flatness problem* arises because the Universe today has Ω very close to 1. The deviation away from 1 of Ω is an increasing function of time. For the Universe to have $\Omega \sim 1$ now requires $|\Omega - 1| \leq 10^{-16}$ 1 second after the Big Bang. There is no reason to expect the Universe to have the critical density, so this requires a large degree of fine-tuning. The *horizon problem* refers to the fact that the CMB actually appears to be too isotropic. Parts of the sky which could not have been in causal contact with each other, given the age of the Universe and the finite speed of light, appear to have the same temperature. These two problems are solved if we invoke a period of accelerated expansion (i.e. $\ddot{a} > 0$) when the Universe was $\lesssim 10^{-37}$ seconds

old, called *Inflation* (Guth, 1981). This period of accelerated expansion naturally drives Ω towards 1 and gives a value very close to unity today. Inflation also causes parts of the Universe in causal contact to expand such that they are no longer in causal contact, thus solving the horizon problem.

We now turn to the energy density of the Universe and the different components of Ω. The first component is that of Baryonic matter which makes up the stars and galaxies that we can see. In addition to Baryonic matter the Universe appears to be made up of two further components. The first is *Dark Matter* which interacts only via gravitation and does not emit any kind of radiation that can be observed. This component was first proposed by Zwicky (1937) from the velocities of galaxies in the Coma cluster. Since then there have been many pieces of confirming evidence. The rotational velocities of stars in galaxies do not show the fall off with radius as expected for the observed mass distribution. They are consistent with the existence of a large halo of gravitating matter that is not observed (see e.g. Rubin et al., 1980). Further evidence for dark matter includes the gravitational lensing of galaxy clusters and the temperatures of the hot gas in clusters, which show mass determinations far in excess of that which can be seen. Initially it was thought that this missing matter could be explained by small stars, such as brown dwarfs, which are baryonic, but are not massive enough for nuclear fusion to occur (e.g. Marley et al., 1996). However, the abundance of light elements (in particular Hydrogen, Deuterium, Helium-3, Helium-4 and Lithium) have been predicted for the big bang model by Wagoner et al. (1967). Comparing the predicted ratio of the baryons to photons to that measured by WMAP showed that dark matter must be non-baryonic (Cyburt et al., 2003).

The final component of energy in the Universe is referred to as *Dark Energy*. This component causes the expansion of the Universe to accelerate at late times. The primary evidence for Dark Energy comes from distances to Type Ia Supernovae (SNe Ia). SNe Ia are the explosion of White Dwarf stars which have reached the Chandrasekhar mass (Chandrasekhar, 1931). White Dwarf stars are supported by electron degeneracy pressure, however, above the Chandrasekhar mass this pressure is insufficient and the stars collapse and explode (see e.g. Livio, 2001; Podsiadlowski et al., 2008, for a review). Phillips (1993) showed that SNe Ia are standardisable candles. There is a tight relationship between the brightness of a SN Ia and the width of its light-curve. By using a calibration set of low redshift SNe Ia , this relationship can be used to measure the distances to these explosions. Using this technique, Riess et al. (1998); Perlmutter et al. (1999) showed that high redshift SNe Ia are more distant than expected. This can be explained if we invoke dark energy

as an extra component of the Universe which causes the expansion to accelerate at late times. While the nature of dark-energy is an unknown and highly researched and debated topic, current observations are consistent with a constant dark energy equation of state (see e.g. Kowalski et al., 2008). This can be introduced into the Friedmann equation with the addition of Einstein's cosmological constant, Λ

$$\left(\frac{\dot{a}}{a}\right)^2 = \frac{8\pi G}{3}\rho - \frac{kc^2}{a^2} + \frac{\Lambda}{3} \tag{1.6}$$

We can now write Ω as the sum of its constituent parts

$$\Omega = \Omega_b + \Omega_{dm} + \Omega_\Lambda \tag{1.7}$$

where Ω_b is the energy density of baryonic matter, Ω_{dm} is the energy density in dark matter and Ω_Λ is the energy density in dark energy, as a fraction of the critical density. The values of these parameters have been well constrained from several observations. Measurements by the WMAP probe of the CMB along with constraints such as those from SNe Ia have showed that data are best described by a Universe that is spatially flat with $\Omega_b = 0.0456 \pm 0.0016$, $\Omega_\Lambda = 0.728^{+0.015}_{-0.016}$, $\Omega_{dm} = 0.227 \pm 0.014$ and $H_0 = 70.4^{+1.3}_{-1.4}$km s^{-1} Mpc^{-1} (Komatsu et al., 2010). This is the so-called Λ Cold Dark Matter (ΛCDM) cosmology and is the current consensus theory of cosmology. While alternatives exist to explain the observations without invoking dark matter and dark energy, such as the Modified Newtonian Dynamics of Milgrom (1983), none explain the observations completely and as such we assume ΛCDM for this work. Note, however, that (unless otherwise stated) we use the values rounded to one decimal place, $\Omega_b + \Omega_{dm} = 0.3$, $\Omega_\Lambda = 0.7$ and $H_0 = 70$km s^{-1} Mpc^{-1} to facilitate comparisons with previous work.

1.2 The Growth Of Structure

While the CMB shows that the Universe is very isotropic, it is not on all scales. This is seen simply in the formation of galaxies and clusters of galaxies. At small angular scales there are small ($\Delta T/T \sim 10^{-5}$) fluctuations across the sky in the temperature, T, of the CMB. These fluctuations are caused by small gravitational potential wells. Where there is a slight over-density of matter, the CMB photons will be redshifted as they escape from the gravitational potential. Similarly, photons coming from an under-density will be blue shifted. It is these over-densities that will form the large scale structures of galaxies and clusters we see today.

The gravitating mass of the early Universe was dominated by dark matter. It is thought that gaussian quantum fluctuations in the dark matter density field immediately prior to

inflation produced the seeds of over-densities. Inflation caused these over-densities to accelerate away from each other, meaning they remained over-densities. As the Universe expanded, these over-densities were attracted to each other to form larger over-densities and these gave rise to the fluctuations in the CMB temperature. Over time these over-densities merged together to form large concentrations of dark matter, called haloes. These haloes subsequently merged together to form still larger structures. This process is commonly referred to as *hierarchical structure formation*. Baryonic matter will be gravitationally attracted to these dark matter haloes. As the baryonic matter cools it will condense and eventually form stars and galaxies (see e.g. White & Rees, 1978; White & Frenk, 1991; Cole et al., 2000).

As dark matter only interacts gravitationally it is possible to perform large numerical computer simulations of its evolution from early to late times. This was achieved by the Millennium Simulation (Springel et al., 2005). The simulation showed that as time goes by structures form and merge to give large clusters of dark matter haloes connected by filaments of haloes with large voids bereft of matter. Baryonic matter, however, is much more complex. While it follows closely the dark-matter distribution due to gravity it does not do so precisely. There is a bias between the distribution of baryonic matter and dark matter. This is due to the complex physical processes involved in the formation of stars and galaxies. In order to compare the statistical properties of galaxies from simulations to observed galaxy distributions one must make various assumptions about how galaxies form, such as the mass and temperature at which this occurs. However, parameters describing these various physical processes can be constrained by fitting to observations such as the Luminosity Function (LF) of galaxies (which measures the number density of galaxies as a function of luminosity) and galaxy scaling relations. These scaling relations include, for example, an observed correlation between the radius, surface brightness and velocity dispersion of a particular type of galaxy (elliptical galaxies, see section 1.3.1) referred to as the 'fundamental plane' (Djorgovski & Davis, 1987; Dressler et al., 1987). Large surveys of galaxies, such as the Sloan Digital Sky Survey (SDSS; York et al., 2000) and the 2 Degree Field Galaxy Redshift Survey (2dfGRS; Colless et al., 2001; Norberg et al., 2002), have allowed accurate measurements of the LF (see e.g. Blanton et al., 2003; Norberg et al., 2002). From these fits, simulations are able to qualitatively reproduce the observed galaxy distribution. Figure 1.1 shows a comparison between the large scale structure of galaxies as found by 2dFGRS and a simulation (Springel et al., 2006).

However, there are problems. The simulation overestimates the abundance of galaxies

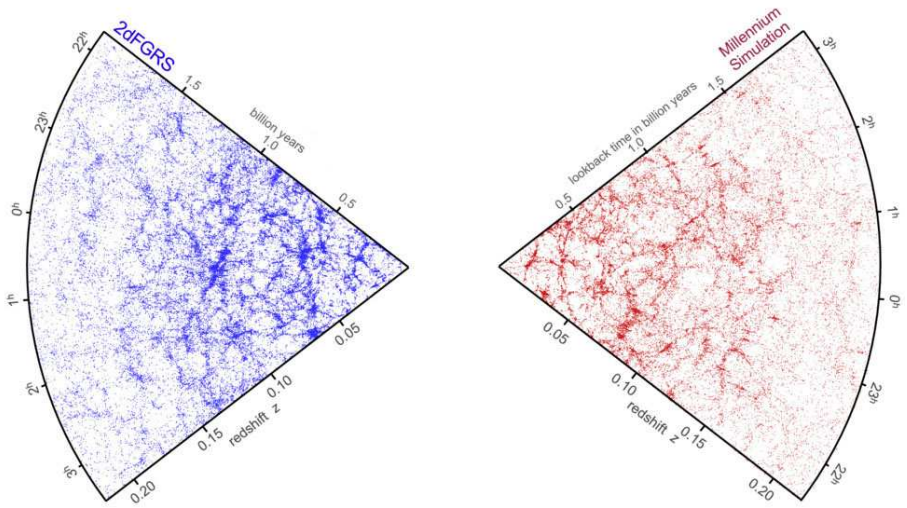

Figure 1.1: Large Scale Structure observed in 2dFGRS (left-hand wedge) as compared to that in the Millennium Simulation (right-hand wedge). Figure is adapted from Springel et al. (2006).

at both the bright and faint end of the luminosity function. These discrepancies have been partially solved by the introduction of feedback into the simulations. Typically, this is in the form of energy injection from supernova explosions and Active Galactic Nuclei (i.e. galaxies which show large amounts of non-stellar emission from their nucleus). The energy released from these systems heats up the local gas and prevents it from cooling and collapsing to form stars (see e.g. Cole et al., 2000; Croton et al., 2006; Bower et al., 2006).

However, there is still a long way to go before simulations accurately predict the detailed nature of galaxies in terms of their colour, luminosity, mass, density etc. (see e.g. Baugh, 2006, for a review). Furthermore, there is a large volume of observational evidence to show that massive galaxies were assembled at early times ($z \gtrsim 1$). Massive galaxies ($M > 10^{11}\mathrm{M}_{\odot}$) are numerously present up to high redshift (at least $z \sim 2.5$ Fontana et al., 2004; Pozzetti et al., 2007) with only mild evolution at low redshifts ($z \lesssim 1$ Fontana et al., 2006; Cimatti et al., 2006). In the hierarchical galaxy formation model, one expects massive galaxies to form at late times, as they have had most time to merge together. This phenomenon of stellar mass assembly at high redshift is commonly referred to as 'downsizing' (see e.g. Cowie et al., 1996).

1.3 Galaxies

Having outlined the main features of the current theory of structure formation, we now turn our attention to the specifics of the galaxies that we observe. Galaxies are large assemblages of stars, gas and dust, gravitationally bound within a dark matter halo. They have a typical size of a few kpc and have a stellar mass $\gtrsim 10^{8}\mathrm{M}_{\odot}$. We will first discuss the classification of galaxies into different types before discussing some observations of the evolution of galaxies.

1.3.1 Classification

Galaxies have long been classified into different types based on their appearance. The tuning fork diagram of Hubble (1922, 1926) classified galaxies into two distinct types, those of *Spiral* and *Elliptical* galaxies. These different types of galaxies have very different properties. Elliptical galaxies are those which are elliptical in shape and broadly featureless. Hubble allowed for several sub-classes depending on their ellipticity, from spherical E0 to very elliptical E7 galaxies. Elliptical galaxies generally have red colours as they harbour old stellar populations with little or no star-formation (see e.g. Bower et al., 1992).

Elliptical galaxies also dominate the population of massive galaxies (with $M \gtrsim 10^{10.5}\mathrm{M}_{\odot}$ Kauffmann et al., 2003).

Spiral galaxies have a broadly spherical nucleus or bulge but also have a flattened disk. This disk is often in the form of spiral arms which gives them their name. Hubble saw two sub-classes depending on whether a bar existed at the nucleus. These sub-classes were further classed by how tightly wound are their spiral arms, giving Sa-Sc for galaxies which have no bar and increasingly loose spirals and SBa-SBc for barred spirals. Spiral galaxies have blue colours, are much younger and are actively forming stars, although they contain an older stellar population in the bulge. Spiral galaxies are generally fainter, with lower masses than ellipticals (see e.g. Kauffmann et al., 2003; Brinchmann et al., 2004; Baldry et al., 2004). S0 galaxies are the galaxies which appear at the apex of the tuning fork and are either classed as very flattened ellipticals or spirals with no spiral arms. The shape of a galaxy is also referred to as its morphology. Elliptical and S0 galaxies are also referred to as Early-type galaxies and Spirals are referred to as Late type galaxies, due to the position Hubble placed these galaxies on his diagram.

Since Hubble's first classification, observations have confirmed that the galaxy population has a distinct bi-modality into red and blue galaxies (see e.g. Strateva et al., 2001; Baldry et al., 2004; Balogh et al., 2004b). Colour-magnitude diagrams show that red galaxies form a tight 'red-sequence', whereas blue galaxies do not show such a strong correlation, but instead form a 'blue cloud'. There are, however, populations both of blue, elliptical galaxies and red, spiral galaxies (see e.g. Bamford et al., 2008).

Two additional 'types' of galaxies are also observed, those of starburst galaxies and Active Galactic Nuclei (AGN). A starburst is an enhanced period of rapid star-formation in a galaxy that produces a large population of hot, young stars which emit strongly in the UV (see e.g. Rieke et al., 1980). This star-formation is thought to be triggered by galaxy-galaxy mergers, which can lead to collisions between gas clouds, as suggested by their generally disturbed morphology (see e.g. Sanders et al., 1988). AGN are galaxies which show strong emission from their nucleus which does not arise from the stellar population of the galaxy. This non-thermal emission is thought to be due to accretion of matter onto a super-massive black hole at the centre of the galaxy. These galaxies also exhibit a dusty torus surrounding the nucleus, when they are viewed face on the powerful jets from the accreting matter are observed as bright objects called quasi-stellar objects (QSOs; Schmidt, 1963). When viewed through the torus the objects appear much less luminous (see e.g. Blandford & Rees, 1978; Orr & Browne, 1982; Scheuer, 1987; Peacock,

1987; Barthel, 1989)

1.3.2 Evolution

The separation into red and blue galaxies seems to exist to high redshift (at least $z \sim 2$ Bell et al., 2004; Kriek et al., 2008). However, these high-redshift studies also show that there has been significant evolution in this bi-modality over time. At high redshift the number density of blue, spiral galaxies is larger than that at low redshift (see e.g. Lilly et al., 1995; Cowie et al., 1996; Bell et al., 2004). This evolution is also observed for low and high redshift clusters (see e.g. Dressler et al., 1997, and section 1.5.2). This implies that the star formation of a significant fraction of the blue galaxy population is quenched at late times. This evolution could be explained in the hierarchical model by mergers of spiral galaxies to form ellipticals (Toomre & Toomre, 1972; Toomre, 1977). Mergers of gas-rich spiral galaxies trigger a period of enhanced star-formation and growth of the central black hole. Once the black hole is sufficiently large enough, accretion could lead to energy injection which heats the surrounding gas, leaving an elliptical galaxy with little ongoing star formation (see e.g. Sanders et al., 1988; Barnes et al., 1991; Mihos & Hernquist, 1994; Hopkins et al., 2007). As we shall see in more detail below, the environment a galaxy inhabits can also affect its evolution. For example, within the galaxy cluster environment dynamical processes can affect galaxies. Clusters of galaxies are the most massive gravitationally bound systems in the Universe. They can contain anywhere from a handful to several thousand galaxies. They also contain a large amount of gas in the intra-cluster medium. Within these environments processes such as ram-pressure stripping (the removal of gas from a galaxy due to rapid motion through the intra-cluster medium Gunn & Gott, 1972; Balogh et al., 2000), or galaxy harassment (the disruption of galaxies due to the tidal forces of a cluster potential Moore et al., 1999) can quench star formation. Finally, it has been known for some time that the star formation rate (SFR) density of the Universe increases with redshift, peaking at $z \sim 2.5$ and decreasing thereafter (Lilly et al., 1996; Madau et al., 1996; Le Floc'h et al., 2005; Baldry et al., 2005; Hopkins & Beacom, 2006).

1.4 Galaxy Surveys

Many of the above results have arisen from galaxy surveys. There has been great interest in galaxy surveys and their use to study the population of galaxies and their evolution for many years. In the present work we focus on wide-field imaging surveys. Such surveys allow us to obtain large, unbiased samples of objects to high redshift, assuming a large

enough area is covered to account for cosmic variance, the variation between different fields (i.e. different areas of the sky) due to large-scale structure.

There are broadly speaking two regimes for galaxy surveys. The first are the so called 'pencil beam' surveys, which are narrow, covering only very small regions of the sky but selecting the faintest galaxies. The most famous example of such a survey is that of the Hubble Deep Field (HDF; Williams et al., 1996) by the *Hubble Space Telescope* (*HST*). Such surveys allow us to probe the faint end of the luminosity function in the distant Universe. However, the small area of sky covered means that these surveys are not representative volumes of the Universe. The Hubble Deep Field is $\sim$ 5 sq. arcmins and hence observes only a small fraction of the sky. If these surveys happen to centre on a void or an over-density they will produce biased samples of galaxies. Alternatively, observers survey large areas of sky but to shallow depths. The SDSS Legacy Survey covered $\sim$8400 sq. degs. but was only able to probe all but the very brightest objects out to z $\sim$0.3 and so is only able to assess the relatively local Universe[2]. The wide-area of the survey, however, allows a representative sample of galaxies to be obtained at these redshifts. This is only two of a very long list of optical surveys that have been conducted over the years and indeed that are still on-going. Other examples include the Galaxy and Mass Assembly (GAMA; Driver et al., 2009) survey; Great Observatories Origins Deep Survey (GOODS; Giavalisco et al., 2004; Dickinson et al., 2003); Canada France Hawaii Telescope Legacy Survey (CFHTLS; Cuillandre & Bertin, 2006); Cosmic Evolution Survey (COSMOS; Scoville et al., 2007b); Classifying Objects By Medium Band Filter Observations - a spectrophotometric 17 filter survey (COMBO-17; Wolf et al., 2004). In the present work we primarily concentrate on the intermediate class of surveys, which probe tens of square degrees as a compromise between the need to observe representative volumes and to probe to redshifts of $\sim 1-2$. This allows us to study the evolution of galaxies in the distant Universe, during a time when massive red-sequence galaxies exhibit a rapid rise in their space density (see e.g. Cirasuolo et al., 2007; Arnouts et al., 2007) and galaxies are forming stars at a greater rate than today (see e.g. Le Floc'h et al., 2005). The large area will allow us to probe the environment of star formation at these redshifts. These surveys also allow us to search for rare objects (see section 1.6 and chapter 4). We do, however, utilise the superior photometry of a narrow, deep survey to explore the host galaxies of high redshift SNe Ia in chapter 5. This work is also primarily focused on Infrared (IR) wavelengths, we now discuss infrared, wide-area surveys.

[2]Note that the large area of SDSS has allowed the discovery of the most distant quasars as they are exceptionally bright objects

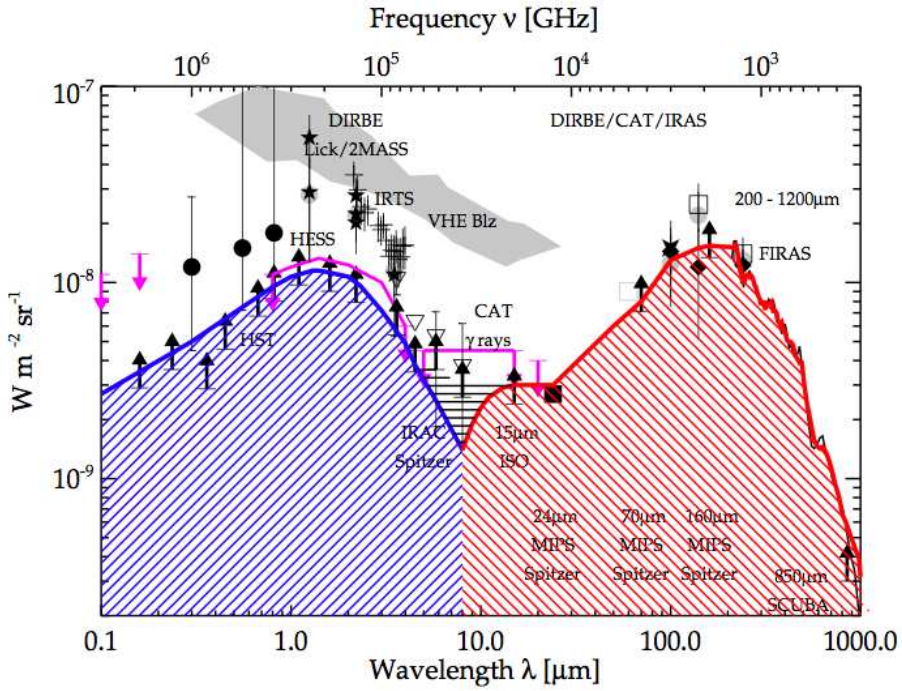

Figure 1.2: The cosmic optical and infrared background, showing the energy density as a function of wavelength received at Earth. This is figure 13 from Dole et al. (2006).

1.4.1 Infrared surveys

It has been known for some time that in order to get a full handle on the nature of astronomical objects, data across all wavelength bands is required. Figure 1.2 (which is figure 13 from Dole et al., 2006) shows the energy density of radiation received at the Earth as a function of wavelength. The figure shows that an approximately equal density of energy is received at the Earth at IR wavelengths as is received at optical and Ultra-Violet (UV) wavelengths.

Much work has been done on the ground in the Near-Infrared (NIR). The 2-Micron All-Sky Survey (2MASS; Skrutskie et al., 2006) was the first all-sky survey in the NIR. This survey built on the first large area NIR survey, the Two-Micron Sky Survey (TMSS; Neugebauer & Leighton, 1969). 2MASS observed the whole sky in the JHK bands, centred at the wavelengths 1.25, 1.65 and 2.17μm and to a depth of $\sim$15.8, 15.1 and 14.3 (Vega magnitudes) respectively. Surveys with the UK Infrared Telescope (UKIRT) such as the UKIRT Infrared Deep Sky Survey (UKIDSS; Lawrence et al., 2007) Deep Extragalactic Survey (DXS) and Ultra-Deep Survey (UDS) have also surveyed the sky in the NIR. When completed the DXS and UDS will reach a depth of $K \sim 21, 23$ (Vega magnitudes) over an area of 35 and 0.8 sq. degs. respectively. More recently, the Visible and Infrared Survey Telescope for Astronomy (VISTA; Emerson et al., 2006) has begun obser-

vations. Several surveys will be conducted on this telescope which observes at $0.85-2.3\mu$m. These surveys range in size from 0.83 sq. degs. to 20, 000 sq. degs. with K_s-band depths of 25.6 and 20.0 (AB magnitude) respectively.

The Earth's atmosphere radiates in the mid and far infrared wavelength ranges and so to study at these wavelengths we must use space-based telescopes. The first infrared space telescope was the InfraRed Astronomical Satellite (IRAS; Neugebauer et al., 1984) launched in 1983. This telescope observed the whole sky in 4 bands centred at 12, 25, 60 and 100μm and was complete to $\sim$ 1.5 Jy at 100μm and to $\sim$ 0.5 Jy for the shorter wavelengths, for point sources (*Point Source Catalogue; PSC* Beichmann, 1985). The *Faint Source Catalogue* (*FSC*; Moshir et al., 1992) reached $\sim$ 0.2 Jy at 12, 25 and 60μm and $\sim$ 1 Jy at 100μm, limited to galactic latitude $|b| > 20°$. The angular resolution of the instrument varied between $\sim 0'.5$ at 12 μm to $\sim 2'$ at 100μm.

IRAS revealed new populations of galaxies which were optically faint but luminous in the infrared (Soifer et al., 1984). This was due to stars forming in dusty regions in galaxies, the UV emission from these stars was absorbed by the dust and re-emitted in the infrared. In order to study how stars are formed in galaxies and how galaxies build up their stellar mass we must look in the infrared. The Infrared Space Observatory (*ISO*; Kessler et al., 1996) launched in 1995 had a large imaging wavelength range of 2.5-240μm and spatial resolution of $1''.5$ - $90''$ with the imaging photo-polarimeter ISOPHOT. This telescope was able to observe in the mid and far infrared to much greater depths than IRAS. The largest survey conducted with ISO was the European Large Area ISO Survey (ELAIS; Oliver et al., 2000) covering 12 sq. degs. and began to shed light on the high redshift IR galaxy population. More recently, the NASA *Spitzer* Space Telescope (Werner et al., 2004) launched in 2003 observed the sky in a larger wavelength range and to greater depths than ever before in the infrared. *Spitzer* increased the area observed at these depths, the largest survey being the *Spitzer* Wide-area InfraRed Extragalactic (SWIRE; Lonsdale et al., 2003) survey, covering 50 sq. degs. The AKARI (formerly ASTRO-F) satellite (Murakami et al., 2007) was launched in 2006. This satellite has conducted the first all-sky survey in the Far-Infrared ($65-160\mu$m) since IRAS. In chapter 3 we calculate the completeness and reliability of this survey to assess its usefulness as a probe of infrared galaxies and their environment. The ESA Herschel Space Telescope, launched in 2009 develops the *Spitzer* concept further, extending the wavelength range into the Far-Infrared (FIR) and sub-mm. The NASA Wide-field Infrared Survey Explorer (WISE) satellite was also launched in 2009 and will observe the whole sky a minimum

of 8 times, covering the wavelengths 3.4, 4.6, 12 and 22μm with a resolution of 6″ at the shorter wavelengths and 12″ at the longer wavelengths.

1.5 Galaxy Properties and Environment

With large-scale surveys it is possible to investigate how galaxy properties vary with environment. The environment of a galaxy refers to its location compared to other galaxies. Over-dense environments are often referred to as galaxy groups, which contain a handful of galaxies, and galaxy clusters, which can contain several thousand galaxies. Strictly, a galaxy cluster is an object which is gravitationally bound, with an intracluster gas in hydrostatic equilibrium. However, in the literature (and in the present work) this strict definition is not always applied and many objects referred to as 'clusters' would more accurately be described as groups or galaxy over-densities. This is especially true at high redshift; in chapter 2 the objects we describe as 'cluster candidates' are not virialised structures in the sense of local clusters, rather they are galaxy over-densities and are candidates for the dense environments at these redshifts. However, we refer to them as clusters for brevity.

In order to understand galaxy evolution we must understand the effect that environment plays. The environment of a galaxy is likely to have an impact on its evolution due to interactions with other galaxies or the surrounding inter-galactic medium. Indeed, relationships between the properties of cluster galaxies and 'field' galaxies (i.e. those in under-dense environments) and how this changes with redshift have been studied ever since Abell (1958) produced the first statistical lists of such objects. For example, Butcher & Oemler (1978) found that more distant clusters have a higher fraction of blue galaxies compared to local clusters (the 'Butcher-Oemler' effect). There have been many subsequent studies of the properties of galaxies in different environments (see Blanton & Moustakas, 2009, for a review). We first review the relations observed in the low redshift Universe and follow on by reviewing studies at higher redshift.

1.5.1 Low Redshift

One of the earliest observations of cluster and field galaxies showed that Early type galaxies are preferentially found in clusters whereas field galaxies are typically Late type (Dressler, 1980; Postman & Geller, 1984). This relationship is commonly referred to as the morphology-density relation. This observation has been confirmed with the SDSS and 2dF-GRS surveys (see e.g. Norberg et al., 2002; Goto et al., 2003). This relation exists when

galaxies are considered at fixed luminosity (Weinmann et al., 2006) and persists when a more quantifiable measure, such as colour, is considered. Red galaxies reside preferentially in clusters compared to blue galaxies which tend to reside in the field, referred to as the colour-density relation (Zehavi et al., 2002; Madgwick et al., 2002; Hogg et al., 2004; Blanton et al., 2005). Furthermore, the Star-Formation Rate (SFR)-density relation refers to the trend of a decreasing SFR of galaxies with increasing density (Lewis et al., 2002; Gómez et al., 2003; Kauffmann et al., 2004; Gerken et al., 2004; Balogh et al., 2004a). These relationships all point to clusters containing red, elliptical galaxies which do not form stars in significant numbers and field galaxies being blue, late-type galaxies which are actively star-forming. The luminosity of galaxies also varies with density, more luminous galaxies reside in denser environments (Croton et al., 2005; Popesso et al., 2005). When studied as a function of colour, this relation holds for red galaxies, but the luminosity of blue galaxies does not depend strongly on environment (Hogg et al., 2004). Furthermore, galaxy stellar mass increases with local density (Kauffmann et al., 2004; Li et al., 2006; Baldry et al., 2008; Blanton & Moustakas, 2009). Finally, cluster core galaxies tend to be deficient in HI gas compared to field galaxies which suggests that these galaxies have had their gas removed (eg Giovanelli & Haynes, 1985; Boselli & Gavazzi, 2006; Bravo-Alfaro et al., 2009; Yagi et al., 2010, and references therein).

It is unclear whether these relationships are established early on when the galaxies formed or whether they are due to some environmental evolution, or a combination of the two. It is, however, given the above observations, reasonable to think that at least part of these relations stem from some effect which restricts the star-formation of galaxies in dense environments. Cluster environments may drive the relation as the effects of environment are most significant on group and cluster scales, $\lesssim 1$ h^{-1}Mpc (Kauffmann et al., 2004; Blanton & Moustakas, 2009). When environment is considered at fixed stellar mass or SFR then structural galaxy properties such as size and concentration do not vary with density (Kauffmann et al., 2004; Blanton et al., 2005). This suggests that the quenching of star-formation in high density environments does not arise from processes that alter the structure of a galaxy. However, the gaussian distribution of red and blue galaxies along with an observation that the colour distribution is independent of environment by Balogh et al. (2004b) led those authors to suggest that galaxies evolve independently of environment.

1.5.2 Redshift Evolution

Some of the relationships found locally seem to evolve with redshift. The strength of the morphology-density relation decreases with redshift (Dressler et al., 1997; Postman et al., 2005; Smith et al., 2005; Capak et al., 2007) but Early types are still preferentially found in high density regions out to $z \sim 1.1$ (Meneux et al., 2006; Scoville et al., 2007a; Poggianti et al., 2008). The colour-density relation also weakens with redshift (Coil et al., 2006; Cucciati et al., 2006; Cooper et al., 2006; Coil et al., 2008; McCracken et al., 2008), although it is still present at $z \sim 2.5$ (Daddi et al., 2003; Grazian et al., 2006; Quadri et al., 2007).

As mentioned above, the fraction of blue, spiral galaxies in clusters is larger at high-z while the S0 fraction decreases with redshift and the elliptical fraction stays relatively constant (Butcher & Oemler, 1984; Dressler et al., 1997; Smail et al., 1998; Kodama & Bower, 2001; Postman et al., 2005; Desai et al., 2007b). The implication is that cluster and group galaxies are evolving such that spiral galaxies are transforming into S0 galaxies. The relationship seems to be stronger for clusters with lower velocity dispersion (σ), i.e. those with lower mass (Poggianti et al., 2009b; Just et al., 2010). The transformation of spirals into S0's via galaxy-galaxy interactions (e.g. mergers) are more effective for lower σ systems (see e.g. Icke, 1985) suggesting that such interactions are the primary driver of this observed evolution (Just et al., 2010). A population of dusty red galaxies in the outskirts of a large $z \sim 0.17$ super-cluster is possible further evidence of the transformation of blue star forming galaxies into red passive galaxies (Wolf et al., 2009).

Further evidence for redshift evolution comes from the SFR-density relation. The relation in the local Universe seems to be reversed at higher redshifts. Muzzin et al. (2008) showed that dusty star-forming galaxies are more frequently found in clusters rather than the field by $z \sim 0.65$. Similarly, observations with ISO and *Spitzer* have shown evidence for dust obscured star formation within cluster environments possibly out to $z \sim 0.8$ (see e.g. Fadda et al., 2000; Coia et al., 2005; Geach et al., 2006; Dressler et al., 2009). At $z \sim 1$ the SFR of field galaxies increases with galaxy density (Elbaz et al., 2007; Cooper et al., 2008). Similar results are found at higher redshifts ($1 < z < 1.5$) with a combination of sub-mm and *Spitzer* data in the SCUBA Half Degree Extragalactic Survey (Serjeant et al., 2008). Furthermore, galaxies with large SFRs inferred from their extreme infrared luminosities (Luminous Infrared Galaxies, LIRGs) inhabit dense environments at $0.7 < z < 1.0$ (Farrah et al., 2004, 2006; Marcillac et al., 2008). Although Caputi et al. (2009) found that Ultra-Luminous Infrared Galaxies (ULIRGs) with the very highest SFRs ($\gtrsim 100 M_{\odot} yr^{-1}$) are found in under-dense environments at $0.6 < z < 0.8$. Frost et al.

(2010) used the SWIRE dataset to suggest that at $z \sim 1.4$ environmental effects are more important for triggering star-formation than a galaxy's stellar mass. They also suggested that at $z \sim 0.5$ environmental effects are likely responsible for the quenching of star-formation.

Observations in the optical suggests that at $z \sim 0.6$ the high density regions of clusters contain proportionally fewer star forming galaxies (as defined by the OII equivalent width) than low density regions (Poggianti et al., 2004, 2008, 2009a). Similarly, Vulcani et al. (2010) suggested that star forming cluster galaxies have a lower specific SFR (SSFR, SFR per unit stellar mass) than the field at $z \sim 0.6$.

There is also evidence that the stellar populations of elliptical galaxies are not affected by environmental processes. Comparisons of the colours of cluster elliptical galaxies to stellar population synthesis models are consistent with a population that formed at high redshift ($z \gtrsim 2$) and has evolved passively since then (Ellis et al., 1997; van Dokkum et al., 1998; Gladders et al., 1998; Holden et al., 2005). Furthermore, the K-band, 3.6μm and 4.5μm luminosity functions appear to be similar in both cluster and field environments (Rines et al., 2004; Muzzin et al., 2008). Balogh et al. (2001) do find a difference between field and cluster environments with 2MASS K-band selected galaxies, however, the difference is not highly significant.

Finally, there is evidence that we see environmental effects on galaxies more directly. k+a galaxies are galaxies which show signs of recently truncated star formation and it has been suggested that they are galaxies in a transition phase (see Poggianti et al. (2004) for a review; Poggianti et al. (1999); Tran et al. (2003); Roseboom et al. (2009)). The hypothesis being that star-forming galaxies transition to massive S0 and Sa galaxies (when we see them as k+a's) to passive elliptical galaxies. Higher mass clusters have more k+a's so this seems a plausible hypothesis (Poggianti et al., 2009a; Vergani et al., 2010).

1.5.3 Summary

We see that at low redshift, cluster galaxies tend to be red, elliptical galaxies harbouring old stellar populations with little or no star formation, whereas isolated or field galaxies are young, actively forming stars have blue colours and are generally of late type. There are of course exceptions to these rules, in particular there is a population of field elliptical galaxies. As we move to higher redshifts the fraction of cluster galaxies which are star-forming and are of late type increases. This is evident much more in the infrared than in the optical, suggesting that the star-formation in clusters is largely in dusty galaxies. There

could also be a shift in the predominant environment of star formation from under-dense to over-dense regions by $z \sim 1$. There is still much debate about the physical processes at work and whether relations such as the colour-density relation are in place at the formation of these systems at $z \gtrsim 2$, or whether it is a more dynamical process whereby galaxies are transformed from late types into early types in high density environments. Clearly, further investigations are required, especially at high redshift, to try and understand these different processes. In chapter 2 we identify a large catalogue of cluster candidates (galaxy over-densities) at high redshift ($z \sim 1$ and 1.5) and investigate the effect that environment has on the near and mid-infrared properties of galaxies at $z \sim 1$. The large area at our disposal ($\sim$ 10 sq. degs.) allows us to explore large stellar masses ($\gtrsim 10^{11} M_{\odot}$) in the densest environments. Furthermore, by using mid-infrared (24μm) data we can further explore the obscured star-formation of these high-redshift systems.

1.6 Rare Objects

Astronomy has often been driven by the pursuit of rare or extreme phenomena. Such discoveries challenge existing theories and stimulate new activity, both observational and theoretical. With wide-field surveys it is possible to increase the likelihood of such discoveries. Perhaps the most obvious example of such discoveries, at least in infrared extra-galactic astronomy, is that of Ultra-Luminous Infrared Galaxies (ULIRGs). More recently a large population of highly obscured AGN have been discovered in 24μm surveys (Dust Obscured Galaxies, DOGs). We now discuss each in turn to explore the significance of these discoveries.

1.6.1 Ultra-Luminous Infrared Galaxies

The first hints of a population of extra-galactic sources which were significantly more luminous in the infrared than in the optical was discovered by Rieke & Low (1972). But it was only later, with the launch of IRAS in 1983 that the first samples of ULIRGs were identified with the now accepted definition (infrared bolometric luminosity $L_{ir} \geq 10^{12} L_{\odot}$ Houck et al., 1985). ULIRGs were initially thought to be interesting solely due to their extreme luminosity, being very rare in the local Universe. However, they are much more numerous at high redshift and are thought to play a crucial role in galaxy evolution (see e.g. Lonsdale et al., 2006, for a review). With IRAS the first Hyper-Luminous Infrared Galaxy (HLIRG, with $L_{ir} \geq 10^{13} L_{\odot}$) was discovered in F10214+4724 (Rowan-Robinson et al., 1991). This was an entirely unexpected discovery that implies the formation of a massive

galaxy with a large mass of dust at high redshift, although this object was later shown to be strongly gravitationally lensed (see e.g. Broadhurst & Lehar, 1995). This has added to a body of evidence that structure formation models must satisfy.

Since the initial discovery, many large samples of ULIRGs have been obtained from surveys with ISO and *Spitzer* as well as IRAS (see e.g. Soifer et al., 1987; Sanders et al., 2003; Yan et al., 2007). For some time the power source behind such high luminosities was hotly debated, however, there is now a general consensus that ULIRGs are luminous in the infrared from dust re-processing of light from a combination of starburst and AGN activity. Enhanced AGN activity arises from the rapid accretion of a large volume of matter onto a super-massive black hole, producing strong optical, X-ray and radio emission (see Rees, 1984, for a review). As discussed in section 1.3.1, starbursts are galaxies experiencing an enhanced period of rapid star formation. In either case the UV and optical emission from the power source is absorbed by dust and re-emitted at infrared wavelengths (see Lonsdale et al., 2006, and references therein). Most ULIRGs contain a component of emission from both power sources, although the starburst component is usually dominant, especially for low-redshift systems. Furthermore, nearly all low-redshift ULIRGs show signs of merger activity, which could trigger the enhanced star-formation or AGN activity, (Soifer et al., 1984; Mihos & Hernquist, 1994; Sanders & Mirabel, 1996; Genzel et al., 1998; Farrah et al., 2001; Tacconi et al., 2002; Farrah et al., 2003).

There is much evidence for the evolution of the ULIRG luminosity function with redshift. Surveys with ISO (Rowan-Robinson et al., 1997; Dole et al., 2001; Elbaz et al., 2002; Mann et al., 2002; Verma et al., 2005) and *Spitzer* , along with observations at sub-millimetre wavelengths (Hughes et al., 1998; Eales et al., 2000; Scott et al., 2002; Borys et al., 2003; Mortier et al., 2005), showed that ULIRGs are much more numerous at high redshift, confirming the results obtained with IRAS (Hacking & Houck, 1987; Saunders et al., 1990; Rowan-Robinson et al., 1991; Lonsdale et al., 1990; Lawrence et al., 1999). At redshifts $\gtrsim$ 1 LIRGs and ULIRGs dominate the high redshift star formation rate density and cosmic infrared background (see e.g. Chary & Elbaz, 2001; Franceschini et al., 2001; Lagache et al., 2003; Smail et al., 2002; Blain & Phillips, 2002; Chapman et al., 2004, 2005; Le Floc'h et al., 2005; Daddi et al., 2005; Magnelli et al., 2009).

With *Spitzer* it has been possible to make significant in-roads into studying the high redshift ULIRG population in more detail, with high-resolution, mid-infrared spectroscopy. As at low redshift, high redshift ULIRGs are composite objects powered by both AGN and starbursts, (see e.g. Yan et al., 2005, 2007; Sajina et al., 2007), but they are generally

more luminous. The high redshift population is starburst dominated (Farrah et al., 2009) but there is also a significant population which are AGN dominated (Yan et al., 2007; Polletta et al., 2008a).

Several questions remain, in particular the precise evolution of ULIRGs is still unknown. For example, while it is clear that most ULIRGs have merger triggered starburst and/or AGN activity it is unclear how long the starburst lasts, what the connection is between starburst and AGN activity, and whether ULIRGs go through different phases, for example harbouring buried AGN (see e.g. Farrah et al., 2009).

1.6.2 Dust Obscured Galaxies

Surveys at 24μm revealed another population of objects that had been previously missed. These are objects which are extremely faint in the optical, most likely due to dust obscuration, but very luminous in the infrared. The IRS spectra of a sample of such objects obtained by Houck et al. (2005) showed that most of these $z \gtrsim 2$ objects are powered by AGN with similar spectral shapes to ULIRGs but with $L_{ir} > 10^{13} L_{\odot}$. These results were confirmed by Weedman et al. (2006a,b) who showed that for $F_{\nu}(24) > 1$ mJy the high-z mid-infrared source counts are dominated by AGN. These objects had been missed in previous surveys of AGN.

Following this discovery, Dey et al. (2008) developed a selection technique to identify these extremely dusty high-redshift galaxies in a clean and systematic way in order to obtain a complete census of the population. Their selection was based on the ratio between 24μm and R-band emission ($R - [24] \geq 14$ (Vega mag) and $F_{24} \geq 0.3$ mJy), identifying a sample of $\sim$ 2600 DOGs over $\sim$ 8.6 sq. degs. in the NOAO Deep-Wide Field Survey Boötes field. This method selects a sample of galaxies at $z \sim 2$ which contribute $\sim$ 26% of the total infrared luminosity density contributed by all galaxies at this redshift (Weedman et al., 2006c; Dey et al., 2008). These galaxies have unusually red spectral energy distributions and do not have local equivalents.

DOGs are strongly clustered, with more luminous DOGs residing in richer environments (Brodwin et al., 2008). The similarity between the DOG clustering, redshift distribution and space density to those of sub-millimetre galaxies (SMGs with extreme star-formation rates see e.g. Blain & Phillips (2002) for a review) suggests a link between these two populations. Pope et al. (2008) showed from a sample of DOGs in the GOODS-N survey that the majority of their sample are dominated by star-formation and that they contribute 5-10% to the star formation rate density at $z \sim 2$. However, they also showed

that DOGs are 8 times less luminous and 3 times more numerous than SMGs. Observations with Keck suggest only a fraction of DOGs are ongoing mergers (Melbourne et al., 2009) and observations with *Hubble* suggest they are generally more relaxed systems than local ULIRGs and that they most likely represent a post-merger stage (Bussmann et al., 2009). An X-ray stacking analysis confirmed previous results that these objects are highly obscured AGN (Fiore et al., 2008; Georgantopoulos et al., 2008).

One tantalising possibility is that these DOGs are the highly obscured AGNs required to explain the X-ray background. At present, surveys with the state of the art X-ray telescopes *Chandra* and *XMM-Newton* (Weisskopf et al., 2000; Jansen et al., 2001) are only able to resolve ∼50-60% of the cosmic X-ray Background (CXRB) in the 5-10 keV band (Worsley et al., 2004, 2005) and only a few percent has been resolved in the 10-100 keV range (Krivonos et al., 2005). In order to explain this discrepancy a heavily obscured population of AGN is usually invoked (see e.g. Brandt & Hasinger (2005) for a review). In particular, a population with an obscuring matter with column density $N_H \gtrsim 1.5 \times 10^{24}$ cm^{-2} (which corresponds to the inverse of the Thomson scattering cross-section) known as Compton Thick AGN are often favoured (see e.g. Comastri, 2004, for a review). X-ray surveys are unable to find such Compton Thick AGN and therefore unable to obtain a complete census of AGN. Lanzuisi et al. (2009) obtained X-ray spectroscopy of a sub-sample of the most extreme DOGs (with $F_{24}/F_R > 2000$ and $F_{24} > 1.3$mJy) and combined it with archival X-ray data to show that 50% of the selected sources have column densities $> 10^{22}$cm^{-2} and that three are likely to be Compton thick AGN. They also showed that their selection criteria selects high-z sources occupying the bright end of the X-ray luminosity function.

1.6.3 Our Search

The high-redshift ULIRG, sub-millimeter galaxies have presented a challenge to theoretical models which are unable to simultaneously reproduce these high redshift luminous galaxies with large masses of cold dust as well as the abundance of bright, local galaxies (Baugh et al., 2005; Swinbank et al., 2008). In chapter 4 we conduct a search for a sample of the most extreme galaxies observable with *Spitzer* by requiring high 24μm to NIR flux density (flux hereafter) ratios. The SWIRE survey is the largest survey with the *Spitzer* telescope covering ∼50 sq. degrees. As such it is ideally suited to the discovery of such rare and extreme objects. We present the discovery of 4 objects with very red colours, the most extreme having a 24μm to 3.6μm flux ratio ($F_{24}/F_{3.6}$) of 470. The

objects are reliably identified from the detection in two independent MIPS (Multiband Imaging Photometer for *Spitzer* Rieke et al., 2004) 24μm images but do not have catalogue detections in the shorter wavelength *Spitzer* bands. In order to further characterise these objects, and specifically in the hope of obtaining a redshift, we undertook follow-up spectroscopy with the Infrared Spectrograph (IRS; Houck et al., 2004) aboard *Spitzer* and have additional data from the CFHTLS and the Max Planck Millimetre Bolometer Array (MAMBO; Kreysa et al., 1998) instrument on the 30m Institut de Radioastronomie Millimétrique (IRAM) antenna at Pico Veleta.

1.7 Thesis Summary

In this thesis we investigate several aspects of galaxy evolution. We have given a brief introduction to the subject of galaxy evolution in the context of the Universe as we know it today. We have discussed infrared surveys of galaxies as a tool for studying galaxy evolution. Initially, in chapter 2, we are interested in the large scale environment of galaxies. We identify a large sample of galaxy cluster candidates at $z \sim 1$ and $z \sim 1.5$, significantly increasing the sample size of these high redshift objects. Using this catalogue we compare the mass and star-formation properties of galaxies in the cluster and field environments. To take this further we look to the AKARI all-sky survey and assess the potential of this survey for future studies. We calculate the completeness and reliability of the survey in chapter 3. Such wide surveys also allow for the possibility of studying rare and extreme phenomena. Such phenomena can push theories of galaxy evolution to their extremes and help to constrain them. In chapter 4 we present the discovery of four such objects in the SWIRE survey which have extremely red spectral energy distributions. Finally, since environment plays a large role in the evolution of galaxies we extend this investigation to smaller scales. In chapter 5 we study the host galaxies of Type Ia supernovae. We calculate the ages of the host galaxies of a sample of high redshift SNe Ia and calculate the delay time distribution of these explosions (the delay time is the time between the formation of the binary system and the supernova explosion). These calculations have implications for the progenitors of SNe Ia and their use as standardisable candles.

Chapter 2

Cluster Candidates in the SWIRE/DXS survey at Redshifts ~ 1 and ~ 1.5 Selected Using the 1.6μm Bump

2.1 Introduction

As we have seen, environment plays a large role in the evolution of galaxies. By studying the relationships between galaxy properties and their environment we can begin to quantify what effect environment has. In particular, the role of environment at high redshift remains unclear. This is largely due to the difficult nature of identifying large samples of high-redshift clusters in order to probe the densest environments. In this chapter we identify a large catalogue of high redshift cluster candidates and compare the properties of galaxies located within these environments to the field population. Before we can do this, however, we must in some way characterise the local environment of a galaxy. Therefore, we first give a brief review both of such estimators and of techniques for cluster finding.

The work presented in this chapter was done with supervision from S. Oliver and collaborators. Notably, the IRAC completeness curves were produced by M. Vacari, UKIDSS masks were produced using a method produced by E. Gonzalez and the figures of the bump feature in SED templates, their colour evolution with redshift, along with the redshift of VVDS and photo-z bump galaxies were adapted from preliminary versions produced by I. Roseboom. Part of this work, together with additional *Herschel* data, is being pursued for publication by collaborators.

2.2 Density Estimators

A number of different methods have been employed to characterise the local environment of a galaxy. These are separated into methods which study the members of clusters and groups to field populations and those which measure the local space density of galaxies for all galaxies in a survey. We first consider such estimators and then review cluster finding.

2.2.1 Estimating Local Galaxy Density

One of the earliest methods for measuring the space density of galaxies is known as the nth nearest neighbour method (Dressler, 1980). In this method the distance, d, from the target galaxy to the nth nearest galaxy is calculated either in projection or in 3D space, where n is typically 3, 5 or 10. In either case the surface density is calculated as $n/\pi d^2$ for the projected distance and $n/\pi d^3$ when d is in 3D. An alternative method is to simply count the galaxies within an aperture, which is either a sphere or a cylinder, effectively smoothing the data over some volume. A third method is the Voronoi volume method, based on Ebeling & Wiedenmann (1993); Ramella et al. (2001); Kim et al. (2002); Marinoni et al. (2002). In this method the density for each galaxy is measured according to the area or volume of a cell which contains the galaxy in question. The boundary of the cell is defined as the points that lie closer to its constituent galaxy than to any other. In a thorough examination of each of these methods with mock catalogues, Cooper et al. (2005) showed that to estimate environment in this way spectroscopic redshifts are required, the large errors of photometric redshifts smearing out the density measure. They also examined these methods with real data from the Deep Extragalactic Evolutionary Probe 2 (DEEP2; Davis et al., 2003) spectroscopic survey. They found that the most accurate method is that of the projected nth nearest neighbour, but also note that (except the counts in an aperture measure) all methods produced spurious results near to survey edges. This is particularly problematic for small surveys. Additional methods include the friends-of-friends algorithm, which groups galaxies together which are closer together than some projected distance (Huchra & Geller, 1982). The adaptive kernel technique is a measure of overdensity whereby the distribution of galaxies in position (and redshift) space are smoothed with a kernel which varies according to the local density of galaxies (see e.g. Biviano et al., 1996, and references therein). Schawinski et al. (2007) developed a method which combined the nth nearest neighbour method with an additional weighting for closer galaxies in redshift space (to account for peculiar velocities). Finally, the method of Eisenstein (2003) which estimates density from a cross-correlation of imaging and spectroscopic catalogues,

weighting the number of imaging objects by a gaussian window function.

These methods calculate the environment of individual objects. An alternative approach is to measure the global environment of galaxies. The most popular such method is that of the correlation function, which measures the excess probability of finding a galaxy in a volume or angle element on the sky compared to a random distribution of galaxies (Peebles, 1980). Such methods have produced many interesting results (see e.g. Coil et al., 2008; McCracken et al., 2008, and references therein and several of the above works). Such works do, however, require spectroscopic redshifts and/or a careful analysis of the photometric redshift selection function in order to extract astrophysically relevant values (eg Frost et al., 2010).

2.2.2 Cluster Finding

The alternative to a local galaxy density measure is that of cluster finding (although in many cases this requires first calculating a local galaxy density, see below). This has the advantage that it picks out the densest environments and does not necessarily require spectroscopic redshifts. It can therefore be done over a wider area. However, it is still a great observational challenge to identify high-redshift ($z \gtrsim 1$) clusters, especially rare, rich clusters which have the most extreme environments.

X-ray Detection

Galaxy clusters emit strongly in the X-ray due to Bremsstrahlung radiation from the electrons in the inter-cluster medium (Sarazin, 1986). As such, many clusters have been found from large X-ray surveys such as the all-sky survey with *ROSAT* (see e.g. Rosati et al., 2002, for a review). This technique first searches for extended sources in X-ray images (Rosati et al., 1995; Lazzati et al., 1999). Cluster galaxies are then confirmed using either spectroscopic or photometric redshift determinations (Finoguenov et al., 2007, 2009; Andreon et al., 2005). There have been a number of surveys identifying clusters using *ROSAT* pointed observations data. Examples include the Serendipitous High-Redshift Archival *ROSAT* Cluster (SHARC) survey, Romer et al. (2000), which identified 37 clusters up to redshifts of 0.83, and the Wide Angle *ROSAT* Pointed Survey (WARPS Scharf et al., 1997; Perlman et al., 2002; Horner et al., 2008) in which 125 clusters up to redshifts of 0.9 were identified. The *ROSAT* cluster surveys all followed from those using the earlier *Einstein* space observatory, such as the *Einstein* Observatory Extended Medium Sensitivity Survey (EMSS Gioia et al., 1990). More recently,

the *Chandra* (Weisskopf, 2000) and in particular the *X-ray Multi-Mirror Mission-Newton* (*XMM-Newton* Jansen et al., 2001) satellites have made further progress in this field. The largest survey looking for X-ray clusters is the $XMM-Newton$ Cluster Survey (XCS; Romer et al., 2001). The XMM Large Scale Structure Survey has also found X-ray clusters, Valtchanov et al. (2004) identified 5 clusters at $z > 0.6$. The furthest spectroscopically confirmed X-Ray cluster currently known was identified from a wavelet analysis of $XMM-Newton$ data by Henry et al. (2010) with $z = 1.75$.

Cluster Finding in Galaxy Surveys

While X-ray cluster searches have a high reliability (i.e. there are very few false positives) they lack the depth and wide-area necessary for large samples, especially at high redshift. Due to the small numbers of X-ray clusters that have so far been identified, many studies have used optical and near infrared galaxy surveys to look for clusters. Such studies are able to produce statistically significant samples of clusters, especially at low-z with the large SDSS and 2dFGRS surveys. These studies can also achieve much higher redshifts, with proto-clusters identified out to $z \sim 6$, primarily from Lyman-α emission (Overzier et al., 2006; Ouchi & SXDS, 2007; Pentericci et al., 2000; Venemans et al., 2002, 2005, although we note that these objects are not the virialised structures identified in lower redshift searches).

The most reliable cluster searches make use of spectroscopic redshifts. Typically, these involve the application of a local galaxy density measure as described in section 2.2.1 and identifying peaks in the resulting density map as cluster candidates. The first large area spectroscopic redshift survey reaching beyond the local super-cluster was the CfA Redshift Survey (Davis et al., 1982; Huchra et al., 1983) which found 176 low redshift groups and clusters (Huchra & Geller, 1982). Since then many such surveys have been conducted, we list a few examples. Yoon et al. (2008) identified 924 clusters in the range $0.05 < z < 0.1$ in a spectroscopic SDSS sample using an adapted version of the Schawinski et al. (2007) algorithm. 7000 groups with at least 4 members are found in the 2dFGRS by Norberg et al. (2003) using a friends-of-friends algorithm. 899 groups and clusters have been found with the DEEP2 survey in the range $0.7 < z < 1.4$ using the Voronoi method (Gerke et al., 2005). In the VIMOS (Visible MultiObject Spectrograph) VLT (Very Large Telescope) Deep Survey (VVDS; Le Fèvre et al., 2005) deep field Cucciati et al. (2009) also used a Voronoi method to identify a sample of 144 groups up to $z \sim 1$. Knobel et al. (2009) used the zCOSMOS 10k sample covering 1.7 sq. degs. to find ~ 286 groups of at least 3

galaxies using a Friends-of-Friends and Voronoi technique out to $z \sim 1.1$.

However, such surveys are limited by their size, the largest of the above high-z works being the 3 sq. degs. of the DEEP2 survey. Only 39 of the cluster candidates found by Gerke et al. (2005) contain at least 3 galaxies, have $\sigma \geq 350$ km s^{-1} and $z \geq 0.9$. The only practical way to identify large samples of high redshift clusters is from imaging surveys over large areas of sky. Such surveys have been used to search for galaxy clusters for some time. While initially these involved eye-balling optical images (see e.g. Abell, 1958) for apparent increased overcrowding of objects compared to the average, the digitisation of photographic plates and the following development of CCD cameras have allowed automated methods to be used. The first machine-based cluster finder was that of Lumsden et al. (1992) which used the Edinburgh-Durham Galaxy Catalogue to identify 737 clusters, searching for galaxy over-densities by binning and smoothing the galaxy catalogue together with a calculation of the Abell radius (the angle on the sky subtended by a fixed comoving radius at the cluster Abell, 1958). A similar method was that of Dalton et al. (1997) who used the APM Galaxy Survey to identify a list of 957 cluster candidates up to a redshift of ~ 0.2. Another early automated cluster finder was the matched filter algorithm developed by Postman et al. (1996). This was based on a single passband to identify clusters in the Palomar distant cluster survey, using typical cluster luminosity functions and radial profiles. Using a similar method Postman et al. (2002) identified 444 clusters in the redshift range $0.2 < z < 1.2$ over a 16 sq. deg. I band survey. This method has been extended to include additional passbands in many further searches, including the identification of 302 clusters at $z \sim 0.5$ over 7 sq. degs. in the ESO Imaging Survey (Olsen et al., 1999; Scodeggio et al., 1999); 162 clusters at similar redshifts over the ~ 3 sq. degs. of the Deep CFHTLS survey (Olsen et al., 2007), which was subsequently extended by Grove et al. (2009) to ~ 350 clusters.

Alternative methods can be based on the properties of the cluster population. Elliptical galaxies in clusters show a tight correlation between colour and magnitude, brighter ellipticals are also redder. This correlation is known as the cluster red-sequence and was first noted in clusters by Bower et al. (1992). The cluster red-sequence has been shown to exist to high redshift (see for example Gladders et al., 1998; Ellis et al., 1997; Stanford et al., 1998, 2006; Andreon et al., 2005, 2009; Wilson et al., 2009, and references therein). This correlation shows little variation between different clusters, and can be used to measure the redshift of the cluster to high accuracy (García López et al., 2000). By using two passbands which straddle the 4000Å break (to efficiently remove foreground

galaxies) clusters can be identified as an over-density of galaxies in position and colour space (Gladders & Yee, 2000, 2005). This technique was used in the Red Sequence Cluster Survey (RCS; Gladders & Yee, 2000, 2005) to produce a catalogue of $\sim$ 1000 clusters up to $z \sim 1$ over $\sim$ 90 sq. deg. This survey is currently being expanded to cover $\sim$ 1000 sq. degs (Yee et al., 2007).

The red-sequence method has been extended to include other cluster properties. At or near the centre of local galaxy clusters are giant, bright elliptical galaxies which are significantly larger and brighter than other cluster galaxies. They are referred to as the Brightest Cluster Galaxy (BCG). By looking for the combination of a red-sequence over-density and the presence of a BCG, clusters can be more reliably identified (Annis et al., 1999; Koester et al., 2007a). This algorithm (the maxBCG code) has been used to identify nearly 14,000 low-z clusters in SDSS (Bahcall et al., 2003; Koester et al., 2007b).

The red-sequence technique has also been adapted for use with Infrared data. Muzzin et al. (2008) used R-[3.6μm] colours to identify 99 cluster candidates in the *Spitzer* First Look Survey (FLS; Marleau et al., 2004; Lacy et al., 2005; Frayer et al., 2006), 29 of which are spectroscopically confirmed. This work was a precursor to a much larger survey to detect clusters with *Spitzer*, the *Spitzer* Adaptation of the Red-sequence technique (SpARCS; Wilson et al., 2006). This survey is combining z'-band observations[1] with the SWIRE survey to identify clusters in the redshift range $1 < z < 2$ (Wilson et al., 2005). Currently 6 spectroscopically confirmed clusters have been published from this survey (Wilson et al., 2009; Muzzin et al., 2009; Demarco et al., 2010).

However, it is possible that such methods introduce a bias in cluster detection. Clusters which have only a weak red-sequence are less likely to be detected. This means that clusters containing galaxies with recent star formation could be missed as will galaxy-overdensities of blue galaxies such as that found by Steidel et al. (2005) at high redshift. This problem is likely to increase with redshift as one approaches the redshift of formation of the cluster. Furthermore, the red-sequence can become a mixture of galaxy types, including both young star forming galaxies as well as old passive ellipticals in the reddest of the SDSS filters (Miller et al., 2005). This led Miller et al. (2005) to develop an algorithm to search for clusters in a 7-D position and colour space. Although still requiring that cluster galaxies have *similar* colours, this method was used to identified a cluster catalogue of 748 clusters over an area of $\sim$2,600 sq. degs. out to $z = 0.17$ with SDSS.

Several authors have previously compared the effectiveness of different techniques on

[1]with the Canada France Hawaii Telescope (CFHT) and the Cerro Tololo Inter-American Observatory

SDSS data. Kim et al. (2002) compared the matched filter technique to the adapted matched filter algorithm of Kepner et al. (1999) and to a Voronoi method. Goto et al. (2002) compared their own method, combining spatial over-densities with simple colour cuts, to the maxBCG method, matched filter and Voronoi methods. Although each method has a large overlap in the clusters they detect, each identifies a different set of clusters due to the different selection effects. Although Kim et al. (2002) preferred a combination of the methods of Postman et al. (1996) and Kepner et al. (1999). In view of their orthogonality, Bahcall et al. (2003) used the maxBCG method and the hybrid matched filter method of Kim et al. (2002) to produce a combined cluster catalogue. Similar results are obtained by Lopes et al. (2004) who combined a Voronoi method with an adaptive kernel method.

Alternative methods for cluster identification take advantage of the magnifying and distorting effects of a cluster on background galaxies in the form of both strong (see e.g. Cabanac et al., 2007; Limousin et al., 2009) and weak gravitational lensing (see e.g. Gavazzi & Soucail, 2007; Bergé et al., 2008). However, samples of clusters detected in this way are still small, for example the search of Bergé et al. (2008) found 6 clusters over ~ 4 sq. degs.

Finally, photometric redshift surveys have been used to find high redshift clusters. Eisenhardt et al. (2008) used the photometric redshifts of the *Spitzer* Infrared Array Camera (IRAC; Fazio et al., 2004) shallow survey (Brodwin et al., 2006) to identify 335 cluster and group candidates, with 106 at $z > 1$, over an area of 7.25 sq. degs. Zatloukal et al. (2007) used H-band data in combination with COSMOS data to find 12 clusters over a 0.66 sq. deg area at $z > 1$. By constructing a density map using an adaptive kernel technique in bins of photometric redshift Adami et al. (2010) identified 1,200 clusters in the CFHTLS out to $z \sim 1.5$. This extended the earlier work of Mazure et al. (2007) who used a similar technique to successfully identify all XMM-LSS clusters in the overlap region of their 0.8 sq. degs. dataset from the CFHTLS. By combining a friends-of-friends density measure with the Voronoi measure van Breukelen et al. (2006) found 13 clusters in the Early Data Release from the UKIDSS UDS in the range $0.6 < z < 1.4$. This method also included the photo-z probability distribution to increase the reliability.

2.2.3 Introduction to Our Method

We have seen that there are a number of different methods both for estimating the galaxy density in a survey and of identifying clusters. In order to accurately characterise a density map to investigate the variation of galaxy properties with density continuously, spectro-

scopic redshifts are seemingly required. However, since spectroscopic surveys do not cover the wide areas and high redshifts necessary to probe the densest environments we instead use the *Spitzer* Wide-Area Infrared Extragalactic (SWIRE; Lonsdale et al., 2003) survey and the UK Infrared Telescope (UKIRT) Infrared Deep Sky Survey (UKIDSS; Lawrence et al., 2007) Deep eXtragalactic Survey (DXS) imaging surveys to look for the most extreme densities at redshift ~ 1 and 1.5. We then separate our galaxies into cluster and field galaxies in order to compare the populations of the different environments. We use a similar, albeit simpler, technique to that of Mazure et al. (2007). We estimate a density map with a simple counts-in-cells method. While this method is perhaps not the most accurate it is a simple method that can easily be reproduced and in any case will accurately identify the highest densities. Since we do not have spectroscopic redshifts at our disposal over the large area we are interested in, a more sophisticated density estimate is unlikely to yield more accurate results. We calculate this density map and hence perform a cluster search in 2 redshift slices, out to $z \sim 1.5$. By looking for clusters in this way we avoid any requirement of the presence of a red-sequence or assumptions on the cluster luminosity or radial profile. 15 cluster candidates, 6 of which have spectroscopic confirmation have already been identified using the DXS data in this region (Swinbank et al., 2007). This cluster search looked for galaxy over-densities in slices of colour-magnitude space to identify red-sequences. Candidate cluster galaxies were followed-up with optical spectroscopy on the Gemini Multi-Object Spectrograph to confirm them. This only used an area of 0.74 sq. degs. and as such we hope to vastly increase the number of DXS identified clusters.

2.3 Data

The primary dataset for this work is the SWIRE survey. The survey consists of moderate depth, near-to-far IR imaging of 6 fields across all of the *Spitzer* bands. Full details of the survey can be found in Lonsdale et al. (2003). The fields observed for the survey are shown in table 2.1. The survey was designed to cover as large an area as possible whilst achieving enough depth to allow detection of high redshift objects. The final survey covered $\sim$49 sq. degs. giving a comoving volume of $\sim$0.2 $h^{-3}Gpc^3$ to $z = 2$. The survey makes use of all filters of both the Infrared Array Camera (IRAC; Fazio et al., 2004) and Multiband Imaging Photometer for *Spitzer* (MIPS; Rieke et al., 2004). The IRAC instrument consists of four broad-band cameras which observe the sky simultaneously. The four bands are centred at 3.6, 4.5, 5.8 and 8.0μm, each of which have 256$\times$256

Table 2.1. The central J2000 co-ordinates of the SWIRE fields and the area covered in each of the IRAC and MIPS bands.

Field Name	RA	Dec	IRAC Area	MIPS Area
	h m s	deg ′ ″	[sq. degs.]	[sq. degs.]
ELAIS-S1 (ES1)	00 38 30	−44 00 00	6.8	7.9
ELAIS-N1 (EN1)	16 11 00	+55 00 00	9.3	10.7
ELAIS-N2 (EN2)	12 36 48	+41 01 45	4.2	5.9
CDFS	03 32 00	−28 16 00	7.7	9.1
Lockman Hole	10 45 00	+58 00 00	11.1	12.7
XMM-LSS	02 21 00	−5 00 00	9.1	10.6

detector array pixels with a 5.′12×5.′12 field of view. The MIPS instrument consists of three broad-band cameras which also image simultaneously, centred at 24, 70 and 160μm. The detectors have 128×128 pixels, 32×32 pixels and 2×20 pixels with angular resolutions of 6″, 18″ and 40″ for the 24, 70 and 160μm bands respectively. The area of each SWIRE field covered by both the IRAC and MIPS instruments are given in table 2.1 and the depths reached in each band across the whole survey are shown in table 2.2. The SWIRE data used in this and subsequent chapters are the latest SWIRE team catalogues (see Surace et al., 2005, for details of the data reduction). In the present work we use the superior depth and spatial resolution of IRAC for cluster detection. We later use the 24μm data to assess the obscured star formation in different environments.

In addition to the *Spitzer* data we use K-band imaging from the UKIDSS DXS and Ultra Deep Survey (UDS). Further details of the UKIDSS survey can be found in Lawrence et al. (2007). The DXS survey is a wide field survey with the Wide Field Camera (WFCAM; Casali et al., 2007) on the 3.8m UK Infrared Telescope, utilising the JK near-infrared filters centred at 1.2 and 2.2μm respectively. The photometric system is described in Hewett et al. (2006) and the WFCAM science archive (from which we obtained the catalogues) and pipeline processing are described in Hambly et al. (2008); Irwin (2008). The DXS plans to image 4 fields (35 sq. degs) to a depth of 22.5 and 21.0 Vega magnitudes in J and K respectively. The UDS is a single UKIRT pointing field located within the XMM-LSS field which will be imaged in JHK to depths of ∼25, 24, 23 Vega magnitudes. For the work presented here we utilise the DR5 release of both the DXS and UDS data, which have an approximate depth in K of $20-21.2$ and 22.3 Vega magnitudes

Table 2.2. The 5σ estimated survey limits of the SWIRE survey[a] for each of the IRAC and MIPS filters, denoted by their effective wavelengths λ.

λ [μm]	5σ Sensitivity [μJy]
IRAC	
3.6 (Ch1)	3.7
4.5 (Ch2)	5.4
5.8 (Ch3)	48
8.0 (Ch4)	37.8
MIPS	
24	230
70	18 [mJy]
160	150 [mJy]

[a]http://swire.ipac.caltech.edu/swire/astronomers/program.html

respectively, in the fields utilised here. Earlier data releases are described in Warren et al. (2007a,b); Dye et al. (2006). A summary of the DXS and UDS data we use is shown in table 2.3. We now assess the sensitivity of the above datasets for their use in cluster searches via a calculation of the 'completeness' of the surveys.

Table 2.3. UKIDSS DXS and UDS DR5 fields used, areas and depths. DXS depths are calculated as the average depth achieved across the field and are given in Vega magnitudes. UDS depth is from http://surveys.roe.ac.uk/wsa/dr5plus_release.html. Areas are given in square degrees, including the total area of overlap between the SWIRE IRAC and the K-band surveys. RA and Dec are J2000 Co-ordinates.

Field Name	RA	Dec	Area	IRAC/K overlap	K-band Depth
	h m s	deg ′ ″	[sq. degs.]	[sq. degs].	[Vega mag]
ELAIS-N1	16 10 00	+54 00 00	4.33	4.33	20.5
Lockman Hole	10 57 00	+57 40 00	3.06	3.04	20.7
XMM-LSS	02 25 00	−4 30 00	2.37	2.25	20.3
UDS	02 18 00	−05 10 00	0.75	0.74	22.3

2.3.1 Completeness

An astronomical survey will be limited by the sensitivity of the instrument used for the survey and the efficiency of the source extraction software. At a given flux the fraction of sources that we detect with our survey compared to the real number of objects on the sky decreases as we go to fainter fluxes. This fraction is the 'completeness' of the survey. As well as being a function of flux, completeness will be a function of position, due to different exposure lengths and different observing conditions (in the case of ground-based data). This has serious implications for cluster detection - we must account for the fact that we will detect different numbers of galaxies depending on where we are looking in the sky and in which band we are observing, as well as when we compare galaxies of different fluxes.

Within each SWIRE field the integration time of *Spitzer* data varies with position due to the dithering pattern of the scan strategy and overlap between rotated scans. This variation is described by the coverage maps produced by the data reduction team. Each coverage map pixel gives the number of images obtained in each channel. These maps also include corrections for bad data removal (e.g. due to cosmic ray hits). The IRAC completeness was calculated by the SWIRE team for the average coverage level by injecting synthetic sources with different fluxes into the data, running the source extraction software and calculating what fraction of the synthetic sources are found as a function of flux (M. Vaccari, priv. com.). Figure 2.1 shows the resulting IRAC completeness curves for the EN1 and EN2 fields averaged together and for the XMM field. Completeness curves for the remaining fields were not produced by the SWIRE team as the average of the EN1 and EN2 curves should provide good estimates for the CDFS, Lockman and ES1 fields. The high galactic latitude of the XMM field means that this field is slightly noisier and is thus treated separately. We limit the catalogues to have 50% completeness (averaged over coverage) corresponding to $F_{36} > 4.2\mu$Jy, $F_{45} > 6.5\mu$Jy, $F_{58} > 36\mu$Jy and $F_8 > 37.5\mu$Jy. Where F_{36} is the flux in the 3.6μm IRAC band and similarly for the other bands.

We calculate the completeness of the K-band data by taking the ratio of the number counts of the DXS to the deeper, UDS data. This is a well known method to calculate completeness (see e.g. Moshir et al., 1992). To calculate the number counts, we first remove any spurious sources. Bright, extended objects can saturate the detectors, leading to spurious sources being identified by the source extraction software. We therefore remove objects which are near $K < 12$ (AB mag) 2MASS objects, following Waddington et al. (2007). In this procedure we generate a simple binary mask of the area imaged by the

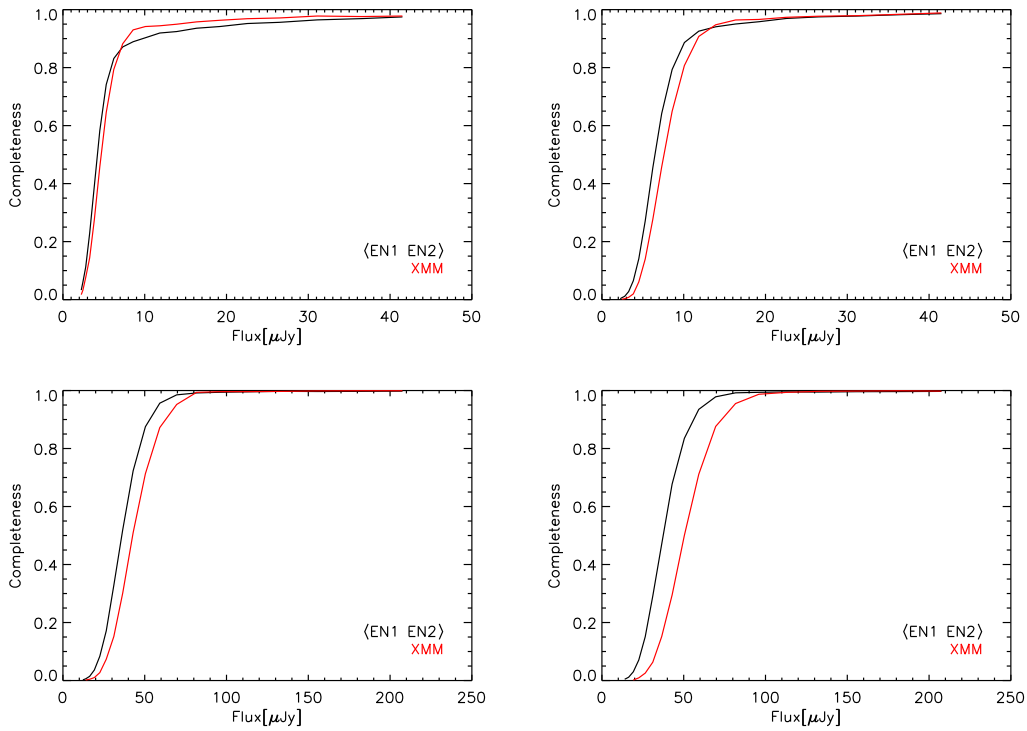

Figure 2.1: The IRAC completeness curves. Top-left is 3.6μm; top-right is 4.5μm; bottom-left is 5.8μm; bottom-right is 8.0μm. In all cases completeness is shown for average coverage. The IRAC completeness is estimated from the injection of synthetic sources.

survey and remove the effect of these bright stars by masking out a circle of radius R'' around the star positions, where $\log_{10}(R) = 3.1 - 0.16[K]$. We then separate the DXS data into regions of similar quality due to a varying depth within each field. Using the sky noise, aperture corrections and exposure time as a function of position, we bin together areas of the sky which have similar magnitude limits (E. Gonzalez, priv. com.). In each of these regions of similar quality we bin the galaxies into magnitude bins and do this again for the deeper, UDS dataset (using the same magnitude bins). The resulting number counts for each region and for the UDS dataset, normalised by area, along with the completeness curves obtained by the ratio of these are shown in figure 2.2. There is an excess of objects in the DXS compared to the UDS in some regions, and especially in the EN1 field. The reason for this discrepancy is unclear. The EN1 field is closer to the galactic plane than the UDS field and thus there could be a larger number of stars in the EN1 field. The UDS number counts we find here are consistent with the UDS DR1 counts of Hartley et al. (2008). For both the UDS and DXS the area used to normalise the number counts is calculated as the area of a single mask pixel multiplied by the number of pixels with good coverage and which are not in the vicinity of a bright 2MASS star. We also exclude the northern most portion of the UDS field which has a reduced depth. At the bright end ($K \lesssim 20$ petrosian, Vega mag) the completeness increases above unity due to this excess. Due to this uncertainty we take a conservative K-band limit selecting only galaxies with $K \leq 20$ (petrosian, Vega mag). This limit is less than the depths for all fields given in table 2.3 and should give a complete sample.

2.4 Bumps Selection

Using the above datasets we look to identify galaxy over-densities in three well-defined redshift ranges. Elliptical, Spiral and Starburst galaxies all show a "bump" feature in their spectral energy distribution (SED) at 1.6μm. This bump arises from a minimum in the H^- ion opacity in the atmospheres of cool stars (see e.g. John, 1988; Simpson & Eisenhardt, 1999). By selecting objects which show a peak in one photometric band compared to bands blue-ward and red-ward of it, galaxies can be selected in a particular redshift range. Comparisons between the Hubble Deep Field $JHKL$ photometry and photometric redshifts by Sawicki (2002) showed that this feature can be successfully used as a photometric redshift indicator. The possible application of this technique to the *Spitzer* datasets was first noted by Wright et al. (1994) and developed further by Sawicki (2002). This technique has since been used with *Spitzer* several times (Farrah et al., 2006; Berta et al., 2007; Farrah et al.,

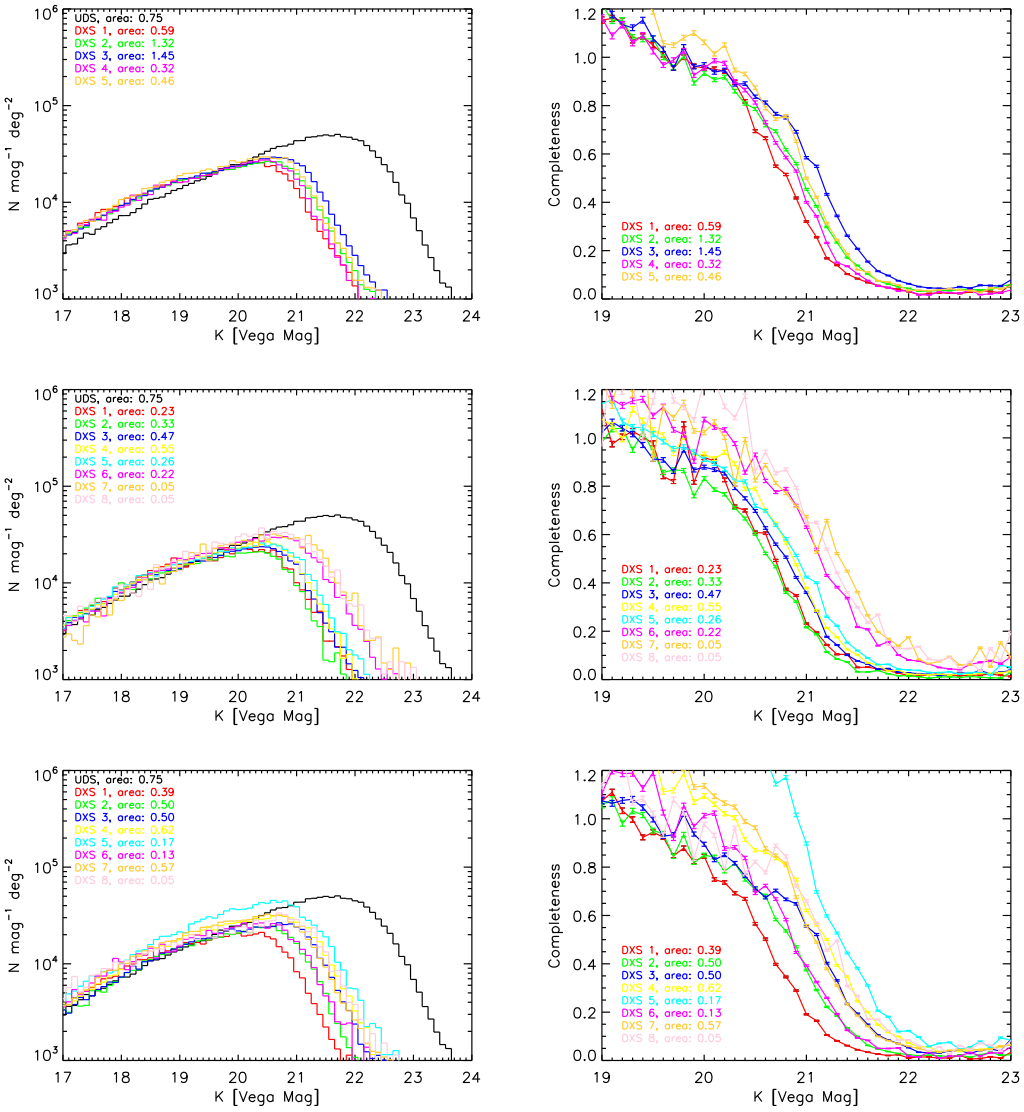

Figure 2.2: Number counts for the DXS and UDS K-band (left hand panels) with the resulting completeness curves in the right hand panel. Each row shows a different field, from top to bottom these are EN1, XMM and Lockman Hole. In each case the UDS number counts (normalised by area) are shown in black and the number counts for the various different regions within the DXS field are as given in the plot legend. The completeness is calculated as the ratio between the DXS number counts and the deeper UDS number counts.

2008) demonstrating its power. In these works, the bump is identified by an excess in the 4.5μm or 5.8μm bands compared to both the shorter and longer IRAC bands to obtain samples of galaxies at $z \sim 2$ and $z \sim 3$ respectively. By combining the *Spitzer* data with the shorter wavelength K-band data of the UKIDSS DXS we can also obtain a sample of $z \sim 1$ galaxies which have an excess in the 3.6μm band. We cross-match the DXS K-band and SWIRE IRAC catalogues using a radius of $1''$ (only including the nearest match) using the Virtual Observatory software *topcat*, (Taylor, 2003) to produce a combined catalogue of objects with IRAC and DXS photometry.

The concept of using simple photometric colours to identify high redshift galaxies has been used many times previously. For example, the Lyman break technique - looking for galaxies detected in one band but not detected in an adjacent, bluer, band as the Lyman break is located between them was originally used by Steidel et al. (1996) in the Hubble Deep Field to find $z \sim 3$ galaxies. By using infrared bands this technique has pushed to higher redshifts ($z \sim 7$ Wilkins et al., 2010).

Rowan-Robinson et al. (2008, hereafter RR08) have previously produced a photometric redshift catalogue for the SWIRE survey. This used the *Spitzer* data, along with ancilliary optical data from a number of sources including the Wide Field Survey of McMahon et al. (2001), the VVDS survey (McCracken et al., 2003; Le Fèvre et al., 2004, 2005) and the Subaru XMM Deep Survey (Sekiguchi et al., 2004; Furusawa et al., 2008). The multi-wavelength data together with modified empirical galaxy templates covering a wide range of galaxy types and the $IMPz$ code of Rowan-Robinson (2003); Rowan-Robinson et al. (2004, 2005); Babbedge et al. (2004) were used to produce a photometric redshift catalogue of SWIRE sources in all fields except the ES1 field. While it might at first glance be most obvious to use this large photometric redshift catalogue to identify clusters in this region, there is a very complicated selection function associated with this data due to variation in the depth of available optical data and hence a variation of the photo-z success rate with position on the sky, which is also dependent on galaxy type (Frost et al., 2010). For objects with 5 band optical data and $r < 23.5$, RR08 estimate that 29% of $z > 1.5$ galaxies in their catalogue are outliers. By using the Bumps technique we can ensure a clean, well defined sample at high redshifts. Farrah et al. (2008) showed that an excess at 4.5μm combined with a 24μm flux $> 500\mu$Jy selects galaxies in a very narrow redshift range centered around 1.7. Furthermore, since our selection only requires coverage in 3 or 4 bands we can calculate the selection function so as to be confident in our cluster identification.

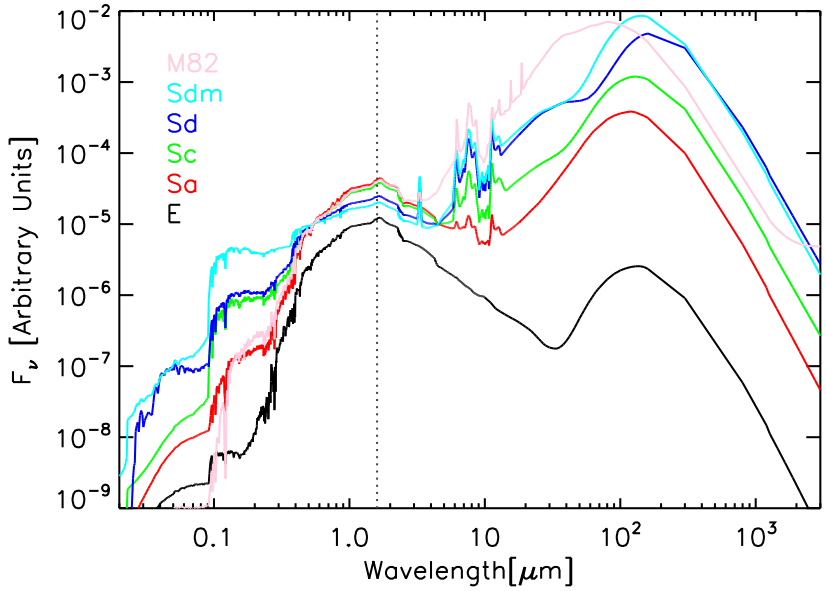

Figure 2.3: SED templates from Polletta et al. (2007) for several spectral types. The 1.6μm feature is marked by the dashed line. Figure adapted from preliminary version of I. Roseboom, priv. comm.

Papovich et al. (2010) identified a high-redshift cluster, spectroscopically confirmed at $z = 1.62$. This cluster was detected as a red-sequence over-density in a sample of SWIRE galaxies satisfying $[3.6]-[4.5] > 0.1$, where the square brackets denote AB magnitudes (unless otherwise stated). This cluster, along with a neighbouring cluster, was independently identified in X-ray observations and spectroscopically confirmed by Tanaka et al. (2010). Since this approach is similar to that used here we are encouraged that they successfully identify such a high-redshift cluster. As we are using more than just one colour we should expect to select clusters in a well-defined redshift range.

2.4.1 Modelling the Bump selection

We now investigate how the bump feature varies with spectral type and outline an initial selection based on SED templates of typical galaxies. Figure 2.3 shows the SED of several different galaxy types using the templates of Polletta et al. (2007). The figure shows that the Bump feature appears in all spectral types (except pure AGN, which are not shown). The Bump feature can be identified in each type shown, although its strength varies with spectral type.

In figures 2.4 - 2.6 (adapted from I. Roseboom, similarly for figures 2.7 and 2.8, priv. comm.) we show the redshift evolution of each of the DXS and SWIRE colours

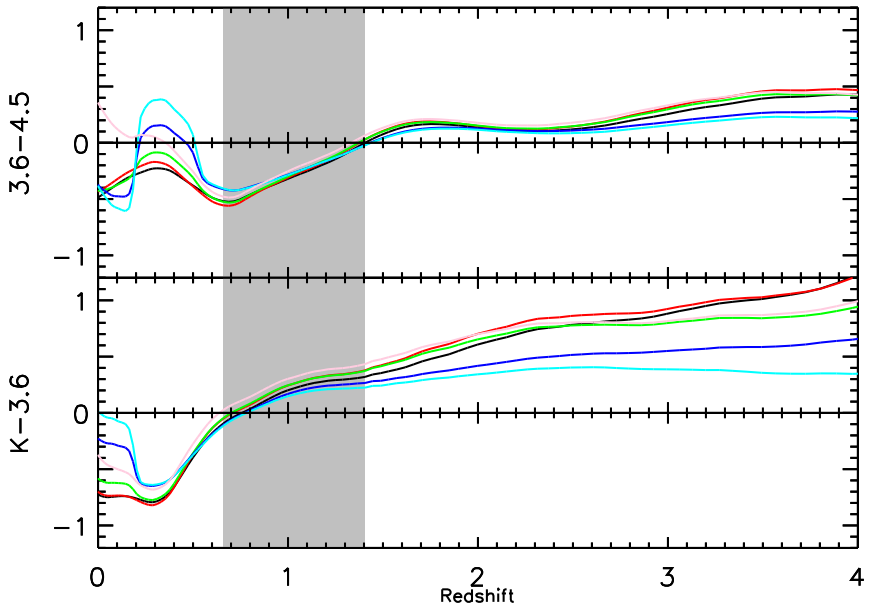

Figure 2.4: Colour evolution with redshift of the templates from figure 2.3 with the same colour-coding through the Bump-1 selection. The grey shaded area shows where there is a template which satisfies the criterion $[K]-[3.6]>0$ & $[3.6]-[4.5]<0$.

available to us, from $[K]-[3.6]$ to $[5.8]-[8.0]$. The AB magnitude is determined for each template at each redshift by convolving the observed frame SED with the instrument filter function (I. Roseboom, priv. comm.). Figure 2.4 shows that, by requiring $[K]-[3.6]>0$ & $[3.6]-[4.5]<0$, we select galaxies in the range $0.7\lesssim z\lesssim 1.4$ (Bump-1 selection). Defining Bump-2 and Bump-3 selections as those sources with an excess in IRAC 4.5μm and 5.8μm respectively, figures 2.5 and 2.6 shows that a similar approach results in a sample with contamination from low-z star forming galaxies. A selection of $[3.6]-[4.5]>0$ & $[5.8]-[4.5]<0$ for Bump-2 is contaminated by star forming galaxies at $z\sim 0.3$. Similarly, a selection of $[4.5]-[5.8]>0$ & $[5.8]-[8.0]<0$ for Bump-3 is contaminated by star forming galaxies at $z\sim 0.8$. This is because the 3.3μm Polycyclic Aromatic Hydrocarbon (PAH) feature indicative of star formation (see section 4.3.1 for more details) falls in the 4.5μm and 5.8μm bands at $z\sim 0.3$ and $z\sim 0.8$ respectively. However, if we require that the adjacent, bluer, colour also be greater than 0, i.e. $[K]-[3.6]>0$ for Bump-2 and $[3.6]-[4.5]>0$ for Bump-3 then, as shown by figures 2.7 and 2.8, this contamination is removed. This contamination was removed in the sample of Farrah et al. (2008) by demanding a 24μm detection $>500\mu$Jy. However, such a selection preferentially selects highly star forming galaxies.

The figures also show that the different spectral types have a tight colour evolution

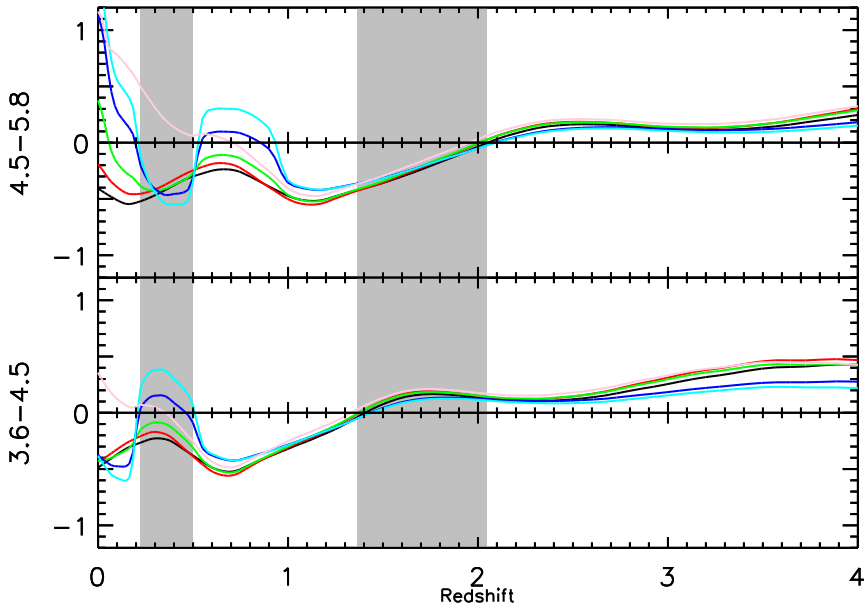

Figure 2.5: Colour evolution with redshift of the templates from figure 2.3 with the same colour-coding through the Bump-2 selection. The grey shaded area shows where there is a template which satisfies the criterion $[3.6] - [4.5] > 0$ & $[4.5] - [5.8] < 0$.

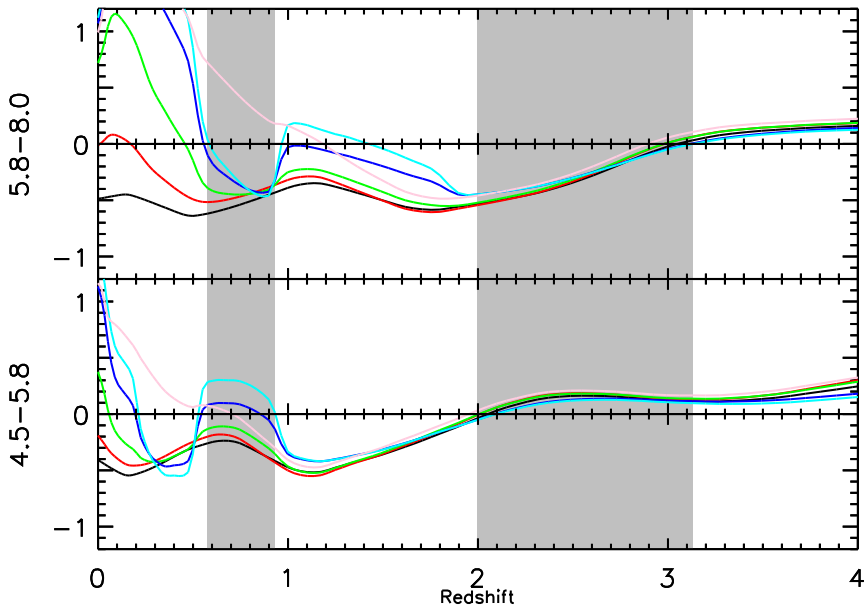

Figure 2.6: Colour evolution with redshift of the templates from figure 2.3 with the same colour-coding through the Bump-3 selection. The grey shaded area shows where there is a template which satisfies the criterion $[4.5] - [5.8] > 0$ & $[5.8] - [8.0] < 0$.

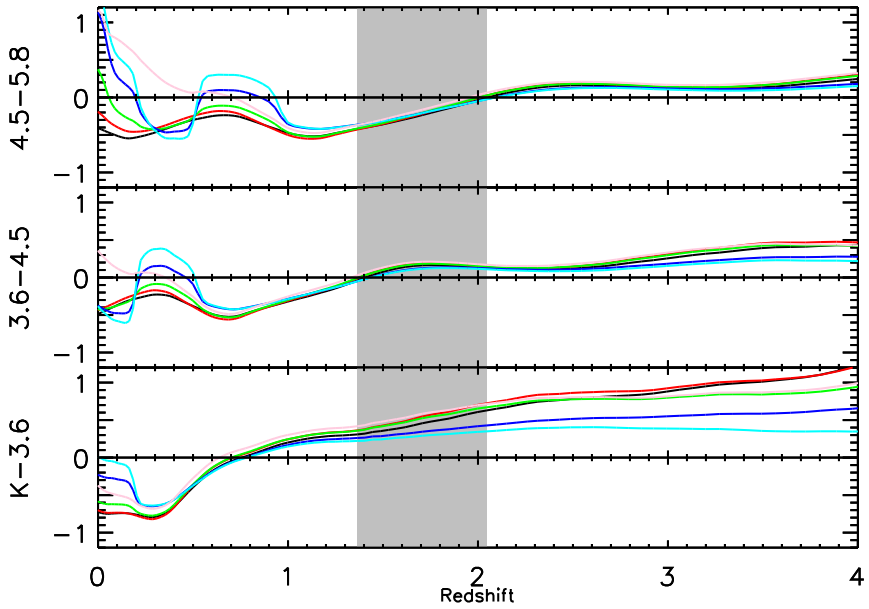

Figure 2.7: Colour evolution with redshift of the templates from figure 2.3 with the same colour-coding through a revised Bump-2 selection. The grey shaded area shows where there is a template which satisfies the criterion $[K] - [3.6] > 0$ & $[3.6] - [4.5] > 0$ & $[4.5] - [5.8] < 0$.

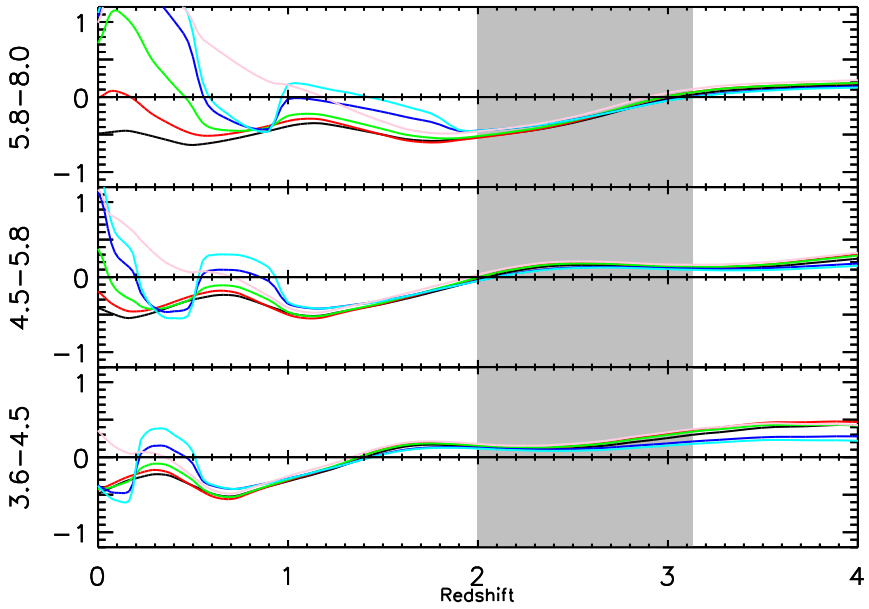

Figure 2.8: Colour evolution with redshift of the templates from figure 2.3 with the same colour-coding through a revised Bump-3 selection. The grey shaded area shows where there is a template which satisfies the criterion $[3.6] - [4.5] > 0$ & $[4.5] - [5.8] > 0$ & $[5.8] - [8.0] < 0$.

through the bump selection. This means the bump selection is largely un-biased towards a certain spectral type at any given redshift (although as mentioned above, pure AGN are not identified). Table 2.4 gives the minimum and maximum redshift at which each of our bump selections is sensitive to each spectral type.

Table 2.4: Redshift range of each Bump selection for each template from Figure 2.3.

	Bump-1		Bump-2		Bump-3	
Selection	$K-3.6>0$ & $3.6-4.5<0$		$K-3.6>0$ & $3.6-4.5>0$ & $4.5-5.8<0$		$3.6-4.5>0$ & $4.5-5.8>0$ & $5.8-8.0<0$	
Spectral Type	z_{min}	z_{max}	z_{min}	z_{max}	z_{min}	z_{max}
E	0.78	1.41	1.45	2.05	2.10	2.99
Sa	0.72	1.36	1.41	2.00	2.05	2.92
Sc	0.72	1.36	1.41	2.00	2.05	2.92
Sd	0.78	1.41	1.45	2.05	2.10	3.06
Sdm	0.81	1.41	1.45	2.05	2.10	3.13
Starburst (M82)	0.66	1.32	1.36	1.95	2.00	2.86

2.4.2 Bump-1 Selected VVDS Galaxies

We now wish to assess the effectiveness of the Bump selections. We use the VIMOS VLT Deep Survey (VVDS; Le Fèvre et al., 2005) data. This survey contains spectroscopic redshifts for ∼9000 galaxies with $17.5 < I < 24.0$. In this survey there is a ∼ 1.5 sq. deg. region which overlaps with both the SWIRE survey and the UKIDSS DXS survey.

We cross-match the VVDS catalogue with the SWIRE and DXS catalogues in XMM with a $0\farcs5$ cross-matching radius. This gives us a sample of 1644 galaxies with spectroscopic redshifts. We then apply the Bump-1 selection of table 2.4, along with the completeness limits to this sample. This gives us a sample of 531 VVDS galaxies. The mean redshift of this sample is $\bar{z} = 0.86$ with a variance of $\sigma_z = 0.07$. 24.5% of this sample lie outside the expected range of $0.7 < z < 1.4$, however, only 3.2% of objects do not lie in the range of $0.5 < z < 1.5$. We tighten the selection slightly to $[K] - [3.6] > 0.1$ & $[3.6] - [4.5] < 0$ producing a sample of 448 galaxies, with a mean redshift of $\bar{z} = 0.88$ and variance $\sigma_z = 0.07$. Of this sample, 20.3% lie outside the range $0.7 < z < 1.4$ but only 11 (2.5%) fall outside the range $0.5 < z < 1.5$. The redshift distribution of these Bump-1 selections are shown in figure 2.9.

2.4.3 Bump-2 and 3 Selected Photo-z Galaxies

The VVDS data is not deep enough to investigate the Bump-2 and Bump-3 selections. Optical and mid-IR spectroscopy of small samples of Bump-2 and 3 selected objects has been previously obtained by Berta et al. (2007) and Farrah et al. (2008) showing that the selection is effective. However, the selection employed here is slightly different and the sample is larger. We use the photometric redshift (photo-z) catalogue of RR08 to assess the Bump-2 and 3 selection, using only the most accurate photo-z's. We use objects in the EN1 field which have a $\chi^2 < 10$, r-band AB magnitude < 23.5 and which have at least 5 photometric bands. Cross-matching this photo-z catalogue with the DXS catalogue with a $1''$ radius results in 64587 objects. There is no requirement for K-band photometry for Bump-3, so in the case of Bump-3 we are able to use the whole photo-z catalogue. We apply the Bump-2 and 3 selections from table 2.4 and the completeness limits from section 2.3.1 to these samples. This gives 113 Bump-2 and 52 Bump-3 galaxies. The photometric redshift distribution of these objects is shown in figure 2.10. The photo-z distribution of Bump-2 selected galaxies has a mean redshift of 1.46 and agrees well with that of the templates in table 2.4, although there is a significant population of low-z interlopers. The Bump-2 galaxies should lie in the range $1.2 < z_{phot} < 2.3$, where we

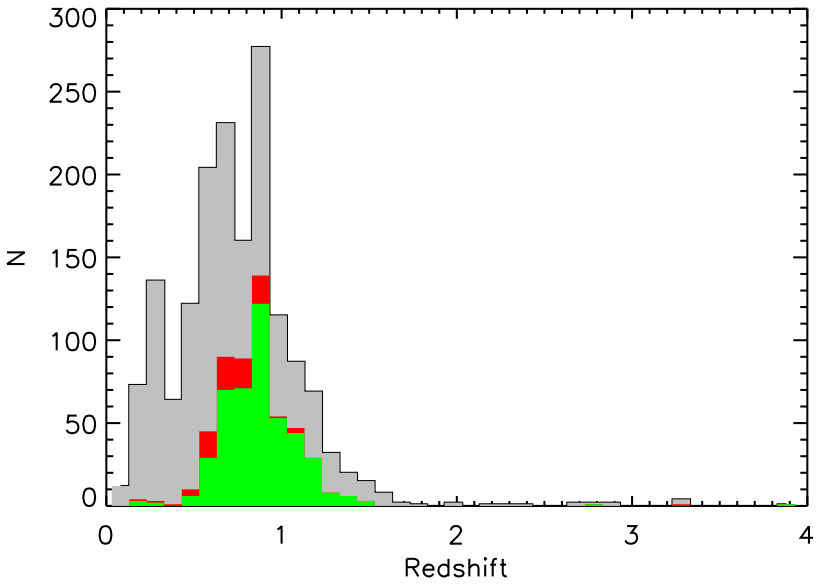

Figure 2.9: Redshift distribution of the Bump-1 selection in VVDS. The grey histogram is that of the sample of 1644 VVDS galaxies with DXS and SWIRE matches. The red histogram is that of the 531 VVDS galaxies which satisfy our initial Bump-1 selection. The green histogram shows the redshift distribution obtained if we slightly tighten the selection to $[K]-[3.6] < 0.1$ & $[3.6]-[4.5] > 0.1$. Figure adapted from preliminary version of I. Roseboom, priv. comm.

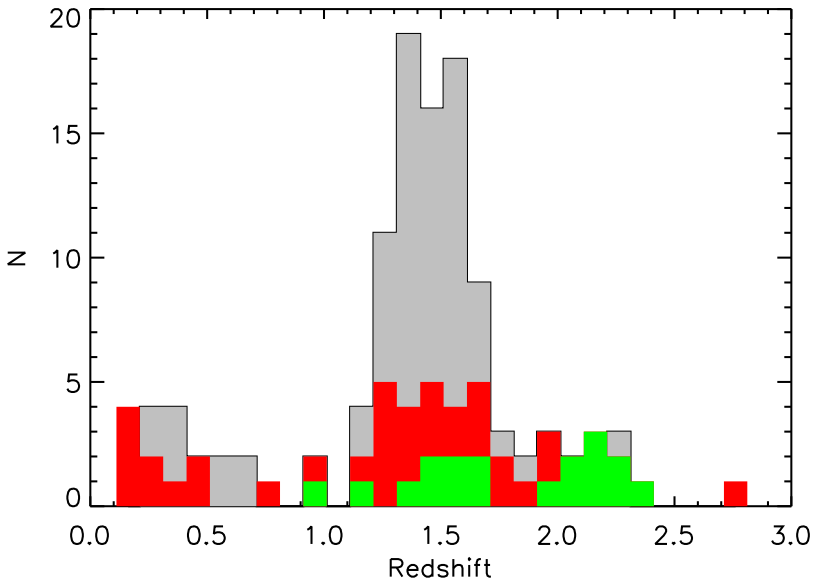

Figure 2.10: Photometric redshift distribution of Bump-2 (grey histogram) and Bump-3 (red histogram) galaxies in the EN1 field. Photometric redshifts are from the catalogues of RR08. The Bump-2 galaxies show a peak at the expected redshift ($z \sim 1.5$) with a few low and high-z interlopers. The distribution of Bump-3 galaxies however, has a significant fraction at $z < 2$. Even if we tighten the Bump-3 selection a significant fraction of low-z interlopers remain (green histogram). Figure adapted from preliminary version of I. Roseboom, priv. comm.

have assumed a typical error of 10% for the photometric redshifts. However, 25 (22%) lie outside this range, most with $z < 0.8$. The results for Bump-3 are not as encouraging. The mean photo-z is 1.40 with many low-z interlopers around $z \sim 0.2$. Only 15 of the 52 (29%) Bump-3 sources with photo-z's are in the expected redshift range of $1.7 < z_{phot} < 3.4$.

We now briefly investigate the source of these discrepancies. For 9 Bump-2 and 13 Bump-3 selected galaxies which do not fall in the expected range, no χ^2 is given in the RR08 catalogue for some part of the expected range due to the luminosity cuts they impose. However, for the remaining galaxies there is no reason (such as an alternative peak in the χ^2 distribution) for the discrepancy. Thus at least 16 (14%) Bump-2 and 24 (46%) Bump-3 selected galaxies have photometric redshifts from RR08 which cannot be reconciled with their predicted redshift range from the bump selection.

This level of contamination is acceptable for the Bump-2 selection. However, the contamination of the Bump-3 selection is large. Surprisingly, none of this contamination comes from $z << 1$ interlopers but most come from the Bump-2 region of $1.3 < z < 2$.

Table 2.5: Revised version of table 2.4 with the final Bump-1 and 2 selections

	Bump-1		Bump-2	
Selection	$K-3.6>0.1$ & $3.6-4.5<0$		$K-3.6>0$ & $3.6-4.5>0$ & $4.5-5.8<0$	
Spectral Type	z_{min}	z_{max}	z_{min}	z_{max}
E	0.90	1.41	1.45	2.05
Sa	0.84	1.36	1.41	2.00
Sc	0.84	1.36	1.41	2.00
Sd	0.90	1.41	1.45	2.05
Sdm	0.93	1.41	1.45	2.05
Starburst (M82)	0.75	1.32	1.36	1.95

A similar result is found by Berta et al. (2007) in their spectroscopic survey of Bump-2 and Bump-3 sources. Berta et al. (2007) suggest that this contamination is explained by assuming an increasing contribution of AGN dust tori with redshift. The $[5.8]-[8.0]$ colour is reddened by the AGN dust torus, causing a Bump-2 galaxy to appear as a Bump-3. A possible solution to this problem might be to pick only those Bump-3 galaxies which have steep $[3.6]-[4.5]$ and $[4.5]-[5.8]$ colours. However, even if we revise our Bump-3 selection to $[3.6]-[4.5]>0.15$ & $[4.5]-[5.8]>0.15$ & $[5.8]-[8.0]<0$ half of the resulting sample of 18 galaxies have $z<1.7$ (none of which have plausible alternative redshifts in the expected redshift range) and the mean redshift is 1.8. This fraction of low-z interlopers is still large and as such we remove the Bump-3 sample from the rest of this analysis, although we note that these interlopers could be a result of incorrect photo-z's.

2.4.4 Final Bumps Selection

Table 2.5 is a revised version of table 2.4 with the slightly tightened constraints for Bump-1 and removing the Bump-3 selection altogether. Using these selections we identify Bump-1 and Bump-2 galaxies in the SWIRE and DXS overlap regions in the Lockman Hole, EN1 and XMM fields. Table 2.6 gives the number of galaxies selected in each Bump selection in each SWIRE field.

Table 2.6: Numbers of galaxies in each Bump selection per SWIRE field and the total number in the field above our completeness limits.

	Total C(B1)	Bump-1	Total C(B2)	Bump-2
Lockman	83292	26908	12826	700
EN1	128124	38140	22521	946
XMM	58530	20106	8083	362

2.5 Cluster Identification

Given a sample of bump selected galaxies, we look for projected over-densities using a counts-in-cells method. We exploit the large area of the DXS and SWIRE overlap regions of ~ 9.6 sq.degs.

In order to search for clusters we look for statistically significant over-densities in each bump catalogue. For each field and for each bump catalogue we calculate a density map based on a counts in cells method. After a gaussian smoothing of the density map we identify peaks as candidate clusters, with the additional constraint requiring that at least 3 galaxies are found within the radius of the smoothing kernel (the radius is the standard deviation of a gaussian kernel). We calculate the reliability of the method from a simulation and identify the smoothing radius maximising the number of clusters and reliability.

2.5.1 Density Estimation

Density map calculation

To calculate the density map we first calculate a simple 2d-histogram of the spatial positions of each of the bumps catalogues for each field. This bins the galaxies together into $4''$ pixels. This map is then smoothed by a convolution with a gaussian kernel of the form

$$k(x) = e^{-x^2/2s^2} \tag{2.1}$$

where x is the radial position in the kernel and s is the standard deviation of the gaussian, which we define as the angular smoothing radius. The kernel is normalised so that the total integral is 1.

Once the density map has been calculated we look for peaks in the map which are 5σ above the mean density, where σ is the standard deviation of the smoothed density map. We choose this threshold to ensure that we only identify significant over-densities which

are above the uncertainties in the K-band completeness calculation. The mean density and σ are calculated as the mean and standard deviation of all pixels in the density map with good coverage. We repeat this process for all fields before finally combining the candidate cluster list into one catalogue (see section 2.5.2). To ensure that the peaks are highly likely to be clusters, we only include peak detections which have at least 3 galaxies within the smoothing radius. Finally, we remove any duplicate objects via an internal cross-match using the smoothing radius as the cross-matching radius. In order to optimise the smoothing radius over which we calculate the density, and to ensure that any clusters found could not be generated (at these significance levels) either by random coincidence of galaxies or because of some selection effect in the SWIRE or DXS data we perform simulations for each field and each bump selection.

Simulations

We wish to simulate the selection of bumps galaxies in the SWIRE and DXS surveys and the subsequent cluster search. In order to do this we must calculate the probability of a galaxy of a given flux being detected at all positions in the survey. We can then combine these maps into a 'selection function', which is a map of the expected galaxy number density. We follow the procedure of Frost et al. (2010). If the 'true' number density of galaxies of a given type i is n_i then the observed number density n_i' is

$$n_i'(\alpha, \delta) = p_i(\alpha, \delta) n_i(\alpha, \delta) \tag{2.2}$$

where p_i is the probability of observing a galaxy of type i at position α, δ. If i only refers to one galaxy (i.e. classing each galaxy separately as its own type) then

$$n_i = \frac{1}{\Omega_i} \tag{2.3}$$

where Ω_i is the observable area, i.e

$$\Omega_i = \int p_i(\alpha, \delta) \mathrm{d}\Omega \tag{2.4}$$

So for all galaxies in a sample,

$$n'(\alpha, \delta) = \sum_i \frac{p_i(\alpha, \delta)}{\int p_i(\alpha, \delta) \mathrm{d}\Omega} \tag{2.5}$$

Therefore, given $p_i(\alpha, \delta)$ one can calculate a map of the observed selection function for a given sample of galaxies. $p_i(\alpha, \delta)$ is given by the product of the completeness for each band in which a detection is required at the flux of galaxy i and at position (α, δ). We calculate

this at all positions in the survey to give us our selection function. So for Bump-1

$$p_i(\alpha, \delta) = C_k(F_{k_i}) \times C_{36}(F_{36_i}) \times C_{45}(F_{45_i}) \tag{2.6}$$

and for Bump 2

$$p_i(\alpha, \delta) = C_k(S_{k_i}) \times C_{36}(F_{36_i}) \times C_{45}(F_{45_i}) \times C_{58}(F_{58_i}) \tag{2.7}$$

where $C_k(F_{k_i})$ is the K-band completeness at the position (α, δ) at the K-band flux of galaxy i, F_{k_i} and $C_{36}(F_{36_i})$ - $C_{58}(F_{58_i})$ is that for the IRAC bands.

The K-band completeness is calculated as in section 2.3.1. Note that due to the conservative K-band limit we impose we assume that the K-band completeness is always unity. In the case of the IRAC data, the completeness curves were calculated at an average coverage. We calculate the completeness curves at a different coverage in the following manner. From the source injection technique the completeness has been calculated for a given band at a flux F_0 from a coverage (i.e. number of scans) N_0. We wish to calculate the flux at which we would achieve the same completeness at a different coverage level, N_1. If the noise for N_0 coverage is σ_0, then the signal-to-noise ratio, SNR, per pixel is F_0/σ_0. In order to get the same completeness for a different coverage we need to have the same SNR, i.e:

$$\frac{F_0}{\sigma_0} = \frac{F_1}{\sigma_1} \tag{2.8}$$

Furthermore, if we assume that the noise is inversely proportional to the square-root of the number of scans then the flux we wish to find, F_1, is given by

$$F_1 = F_0 \times \sqrt{\frac{N_0}{N_1}} \tag{2.9}$$

This gives the flux which corresponds to the original completeness but in the new coverage. The IRAC coverage maps, therefore, together with these curves allows us to generate a completeness map (completeness as a function of position and flux). We use this information to calculate a number density map for each bump sample. We then have a map of probabilities of detection for each bump sample. This means we have explicitly calculated the selection function of the sample.

Once this map has been calculated we use it to generate random catalogues which have the same selection effects as the survey, but which don't have the same intrinsic clustering as the SWIRE catalogue. Using a catalogue of random SWIRE objects would underestimate our reliability due to this clustering. We first generate a random set of 200,000 x, y co-ordinates in the map with a uniform distribution. Each 'object' is also

given a random number between 0 and 1, again with a uniform distribution. Only those random objects which have a probability in the map at position x, y larger than the assigned random number are included. We then pick a random sample of the remaining simulated objects to give us the same number of objects as are found in the bumps sample. We then look for clusters in the simulated sample. We do this in the same way as for the bumps sample, requiring that the simulated clusters have a peak pixel value larger than the value of the threshold used in the real bumps sample, as well as containing at least 3 objects.

We perform this simulation 20 times and over a range of smoothing radii in order to assess the effect this parameter has on our searching algorithm. So, for each bump catalogue in each field we have simulations on several different smoothing scales. For Bump-1 we have 8 sets of 20 simulations corresponding to smoothing scales in the range 0.′13 - 0.′6 which is 0.09 - 0.40 h^{-1}Mpc at $z = 1$, (beyond this no clusters are found in any simulation). For Bump-2 the range is 0.′13 - 2′, corresponding to 0.11 - 1.78 h^{-1}Mpc at $z = 1.5$, giving 27 sets of simulations. Since this is a random catalogue all cluster candidates found in the simulations are spurious. We calculate the average number of spurious clusters per square degree, N_s, across all three fields, as a function of smoothing radius. Similarly, we calculate the average number of cluster candidates per square degree we find in the real bumps catalogues, N_t. We then calculate the reliability, R

$$R = \frac{N_t - N_s}{N_t} \tag{2.10}$$

We choose the smoothing scale for each bump selection which maximises R and N_t. Figures 2.11 and 2.12 show the results of these simulations. Figure 2.11 shows that for Bump-1 sources we are very reliable at all but the smallest smoothing scales. We choose a smoothing radius of 0.′33, giving us 118 cluster candidates at 95% reliability. Assuming a Bump-1 redshift of 1, this smoothing scale corresponds to a comoving scale of $\sim 0.22h^{-1}$Mpc, which corresponds nicely to the typical cluster core radius of $\sim 0.3h^{-1}$Mpc (Gerke et al., 2005).

The results are less encouraging for Bump-2 sources, figure 2.12. Nevertheless, by choosing a smoothing radius of 0.′93 we achieve 55% reliability and find 40 cluster candidates, suggesting that 22 cluster candidates are expected to be real clusters. This corresponds to a comoving scale of $\sim 1.65h^{-1}$Mpc, where a redshift of 1.5 is assumed. The Bump-2 smoothing scale is similar to the typical virial radius of local clusters ($1-2h^{-1}$Mpc Pointecouteau et al., 2005). However, the Bump-1 smoothing scale is much smaller than this.

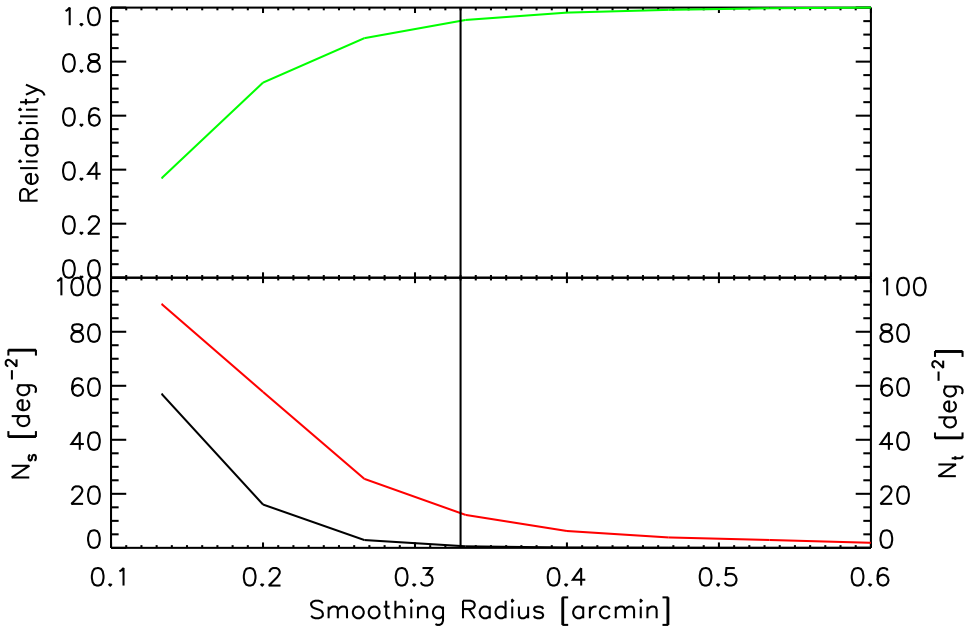

Figure 2.11: Reliability (top panel) of Bump-1 clusters for different smoothing radii. The bottom panel shows the number of simulated (i.e. spurious) clusters in black and the number of candidate clusters in red. The vertical black line shows the smoothing scale that we use for cluster identification (0.′33).

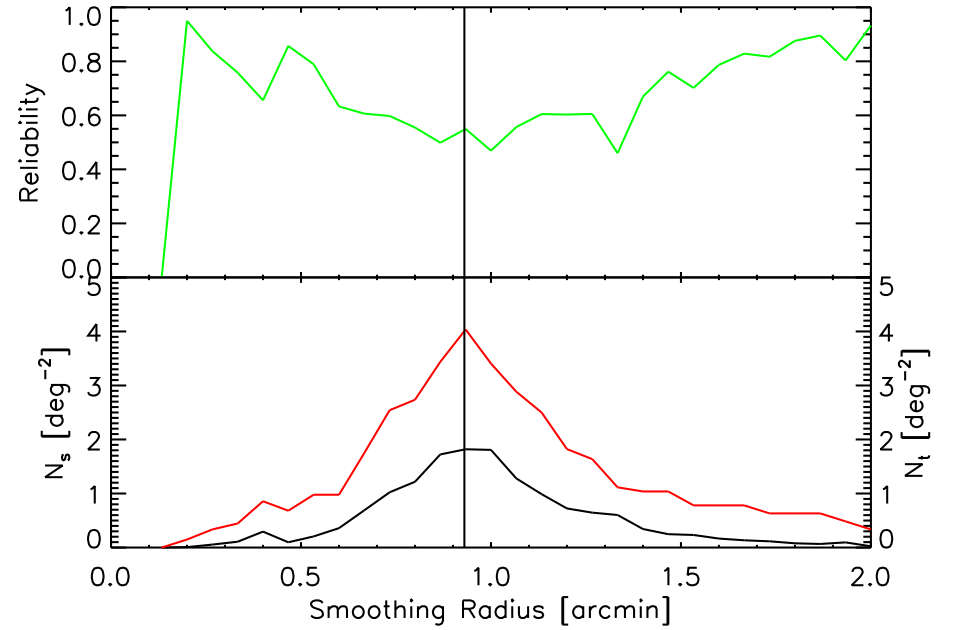

Figure 2.12: As figure 2.11 but for Bump-2 candidate clusters. The vertical black line shows the smoothing scale that we use for cluster identification (0.′93).

2.5.2 Cluster Candidates

Given the selection of smoothing kernels in the previous section we give a list of candidate clusters for the Bump-1 and 2 selections in tables 2.7 and 2.8.

Table 2.7: Bump-1 cluster candidates found with a smoothing radius of 0.′33. Columns are: Ra, Dec of the centre of the peak in the density map, SWIRE Field of the candidate cluster, Ngals is the number of galaxies within the smoothing radius of the peak, z is the redshift estimate (see text for details), δ is the density contrast of the peak pixel, i.e. peak pixel density/average density across the whole field and Stellar Mass, M.

Ra	Dec	Field	Ngals	z	δ	$\log_{10}$(M) [$M_\odot$]
242.298028	54.194763	EN1	5	1.16 ± 0.12	6.66	11.70 ± 0.11
241.465982	54.203225	EN1	8	1.09 ± 0.11	8.89	12.15 ± 0.09
242.919156	54.228818	EN1	7	1.23 ± 0.17	6.99	11.98 ± 0.09
242.041924	54.289074	EN1	6	1.27 ± 0.11	7.27	12.04 ± 0.10
242.019046	54.291160	EN1	6	1.25 ± 0.22	6.93	11.84 ± 0.10
240.755642	54.319139	EN1	6	1.12 ± 0.20	7.05	11.98 ± 0.10
244.249135	54.371849	EN1	9	1.16 ± 0.18	7.31	12.11 ± 0.08
242.375047	54.493878	EN1	5	1.02 ± 0.13	6.89	11.64 ± 0.12
243.637586	54.491207	EN1	6	1.07 ± 0.11	6.92	12.06 ± 0.10
241.560896	54.531957	EN1	4	1.26 ± 0.25	7.04	11.77 ± 0.12
243.797986	54.554370	EN1	5	1.28 ± 0.11	6.64	11.78 ± 0.11
244.122075	54.620027	EN1	6	1.24 ± 0.15	6.91	11.88 ± 0.10
241.583098	54.625507	EN1	6	1.10 ± 0.24	6.63	11.76 ± 0.11
242.120497	54.748372	EN1	6	0.98 ± 0.07	7.04	12.08 ± 0.10 [1]
241.644271	54.774974	EN1	6	1.19 ± 0.13	6.69	11.90 ± 0.10
240.662004	54.808747	EN1	7	1.23 ± 0.14	6.60	11.74 ± 0.09
244.790216	54.855123	EN1	8	1.22 ± 0.18	6.81	12.05 ± 0.09
243.020474	54.891922	EN1	7	1.15 ± 0.14	8.10	11.75 ± 0.09
243.783492	54.887837	EN1	7	1.17 ± 0.19	6.80	12.05 ± 0.09
243.364023	54.996232	EN1	6	1.16 ± 0.14	7.07	11.97 ± 0.10
242.711250	55.006661	EN1	5	1.31 ± 0.10	6.50	11.73 ± 0.10
242.678281	55.024423	EN1	7	1.08 ± 0.10	8.33	11.99 ± 0.10 [1]
243.147552	55.043797	EN1	7	1.12 ± 0.19	6.63	11.95 ± 0.10
243.543589	55.065198	EN1	7	1.19 ± 0.13	7.51	11.99 ± 0.10
242.161888	55.078583	EN1	8	1.17 ± 0.21	7.38	12.27 ± 0.09
244.230668	55.123246	EN1	7	1.21 ± 0.14	6.53	11.89 ± 0.11
240.639948	55.119548	EN1	7	1.32 ± 0.09	6.56	11.79 ± 0.09
242.409804	55.140637	EN1	7	1.32 ± 0.08	6.73	12.04 ± 0.09
243.700740	55.146300	EN1	6	1.24 ± 0.08	7.33	11.76 ± 0.10
242.283269	55.155775	EN1	7	1.30 ± 0.17	7.54	11.78 ± 0.10

continued on next page

Table 2.7: *continued*

Ra	Dec	Field	Ngals	z	δ	$\log_{10}$(M) [$M_\odot$]
241.622062	55.155904	EN1	5	1.20 ± 0.26	6.51	11.84 ± 0.14
241.629091	55.182637	EN1	8	1.23 ± 0.20	7.58	12.14 ± 0.09
242.364494	55.202725	EN1	8	1.33 ± 0.06	7.04	12.13 ± 0.09
241.059010	55.226085	EN1	7	1.15 ± 0.15	6.66	12.02 ± 0.10
241.775494	55.243894	EN1	7	1.07 ± 0.16	6.94	12.09 ± 0.10
242.338313	55.287083	EN1	9	1.18 ± 0.17	8.50	11.99 ± 0.08
241.382122	55.347913	EN1	7	1.25 ± 0.10	7.23	11.73 ± 0.09
244.685770	55.372480	EN1	8	1.15 ± 0.14	7.64	11.91 ± 0.09
242.636510	55.401052	EN1	7	1.27 ± 0.12	7.73	11.87 ± 0.09 [2]
242.082432	55.420397	EN1	7	1.29 ± 0.16	7.41	11.95 ± 0.09
243.856712	55.442775	EN1	8	1.20 ± 0.18	6.82	12.20 ± 0.10
241.667837	55.476327	EN1	8	0.94 ± 0.09	7.92	12.26 ± 0.09
244.914161	55.473122	EN1	7	1.12 ± 0.20	6.55	12.11 ± 0.09
244.789121	55.557498	EN1	7	1.09 ± 0.15	7.16	12.02 ± 0.09
243.597936	55.615940	EN1	9	1.26 ± 0.13	6.59	12.06 ± 0.09
241.690138	55.668736	EN1	4	1.32 ± 0.08	6.96	11.55 ± 0.13
242.677083	55.683279	EN1	8	1.19 ± 0.16	6.85	12.04 ± 0.09
243.493090	55.689944	EN1	6	1.23 ± 0.17	6.63	11.79 ± 0.10
243.523110	55.713090	EN1	5	1.04 ± 0.20	6.58	11.87 ± 0.11
240.952876	55.722397	EN1	6	1.15 ± 0.18	6.61	11.84 ± 0.10
241.192583	55.746774	EN1	7	1.12 ± 0.12	6.62	11.93 ± 0.09
244.185210	55.751592	EN1	6	1.29 ± 0.18	6.91	12.04 ± 0.10 [2]
244.187670	55.764896	EN1	6	1.28 ± 0.14	7.07	11.84 ± 0.10
242.923923	55.796492	EN1	5	1.33 ± 0.06	6.51	11.81 ± 0.12
243.693114	55.811892	EN1	6	1.13 ± 0.16	7.45	11.96 ± 0.10
163.673773	57.161278	Lockman	7	1.27 ± 0.15	6.88	12.11 ± 0.10
163.256331	57.257802	Lockman	6	1.18 ± 0.24	6.98	11.98 ± 0.11
163.082734	57.281215	Lockman	8	1.05 ± 0.23	7.04	11.95 ± 0.08
163.836684	57.273927	Lockman	6	1.09 ± 0.10	6.49	11.84 ± 0.10
164.075149	57.303728	Lockman	7	1.28 ± 0.14	7.96	11.91 ± 0.09
163.118370	57.528550	Lockman	7	1.15 ± 0.20	7.37	12.03 ± 0.09
163.417633	57.591044	Lockman	9	1.18 ± 0.21	11.29	11.98 ± 0.08 [1]
163.419794	57.709923	Lockman	7	1.01 ± 0.19	6.62	11.90 ± 0.09
162.798313	57.953384	Lockman	6	1.13 ± 0.20	6.67	11.80 ± 0.11
162.794929	57.975643	Lockman	5	1.02 ± 0.21	6.81	11.97 ± 0.13
162.174914	57.987102	Lockman	8	1.19 ± 0.15	8.20	12.04 ± 0.09
163.576456	57.974193	Lockman	4	1.26 ± 0.17	6.68	11.80 ± 0.13
164.136099	57.976067	Lockman	7	1.24 ± 0.19	7.23	11.94 ± 0.10
163.231767	57.996015	Lockman	7	1.24 ± 0.09	6.58	12.01 ± 0.09

continued on next page

Table 2.7: *continued*

Ra	Dec	Field	Ngals	z	δ	$\log_{10}$(M) [$M_\odot$]
161.797829	58.010763	Lockman	6	1.21 ± 0.22	6.72	11.84 ± 0.10
162.148151	58.013908	Lockman	6	1.09 ± 0.16	6.67	11.85 ± 0.10
163.541115	58.015887	Lockman	7	1.21 ± 0.20	6.62	11.82 ± 0.09
161.823630	58.080701	Lockman	6	1.08 ± 0.17	7.68	11.83 ± 0.11
163.053123	58.082775	Lockman	7	1.02 ± 0.11	6.62	11.92 ± 0.10
161.895300	58.100499	Lockman	4	1.20 ± 0.23	6.73	11.69 ± 0.12
161.937993	58.152583	Lockman	6	1.25 ± 0.09	6.82	12.02 ± 0.10
163.455199	58.209505	Lockman	8	1.24 ± 0.13	9.14	11.91 ± 0.09
162.462094	58.221939	Lockman	8	1.23 ± 0.13	8.09	11.99 ± 0.09
164.311058	58.229127	Lockman	8	1.30 ± 0.12	6.94	11.90 ± 0.09
164.130074	58.236311	Lockman	6	1.27 ± 0.13	6.87	11.86 ± 0.10
163.076116	58.270301	Lockman	7	1.14 ± 0.17	6.75	11.97 ± 0.11
164.066491	58.262058	Lockman	6	1.19 ± 0.11	6.58	11.77 ± 0.10
162.781522	58.303591	Lockman	7	1.15 ± 0.15	8.80	11.89 ± 0.10
162.178088	58.375982	Lockman	8	1.11 ± 0.20	8.67	12.17 ± 0.10
163.732692	58.396133	Lockman	9	0.97 ± 0.17	8.16	11.90 ± 0.08
161.782400	58.447461	Lockman	9	1.16 ± 0.19	7.00	12.12 ± 0.08
161.534022	58.498875	Lockman	5	1.10 ± 0.19	7.55	11.71 ± 0.11
163.046198	58.505140	Lockman	6	1.18 ± 0.18	6.96	11.90 ± 0.12
162.524011	58.540358	Lockman	5	1.08 ± 0.21	6.51	11.85 ± 0.11
163.272100	58.683358	Lockman	5	1.06 ± 0.22	6.61	11.75 ± 0.10
161.577339	58.858811	Lockman	6	1.14 ± 0.14	7.09	11.87 ± 0.09
35.932254	-5.024156	XMM	5	1.07 ± 0.12	6.78	11.90 ± 0.11
35.642260	-4.973250	XMM	8	1.03 ± 0.12	7.06	11.92 ± 0.08
36.600003	-4.931014	XMM	6	1.20 ± 0.12	7.13	11.80 ± 0.10
36.555276	-4.847787	XMM	7	1.30 ± 0.17	7.02	12.01 ± 0.09
36.498207	-4.707919	XMM	5	1.18 ± 0.20	6.70	11.58 ± 0.11
35.596426	-4.671061	XMM	9	1.22 ± 0.17	8.02	12.07 ± 0.08
36.418598	-4.383661	XMM	8	1.10 ± 0.14	7.86	11.99 ± 0.09
35.615241	-4.318838	XMM	6	1.20 ± 0.19	7.50	11.70 ± 0.10
36.801602	-4.309702	XMM	8	1.19 ± 0.12	8.05	12.00 ± 0.09
35.569539	-4.263299	XMM	8	1.31 ± 0.12	6.71	12.02 ± 0.09
36.018523	-4.263031	XMM	10	1.03 ± 0.08	8.75	12.23 ± 0.08
36.183381	-4.252869	XMM	7	1.15 ± 0.20	7.06	11.93 ± 0.09
35.410208	-4.225554	XMM	7	1.18 ± 0.20	7.23	11.83 ± 0.10
36.016256	-4.220815	XMM	7	1.11 ± 0.18	7.35	12.01 ± 0.10 [1]
35.590690	-4.212183	XMM	6	1.27 ± 0.12	6.82	11.84 ± 0.11
35.520463	-4.059988	XMM	5	0.95 ± 0.04	6.82	11.93 ± 0.11
35.932398	-3.845375	XMM	9	1.22 ± 0.17	7.54	12.09 ± 0.08

continued on next page

Table 2.7: *continued*

Ra	Dec	Field	Ngals	z	δ	$\log_{10}$(M) [$M_\odot$]
35.868910	-3.814312	XMM	6	1.10 ± 0.23	6.54	11.96 ± 0.10
35.983502	-3.718699	XMM	8	1.10 ± 0.16	7.11	12.08 ± 0.09
35.486966	-3.676711	XMM	6	1.18 ± 0.16	7.63	11.83 ± 0.10
35.499209	-3.663378	XMM	7	1.30 ± 0.08	8.66	12.01 ± 0.10
36.090184	-3.542004	XMM	6	1.30 ± 0.11	6.60	12.00 ± 0.10
35.619349	-3.432304	XMM	6	1.24 ± 0.15	6.94	11.92 ± 0.10
35.467994	-3.425673	XMM	7	1.24 ± 0.14	7.29	11.82 ± 0.09
35.402332	-3.411241	XMM	5	1.14 ± 0.21	6.62	12.03 ± 0.11
35.413456	-3.372366	XMM	6	1.17 ± 0.09	8.48	11.75 ± 0.10
35.683865	-3.367863	XMM	7	1.27 ± 0.19	6.74	11.90 ± 0.10

Table 2.8: Bump-2 cluster candidates found with a smoothing of radius 0.′93. Columns are Ra, Dec of the centre of the peak in the density map, SWIRE Field in which the candidate cluster is located, Ngals is the number of galaxies within the smoothing radius of the peak, z is the redshift estimate (see text for details) and δ is the density contrast of the peak pixel, i.e. peak pixel density/average density across the whole field.

Ra	Dec	Field	Ngals	z	δ
243.992728	54.250874	EN1	3	1.60 ± 0.19	7.18
241.579315	54.324921	EN1	3	1.78 ± 0.24	6.40
243.315092	54.341487	EN1	3	1.90 ± 0.23	6.77
241.993308	54.395991	EN1	3	1.84 ± 0.33	9.84
244.566682	54.628076	EN1	3	1.72 ± 0.27	7.52
241.337884	54.640125	EN1	3	1.86 ± 0.20	6.03
242.101899	54.647719	EN1	3	1.66 ± 0.32	6.78
241.460646	54.643713	EN1	3	1.76 ± 0.26	5.78
241.877182	54.649645	EN1	3	1.81 ± 0.31	6.35
242.125128	54.760062	EN1	3	1.85 ± 0.24	6.27
242.125111	54.761173	EN1	3	1.85 ± 0.24	6.27
241.538812	55.175664	EN1	3	2.03 ± 0.01	7.05
243.033365	55.213559	EN1	3	1.50 ± 0.02	5.86
240.897763	55.363214	EN1	3	2.03 ± 0.01	7.63
243.522095	55.510336	EN1	3	1.85 ± 0.18	6.11
243.087448	55.621179	EN1	3	1.50 ± 0.08	6.58
242.413857	55.698950	EN1	3	1.72 ± 0.29	7.32

continued on next page

[1]Cluster has NED identification.

[2]Cluster is likely one of the (Demarco et al., 2010) clusters.

Table 2.8: *continued*

Ra	Dec	Field	Ngals	z	δ
242.881173	55.719336	EN1	3	1.99 ± 0.07	6.87
240.635362	55.739019	EN1	3	1.83 ± 0.35	5.96
163.395231	57.301901	Lockman	3	1.69 ± 0.31	5.78
163.342349	57.639392	Lockman	3	1.86 ± 0.29	6.48
163.360251	57.825833	Lockman	3	1.96 ± 0.12	5.83
163.164680	57.928563	Lockman	3	1.95 ± 0.14	5.78
162.840623	57.936833	Lockman	3	1.77 ± 0.31	6.04
161.386874	58.300504	Lockman	4	1.84 ± 0.25	8.07
163.777713	58.321429	Lockman	3	1.77 ± 0.27	5.85
164.385883	58.513723	Lockman	3	1.91 ± 0.12	6.47
162.084643	58.555881	Lockman	3	2.03 ± 0.01	6.11
163.172044	58.669693	Lockman	3	1.98 ± 0.09	6.10
161.711888	58.904762	Lockman	3	1.83 ± 0.35	6.58
162.052126	59.334727	Lockman	4	2.03 ± 0.01	8.78
161.817307	59.378819	Lockman	3	1.58 ± 0.03	6.37
161.827649	59.548691	Lockman	3	1.83 ± 0.35	6.38
36.436901	-5.067379	XMM	3	1.98 ± 0.09	7.96
35.758755	-4.894859	XMM	3	2.03 ± 0.01	6.85
35.447597	-4.647213	XMM	3	1.88 ± 0.26	5.79
36.022733	-4.591336	XMM	3	1.95 ± 0.14	6.98
35.990980	-3.986975	XMM	3	1.83 ± 0.35	7.48
35.633445	-3.881638	XMM	3	1.78 ± 0.26	7.87
36.119513	-3.391487	XMM	6	1.78 ± 0.25	15.97

The redshifts given in tables 2.7 and 2.8 are calculated from a simple fit of the observed K-band, 3.6μm and 4.5μm fluxes (for Bump-1, in the case of Bump-2 5.8μm fluxes are also used) to the bump feature of the Elliptical galaxy template given in figure 2.3. At a given redshift the template is convolved with the instrument filter functions to calculate the flux that would have been observed at that redshift. The template is then scaled by the mean ratio between the template fluxes and the observed fluxes. Finally, the χ^2 between the observed fluxes and the scaled, template fluxes is calculated. This is done over the full bumps redshift range in steps in redshift space of 0.03 and the redshift for a given galaxy is that with the lowest χ^2. The cluster redshift is the mean redshift estimated for all galaxies within the cluster and the error is the standard deviation of these redshifts. Note that this redshift determination is extremely simple and does not account for photometric errors, dust extinction or the other available photometry, rather it is used to give an indication of the position within the bump redshift range that the cluster falls. This 'redshift' is also calculated for the full galaxy population, figure 2.13 gives the distribution of redshifts for the whole bumps sample using this technique. In a number of places in the following analysis of the Bump-1 clusters the redshift of the Bump-1 galaxies are assumed to be 1.0. The figure shows that this assumption is not particularly valid. While ideally we would re-do the analysis below to account for this change we leave this for future work. We note that the accuracy of the redshifts is very low - the technique is simple and we have not made account of the errors involved. In any case, since our cluster finding relies on the simple assumption that the bumps galaxies are at a similar redshift (regardless of what that redshift is) and due to our technique for estimating mass from the RR08 photo-z catalogues (see below), it is unlikely to significantly affect our results.

We have identified a list of 118 clusters at a redshift of $\sim$ 1 and 40 clusters at a redshift of $\sim$ 1.5 with 95% and 55% reliability respectively, giving reliability corrected number densities of 11.7 and 2.3 clusters per square degree. This corresponds to clusters with dark matter halo masses of $\sim 10^{14}$M$_\odot$ and $\sim 10^{15}$M$_\odot$ respectively (estimated simply from simulation cluster densities Łokas et al., 2004). Figures 2.14 - 2.16 and 2.17 - 2.19 show the Bump-1 and Bump-2 density maps for each field for the smoothing scales given above. The clusters are over-plotted as red circles. Figures 2.20 and 2.21 show the sky distribution for each field for the Bump-1 and Bump-2 clusters respectively. Figure 2.15 shows that there is a part of the Lockman Hole field where we do not detect any clusters. The mean density of this region is slightly lower than the rest of the field, however, it is consistent within the errors. The mean density in this region is 9.7×10^{-3} with a

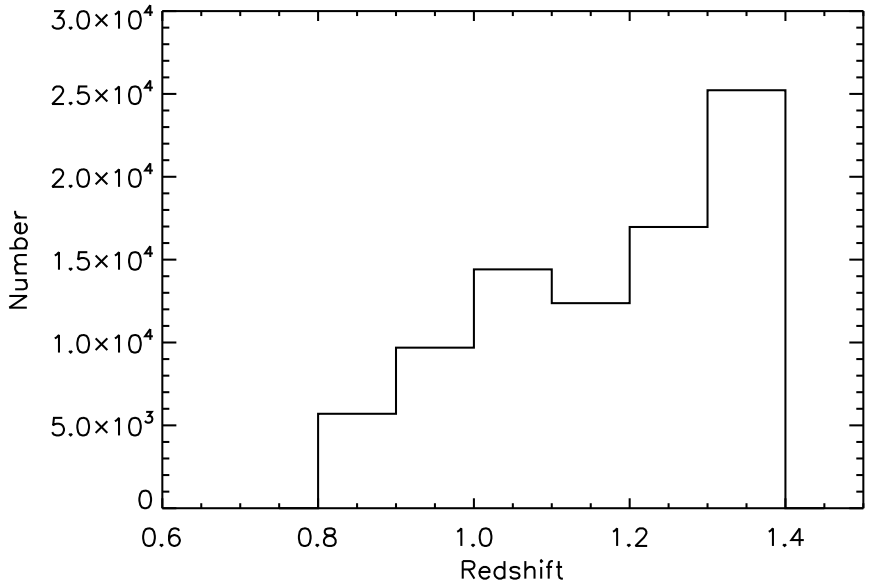

Figure 2.13: Distribution of the Bump-1 redshift estimate.

standard deviation of 6.7×10^{-3}, whereas the remainder of the field has a mean density of 1.1×10^{-2} with a standard deviation of 7.5×10^{-3}. The absence of any clusters in this region could suggest a selection effect causing fewer over-densities of bump galaxies. However, plausible effects such as incompleteness in one or more bands or errors in the source photometry would also appear in the calculation of the mean. A systematic error causing this effect would have to be unusual. Alternatively, it is plausible that this area is a genuine 'void', with a volume of $\sim 1 \times 10^{-3} h^{-3}\mathrm{Gpc}^{-3}$ lacking clusters with a dark matter mass $\gtrsim 10^{14}\mathrm{M}_{\odot}$. Voids are as much a part of large scale structure as are clusters and have been studied for some time (see e.g. Peebles, 1980; Rood, 1988; Einasto et al., 1989; Bond et al., 1996; Lindner et al., 1996, and references therein). Indeed, searching for voids (and studying the supercluster-void network of galaxies) in galaxy surveys is a large topic of research. For example, van de Weygaert et al. (2009) identified around 1000 voids in the SDSS, but there are a number of others, (for example Saunders et al., 1991; Einasto et al., 2003, 2005; von Benda-Beckmann & Müller, 2008, and references therein). However, in order to confirm this hypothesis we would need to search for similar voids in dark matter simulations (such as the millennium simulation Springel et al., 2005) and conduct further observations of the surrounding regions and is left for future work.

We look to find whether any of our clusters have been previously identified. We cross-match our cluster catalogues to previously published lists of clusters with a $25''$ radius. A large radius is used due to the uncertain nature of the central cluster positions (here we

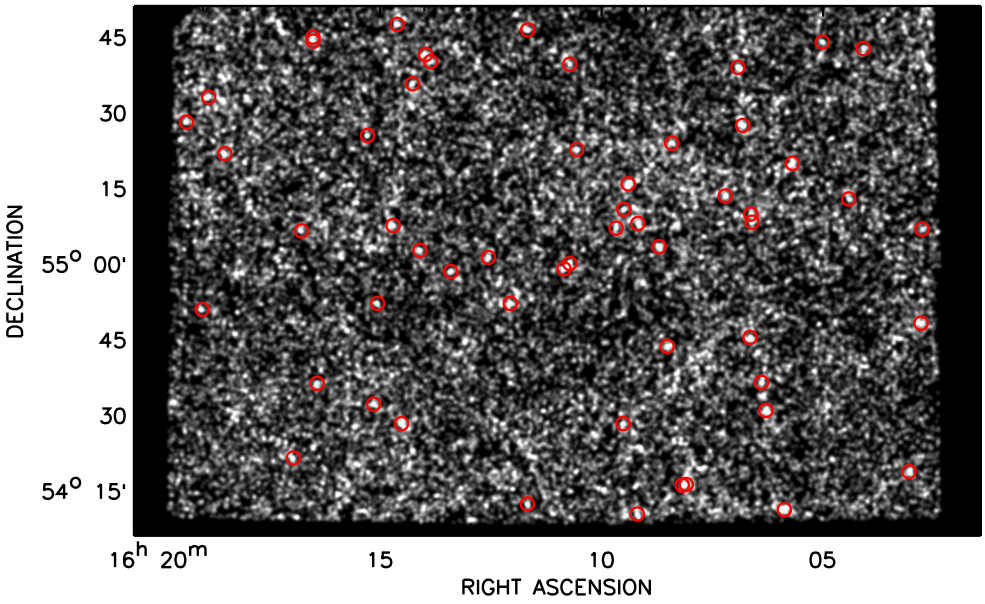

Figure 2.14: Smoothed density map for the Bump-1 selected galaxies for a smoothing scale of 0′.33 in the EN1 field. The cluster candidates are shown as red circles.

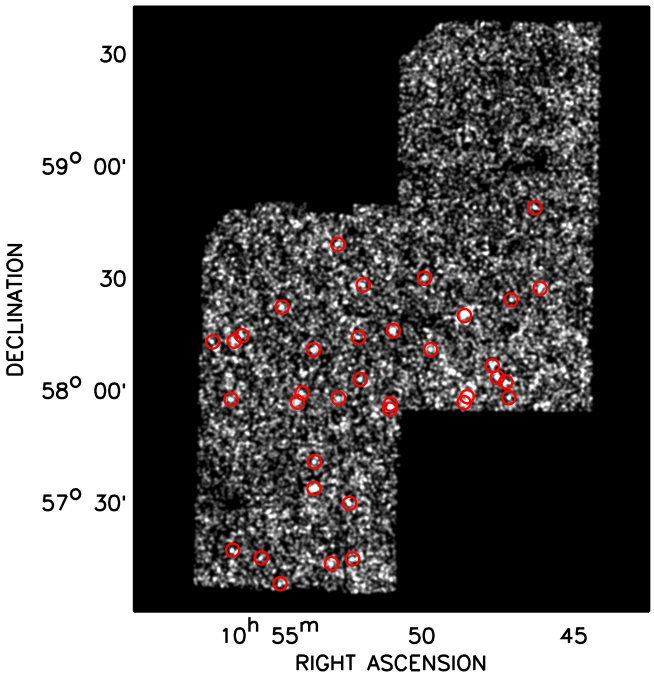

Figure 2.15: As figure 2.14 but for the Lockman Hole field.

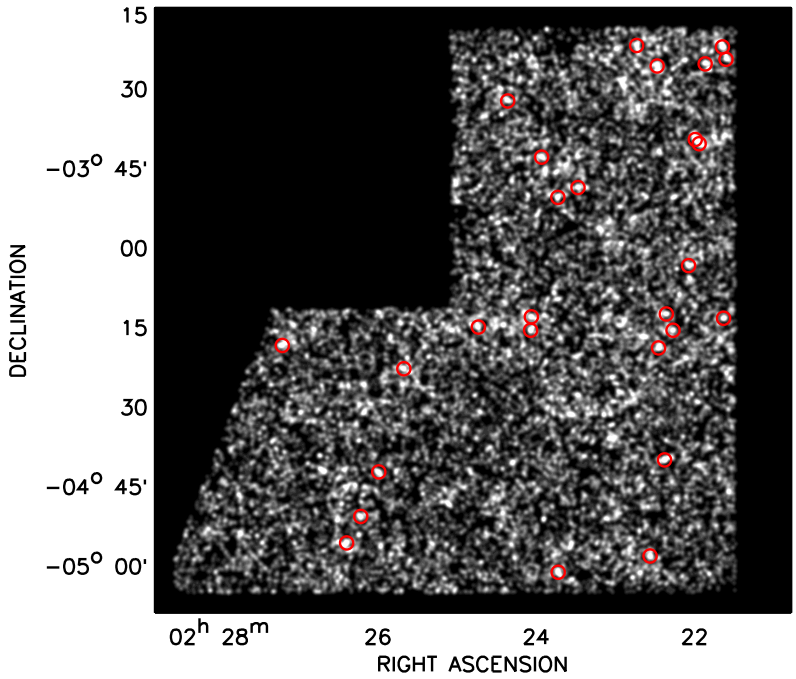

Figure 2.16: As figure 2.14 but for the XMM field.

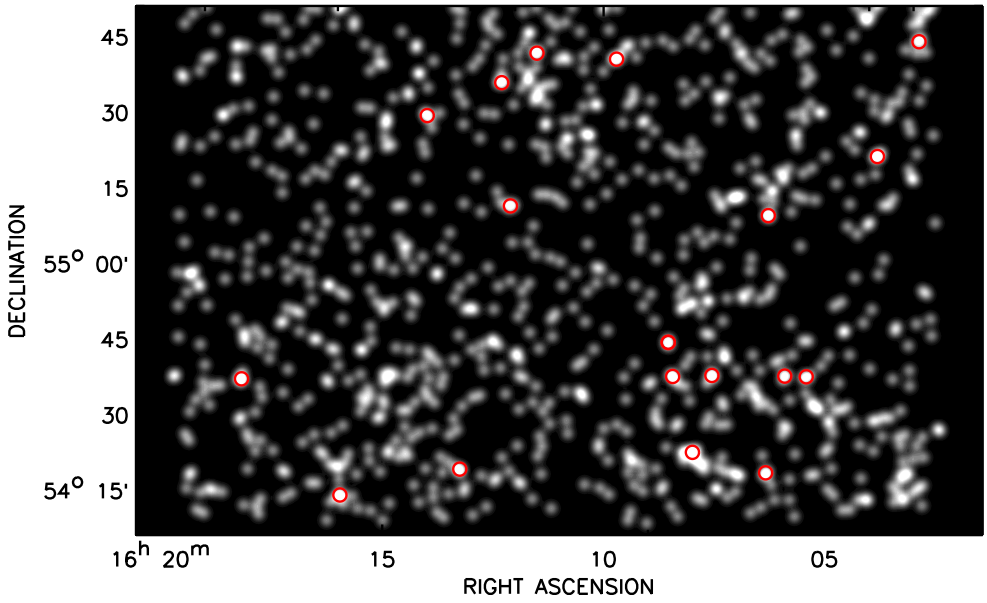

Figure 2.17: Smoothed density map for the Bump-2 selected galaxies for a smoothing scale of 0.′93 in the EN1 field. The cluster candidates are shown as red circles.

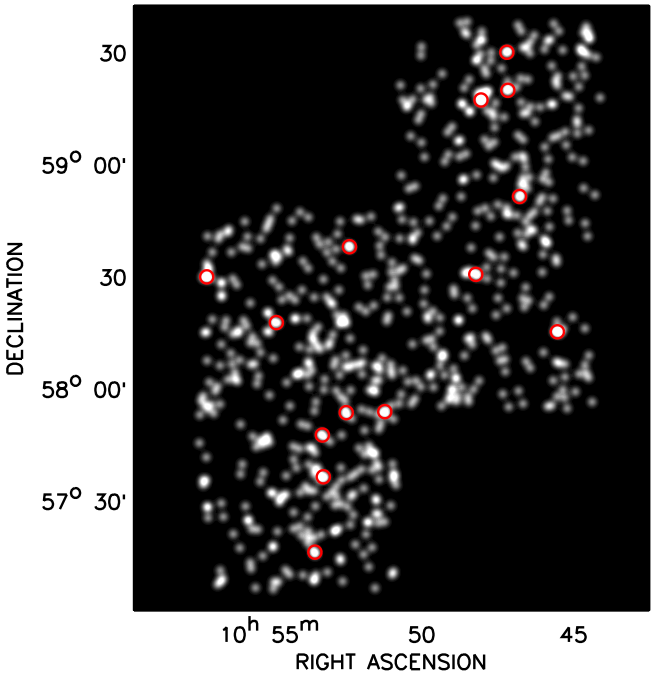

Figure 2.18: As figure 2.17 but for the Lockman Hole field.

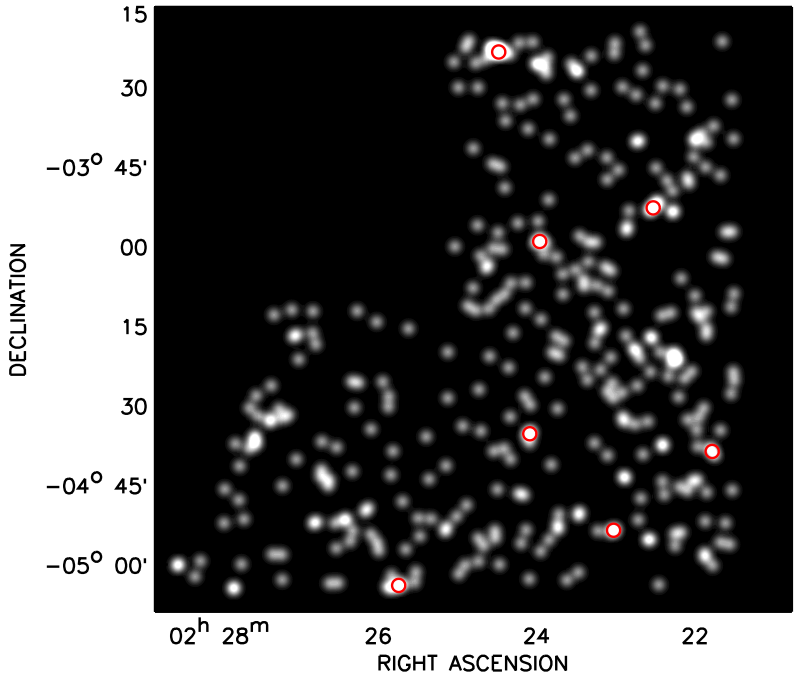

Figure 2.19: As figure 2.17 but for the XMM field.

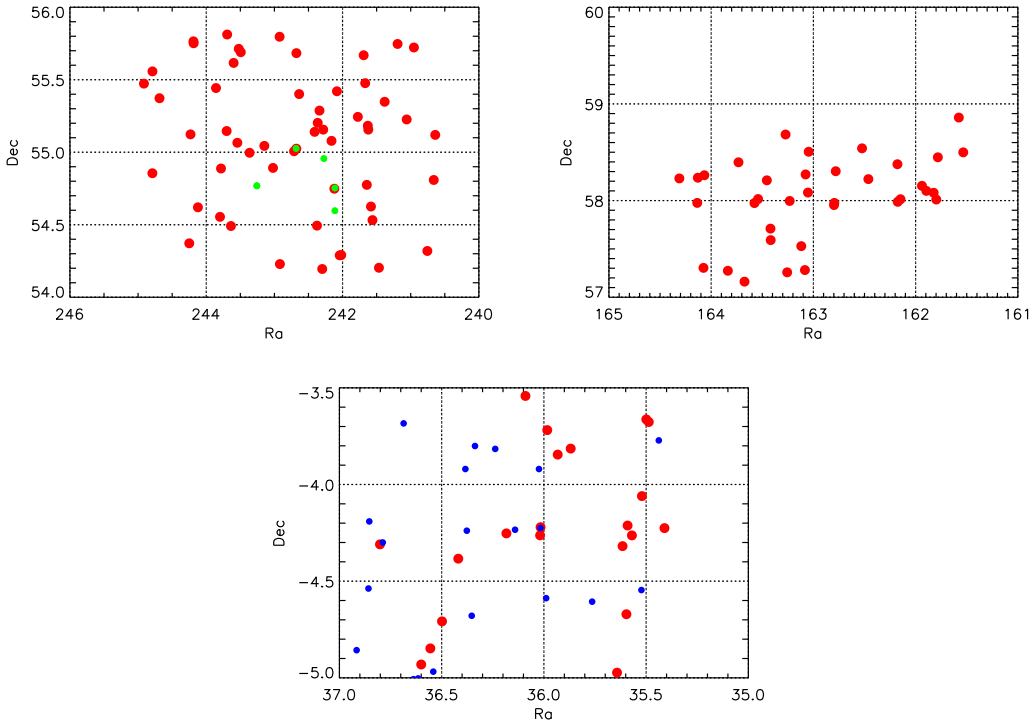

Figure 2.20: Distribution of the Bump-1 cluster candidates in red for EN1 (top left), Lockman (top right) and XMM (bottom). The clusters spectroscopically confirmed from Swinbank et al. (2007) are shown in green and from the XMM-LSS are shown in blue.

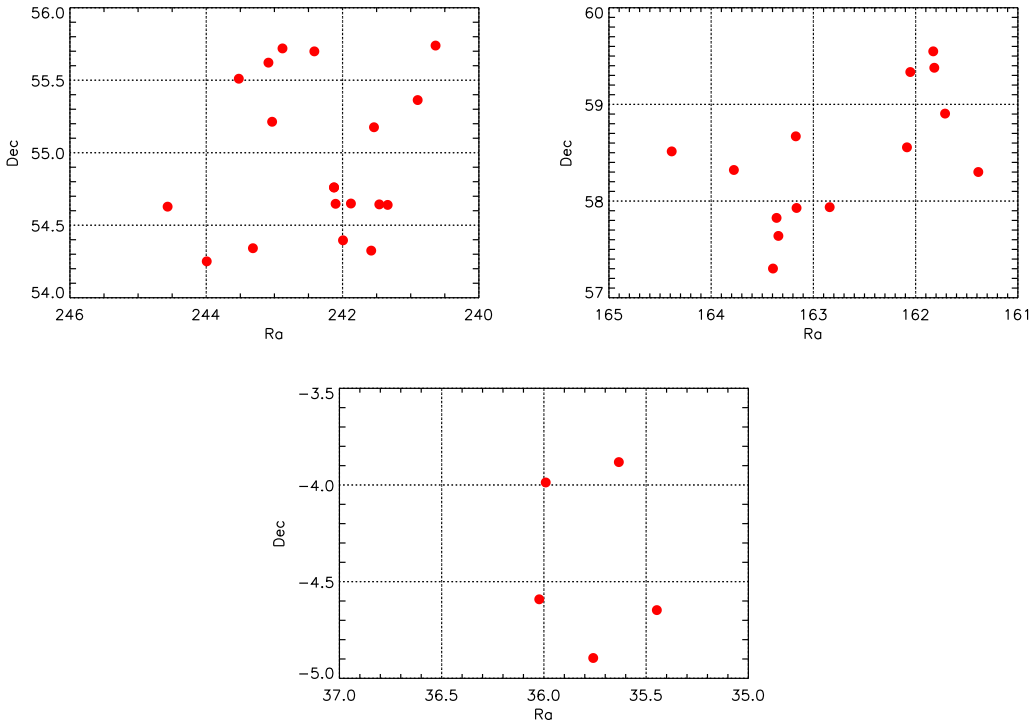

Figure 2.21: Distribution of the Bump-2 cluster candidates in red for EN1 (top left), Lockman (top right) and XMM (bottom).

use the peak of the density map as the central position, whereas many samples have the position of the brightest galaxy in the cluster as the central point). We cross-match with the spectroscopically confirmed members of the Swinbank et al. (2007) $z \sim 0.9$ super-cluster which were identified from a search of the Early Data Release DXS data. We find 2 of these clusters are coincident with cluster candidates in the Bump-1 sample. We briefly investigate the missing three. In one case, the Swinbank et al. (2007) cluster is a 4σ excess rather than the 5σ excess required for a detection in our search. In the final two cases, the Swinbank et al. (2007) positions are only 2 and 1 σ excesses respectively in our maps. The nearest over-densities are 4σ excesses located $36''$ and $46''$ away from the Swinbank et al. (2007) positions. This suggests that perhaps the two cluster searches find a slightly different set of clusters, but that also our conservative approach in Bump-1 to ensure only real clusters are included is also removing some genuine clusters. We have not made any attempt to quantify the completeness of the cluster search, since our Bump-1 reliability is high it is possible that the Bump-1 completeness will be low. To calculate completeness we would need to simulate the clusters that we have found, however this is not a simple problem since the precise nature of our objects are uncertain and we leave this for future work. Note that if these missing clusters are of a similar (or greater) mass, this will add error to the cluster mass estimate which is based simply on the number density of clusters.

Two of the clusters of Demarco et al. (2010) at redshifts of 1.16 and 1.21 overlap with our observations. The nearest cluster candidates we identify are $27''$ and $34''$ from these clusters. We also cross-match to the spectroscopically confirmed XMM-LSS cluster list (Pacaud et al., 2006, 2007; Willis et al., 2005; Valtchanov et al., 2004; Pierre et al., 2007; Maughan et al., 2007; Bremer et al., 2006) and find 1 cluster coincident within the matching radius with the cluster candidates in the Bump-1 samples. Finally, we cross-match to objects classed as clusters or groups in the NASA Extragalactic Database (NED[2]) identifying one further redshift 1.1 cluster from the ROSAT Deep Survey (Lehmann et al., 2001; Thompson et al., 2001; Hashimoto et al., 2004). Table 2.9 shows the results of this literature search. The published redshifts of these clusters match very well to our central Bump-1 redshift of 1, all published redshifts are in the range $0.9 < z < 1.2$. These cluster are over-plotted in figures 2.20 and 2.21. We find no matches for the Bump-2 sample.

[2]http://nedwww.ipac.caltech.edu/

Table 2.9: Cross-match of Bump-1 cluster candidates to clusters in the literature with 25″ radius (see text for references).

Object	RA	DEC	Redshift	Separation [″]
DXS 2	242.112080	54.753330	0.9	25.0
DXS 5	242.681670	55.026390	0.9	10.0
RX J1053.7+5735	163.415830	57.588330	1.1	10.4
XLSSC 29	36.016998	-4.225000	1.05	15.3

2.6 Cluster Galaxy Properties: Stellar Mass and Star Formation Rate

In order to compare the properties of galaxies in different environments we wish to calculate the Stellar Mass, M and star formation rate (SFR) of both the cluster member galaxies and field galaxies. We use the IRAC 3.6μm and MIPS 24μm fluxes as proxies for Stellar Mass and SFR respectively (see RR08 and references therein). Typically, to calculate mass and SFR from the 3.6μm and 24μm fluxes one must calculate the rest-frame 3.6μm and 24μm luminosity. A typical mass-to-light ratio can then be used to calculate the mass and an empirical relation such as that obtained by Kennicutt (1998) between 24μm luminosity and SFR. However, calculation of the luminosity requires knowledge of both the redshift and the K-correction for the galaxy. The K-correction accounts for the fact that the broadband filter spans a range of the galaxy SED, which changes with redshift. However, to calculate a proper K-correction requires an estimate of the SED from spectral fits to the photometry. Such fits would result in the inclusion of large selection effects (such as variation in optical depth) as discussed in section 2.2. However, for a subset of the bump-1 sample which have good optical coverage, photo-z fits have been previously constructed. In order to calculate a stellar mass for the whole of the bumps sample, we calculate a mapping between the 3.6μm and 24μm flux and the Stellar Mass and star formation rate of galaxies in the photo-z catalogue of RR08.

We again focus on the EN1 field, removing objects with no mass estimate. We cross-match the Bump-1 and 2 catalogues with the catalogue of RR08, 10415 (99) out of 38140 (946) Bump-1 (2) objects are matched successfully. We find the average conversion between stellar mass and 3.6μm flux and between 24μm flux and SFR of these galaxies by calculating the average of $\log_{10}(M) - \log_{10}(F_{3.6})$ and $\log_{10}(SFR) - \log_{10}(F_{24})$ respectively. Figures 2.22 shows how this conversion varies with redshift for the Bump-1 photo-z

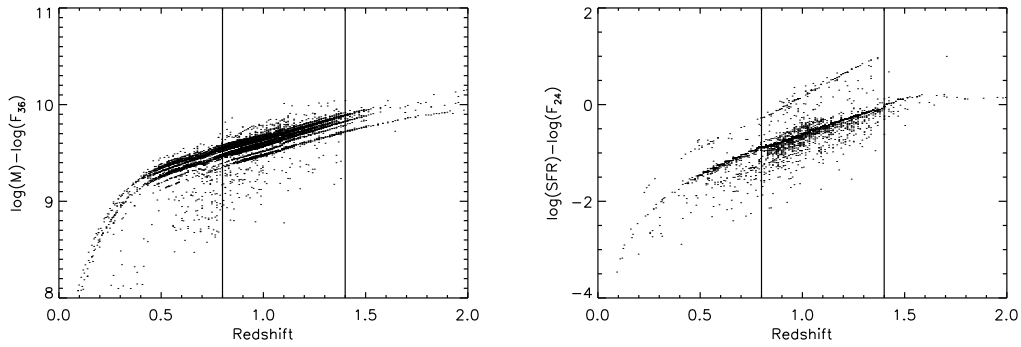

Figure 2.22: Comparison between Bump-1 sources and the photo-z catalogue. The left panel shows the relationship between 3.6μm flux and Stellar Mass as a function of photo-z for Bump-1 selected galaxies in the RR08 catalogue. The right panel similarly shows the conversion between 24μm flux and SFR. The vertical lines show the Bump-1 redshift range of $0.8 < z < 1.4$ from table 2.5.

matches. Clearly there is a large range in both mass and SFR and so our inferred Stellar Masses and star formation rates are only very approximate.

Despite this, we use the Bump galaxies 3.6μm and 24μm flux and this average conversion to estimate the Stellar Mass and SFR of the cluster and field galaxies. Figure 2.23 shows a comparison between the stellar mass estimated in this manner and that of RR08. The figure shows that for the most part this mapping reproduces the RR08 mass reasonably well, however, there are outliers. A similar comparison between the estimated SFR and that in RR08 is shown in figure 2.24. The figure shows that there is a large discrepancy between the two and as such we do not investigate this further.

We find the cluster Stellar Mass by simply summing that of the individual galaxies. These are listed in table 2.7. The errors quoted in table 2.7 are from a simple propagation of errors of the member galaxies, which are in turn calculated from a propagation of errors on the 3.6μm flux and the standard deviation of the conversion between mass and 3.6μm flux from the RR08 photo-z catalogue. Unfortunately there are insufficient matches in Bump-2 to make even this rather crude comparison and we do not attempt to calculate the stellar mass or SFR of the Bump-2 galaxies.

In figure 2.25 we show the $[K] - [3.6]$ and $[3.6] - [4.5]$ colour as a function of mass for both cluster and field galaxies. The plots suggest that the cluster and field galaxies are not separate populations, which we investigate further in section 2.7. The plots also show the effects of our selection. It is clear that there are a number of galaxies at low masses with large $[K] - [3.6]$ and low $[3.6] - [4.5]$ that are not included in our sample. This

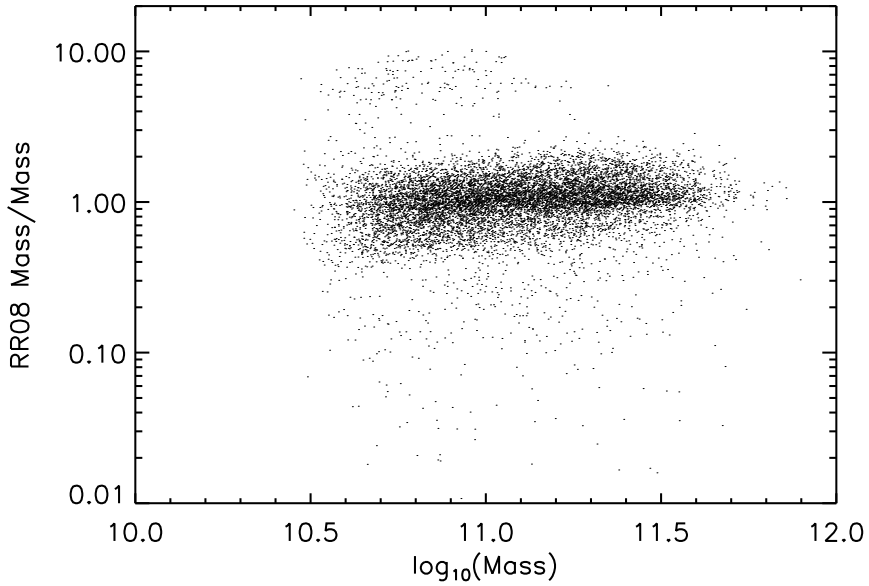

Figure 2.23: Comparison between the mass calculated for the Bump-1 galaxies and the mass calculated by RR08 where available.

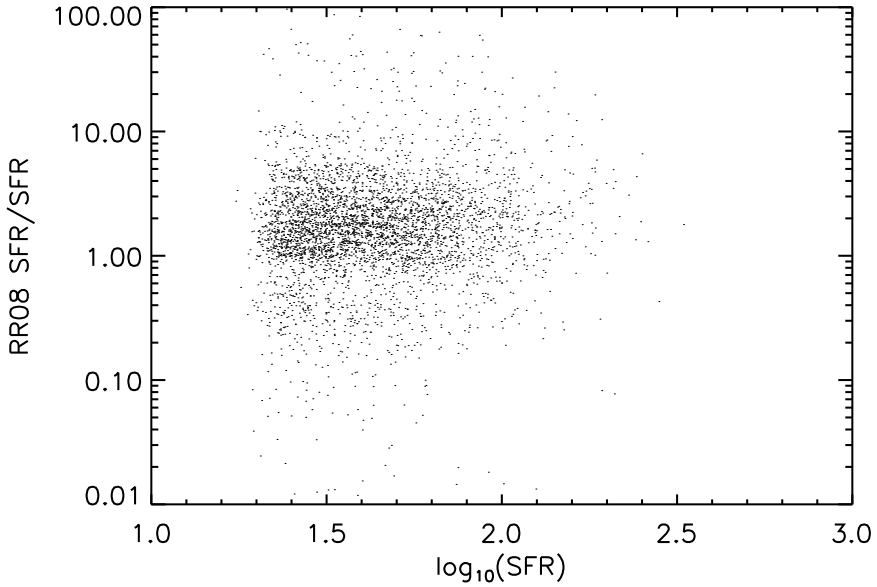

Figure 2.24: Comparison between the SFR calculated for the Bump-1 galaxies and the SFR calculated by RR08 where available.

comes from the K-band completeness limit. The plots suggest that this incompleteness is significant for $M < 10^{11}\mathrm{M}_{\odot}$. Figure 2.26 shows the mass of all galaxies as a function of redshift in the RR08 catalogue. The plot shows that the survey is complete to $10^{11}\mathrm{M}_{\odot}$ for the Bump-1 redshift range. We therefore concentrate on objects with mass $> 10^{11}\mathrm{M}_{\odot}$,

for a comparison, the mass of the Milky Way is estimated to be around $7 \times 10^{11} M_{\odot}$ (Gnedin et al., 2010).

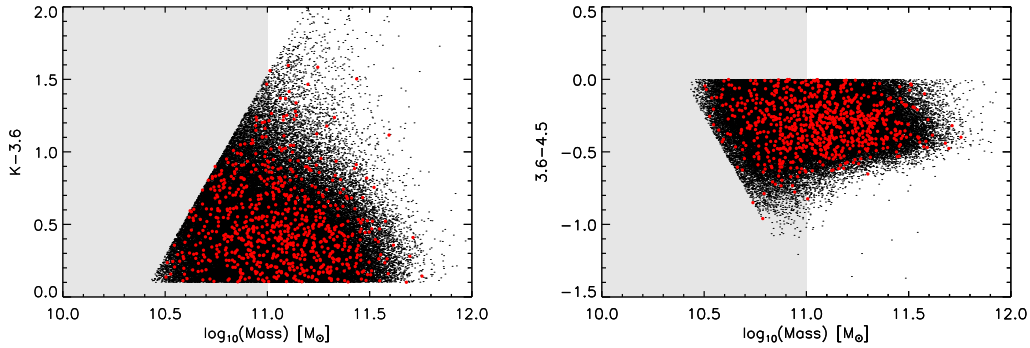

Figure 2.25: The $[K] - [3.6]$ (left-hand panel) and $[3.6] - [4.5]$ (right hand panel) colour as a function of stellar mass for cluster and field galaxies. Field galaxies are shown in black and cluster galaxies are shown in red. The grey shaded area is where the selection is significantly incomplete.

2.6.1 Stellar Mass of Galaxies in Different Environments

In order to compare cluster and field galaxies we attempt to calculate the Mass Function of both samples of galaxies. The Mass Function of galaxies, $\Phi(M)$, is the number density of galaxies as a function of mass M and has been shown to be well described by a Schechter function, (see e.g. Schechter, 1976; Balogh et al., 2001, and references therein) such that

$$\Phi(M)\mathrm{d}M = \Phi^*(M/M^*)^{\alpha} exp(-M/M^*)\mathrm{d}(M/M^*) \tag{2.11}$$

where Φ^* is the normalisation and M^* is the characteristic mass. There are many estimators of the Mass Function with the completeness limits of a survey, although they are usually in the guise of calculating a Luminosity Function. The most common estimators are the $1/V_{max}$ estimator of Schmidt (1968) (this is the most widely used), C^+ estimator of Lynden-Bell (1971), the STY estimator of Sandage et al. (1979) and the SWML estimator of Efstathiou et al. (1988). Each estimator has its own set of assumptions and biases, (see e.g. Willmer, 1997; Takeuchi et al., 2000; Ilbert et al., 2004, for a review). In the present work we use the $1/V_{max}$ estimator, primarily due to its simplicity but also to facilitate comparisons with previous work. We did attempt to derive a Mass Function using a maximum likelihood method as in Efstathiou et al. (1988), parameterising the Mass Function as a Schechter function. In this method only the shape of the Mass Function can be obtained, the normalisation must be derived from a different technique.

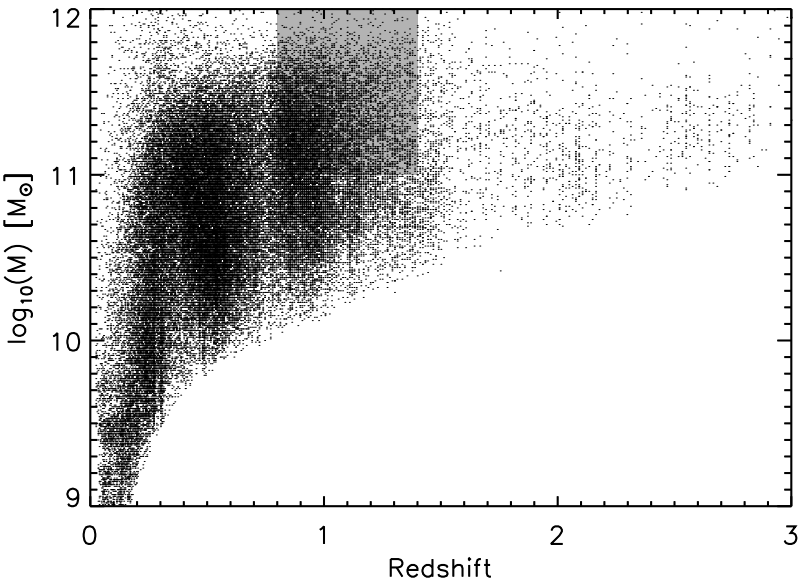

Figure 2.26: Mass as a function of redshift for the RR08 photo-z catalogue. The shaded area shows the bumps selection redshift and the mass above which the selection is complete.

However, since we could only use galaxies where we are complete ($M \geq 10^{11}\mathrm{M}_{\odot}$) we were not able to constrain the faint end slope (i.e. α). Furthermore, from the literature (see below) we expect that M^* is less than $10^{11}\mathrm{M}_{\odot}$. Therefore we were not able to constrain the Schechter function parameters. Since our uncertainties in mass and redshift are large a simple $1/V_{max}$ technique will suffice for our needs. Furthermore, in the region where we are complete ($M \geq 10^{11}\mathrm{M}_{\odot}$), the correction for objects falling below the completeness limit is not necessary, and the Mass Function is simply the number of objects in each mass bin divided by the volume of the Bump-1 redshift range of $0.8 < z < 1.4$ (from table 2.5). The procedure described below is only necessary below $10^{11}\mathrm{M}_{\odot}$.

To calculate the Mass Function we must calculate the volume over which each object could have been included in our selection. In principle, one takes the SED of each galaxy and redshifts it to identify at which redshift it would no longer meet the selection criteria of our survey. This gives a redshift interval over which the galaxy could have been observed from which the V_{max} can be calculated. By using the galaxy SED, one can account for the K-correction as well as the reduction in observed brightness due to increased redshift and for the effect of cosmological stretching. However, while the colour selection we have used limits galaxies to be within a likely redshift interval, we do not know the precise redshift of our objects, due to the degeneracy between colour and redshift. The variation in spectral shape is likely to be broader than that given by the templates in figure 2.4. With the

broad-band photometry we have used we are not able to discern between, for example, objects which have a narrow bump and those which have a broad bump. These different shapes would produce different redshift intervals. Finally, the strength of the bump feature is diluted by non-stellar emission, such as that from AGN. Variation in this contribution both within the population and as a function of redshift will also introduce uncertainty. In order to account for these effects properly would require full SED fits. However, as described above, such fits would vary in success rate introducing large selection effects that must be accounted for. Since in the final analysis we concentrate on masses where the V_{max} correction is not necessary, we leave this for future work. Instead, we use the simplified procedure given below.

For a given galaxy we wish to calculate the volume over which the galaxy could have been observed given the completeness limits of our survey. For each galaxy we use an array of redshifts of width $\Delta z = 0.02$. For each redshift element, we convert the calculated mass of the galaxy to the 3.6μm flux the galaxy would have had at that redshift, using the photometric redshift catalogue of RR08 as discussed in section 2.6, however in this case we calculate the conversion at each redshift element separately,

$$\log_{10}(F'_{36}(z)) = \log_{10}(M) - W(z) \tag{2.12}$$

where M is the stellar mass of the galaxy as calculated above; $W(z)$ is the conversion between mass and 3.6μm flux as a function of redshift calculated from the catalogues of RR08; and $F'_{36}(z)$ is the 3.6μm flux the galaxy would have had as a function of redshift. We then estimate the 4.5μm flux and K-band magnitude the galaxy would have had at each redshift element using the true colours of the galaxy and the estimate of the 3.6μm flux of that redshift element (this is clearly simplified since it does not include a colour correction, see above). If the true $[K]-[3.6]$ colour of the galaxy is C_1 and the true $[3.6]-[4.5]$ colour of the galaxy is C_2 then

$$[K](z) = C_1 + [3.6](z) \tag{2.13}$$

and

$$[4.5](z) = [3.6](z) - C_2 \tag{2.14}$$

We then identify at which redshift element the galaxy would fall below one of the completeness limits we impose. We set a minimum and maximum for this redshift of 0.8 and 1.4 from table 2.5, as beyond these redshifts we expect the galaxy to no longer meet the bump selection.

This gives us a maximum and minimum redshift at which the object could have been included in our sample. V_{max} is then given by the volume of the survey at the maximum

redshift less the volume of the survey at the minimum redshift. Then,

$$\Phi(M) = \frac{1}{\Delta M} \sum_{i=1}^{N} \frac{1}{V_{max}} \tag{2.15}$$

where the summation is over all galaxies and ΔM is the binsize.

This process is repeated for different mass bins, for $M < 10^{11}\mathrm{M}_{\odot}$ and combined with the calculation for higher masses described above, to give the final Mass Function. We perform the calculation separately for each field, the final Mass Function is the mean of these and the error is from the variation between the fields. We use this procedure to calculate the field galaxy Mass Function. However, the cluster galaxy Mass Function is not as simple since the volume over which the galaxies could have been observed is reduced since the galaxy resides within the cluster. Since we do not know the true extent of the clusters on the sky, and due to the large redshift errors, this would be difficult to calculate. Furthermore, there is a bias in the cluster detection due to the large redshift window. The number density of objects will be higher at the low redshift end of the window as our survey is flux limited. Thresholding on a fixed number density will therefore bias the cluster sample to lower redshift compared to the field sample. Therefore we do not attempt to calculate the cluster galaxy Mass Function. The field Mass Function is shown in figure 2.27, together with simple histograms per bin of the field and cluster galaxy masses. Note that above the completeness limit of $10^{11}\mathrm{M}_{\odot}$ the only difference between the Mass Function and the histogram is that the histogram is for all fields together whereas the Mass Function is the average over the fields. The plot suggests that there is little difference between the cluster and field galaxies. In order to test this hypothesis we perform a KS-test between the field and cluster galaxy masses in the range where we are complete. Taking all galaxies above 11 $\log_{10}\mathrm{M}_{\odot}$ the KS-statistic between the cluster and field masses is 0.72. Therefore, there is no evidence to suggest that the cluster and field galaxy masses are drawn from different distributions. This suggests that environment has a negligible effect on stellar mass at these redshifts. This result is confirmed if we look at the ratio of the 24μm flux to 3.6μm flux as a function of mass. This ratio is a proxy for the specific star formation rate of galaxies. Figure 2.28 shows that there is no difference between cluster and field galaxies above the completeness limit.

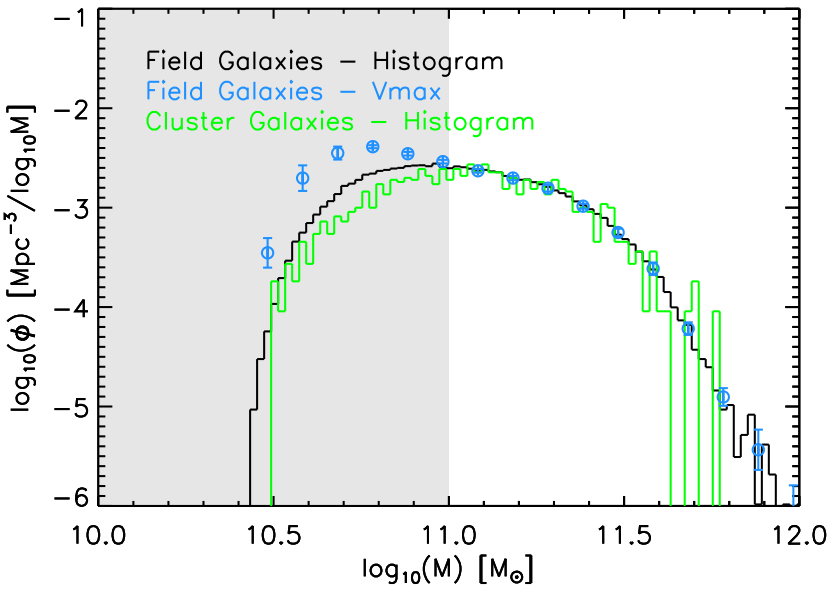

Figure 2.27: The $1/V_{\rm max}$ Mass Function for field galaxies (blue points) is shown together with a simple histogram per bin of the cluster and field galaxies (green and black solid lines). Both histograms have been normalised to the field Mass Function at 11.18 $\log_{10}$ $M_{\odot}$. Note that the figure suggests the incompleteness in our sample begins to have an effect at slightly higher masses than 10^{11}M$_{\odot}$. However, since this will not significantly affect our results we leave further investigation for future work.

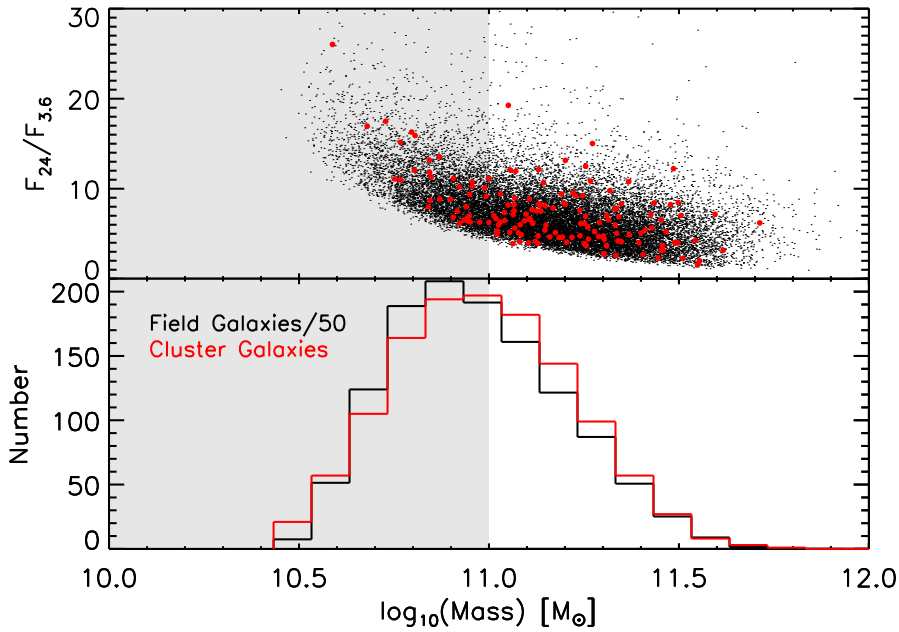

Figure 2.28: Bump-1 24μm to 3.6μm flux ratio as a function of mass and environment. The grey shaded area indicates incomplete regions. Field galaxies are shown as black points and cluster galaxies are shown as red circles. Galaxies with no 24μm detection are shown as a histogram in the bottom panel, where the field distribution has been divided by 50. The star forming properties of Bump selected galaxies do not vary with environment.

2.7 Discussion

2.7.1 High Redshift Clusters

The goal of this work was to identify a catalogue of clusters at high redshifts and provide some simple comparisons of the properties of cluster and field galaxies. We have shown that despite the simple nature of this cluster detection algorithm, we find a large sample of clusters at high redshift with a high degree of reliability. We do not, however, make a calculation of the completeness of this search; since we focus on reliability it is highly likely that many clusters have been missed. To put our results in context we compare to the high redshift cluster searches discussed in section 1.5. In the Bump-1 range a number of clusters have been previously identified. Gerke et al. (2005) found 38 cluster candidates which contain more than 3 galaxies at $z > 0.9$ with $\sigma \geq 350$ km s^{-1} over 1 sq. deg. in DEEP2. Cucciati et al. (2009) found 25 similar objects in VVDS with 50% reliability. Eisenhardt et al. (2008) found 106 cluster candidates at $z > 0.9$ in the IRAC shallow survey. Grove et al. (2009) found 102 clusters at $z > 0.9$ in CFHTLS. Gladders & Yee (2005) identified 67 red-sequence clusters at $0.9 < z_{phot} < 1.4$. Finally, van Breukelen et al. (2006) found 13 clusters in the range $0.6 < z < 1.4$. This shows that our discovery of 118 clusters in the Bump-1 redshift range significantly increases the sample size of high redshift clusters.

It is particularly difficult to find any other cluster catalogues in the Bump-2 range, the high redshift involved is beyond most searches. One example is that of Zatloukal et al. (2007) who use the COSMOS field and complimentary H-band data to identify 12 clusters at $1.23 < z < 1.55$ with photometric redshifts. There are a handful of other examples, such as those of Stanford et al. (2006); Andreon et al. (2009); Papovich et al. (2010). At these redshifts over-dense peaks are rare and as such a large area is required to find significant numbers.

2.7.2 Galaxies in Different Environments

Figure 2.27 together with the KS-test results shows that there is no evidence that the mass distribution of cluster and field Bump selected galaxies is different. In the purely hierarchical model of galaxy formation, we expect cluster galaxies to be more massive due to a larger number of mergers. However, while this is clearly demonstrated at low redshift (Kauffmann et al., 2004; Li et al., 2006; Baldry et al., 2008; Blanton & Moustakas, 2009) it does not appear to be the case for high redshift Bump galaxies. In figure 2.29 we

show high redshift Mass Functions from the literature (Bolzonella et al., 2009; Ilbert et al., 2010, B09 and I10 hereafter). The Mass Function from I10 is derived from the *Spitzer*-COSMOS survey and represents the field environment over an area of ~ 2 sq. degs. I10 showed that these Schechter function fits are similar to field Mass Functions obtained by Fontana et al. (2004, 2006); Bundy et al. (2006); Borch et al. (2006); Pozzetti et al. (2007); Pérez-González et al. (2008). The Mass Function shown from I10 is the sum of their Mass Functions of $0.8 < z < 1.0$, $1.0 < z < 1.2$ and $1.2 < z < 1.5$ to more accurately represent the redshift range of the Bump-1 selection. We also show the $0.7 < z < 1.0$ Mass Functions in high and low densities from B09. This study found that high density environments tend to contain more massive galaxies, as expected, contrary to that found here. Qualitatively similar results to B09 were obtained by Bundy et al. (2006); Scodeggio et al. (2009). The figure shows that the field Mass Function found here is not consistent with those of I10 or the B09 low density Mass Function. Instead, the field Mass Function is reasonably consistent with the high-density Mass Function of B09. This perhaps suggests that the Bumps selection naturally selects galaxies in the most dense environments. It has been previously shown that Bump galaxies are strongly clustered (Farrah et al., 2006), although these included an additional constraint on the sample selection, such as that they are bright 24μm sources. Furthermore, our conservative Bump-1 cluster identification could mean that many of our field galaxies are in fact galaxies residing in over-dense environments, but not as rich as the clusters we have found. This would pollute any difference between cluster and field environments.

Our results are not necessarily at odds with the literature. The area covered by the analyses of I10, B09, Bundy et al. (2006); Scodeggio et al. (2009) is still small and as such does not include the richest environments. In addition, the K-band luminosity function has been shown to be very similar in cluster and field environments previously (Lin et al., 2004; Rines et al., 2004; Muzzin et al., 2007). Similarly, the 3.6 and 4.5μm cluster and field luminosity functions are very similar (Andreon, 2006; Babbedge et al., 2006; De Propris et al., 2007; Muzzin et al., 2008). Since each of these wavelengths are good proxies for stellar mass these results suggest that the distribution of masses is similar in both field and cluster environments.

There is an Eddington bias in our calculation. Figure 2.22 shows that the error associated with the stellar mass calculation is large. Low mass objects will be preferentially scattered to higher mass compared to high mass objects scattered to lower mass (as they are more numerous), producing an excess of high mass objects in our survey.

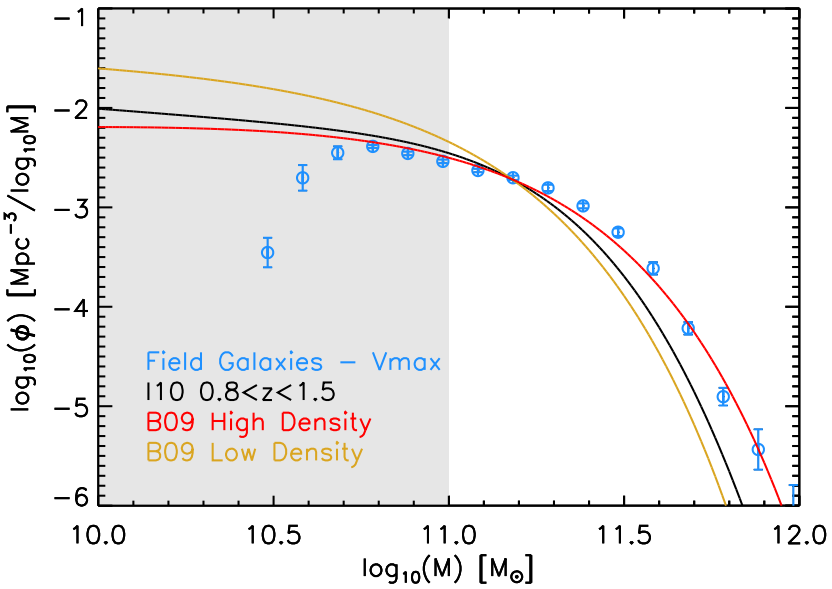

Figure 2.29: A comparison of the field galaxy Mass Function obtained here to the results of Schechter function fits to COSMOS data. The blue points are the Bump-1 $1/V_{\rm max}$ field galaxy Mass Function. The black line is the Mass Function obtained by I10, combining three of their redshift bins to encompass the larger redshift range we use. The red and gold lines are the Mass Functions obtained by B09 and are for galaxies separated into low and high density environments, although the small nature of the survey mean the richest environments are not included. The B09 Mass Functions are given without a normalisation so we normalise both their high and low density Mass Functions to the I10 Mass Function at 11.18 $\log_{10}{\rm M}_{\odot}$.

Furthermore, since the cluster selection threshold varies from field to field, our sensitivity to over-densities of different underlying mass in different fields will differ. However, as the completeness varies across the fields (see section 2.3.1), it would be inappropriate to use a uniform selection threshold, as this may cause many spurious detections in the worst fields. An alternative would be to take the most conservative selection threshold (i.e. highest mean and variance), and apply it to all fields. However this would only remove 7 Bump-1 cluster candidates and 4 Bump-2 cluster candidates from our quoted sample in Tables 2.7 and 2.8, and thus does not significantly affect our results.

That the cluster and field mass distributions are similar suggests that high redshift massive ($\gtrsim 10^{11}\mathrm{M}_{\odot}$) galaxies build up their stellar mass independent of environment. Furthermore, figure 2.28 suggests that the F_{24}/F_{36} ratio (which is a good proxy for the specific star formation rate (SSFR)) is independent of environment at $z \sim 1$. This implies that environment does not significantly affect the star formation of a galaxy at this redshift. Similar results were obtained by Krick et al. (2009) who found that the IR luminosity distribution of star-forming cluster and field galaxies are the same in the IRAC Dark Field. Figure 2.28 also shows that the F_{24}/F_{36} ratio and therefore the SSFR decreases with increasing stellar mass. This has been seen previously both locally and at high redshift (see e.g. Kauffmann et al., 2004; Elbaz et al., 2007; Oliver et al., 2010). The independence of SSFR with environment, however, is in contrast to the results of Elbaz et al. (2007) who suggested that SSFR increases with galaxy density at $z \sim 1$ over the smaller GOODS area. In any case, we certainly see evidence for a population of star forming galaxies in the dense regions of clusters at $z \sim 1$. Previous studies have similarly shown that LIRGs with large SFRs inhabit dense environments at $z \sim 0.8$ (Farrah et al., 2004, 2006; Marcillac et al., 2008).

If confirmed, these results suggest that while at low redshifts star-formation preferentially occurs in field environments, at $z \sim 1$ star-formation occurs independently of environment. This implies that cluster environments are more efficient at quenching star-formation between redshift 1 and 0 than the field. Processes such as ram-pressure stripping (see e.g. Gunn & Gott, 1972; Balogh et al., 2000); galaxy harassment (see e.g. Moore et al., 1999); galaxy "strangulation" (see e.g. Larson et al., 1980, whereby the tidal effects of the cluster gravitational potential on galaxies as they fall into the cluster halo cause their gas to be stripped and their SFR to decline); as well as galaxy-galaxy mergers (see e.g. Toomre & Toomre, 1972) could cause this quenching. Furthermore, studies of high redshift clusters at $z \sim 1.46$ and 1.62 have shown that higher densities show an

increase in the relative fraction of star-forming galaxies (Hilton et al., 2010; Tran et al., 2010). At the Bump-1 redshift ($z \sim 1$) we could be seeing the epoch at which the predominant environment for star-formation changes from higher to lower densities.

Finally, we note that further insights into the relationship between galaxy properties and environment could be gleaned via a calculation of the clustering of the bump galaxies rather than separating the galaxies into cluster and field galaxies as we have done here. However, this is left for future work.

Chapter 3

The AKARI Far-Infrared All-Sky Survey: Completeness and Reliability

3.1 Introduction

In the previous two chapters we have demonstrated the usefulness of large area Infrared surveys for studies of the galaxy population, with a particular emphasis on different environments. We now look to extend these studies in terms of both wavelength and area with the all-sky survey conducted by the Japanese AKARI Space Telescope. We assess the usefulness of this survey in terms of a calculation of the completeness and reliability of the survey.

This work was done with supervision from S. Oliver and was part of work that contributed to the broader analysis of the AKARI satellite. While this work does not directly appear in any publications (and this is not being pursued further) I am co-author of three AKARI papers (Kawada et al., 2007; Murakami et al., 2007; Wang et al., 2008), along with the catalogue release documents (Yamamura et al., 2009), as part of the AKARI team.

3.2 AKARI All-Sky Survey

AKARI is an Infrared Space Satellite mission of the Japanese Aerospace Exploration Agency, JAXA, launched in February 2006 (Murakami et al., 2007). AKARI was designed primarily in order to carry out an all-sky infrared survey in the wavelength range $2-180\mu$m.

The Far-Infrared Surveyor (FIS; Kawada et al., 2007) was designed for the all-sky survey and observes in 4 different bands (centred around the given wavelengths): N60 (65μm), WIDE-S (90μm), N160 (160μm) and WIDE-L (140μm). Approximately 94% of the sky had been observed by two scans of the AKARI FIS until the exhaustion of the helium coolant in August 2007 (Kawada et al., 2007; Nakagawa et al., 2007).

The AKARI all-sky survey is the first of its kind in the Far-Infrared since IRAS. The AKARI satellite is able to observe at longer wavelengths and with much improved spatial resolution: $\sim 27''$ at N60 and WIDE-S and $\sim 44''$ at WIDE-L and N160. The positional accuracy for detected point sources is $\lesssim 5''$ Kawada et al. (2007). The instrument and survey design have been described earlier Kawada et al. (2007). Here we highlight some key points. The satellite orbits the Earth every ∼100 minutes and scans the sky with a scan speed of $3\farcm6$ s^{-1}. Each scan has a width of $8' - 12'$ and on each orbit the scan is shifted by $4'$ in the longitudinal direction, thus a map of the sky is built up. While 94% of the sky has been observed with at least 2 scans a large part of the sky has been observed with more than 2 scans. Version 1 of the Bright Source Catalogue was released to the public on 30 March 2010 (Yamamura et al., 2009).

The FIS detector arrays have $N_{\rm row}$ rows and $N_{\rm col}$ columns. Each pixel has a sky footprint of Δ_α. The sky is mapped following an approximately ecliptic polar orbit, so each scan follows a line of approximately constant ecliptic longitude. The point-spread function in the focal plane is approximately Gaussian with a Full Width at Half Maximum (FWHM) given by $\theta_{\rm psf}$. Table 3.1 (which is adapted from table 2 of Kawada et al., 2007) shows the values of each of these parameters in each band along with the 5σ survey limits.

For any sky-survey producing a catalogue it is important that the characteristics and the quality of the survey are well understood in order to ensure that only true astronomical objects enter into the catalogue, avoiding the inclusion of spurious objects. It is also important to assess at what brightness we are confident that all objects have been detected. To this end we calculate the completeness and reliability of the AKARI all-sky survey (see Moshir et al., 1992, for a detailed review of completeness and reliability as applied to the IRAS Faint Source Catalogue).

3.3 Data

We use data taken as part of the main survey. The data we use has been processed by the upstream processing pipeline of the survey, the *Green Box* (GB; see the Bright Source

Table 3.1. FIS in-flight performance, adapted from table 2 of Kawada et al. (2007)

Band	N60	WIDE-S	WIDE-L	N160
Band center	65	90	140	160 [μm]
Effective band width	21.7	37.9	52.4	34.1 [μm]
Point spread function:				
- measured FWHM ($\theta_{\rm psf}$)	37±1	39±1	58±3	61±4 [$''$]
$N_{\rm row}$	2	3	3	2
$N_{\rm col}$	20	20	15	15
Δ_α	$\sim 27''$	$\sim 27''$	$\sim 44''$	$\sim 44''$
5σ flux density level:	2.4	0.55	1.4	6.3 [Jy]

Catalogue Release Note[1] for more details). The GB processes the raw data from the satellite removing instrumental signatures and glitches from cosmic ray hits and provides an astrometric and photometric calibration.

We focus on the WIDE-S band as this is the most sensitive and is the priority for the survey team. Table 3.1 shows that the WIDE-L, N160 and N60 bands are sensitive down to 1.4, 6.3 and 2.4 Jy (5σ flux density level) whereas the WIDE-S band is sensitive down to 0.55 Jy. For this reason source detection was performed on the WIDE-S band only, with photometry for the remaining 3 bands gained based on the positions of the WIDE-S detections. Therefore, we characterise the completeness and reliability of the WIDE-S survey.

We choose the ELAIS N1 (EN1) blank field, for its relatively high latitude and because it allows comparisons between the results from AKARI and the *Spitzer* 70μm SWIRE source list. Since the *Spitzer* survey is a much deeper one, going to a depth of 18mJy (see section 2.3) the SWIRE catalogue can be used as a list of true sources in the field.

The FIS instrument has two modes of operation, *Normal mode* and *Correlated Double Sampling (CDS) mode*. These two modes refer to how the charge build up on the detectors is reset. In Normal mode this is done at 0.5/1.0/2.0 seconds depending on the expected sky brightness. CDS mode is used to avoid saturation of the detectors in bright regions, with the detectors reset more frequently. The majority of the survey has been conducted in Normal mode and we therefore concentrate on this mode to assess the completeness and reliability of the survey.

[1] http://www.ir.isas.ac.jp/ASTRO-F/Observation/PSC/Public/RN/AKARI-FIS_BSC_V1_RN.pdf

Note that recently improved GB processed data has become available to us and ideally we would re-do the following analysis based on these new data.

3.4 SUSSEXtractor

SUSSEXtractor (SXT, R. Savage) is the astronomical source-extraction software designed specifically for the AKARI all-sky survey. It uses the Bayesian evidence methods of Savage & Oliver (2007) in order to compare the probabilities of a flat background to a flat background plus a point source with the input point response function. The two models are compared using a Bayesian Information Criterion, with the log evidence defining this relative probability. This software has been used to process the entire data-set from the AKARI FIS and has produced a catalogue of astronomical objects. SXT takes the GB processed data as an input. SXT's outputs are source lists and various intermediate products that allow one to estimate the flux density of sources at known positions. A list of sources is selected by thresholding on the log-evidence.

3.4.1 Confirmation

Source confirmation is a process where we look for multiple, independent observations of a source, either in different scans or in different detector rows within the same scan. We do this in order to distinguish genuine astronomical sources (which we expect to see in each independent observation) from false detections, such as glitches (which are unlikely to occur at the same position in both observations). SXT confirmation currently consists of two distinct types. The first is scan-scan confirmation, where we look for observations of each source in different orbital scans. This is done simply by splitting the input data into that obtained for different scans, running the source detection algorithm on each resulting map and selecting objects which are found in both maps within a radius of $20''$. The second type of confirmation is seconds confirmation (a reference to the fact that the confirming data subsets are taken within seconds of one another). In this case, the data from one of the scan-scan data subsets is further divided, with each sub-subset containing only data from a single row of detector pixels. For each detector row, a map is made and the source detection algorithm is used to identify objects found in at least 2 detector rows. However, it was found that signals in adjacent detectors are not always independent, for example a glitch can appear in adjacent pixels (Yamamura et al., 2009). We therefore only consider the scan-scan confirmation. This is a powerful method for discriminating between real and spurious source detections. Its limitation is that, to be confirmed, a source must be bright

enough to be detectable in each data subset. Therefore, confirmation is not possible for the faintest (e.g. ~ 0.5 Jy) sources that can be detected by the overall survey.

3.5 Completeness

As discussed in section 2.3.1, in any survey at a given flux there will be N_d, sources detected. Due to the sensitivity of the survey this is not necessarily the same as the true number of sources on the sky, N_t. Completeness, C, is defined as the fraction of true objects (of a given flux) which are detected in the survey,

$$C = \frac{N_{\rm d}}{N_{\rm t}} \tag{3.1}$$

In order to calculate this we follow a procedure similar to that used by Papovich et al. (2004); Magnelli et al. (2009) for *Spitzer* data (see also section 2.3.1). An image of synthetic objects is generated and injected into the AKARI data stream. SXT is then run on the data containing the simulated sources to calculate how many of the synthetic sources are recovered. The synthetic image is a simple regular array of synthetic sources, each with the same, known, flux and a gaussian Point Spread Function (PSF) with FWHM of $40''$ (this is the approximate PSF of the WIDE-S band). The coverage maps are used to define an area on the sky in which to inject the sources. A number equal to the total desired flux of the synthetic objects is placed at regular positions within this map, always at least $3\farcm3$ away from an edge or another source. This map is then convolved with the gaussian PSF of the survey, normalised so that the total area contains the desired synthetic flux. This creates an image in sky-coordinates with zero background and point sources as they arise in the real survey.

From the GB processed data in the EN1 field we construct two maps of 30 scans, giving approximately single scan coverage (due to the ecliptic orbit there will always be some overlap between scans). This was achieved by manually inspecting the coverage maps of the scans. As these maps are generated from different orbits they are independent. Figure 3.1 shows the SXT coverage maps for the two independent scans of the EN1 field.

The synthetic image is then added to the real timeline data of each of the maps so that the noise characteristics of the survey are retained. We run SXT on these data to generate a source list for each map, removing any synthetic sources which are coincident with genuine SXT detections (i.e. SXT detections found when no synthetic sources are injected). We then cross-match these source lists with the catalogue of input synthetic sources using *topcat* and a search radius of $20''$. The coverage maps are used to ensure

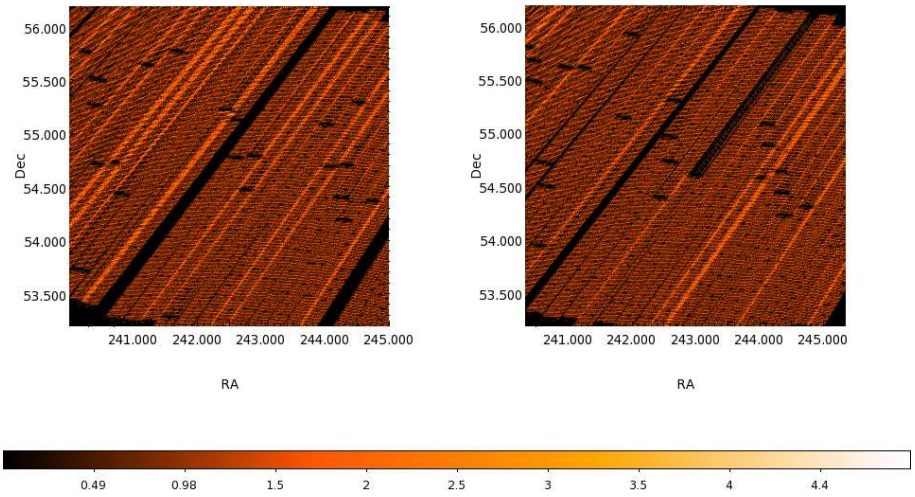

Figure 3.1: SXT coverage maps for the two independent maps for the EN1 field.

that only those areas with good coverage are used. Finally, the fraction of input synthetic sources found by SXT is the completeness in each map.

From analysis of standard stars and asteroids Yamamura et al. (2009) showed that in order to convert from the SXT output to fluxes in Jy, the output must be multiplied by a factor of 2.4. However, since this includes a PSF correction this factor will not be correct for our sources. We therefore derive a new scaling between the input synthetic flux and the output flux. We find that we must multiply the output synthetic fluxes by a factor of 2.04 to produce synthetic sources with calibrated fluxes. In order to ensure that this calibration has been performed correctly figure 3.2 shows the input, synthetic, flux against the SXT output flux. The plot shows a good agreement between the two. The deviation at the lower end is due to an Eddington bias effect since at lower fluxes, where the scatter is larger, more objects will be detected which have been scattered to higher fluxes than have been scattered to lower fluxes.

In order to include confirmation, the synthetic source lists produced by SXT for each map are cross-matched together, again using *topcat* with a search radius of $20''$. This returns a catalogue of synthetic sources found by SXT in both maps, giving the confirmed completeness. Since the two maps used for this experiment are independent, we should be able to recover the confirmed result from a multiplication of the curves from each individual map. Figure 3.3 shows the completeness curve from the two individual maps, from the confirmation and from the multiplication of the curves from the two individual maps. The figure shows that the confirmation curve is different to that expected. This

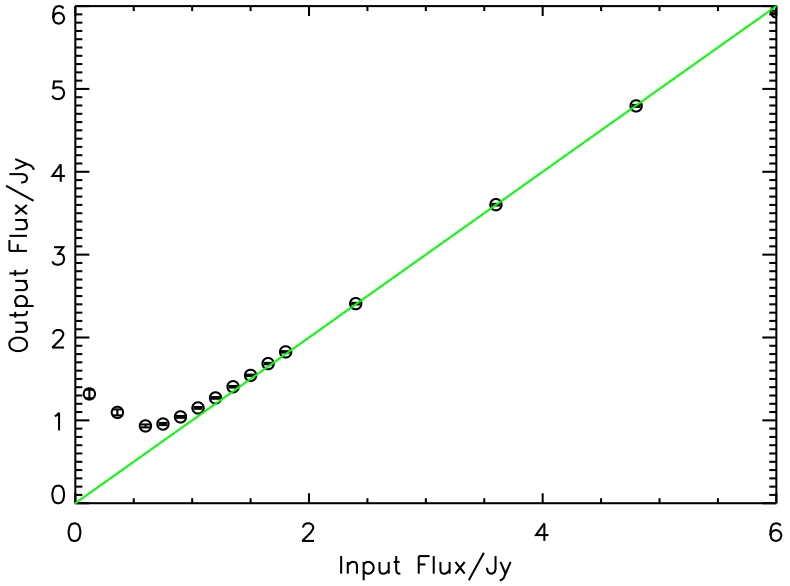

Figure 3.2: The flux of the input synthetic sources against the average output flux of the SXT detected synthetic sources. The error bars are simple 1σ errors and the green line shows a $y = x$ line. The deviation at low flux is due to an Eddington bias effect.

suggests that there is noise in the map which is not independent. It could be that there are real sources which remain in the map, if a synthetic source is placed near such a source it may not be recovered.

Currently we achieve 98% completeness at the high flux end ($\gtrsim$ 4Jy). It is unclear why we do not achieve 100% completeness as this persists to still higher fluxes. It could be due to areas of the map with reduced signal-to-noise or it could be due to the previously observed non-gaussian noise in the AKARI maps. Since the completeness is very close to 100% it is likely to have a negligible effect on the rest of the analysis. The figure shows that once confirmation is included the 50% completeness limit is $\sim$ 1Jy. In a simple flux limited survey in the presence of noise which is symmetric (i.e. equally likely to produce positive or negative fluctuations) the completeness will be 50% at the flux limit. Thus a useful measure of depth for a real survey is the flux, $f_{\frac{1}{2}}$, at which the completeness drops to 50%.

3.6 Reliability

In isolation the completeness does not give a full picture of the survey sensitivity since it does not tell us how many of the sources we detect are real. As discussed in section 2.5.1,

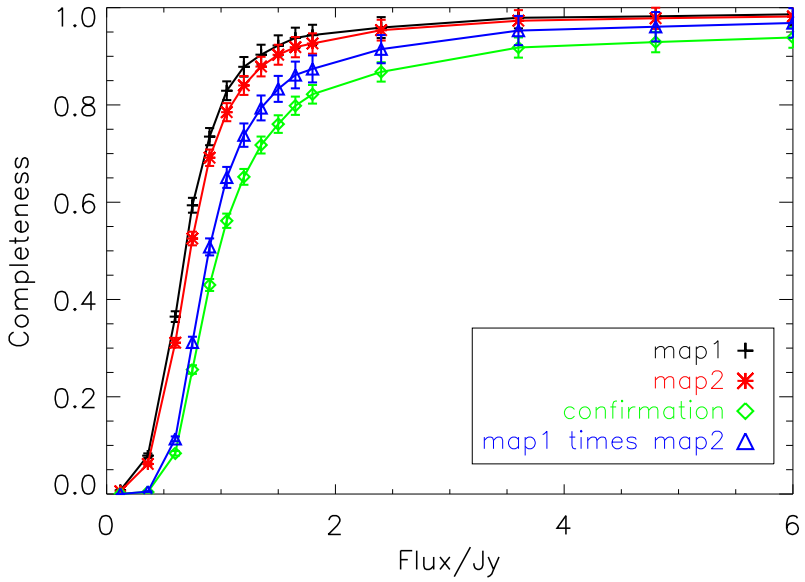

Figure 3.3: Completeness curves for single scan map 1 (black cross), map 2 (red star), measured confirmation (green diamonds) and map 1×map 2 (blue triangles).

reliability is defined as the fraction of detections which are real sources i.e.

$$R = \frac{N_{\rm t}}{N_{\rm d}} = \frac{N_{\rm t}}{N_{\rm t+N_f}} = \frac{N_{\rm d} - N_{\rm f}}{N_{\rm d}} \tag{3.2}$$

where $N_{\rm f}$ is the number of detected sources which are spurious, $N_{\rm t}$ is the number of true sources and $N_{\rm d} = N_{\rm t} + N_{\rm f}$.

We calculate this by comparing the SXT detection lists to the SWIRE EN1 70μm catalogue. The *Spitzer* catalogue is sensitive to $\sim$ 18mJy and hence all objects detected by AKARI in the overlap area will be detected by *Spitzer*. As such, we can identify the real sources and measure the number of spurious sources. First SXT was run on the two single scan maps. For each map, SXT produced a catalogue of detections. These catalogues were then cross-matched with the SWIRE 70μm catalogue limited to sources with 70μm flux > 0.3 Jy, assuming that AKARI will not detect any sources fainter than this. All SXT detections not found in the SWIRE catalogue are assumed to be spurious. The covered area was calculated in order to find the spurious source number density. In order to calculate the reliability we then need to assume a number density of true sources. The number of spurious sources in the EN1 region we have considered is large and therefore the spurious source number density is well estimated. However, the area is small and thus the number density of true sources will be uncertain. We instead model the true number counts as $N_{\rm TRUE} = N_0 \left(f_0/f_{\frac{1}{2}}\right)^{\frac{3}{2}}$ with N_0 and f_0 estimated approximately from IRAS

Table 3.2. A comparison between the expected and measured number density of confirmed spurious sources and the associated reliability. Map1 ($f_{\frac{1}{2}}$) gives the number density of spurious sources and the reliability for map 1 measured at the 50% completeness limit $f_{\frac{1}{2}}$ of map 1. Similarly for the Map2 labels. 'Expected confirmed' is the number density of spurious sources and the reliability calculated from equation 3.2 and 'measured confirmed' is the number density of spurious sources and associated reliability measured when confirmation is included.

	$N_{\rm spurious}$	Reliability	$f_{\frac{1}{2}}$[Jy]
Map1 ($f_{\frac{1}{2}}$)	41.40	1.1%	0.68
Map2 ($f_{\frac{1}{2}}$)	45.50	0.9%	0.73
Expected Confirmed	0.18	58.1%	0.98
Measured Confirmed	0.18	58.1%	0.98

data as $N_0 = 2$ per sq. deg., $f_0 = 0.25$Jy. While this is clearly simplified, it allows an estimate of the reliability to be calculated. Table 3.2 gives the number density of spurious sources and reliability at the 50% completeness limit in each map. The table shows that there is a large spurious source number density ($\gtrsim 40$ per sq. deg.) at this flux limit when confirmation is not included.

In order to include the confirmation we use the catalogue of spurious sources from each of the individual maps (after applying a mask so that only those sources covered in both maps are used), and cross-match them together using a search radius of $20''$, thus producing a list of spurious sources which are found in both maps. The same assumption of the number density of true sources can then be used to calculate the confirmed reliability.

We now check that the confirmation process is increasing the reliability (decreasing the number density of spurious sources) as expected from the number density of spurious sources in the individual maps. Using the number density of spurious sources in each of the two individual maps and assuming that the spurious sources are Poisson distributed (and are indeed spurious) then the number density of confirmed spurious sources is given by

$$N_{\rm confirmed} = N_{\rm s1} N_{\rm s2} \Omega \tag{3.3}$$

where $N_{\rm s1}, N_{\rm s2}$ are the number density of spurious sources in map 1 and map 2 respectively and Ω is the confirmation area, given by $\Omega = \pi r^2$, where r is the confirmation radius of

20″.

We also measure the number density of confirmed spurious sources directly, as given by the above procedure. The results are shown in table 3.2. The table shows that the reliability increases drastically when the confirmation is included (to around 60%), although this is partly due to the higher flux limit. The confirmed number density of sources is as expected from the individual maps. However, the area covered is still relatively low - using the whole area of overlap between the two AKARI maps and the SWIRE data (5.6 sq. degs.) we measure $0.18 \times 5.6 = 1$ spurious confirmed source.

3.7 Discussion

These results suggest that, with a single scan, the flux limit of the survey is ~ 0.7Jy. This is slightly higher than the 5σ depth given in table 3.1, although this latter measurement was performed for a more recent reduction of the data. The reliability, however, at 0.7 Jy is very low. When confirmation is included the 50% completeness flux limit increases to ~ 1 Jy but the reliability is greatly improved, reaching $\sim$60% at this flux. While this is still not greatly encouraging, these results are based on maps with 2-scan coverage, a large part of the sky has been observed by more than 2 scans and both the completeness and reliability will be improved in these areas.

The AKARI All-Sky Survey is the first Far-Infrared all-sky survey since that of IRAS launched in 1983, we put our results in context by comparing to that survey. In regions with galactic latitude $|b| > 20°$ the IRAS Faint Source Catalogue reached depths of ~ 0.2 Jy at 12, 25 and 60μm and ~ 1 Jy at 100μm (Moshir et al., 1992). The AKARI all-sky catalogue, therefore, achieves similar depths in the 90μm WIDE-S band to the IRAS FSC 100μm survey. However, the AKARI satellite has greatly improved spatial resolution ($\sim 5''$ as opposed to $2'$ at 100μm) and thus the survey provides an improved database of Infrared sources across the sky.

The results presented in this chapter were produced for a preliminary version of the AKARI data-processing pipeline. These results were used by the AKARI team as part of a process to refine the parameters and settings of the pipeline, and SXT in particular. Since this work was completed, the pipeline has been further improved, both the green box and SXT. There have been two AKARI team FIS catalogues released since this analysis was conducted, the first of which has now been released to the community. Full details of the public catalogue release can be found in Yamamura et al. (2009). The latest team release includes an all-sky catalogue containing nearly 300,000 confirmed point sources in the

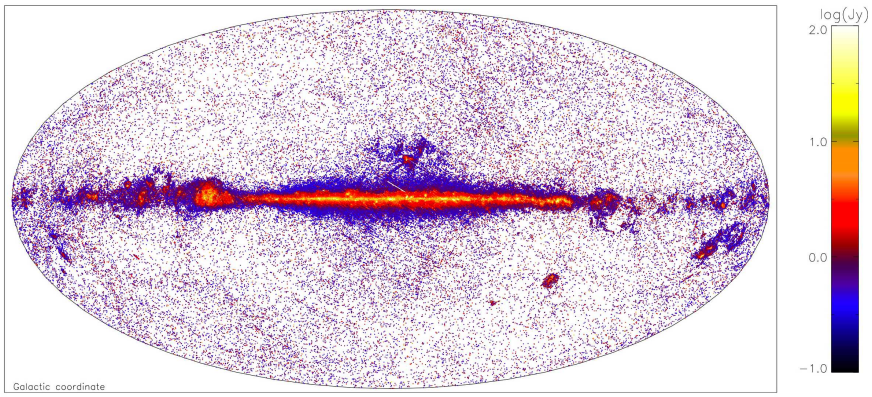

Figure 3.4: Sky-map of the AKARI WIDE-S All-Sky Survey, from Yamamura et al. (2009)

WIDE-S band. The detection limit, calculated as the 90% completeness limit (calculated from a complimentary analysis to that presented here using known standard stars instead of synthetic sources) is $\sim$ 0.56Jy in the WIDE-S band. The limit is 3.2 Jy in N60; 3.5 Jy in WIDE-L and 5.6 Jy in N160. These results show that improvements to the data-processing, in particular the glitch detection modules, have improved the completeness by at least a factor of 2. Figure 3.4 shows the sky-map of WIDE-S detected sources.

Chapter 4

Four Red Objects in the SWIRE-XMM field: IRS Spectra

4.1 Introduction

With large-scale surveys we are able to conduct a search for rare or extreme phenomena. As discussed in section 1.6, such discoveries can constrain models of galaxy evolution and stimulate new research both observational and theoretical. In this chapter we outline a search for objects which are extremely faint at IRAC wavelengths but luminous in the mid-infrared. We return to the *Spitzer* Wide Area Infrared Extragalactic (SWIRE; Lonsdale et al., 2003) survey to search for objects which are detected at 24μm but which are not found in the 5σ *Spitzer* IRAC catalogue. We then present *Spitzer* IRS spectra of a small sample of such objects.

This work was done with supervision from S. Oliver and collaborators, in particular D. Farrah. Two-epoch catalogues were produced by D. Shupe and band-merged fluxes were produced by J. Surace. Some initial template analysis was done by M. Polletta (although this was later re-analysed for the final version). This work is not currently being pursued for publication, although with a re-reduction of the spectra and additional Herschel data this may change in the future.

4.2 Sample Selection

In order to find objects which are detected at 24μm but are not found in the IRAC catalogue, we must ensure that the 24μm detection is reliable. To do this we split the 24μm SWIRE observations into those taken at two different times ('two-epoch' images). By

identifying objects which are detected at both epochs we hope to ensure a reliable catalogue. Initially, these two images were only available in the SWIRE-XMM field (see section 2.3) so we focus on this field to define a sample for observational follow-up.

Source extraction using SExtractor (Bertin & Arnouts, 1996) is performed on the two images individually. This extraction was done as per Shupe et al. (2008). The raw 24μm data were processed by the SSC pipeline version S10.5 to produce Basic Calibrated Data (BCD) images. These images were coadded using the MOsaicker and Point source EXtractor (MOPEX Makovoz & Marleau, 2005) software after a median background subtraction. A 3σ threshold was used to produce two catalogues, one for each epoch. Photometry was performed in a 5.″25 aperture for point sources which was then aperture corrected according to Shupe et al. (2008). These extractions were done by D. Shupe (priv. com.).

The two-epoch catalogues are then cross-matched together with a search radius of 1″ to identify only sources found in both epochs. This gives a catalogue of 15,629 sources at 24μm. This catalogue is then cross-matched with a 6″ radius with the SWIRE IRAC 5σ catalogue of the XMM field to identify objects which are not found in the catalogue in any IRAC band. We use a large cross-matching radius here since we wish to ensure that we have only objects for which we are certain there is no IRAC information. We also remove any objects which have 24μm coverage but not IRAC coverage. This gives a catalogue of 235 sources which have extreme 24μm to 3.6μm colours. These sources are then limited to those with 24μm flux brighter than 500μJy in both epochs to allow follow-up with the *Spitzer* Infrared Spectrograph (IRS; Houck et al., 2004, see below) in reasonable integration times. We then further limit the catalogue to those for which the fluxes in each epoch agree within 40%. This produces a catalogue of 159 sources.

We now further investigate why these sources are not found in the IRAC catalogue. To ensure that it is not due to an artifact in the image or source confusion, we extract postage stamps of the IRAC and 24μm data of each of these objects. A visual inspection of these postage stamps produced a list of sources which had no clear reason for a missing IRAC signal in the catalogues and which had a clear 24μm signal. This visual inspection resulted in a catalogue of four sources. This is a large reduction, in most cases objects were removed because the 24μm detection was due to a diffraction artifact from a nearby bright extended object. Figures 4.1 - 4.4 show the postage stamps for the IRAC and two epoch data for each of the four objects. The figures show that in some cases there is a flux excess in some IRAC channels at the source position. We return to these images in

section 4.3 to obtain flux estimates in these cases. An example of an object which was rejected is shown in figure 4.5.

To check that these sources are reliable, we perform a simple simulation of our selection method. We offset the epoch 1 24μm catalogue in both the RA and Dec directions. The offsets range from 20″ to 2′, chosen so that a wide range is used which is larger than the cross-matching radius. We then apply the selection method to each of these catalogues. For each offset catalogue we cross-match it with the epoch 2 catalogue (which has not been altered). We then find objects which are not found in the 5σ IRAC catalogue, have 24μm flux $> 500\mu$Jy in both catalogues and for which the 24μm fluxes agree within 40%. Any objects that are identified will be spurious due to the offset procedure. We perform this simulation 20 times and find an average of 0.45 ± 0.60 spurious objects. We expect our simulation will contain Np matches (where p is the probability of a spurious association and N is the number in the target sample). Pessimistically, none of the spurious sources would be removed in the visual inspection, meaning in the worst case scenario $N = 4$ giving $Np = 0.45 \pm 0.6$ i.e. $p = (11.25 \pm 15)\%$. Optimistically, all of these spurious sources would be removed, in which case $N = 159$ and $Np = 0.45 \pm 0.6$, i.e. $p = (0.3 \pm 0.4)\%$. We therefore expect $0.3\% < p < 11.3\%$.

4.3 Observations

For each of the objects in our sample we determined a flux or upper-limit from the IRAC images using the standard SWIRE aperture photometry "band-fill" procedure (used when an object is detected in one band but not others, see Surace et al., 2005, for details of the process). The resulting IRAC photometry (J. Surace, priv. com.) as well as the MIPS 24μm flux obtained from the coadded image stack, i.e. the 24μm point response function flux (PRF flux, obtained from matching the source profile to the MIPS 24μm PRF) as it appears in the SWIRE bandmerged catalogue (Shupe et al., 2008) are shown in table 4.1. Also shown are the coordinates of the four objects we have identified. The table shows that in several cases the objects are in fact detected at IRAC wavelengths with greater than 5σ detections. It is unclear why these sources were not in the SWIRE catalogue, although we note that the majority are below the 50% completeness limits discussed in section 2.3.1. However, these objects are still very unusual, with extremely red colours, e.g. the 24/3.6μm flux ratios are 343, 391 (lower limit), 470 and 272 (lower limit). For comparison, a search of the ∼97,000 objects in the SWIRE IRAC catalogue in ELAIS-N1 with detections at both 24μm and 3.6μm reveals only 1 source with a 24/3.6μm flux ratio

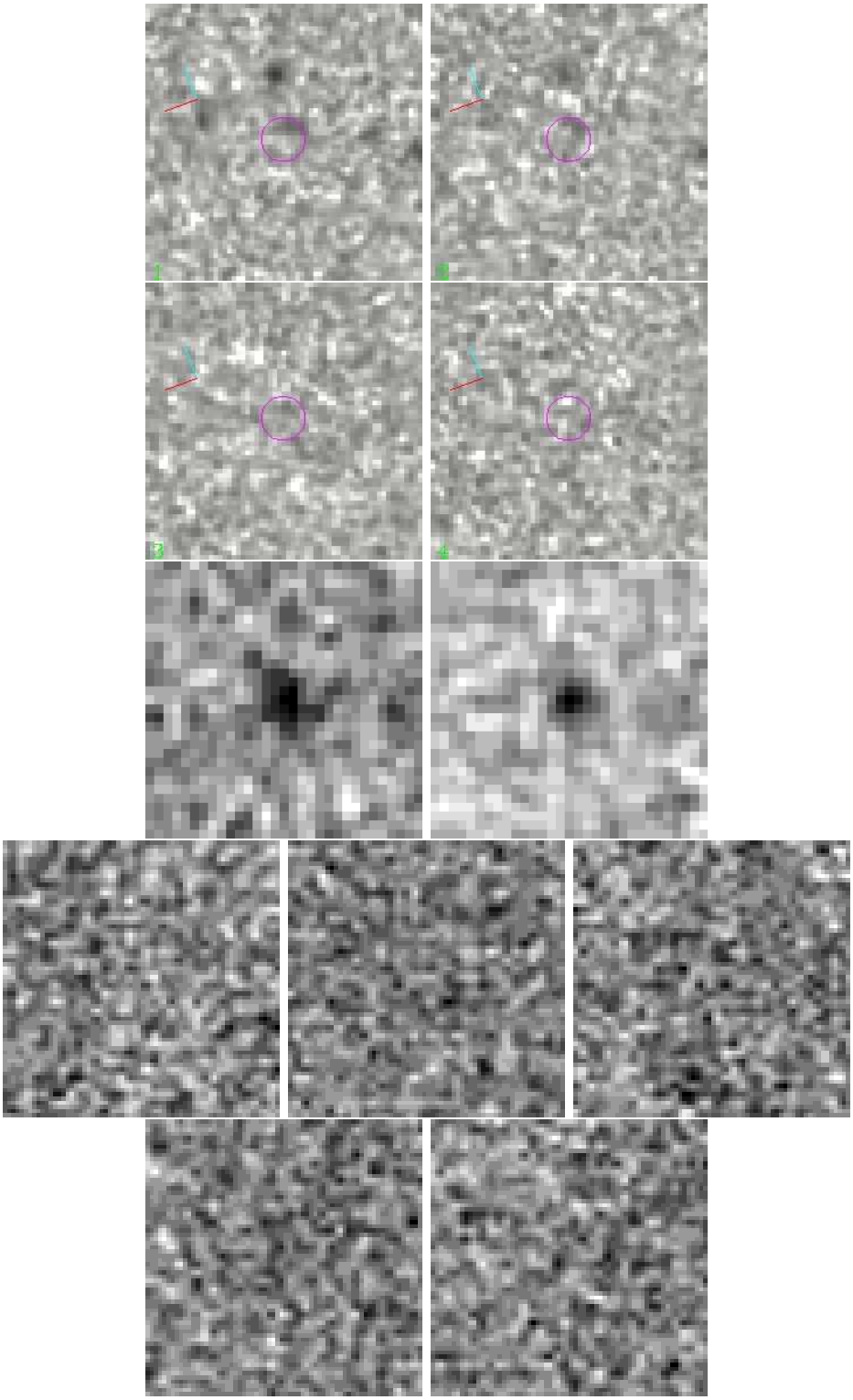

Figure 4.1: Postage stamps for Object 1. Reading from the left, the top two rows show the IRAC ch1 − 4 (3.6μm − 8.0μm) postage stamps. The third row from the top shows the MIPS 24μm epoch 1 and 2 stamps. The bottom two rows show the CFHTLS *ugr* and *iz* bands. The purple circle in the IRAC stamps shows the 24μm epoch 1 source position. Optical stamps are $6'' \times 6''$ in width; *Spitzer* stamps are $36'' \times 36''$.

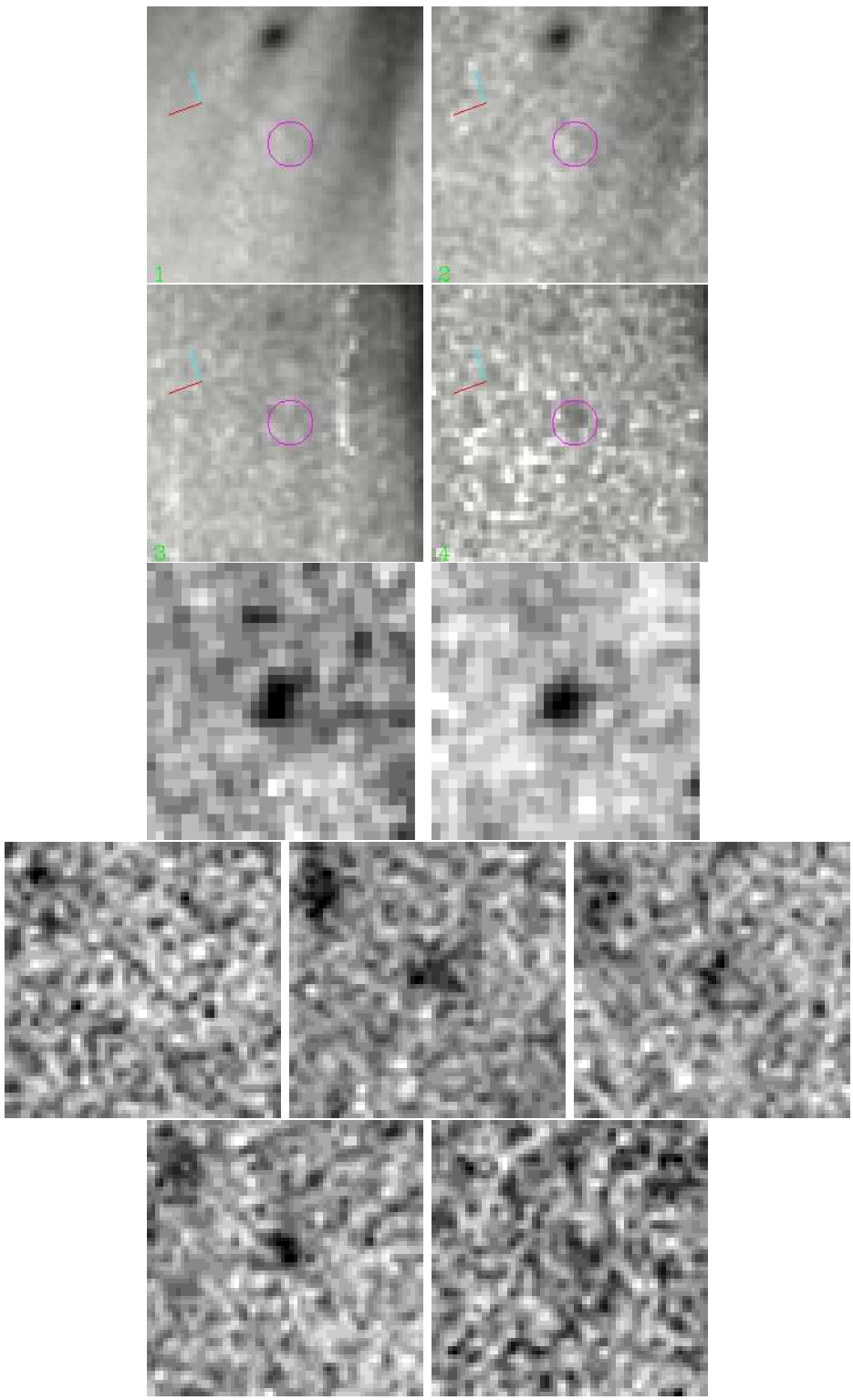

Figure 4.2: As figure 4.1 but object 2.

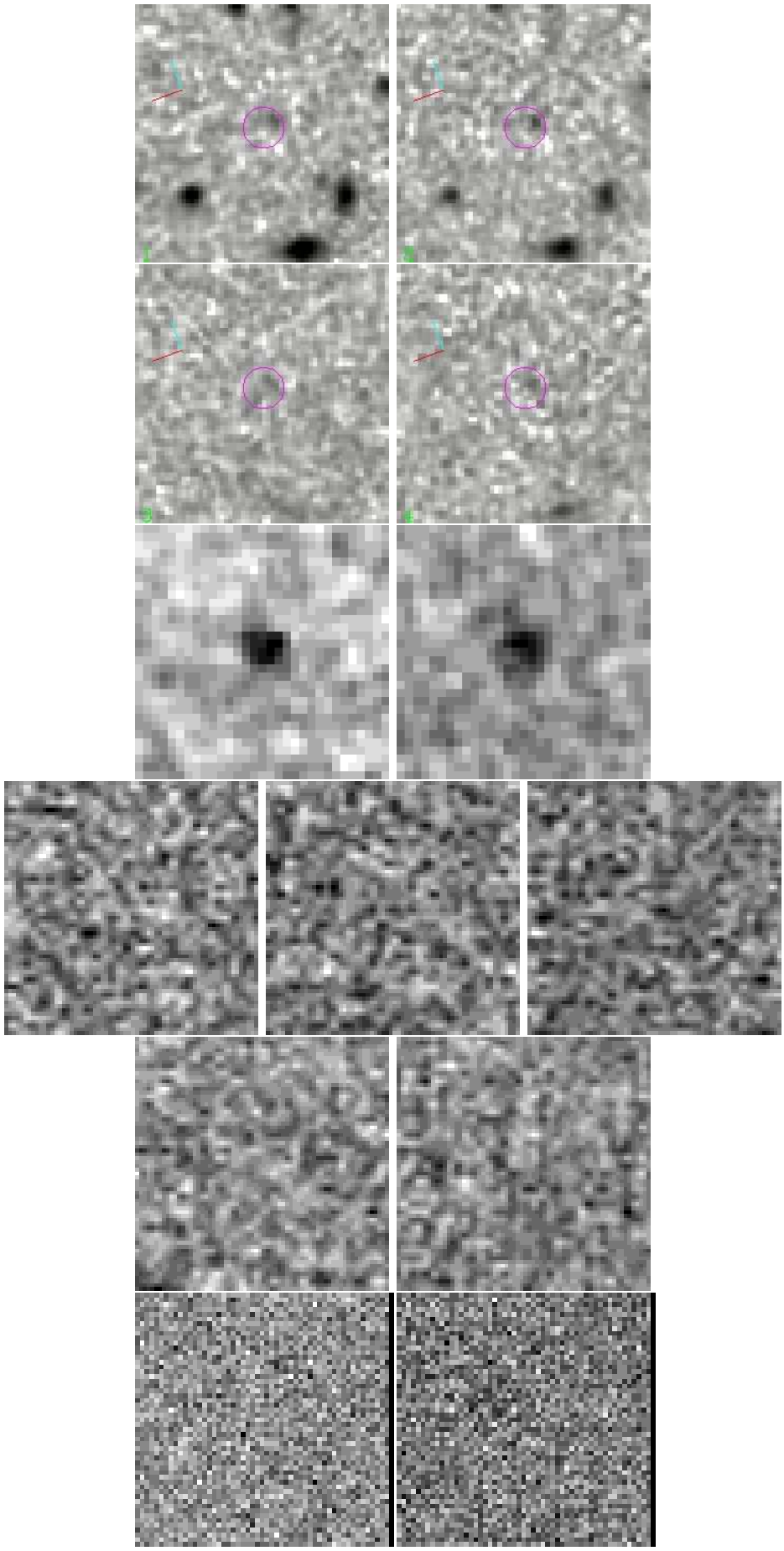

Figure 4.3: As figure 4.1 but object 3. In this case an additional row is added at the bottom to display $11'' \times 11''$ postage stamps from the UKIDSS DXS survey J (left) and K (right) bands.

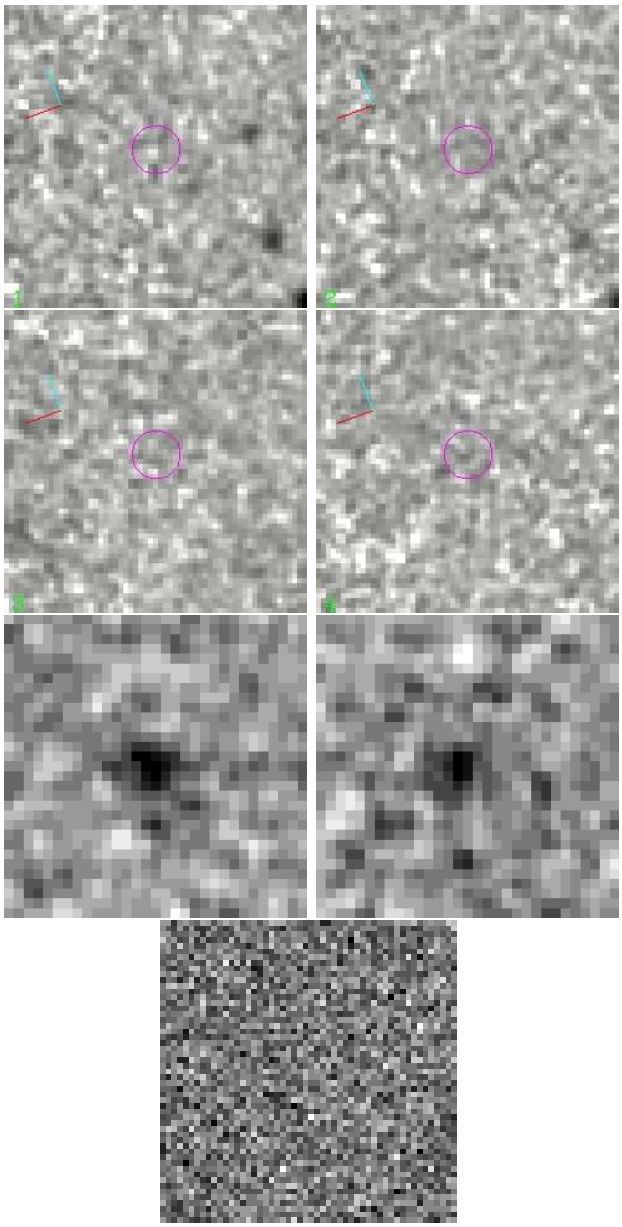

Figure 4.4: As figure 4.1 but object 4. In this case there is no CFHTLS coverage and the bottom row shows the UKIDSS DXS K-band stamp.

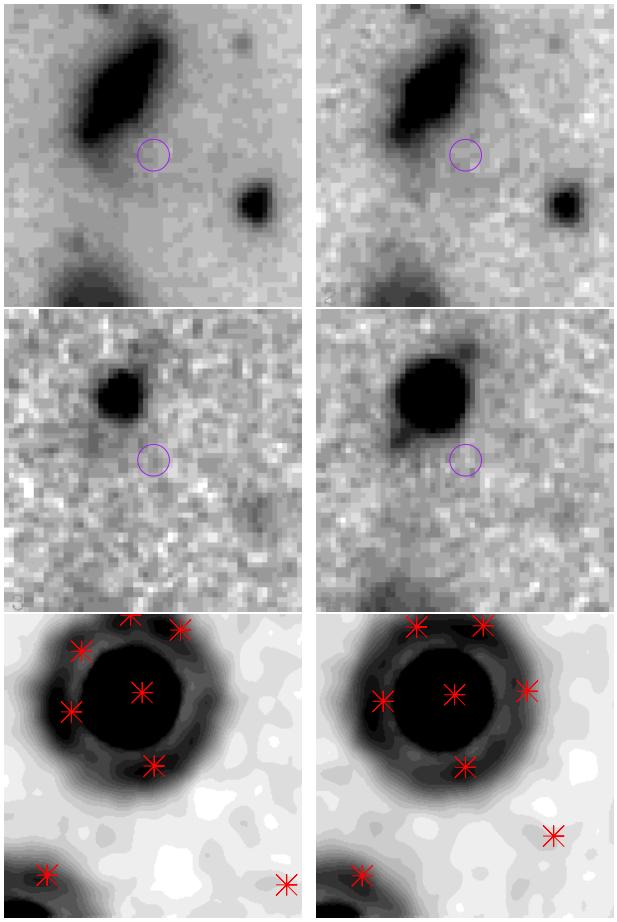

Figure 4.5: As figure 4.1 but for a rejected object. The red stars show the positions of the two-epoch detections in the two-epoch stamps. The detection in the 24μm two-epoch images is an artifact from the nearby bright object so it is rejected.

redder than 340.

Table 4.1. IRAC 3.6, 4.5, 5.8 and 8.0μm and MIPS 24, 70 and 160μm photometry of the four candidate sources. IRAC fluxes are 3σ detections or 5σ upper-limits (calculated by adding the error bar multiplied by 5 to the measured value). The MIPS 24μm fluxes are PRF fluxes in the SWIRE bandmerged catalogue. MIPS 70 and 160μm limits are estimated 5σ limits for the XMM field (Polletta et al., 2008b, no object was detected at either MIPS 70 or 160μm). RA and Dec are J2000 co-ordinates. The final column gives the ratio of the 24μm to 3.6μm flux.

Object	RA [deg]	Dec [deg]	3.6μm[μJy]	4.5μm[μJy]	5.8μm[μJy]	8.0μm[μJy]	24μm[μJy]	70μm [mJy]	160μm [mJy]	$F_{24}/F_{3.6}$
1	36.133542	-5.555333	1.80± 0.36	4.57± 0.64	20.93± 3.77	$<$ 32.72	616.61 ± 18.84	$<$ 24	$<$ 126	343
2	34.610333	-6.029139	$<$ 1.70	$<$ 3.14	61.39± 3.87	49.35± 5.46	665.12 ± 18.36	$<$ 24	$<$ 126	$>$391
3	35.420917	-4.347750	1.81± 0.36	3.70± 0.64	30.94± 3.79	$<$ 43.40	846.30 ± 19.20	$<$ 24	$<$ 126	470
4	36.164292	-3.656000	$<$ 2.31	2.96± 0.64	$<$ 20.57	20.86± 5.45	628.69 ± 21.13	$<$ 24	$<$ 126	$>$ 272

Table 4.2. Infrared Spectrograph Aboard *Spitzer*

Module	Wavelength [μm]	Resolution ($\lambda/\Delta\lambda$)
Short-Wavelength, High-Resolution (SH)	$9.9 - 19.6$	~ 600
Long-Wavelength, High-Resolution (LH)	$18.7 - 37.2$	~ 600
Short-Wavelength, Low-Resolution, Order 1 (SL1)	$7.4 - 14.5$	$\sim 64 - 128$
Short-Wavelength, Low-Resolution, Order 2 (SL2)	$5.2 - 7.7$	$\sim 80 - 128$
Long-Wavelength, Low-Resolution, Order 1 (LL1)	$19.5 - 38$	$\sim 64 - 128$
Long-Wavelength, Low-Resolution, Order 2 (LL2)	$12 - 21.3$	$\sim 80 - 128$

With a sample of extremely unusual objects now defined we wish to further investigate their properties. Based on the extreme colours of these objects we expect them to be highly obscured, possibly at the extreme end of the high redshift Dust Obscured Galaxies (DOGs) discovered by Dey et al. (2008) and discussed in section 1.6 since those objects are identified from high 24μm to optical flux ratios. This would suggest highly obscured objects powered by starburst and/or AGN at redshifts $\gtrsim 2$. To further investigate these objects we obtained 10 hours of observations with the *Spitzer* Infrared Spectrograph (IRS; Houck et al., 2004). We first review the instrument and then discuss some of the features frequently observed in mid-infrared spectra before presenting a discussion of the spectra.

4.3.1 Spitzer Infrared Spectrograph

The IRS consists of 4 modules split into high and low resolution and short and long wavelength. The long wavelength modules are further split into long and short wavelength orders. The details of the modules are given in table 4.2. In all cases the detectors are 128×128 pixels in size, the short-wavelength modules are Si:As detectors and the long-wavelength modules are Si:Sb detectors. The IRS is capable of observing in two modes, mapping and staring mode. IRS staring mode gives observations of the target at the 1/3 and 2/3 positions along the slit (referred to as the Nod 1 and Nod 2 positions and corresponding to an offset of $56''$). The IRS mapping mode gives spectra at several positions along or perpendicular to the slit.

IRS Diagnostics

In view of our use of the IRS we now review some of the diagnostic features frequently observed in the mid-infrared. Spectra from *Spitzer* IRS of large samples of the dusty, infrared luminous galaxies discussed in section 1.6 show a wide variety of characteristics. Spectra of AGN show broad absorption or emission features as well as narrow emission lines and an IR continuum. The broad absorption features arise from the Si-O and O-Si-O bending modes in cold silicate dust grains (Rieke & Low, 1975; Kleinmann et al., 1976; Puget & Leger, 1989; Genzel et al., 1998; Houck et al., 2004; Armus et al., 2004; Hao et al., 2005; Spoon et al., 2006). They are seen in emission from warm silicate dust (Hao et al., 2005). The narrow lines arise from fine structure transitions and are expected in AGN from regions of hot, highly ionised gas (Sturm et al., 2002; Weedman et al., 2005). The strong IR continuum arises from hot carbonaceous dust heated by the AGN. A sample of classical AGN observed with IRS by Weedman et al. (2005) show these features in various combinations. However, the sample also show emission features from Polycyclic Aromatic Hydrocarbons (PAHs). These features arise from the stretching and bending modes of C-H and C-C aromatic dust grains (Gillett et al., 1973; Leger & Puget, 1984; Allamandola et al., 1985; Leger et al., 1989; Allamandola et al., 1989; Desert et al., 1990; Spoon et al., 2004; Brandl et al., 2006; Desai et al., 2007a; Farrah et al., 2003, 2007, 2008, 2009). PAHs are molecules of hydrocarbons with 10's to 100's of Carbon atoms arranged in planar lattices of aromatic rings. Their vibrational modes are excited by UV emission from hot, young stars and hence PAH emission is associated with star-formation; PAH features are frequently observed in the spectra of starburst galaxies (Andriesse & de Vries, 1978; Sellgren, 1984; Leger & Puget, 1984; Leger et al., 1989). Emission from pure-rotational states of warm ($\gtrsim$ 100K) H_2 are also found in mid-infrared spectra, these can arise from both UV pumping and X-ray heating of gas and so can be associated with both star-formation and AGN (Higdon et al., 2006).

Spectra with IRS have confirmed that while local ULIRGs are dominated by starbursts many also contain AGN components (see e.g. Spoon et al., 2006; Farrah et al., 2007; Desai et al., 2007a; Bernard-Salas et al., 2009). Comparisons between AGN dominated and starburst dominated LIRGs and ULIRGs suggest that PAH strength is a reliable feature to discriminate between these power sources (Genzel et al., 1998; Laurent et al., 2000; Desai et al., 2007a).

Table 4.3. IRS observations.

Object	AOR Key	Observation Date	Exposure Time[a] [mins]
1	23797760	2008 Feb 29	69
2	23797504	2008 Jan 21	57
3	23797248	2008 Feb 27	33
4	23796992	2008 Feb 29	63

[a]These exposure times are the same for LL1 and LL2.

IRS Observations

Following the hypothesis that these objects are highly obscured starburst and/or AGN at $z \gtrsim 2$, we expect the rest-frame 6.2μm, 7.7μm and 11.2μm PAH diagnostic features to be at $\gtrsim$ 18.6, 23.1 and 33.6μm in the observed frame. We therefore choose to observe with the LL1 module to ensure good wavelength coverage of these features. LL1 and LL2 spectra are observed simultaneously with IRS due to the instrument setup and so we additionally obtain LL2 spectra. We note, however, that the faintness of the objects at 8μm means it is unlikely that we will detect the objects in LL2. We observe the objects in IRS staring mode as these objects are faint point sources. Table 4.3 gives the details of the observations obtained (*Spitzer* program ID 40682). We used high accuracy blue 'peak-ups', i.e. short exposure imaging is performed with the IRS imaging camera with a filter centered at 16μm, to obtain the positions of known 2MASS stars to ensure placement of the target within $\sim 0\farcs4$ of the LL slit centre. We used 30 second ramps in both LL1 and LL2.

Data Reduction

The spectra were reduced at the Spitzer Science Centre using the S17.2 IRS pipeline. This produced Basic Calibrated Data (BCD) 2D spectral images of the two Nod positions for each order and each exposure (i.e. for LL1 and LL2 there exists several exposures of both Nod 1 and Nod 2 positions). For each object the exposures of the same Nod and order were combined together with a weighted-mean (weighted by the errors) using the Spectral Modeling Analysis and Reduction Tool (SMART; Higdon et al., 2004; Lebouteiller et al., 2010). The sky background was estimated in two ways. Firstly, from the off source order in each Nod ('order-order' sky background; i.e. combining the spectral images taken in

LL1 when the target was placed in LL2 as a sky background and vice versa, for each Nod position). Secondly, from the same order but when it was in the alternate Nod ('Nod-Nod' sky background; i.e. combining the Nod 1 spectral images when the target was in the Nod 2 position and vice versa, for each order). We use these sky background estimates to produce two, separate, sky-subtracted 2D spectral images. The *Spitzer* IRS Custom Extraction (SPICE) software provided by the *Spitzer* Science Center was then used to extract 1D spectra from each background subtracted 2D spectral image. We use the 'optimal' source extraction method provided by SPICE, which weights the flux in each pixel by its uncertainty and the point source profile obtained from the IRS standard star HR 7341. This is an adaption of the method of Horne (1986). The resulting spectra were then checked for consistency. In all cases the spectra calculated with the different background estimates agreed well as shown by figure 4.6, with the possible exception of Nod 2 for object 4. In the remainder of this analysis we elect to use the order-order subtracted spectra.

The spectra are extremely noisy, due to the faintness of our objects. The signal-to-noise ratio (SNR) of two pixels for each object are shown in table 4.4, calculated from the formal pixel errors from SPICE, although we note that the propagation of the pixel errors in SPICE is not well understood for the IRS. The pixels are chosen to be at the start and end of the LL1 wavelength range. The table shows that the spectra have a low signal-to-noise ratio.

We remove outlying pixels from a comparison between the spectra in the two Nod's. We then calculated the equivalent MIPS 24μm flux of the spectra to ensure consistency with that obtained by MIPS. We convolved the order-order subtracted spectra with the MIPS 24μm filter function. Table 4.5, however, shows that the two fluxes are not consistent. In all cases the IRS spectra over-estimates the flux compared to the MIPS 24μm data by factors of 2.4, 1.7, 1.3 and 2.1 for objects $1-4$ respectively. Similar results are obtained if we use Nod-Nod background subtraction instead of order-order subtraction. It is not uncommon for IRS and MIPS 24μm fluxes to disagree. We adopt the procedure used previously (see e.g. Weedman et al., 2006b) and normalise the IRS spectra to have the same flux as the MIPS 24μm flux.

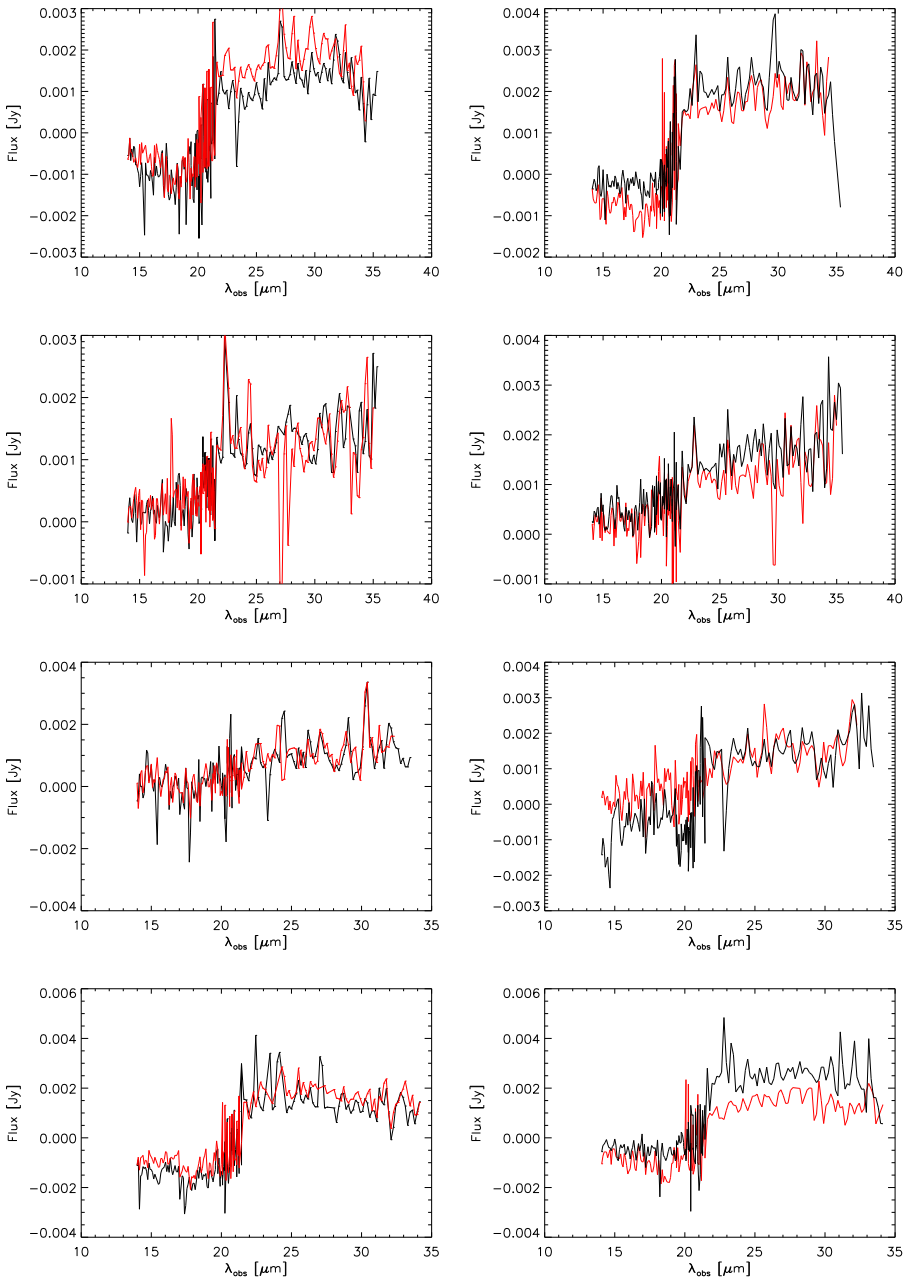

Figure 4.6: Observed frame IRS spectra of each object as obtained from SPICE. Objects $1-4$ are shown from top to bottom, on the left hand side are the Nod 1 spectra and the right hand side are the Nod 2 spectra. Order-order subtracted spectra are shown in red and Nod-Nod subtracted spectra are shown in black. There is good consistency between these methods of background subtraction.

Table 4.4. Signal-to-noise ratio of the IRS spectra calculated from the formal pixel errors from SPICE at two wavelengths selected to be at the start and end of the spectrum. Note, however, that the propagation of IRS errors in SPICE is not well understood.

	Pixel Wavelength [μm]	Nod 1 SNR	Nod 2 SNR
Object 1	22.1	2.7	2.8
	30.1	4.0	4.6
Object 2	22.3	5.5	2.2
	30.2	3.2	1.4
Object 3	21.8	2.4	1.9
	29.6	2.2	0.8
Object 4	22.3	3.6	2.5
	31.0	3.0	3.0

Table 4.5. Fluxes of the 2 epoch detections compared with the MIPS equivalent IRS and MIPS bandmerged catalogue fluxes.

Object	Bandmerged PRF Flux [μJy]	Epoch 1 Flux [μJy]	Epoch 2 Flux [μJy]	IRS Average MIPS Flux [μJy]
IRSS-0001	617 ± 19	617 ± 30	587 ± 25	1483 ± 142
IRSS-0002	665 ± 18	565 ± 29	748 ± 24	1113 ± 135
IRSS-0003	846 ± 19	857 ± 26	767 ± 29	1108 ± 129
IRSS-0004	629 ± 21	689 ± 30	502 ± 30	1345 ± 181

Table 4.6. Available CFHTLS *ugriz* and UKIDSS DXS *JK* magnitude limits for the 4 red objects. All values are given in AB magnitudes. Missing values indicate no coverage.

Object	u	g	r	i	z	J	K
1	>26.8	>27.0	>26.3	>26.2	>25.3		
2	>26.7	>27.0	>26.5	25.4±0.2	>25.3		
3	>26.8	>26.9	>26.5	>26.2	>25.3	>24.6	>25.8
4							>26.2

4.3.2 Ancillary Data

In order to complement the infrared data we have obtained, we also search surveys at other wavelengths for coverage of these four objects. Objects $1-3$ have been observed as part of the CFHTLS and objects 3 and 4 have been observed as part of the UKIDSS DXS. We obtained *ugriz* band postage stamp images for objects $1-3$ from the CFHTLS archive (object 4 had poor coverage). The postage stamps are shown in figures 4.1 - 4.4. Objects 1 and 3 are not detected at any of these optical wavebands at the CFHTLS depths (see below). Object 2, however, appears as a catalogue detection in the i-band. There are no other catalogue detections, but visually there appears to be an excess in the g and r bands, although in the r band the object appears to have been broken up into two. Object 3 has JK coverage in DXS and object 4 has K-band data. Not surprisingly due to their faintness at IRAC wavelengths these stamps show no detection. Table 4.6 shows the CFHTLS and DXS 5σ limits (obtained from the postage stamp header provided by the data reduction team) where available for all objects and the i band detection for object 2.

We gained approximately 8 hours with the Max Planck Millimetre Bolometer Array (MAMBO; Kreysa et al., 1998) instrument on the 30m Institut de Radioastronomie Millimétrique (IRAM) antenna at Pico Veleta to obtain photometry at 1.2mm. This was observed as a backup project, the results of which are summarised in table 4.7. None of the objects were detected, although for object 2 there is a 1.5σ excess. These non-detections are surprising, a large 24μm to 3.6μm flux ratio suggests highly obscured objects which would have significant emission at mm wavelengths, if there is enough cold dust.

Finally, the objects have all been observed with the *XMM-Newton* satellite as part of the XMM-LSS survey (Pierre et al., 2004). In all cases the objects are not detected in

Table 4.7. MAMBO observations and results. For each object we give the flux from aperture photometry (from the MAMBO team) and the observation time. We also give the 5σ limits. We calculate these by adding 5σ (where σ is the error bar) to the measured value.

Object	Flux [mJy]	Observation Time [mins]	5σ Limit [mJy]
IRSS-0001	0.08 ± 0.51	80	< 2.63
IRSS-0002	0.742 ± 0.426	100	< 2.87
IRSS-0003	0.41 ± 0.52	60	< 3.01
IRSS-0004	0.005 ± 0.442	100	< 2.22

Table 4.8. X-ray flux limits for each object from the *XMM-Newton* Large Scale Structure Survey with the EPIC/PN camera (Pfeffermann et al., 1999; Strüder et al., 2001)

Object	$0.2-2$keV Flux [10^{-15} ergs cm^{-2} s^{-1}]	$2-12$keV Flux [10^{-15} ergs cm^{-2} s^{-1}]
1	32.01	3.32
2	65.76	4.76
3	87.43	7.18
4	56.75	5.47

any X-ray band. We calculate 4σ upper limits to the X-ray flux from the FLIX software[1] provided by the XMM-Newton Survey Science Centre (Watson et al., 2001). The resulting limits are shown in table 4.8.

4.4 Results

The reduced order-order subtracted IRS spectra are shown in figures 4.7 - 4.10, where we have calculated the mean spectrum of the two Nod's weighted by the errors calculated by SPICE. However, the IRS pipeline does not propagate the pixel errors properly and we therefore adopt the procedure used by Yan et al. (2005); Weedman et al. (2006c) and calculate the error bars on the mean spectra from the difference between the spectra in

[1] http://www.ledas.ac.uk/flix/flix.html

each Nod. We note, however, that this should be an upper-limit to the errors. We have removed pixels where the difference between the two Nod's is $\geq 25\%$ of the weighted mean. The spectra have been smoothed with a boxcar smoothing of 0.3μm and have been normalised to the MIPS 24μm flux after the error bars were calculated. The figure shows that a continuum was not detected for any object in the low-wavelength order (LL2), as expected from the faint IRAC data. All objects are detected in the LL1 order spectra, however, in all cases the spectra are very noisy.

Note that since this analysis was completed an improvement in the data reduction technique has been identified. This improvement is due to a removal of the effect of a build-up of latent charge in the IRS detectors. Ideally, one would re-do the reduction since it would allow the shorter wavelength data to be used and might lead to spectral lines becoming clearer. It is therefore likely that more robust redshift determinations for these objects could be made. However, the broad conclusions of the chapter are unlikely to be significantly affected and re-reducing and re-analysing this data is therefore left for future work.

We now attempt to estimate the redshift of each of these objects based on both the IRS spectra and the broad-band photometry at our disposal. It is clear that due to the noisy nature of the spectra, along with the few detections obtained at other wavelengths, these attempts will be tentative. Therefore, to get an idea of the error range we adopt two methods for redshift determination. In the first case we try to match the IRS spectra to well known IRS diagnostics and then compare the broad-band photometry to template SEDs. In the second method we perform a fit (using a minimum χ^2 technique) to calculate a redshift and then again compare the broad-band photometry to template SEDs.

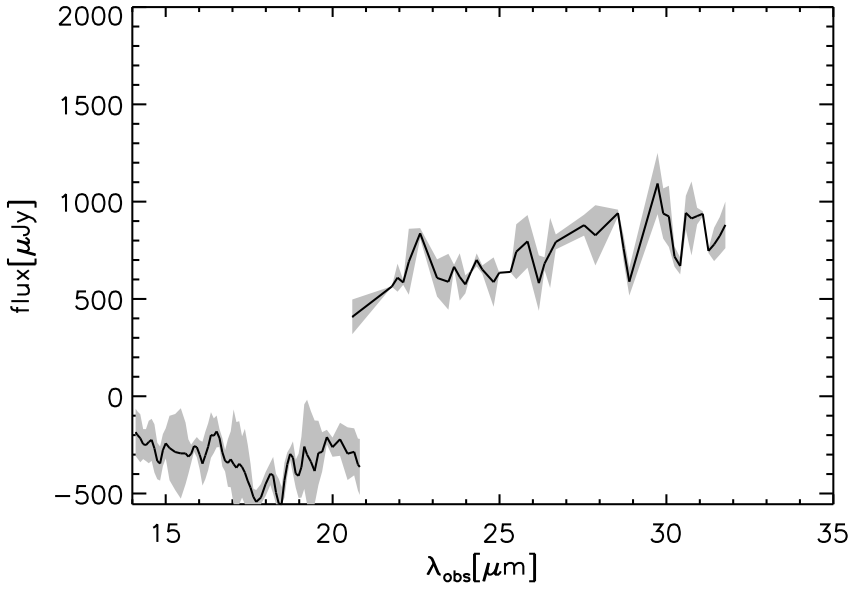

Figure 4.7: IRS spectrum for object 1 normalised to the 24μm MIPS flux.

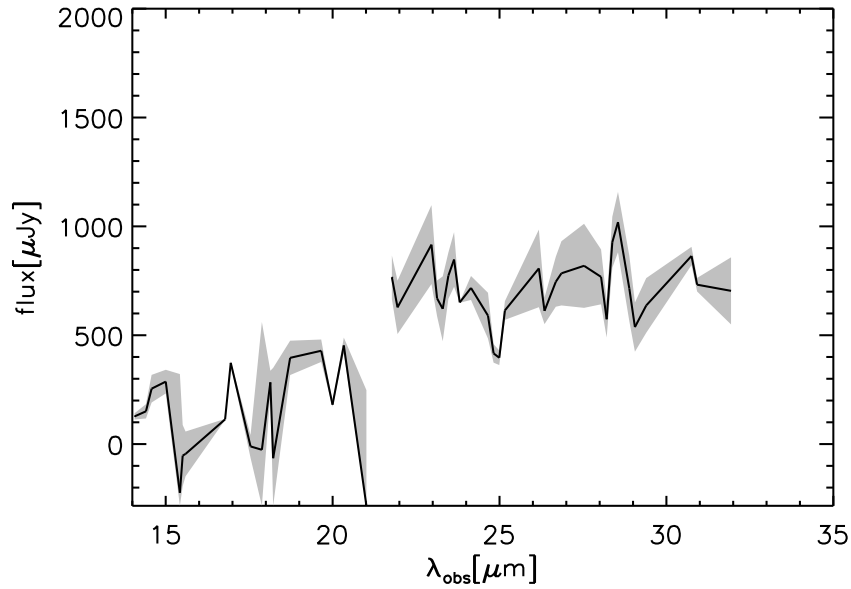

Figure 4.8: IRS spectrum for object 2 normalised to the 24μm MIPS flux.

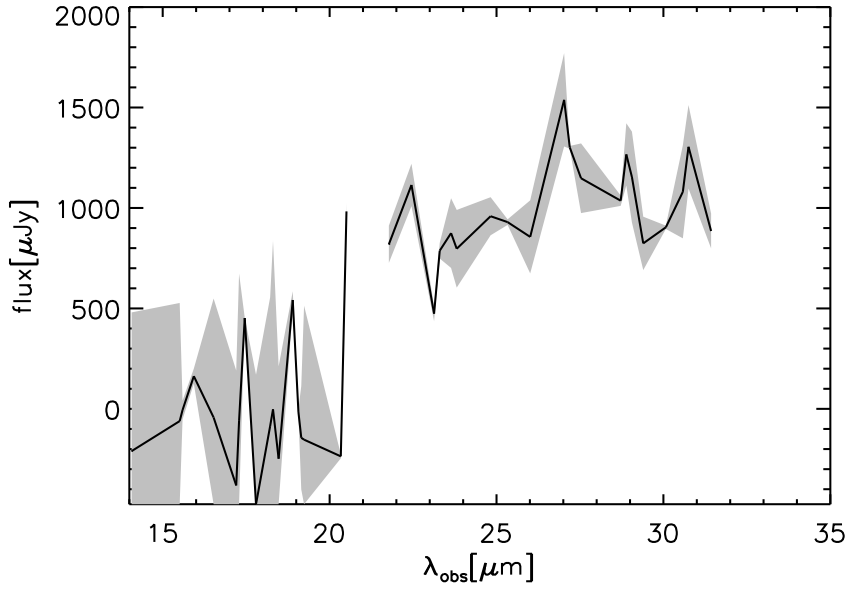

Figure 4.9: IRS spectrum for object 3 normalised to the 24μm MIPS flux.

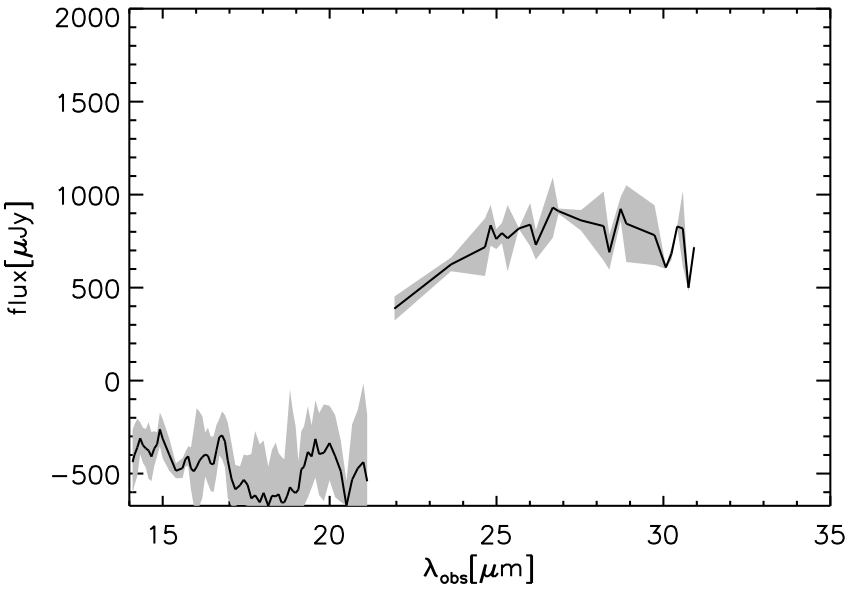

Figure 4.10: IRS spectrum for object 4 normalised to the 24μm MIPS flux.

4.5 Redshift Determination

4.5.1 Matching Features

We look for possible features in the spectra and compare to high signal-to-noise ratio (SNR) long-wavelength, low-resolution, IRS spectra of well known, low redshift objects. The template objects we use are Mrk 3, Mrk 231 and Mrk 1014. These IRS spectra were obtained by Weedman et al. (2005); Armus et al. (2004). Mrk 3 is a Seyfert 2 AGN showing strong emission lines (a Seyfert 2 galaxy is one with narrow optical emission lines from the nucleus Seyfert, 1943). Mrk 231 is a ULIRG showing strong silicate absorption (see below for further details) and Mrk 1014 is an IR luminous, radio-quiet AGN (a radio-quiet AGN is one with radio to optical flux ratio $\lesssim 10$, Schmidt, 1970) and has a strong power-law continuum with PAH emission at 6.2μm and 7.7μm. Together these templates cover a wide range of IRS diagnostics. We then use the broad-band photometry/limits and the estimated redshift to compare to the broad-band SED template for Mrk 231 of Polletta et al. (2007); we do not have access to SEDs for Mrk 3 or Mrk 1014, however, the redshifts we suggest will be speculative, it will be extremely difficult to select a particular template. We then add an additional dust correction to this template to attempt to make it consistent with the photometry of our objects from a visual inspection. We use the dust extinction law of Chiar & Tielens (2006) since it includes a prescription for silicate absorption. Part of this analysis was done by M. Polletta (priv. com.). The results are shown in figure 4.11. We now analyse each object in turn.

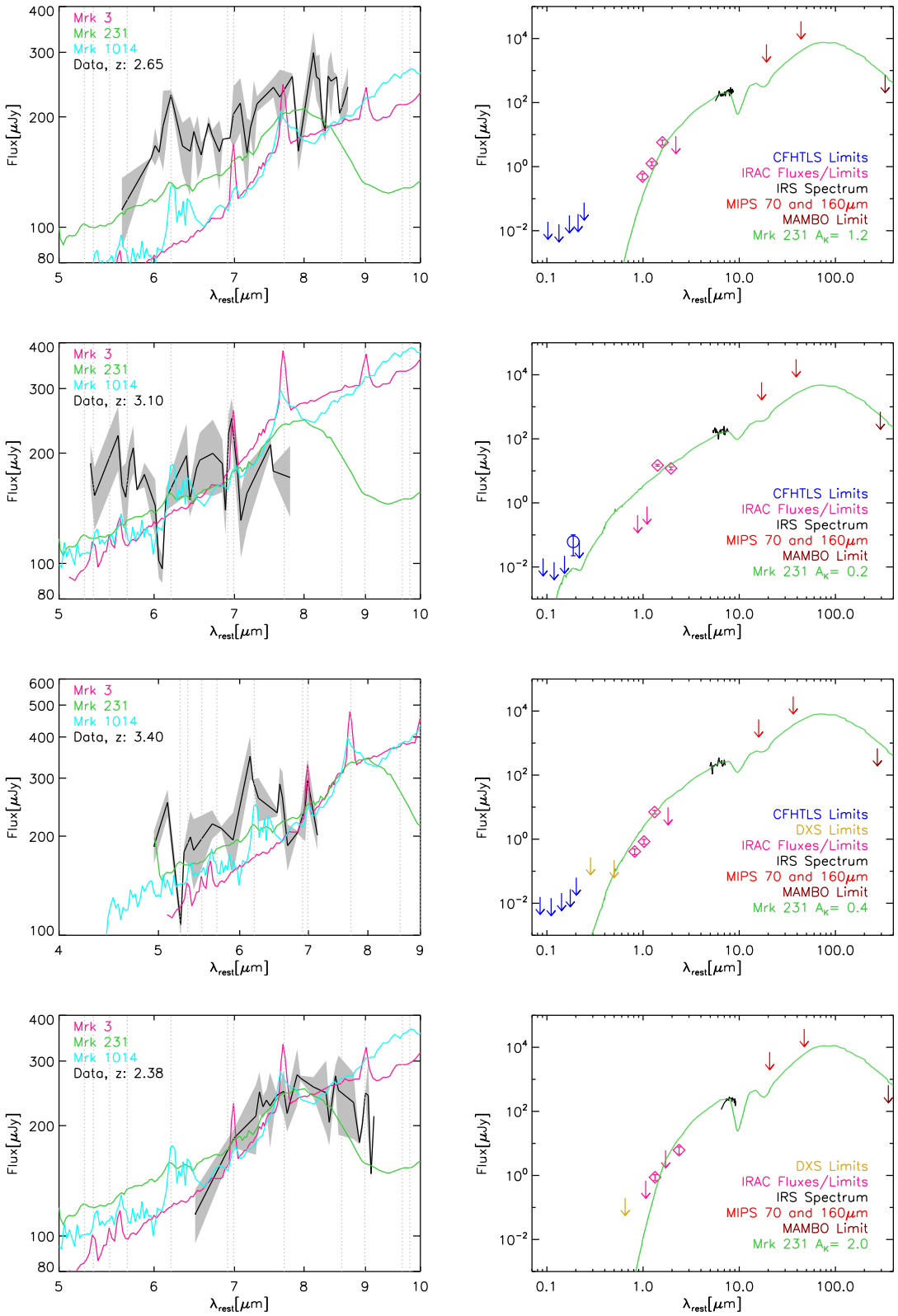

Figure 4.11: Comparison of the IRS spectra to a sample of template spectra. Objects 1 – 4 are shown from top to bottom. In all cases the left hand panel shows the comparison of the IRS spectra. The right hand side shows a comparison of the spectra (black), IRAC fluxes/limits (pink), CFHTLS limits (blue), MIPS 70 and 160μm limits (red), MAMBO limit (dark red) and DXS limits (gold) to the full SED of Mrk 231 (green). The grey dashed lines in the left hand panels show the position of various IRS diagnostic features.

Object 1

For this object we see possible matching with a broad excess at observed wavelength 22.6μm and a second excess at 28μm. These could correspond to the 6.2μm and 7.7μm PAH features, where the former is a fairly broad feature. A further possible excess observed at $\sim$ 25.5μm could be a 6.99μm [ArII] emission line. This would place the object at a redshift of 2.65. The top left hand panel of figure 4.11 shows how these possible features approximately match to the low-redshift IRS spectra. The top right hand panel further shows that at this redshift the channel (ch) $1-3$ IRAC fluxes agree well with the Mrk 231 template with additional dust extinction of $A_K = 1.2$. The CFHTLS, MIPS 70 and 160μm and MAMBO limits are also consistent with this template. The IRAC ch 4 limit is mildly inconsistent however.

Object 2

It is extremely difficult to pick out any features. We tentatively suggest that there is an excess at $\sim$28μm and even more tentatively another at $\sim$25μm. These would match up again to the 6.99μm [ArII] emission line and 6.2μm PAH features at a redshift of 3.1, although this is highly speculative. We would expect to also see the 7.7μm PAH feature, however, it would be observed at $\gtrsim$ 32μm where the LL1 module is not sensitive. The comparison to the template IRS spectra are shown in figure 4.11. The combination of the i band detection with the IRAC channel 1 and 2 limits are highly restrictive, the Mrk 231 template with a dust extinction of $A_K = 0.2$ is the closest match we can find, however, it is not consistent.

Object 3

Again, it is very difficult to pick out any features for this object, there is perhaps an excess at $\sim$27μm and another at 30.8μm. These could correspond to the 6.2μm PAH feature and the 6.99μm [ArII] emission line at a redshift of 3.4. Again, this redshift pushes the 7.7μm PAH beyond the detectable range of LL1. The IRAC channels 1, 2 and 3 seem consistent with Mrk 231 with $A_K = 0.4$ at this redshift as do the DXS and optical limits, but the channel 4 and MAMBO limits seem mildly inconsistent.

Object 4

In this object we see a possible broad emission excess centred at $\sim$26μm with a tentative further excess at 30μm, which could match up to the broad PAH emission feature of Mrk

231 at 7.7μm and 8.99μm [ArIII] emission line at a redshift of 2.38. The SED template of Mrk 231 with an additional dust extinction of $A_K = 2.0$ is a reasonable match to the IRAC photometry, but it is mildly inconsistent with the MAMBO limit.

Summary

In summary, these objects could be at redshifts $\sim 2.65, 3.1, 3.4$ and 2.38. Applying dust corrections to the template of Mrk 231 of $A_K = 1.2, 0.2, 0.4$ and 2.0 produces reasonable consistency for objects 1,3 and 4. However, the template is not consistent with object 2. Furthermore, due to the noisy spectra, we see the redshifts determined above as highly uncertain.

4.5.2 SED Fitting

As an alternative method to attempting to identify features in the spectra, we look to perform SED template fitting. We hope that this analysis might allow us to strengthen or refute the above results. We hope to give general ideas about the power source of these objects as well as their redshift.

In order to perform SED fitting we select a small, representative sample of templates. For highly obscured AGN we choose templates of IRAS 10214+4724, Centaurus A Nucleus and IRAS 00183-7111 (Teplitz et al., 2006; Weedman et al., 2005; Spoon et al., 2004). For moderately obscured AGN we choose IRAS 08572+3915 and I Zw1 (Spoon et al., 2006; Weedman et al., 2005). We also include some classical AGN, 3C273 and PG1211+143 (Hao et al., 2005; Weedman et al., 2005). For starburst objects we choose Arp220 and IRAS 14348-1447 (Spoon et al., 2006; Armus et al., 2007). For composite objects we choose NGC 6240 and Mrk 231 (Armus et al., 2006; Weedman et al., 2005). For each object we obtain both full optical SEDs (where available) and IRS spectra from the literature. The rest-frame IRS spectra used as templates, along with the positions of key features are shown in figure 4.12. All templates consist of high SNR IRS spectra with the LL1 and LL2 modules and were provided by D. Farrah (priv. com.) taken as part of a large IRS Guaranteed Time Observation program to observe ULIRGs (*Spitzer* program ID 105). See Armus et al. (2004); Spoon et al. (2004); Armus et al. (2006) for initial results and data reduction methods. A detailed description of the low resolution spectral properties are presented in Desai et al. (2007a) and further results are given in Spoon et al. (2006, 2007).

We now include a brief description of each of the objects and their IRS spectra that

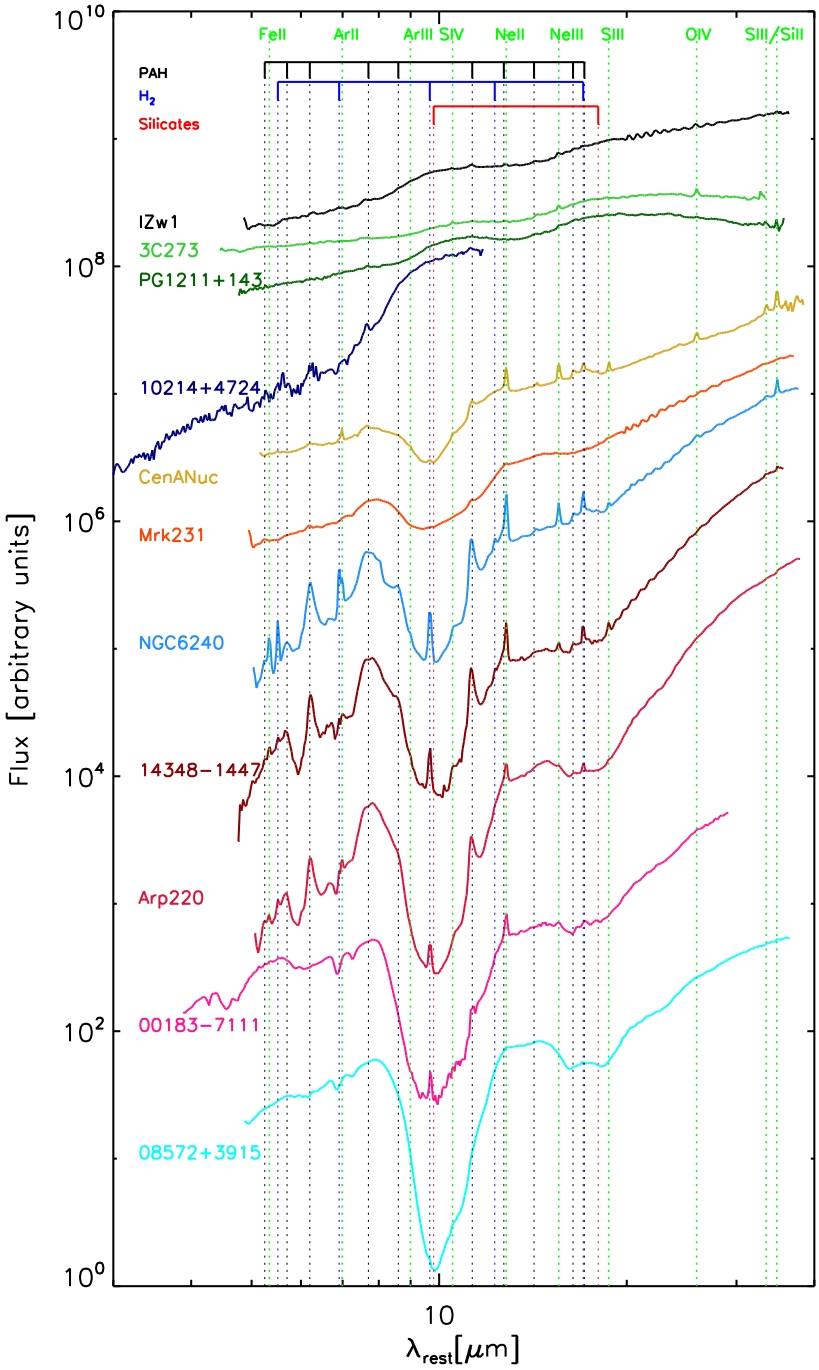

Figure 4.12: Rest-frame IRS spectra of the objects used as templates in order to attempt to identify redshifts of the 4 red objects. Also shown are the positions of diagnostic features common in IRS spectra. These spectra were provided by D. Farrah (priv. com.).

we use as templates, but refer the reader to the individual papers for further details.

I Zw 1

This object was observed as part of the Weedman et al. (2005) campaign to obtain IRS spectra in all modules, i.e. SH, LH, SL1, SL2, LL1, LL2 of a sample of low-redshift objects to provide templates for IRS spectra of higher redshift objects. This is a radio-quiet AGN at a redshift of 0.061 (Solomon et al., 1997). The IRS spectrum shows strong silicate emission at $\sim 10\mu$m with weak 6.99μm [ArII], 15.56μm [NeIII] emission lines and weak 11.2μm PAH emission.

3C273

This is a local ($z = 0.158$ Strauss et al., 1992) radio-loud type 1 AGN (a radio-loud AGN has radio to optical flux density $\gtrsim 10$ and a type 1 AGN is one that exhibits broad optical emission lines Schmidt, 1970; Sandage, 1965). The spectrum shows broad silicate emission features at 10μm and 18μm but also shows 10.51μm [SIV], 12.81μm [NeII]/12.7μm PAH (as these lines are blended together) and 25.89μm [OIV] emission line features. The full SED template is from M. Polletta (priv. com.).

PG1211+143

This object is a nearby ($z = 0.081$, Marziani et al., 1996) radio-loud type 1 AGN (Sanders et al., 1989). Hao et al. (2005) present the IRS spectra in both SL and LL modules for this object. The spectrum shows two broad silicate emission features at 10 and 18μm.

IRAS FSC 10214+4724

This object is a Hyper Luminous Infrared Galaxy (HLIRG), first discovered by *IRAS* and found to be at a redshift of $z = 2.286$ (Rowan-Robinson et al., 1991). It was later discovered to be a lensed system (see for example Broadhurst & Lehar, 1995). Teplitz et al. (2006) present the IRS spectrum of this object using SL1, LL1 and LL2, giving a spectrum spanning the rest-frame wavelength range $2.3 - 11.5\mu$m. The spectrum contains strong silicate emission at $\sim$10μm with only marginal 6.2μm and 7.7μm PAH detection and a mixture of the 5.7μm PAH and the 5.5μm H_2 rotational line. The spectrum also shows a red continuum. While the silicate emission and weak PAH emission suggests an AGN dominated object, substantial emission from cold dust suggests a large starburst component too. Teplitz et al. (2006) suggest that these contradictory diagnostics are explained by a

highly magnified AGN masking a dominant starburst with weak PAH emission. *Chandra* observations of this object are consistent with a Compton-thick AGN (Alexander et al., 2005). For a full SED we use the 3-component dust emission model fit of J. Marshall (priv. com.); Teplitz et al. (2006).

Centaurus A Nucleus

Centaurus A (Cen A) is a local ($z = 0.002$, Graham, 1978) radio-loud AGN with a nucleus which is highly obscured at optical wavelengths. The IRS spectrum (obtained by Weedman et al., 2005) shows strong silicate absorption features at $\sim$10μm and 6.99μm [ArII], 12.81μm [NeII]/12.7μm PAH, 15.56μm [NeIII], 18.71μm [SIII], 25.89μm [OIV] and 34μm [SiII] atomic emission lines. PAH emission at 6.2μm, 7.7μm and 11.2μm are also present, although most are weak with the exception of the 11.2μm feature.

Mrk 231

Due to broad Balmer lines this is classed as a Seyfert 1 galaxy (a galaxy with broad optical emission lines from the nucleus Seyfert, 1943) but it is a ULIRG at $z = 0.042$ (Carilli et al., 1998) with a circumnuclear starburst responsible for most of the IR luminosity (Solomon et al., 1992; Farrah et al., 2003). It also has an AGN component with large amounts of optically absorbing material. The IRS spectrum has strong silicate absorption at $\sim$10μm and steep continuum but no atomic emission lines; only weak PAH emission at 6.2μm and 11.2μm, and a broad 7.7μm PAH feature. Full SED template from Berta (2005); Polletta et al. (2007).

NGC 6240

This is a nearby ($z = 0.025$ Downes et al., 1993) ULIRG and is a double nucleus, merging galaxy. X-ray observations suggest at least one, possibly two, AGN obscured by $N_H = 1 - 2 \times 10^{24}\mathrm{cm}^{-2}$ (Netzer et al., 2005). Armus et al. (2006) obtained a spectrum of the object with all IRS modules, the spectrum shows strong silicate absorption at 10μm and 18μm as well as many PAH emission features (5.7μm, 6.2μm, 7.7μm, 8.6μm, 11.2μm, 12.7μm/12.81μm [NeII] and 17.1μm). There are also H_2 rotational emission features (5.5μm, 6.9μm and 9.66μm) and atomic emission from 5.34μm [FeII], 6.99μm [ArII], 15.56μm [NeIII], 18.71μm [SIII] and 34μm [SiII]. Armus et al. (2006) find that the AGN contributes between 20% and 24% to the luminosity, which is dominated by a starburst. Full SED template from Polletta et al. (2007).

IRAS FSC 14348-1447

This object is another nearby ($z = 0.083$, Murphy et al., 2001) ULIRG. The spectrum is similar to that of NGC 6240 but lacks the 5.34μm [FeII], H_2 5.5μm and 6.99μm [ArII] emission lines.

Arp220

This object is a local ($z = 0.018$, de Vaucouleurs et al., 1991) starburst dominated ULIRG first discovered by Arp (1966) and is the merger of two gas-rich disk galaxies (Sanders & Mirabel, 1996). The spectrum again is similar to the previous two templates but shows much deeper 10μm silicate absorption and lacks most of the atomic emission lines. Full SED template is from Rowan-Robinson (2001).

IRAS FSC 00183-7111

This object is an intermediate redshift ($z = 0.327$, Fisher et al., 1995) ULIRG discovered by *IRAS* and is a highly obscured AGN. The object was observed with IRS by Spoon et al. (2004). The IRS spectrum shows deep 10μm silicate absorption with H_2 emission at 9.66μm , a broad emission feature at $\sim$5.5μm and the blended [NeII] and 12.7μm PAH emission line.

IRAS FSC 08572+3915

This object is a nearby ULIRG ($z = 0.058$, Murphy et al., 2001). The spectrum shows extremely deep silicate absorption at 10μm and 18μm with essentially no emission features. Full SED template from Polletta et al. (2007).

Missing SEDs

In the cases of PG 1211+143, Cen A, IRAS FSC 00183-7111, IRAS FSC 14348-1447 and I Zw 1 we do not have access to full SED templates. Instead, we obtain photometry at all available wavelengths from the NASA Extragalactic Database (NED[2]) and compare to the templates of Polletta et al. (2007) and the above SED templates we do have. This comparison is shown in figure 4.13, where we have only included a likely subset of templates in each case for clarity. From the figures we choose alternative SED templates for these objects, shown in table 4.9. In the case of Cen A there is no template which matches the photometry of Ramos Almeida et al. (2009) as well as the IRS spectrum. However, if we

[2]http://nedwww.ipac.caltech.edu/

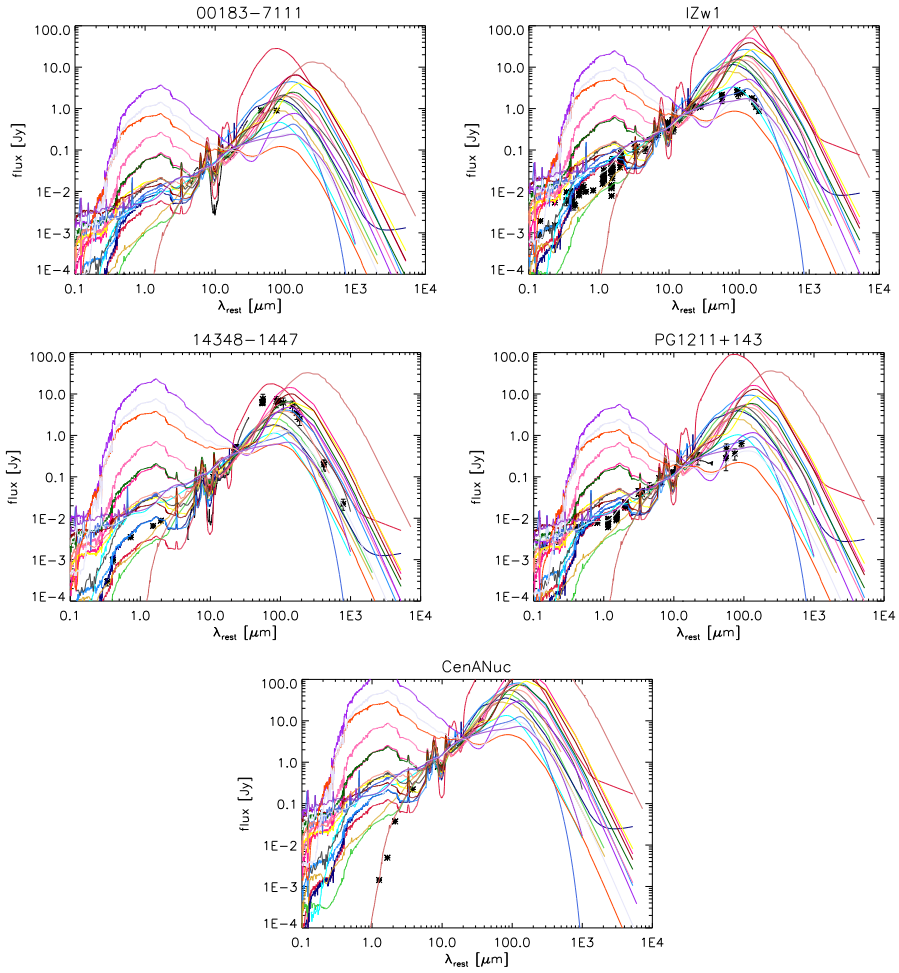

Figure 4.13: Comparison of the photometry from NED of those IRS templates for which we do not have access to full SED templates to alternative templates. The black line is the IRS template and the black stars are the photometry from NED. The alternative templates are shown in various colours and are from Rowan-Robinson (2001); Berta (2005); Teplitz et al. (2006); Polletta et al. (2007).

add a dust extinction correction of $A_K = 2$ with a Chiar & Tielens (2006) dust extinction law to the template of Mrk 231 then the resulting template matches the photometry well. The final, full SED templates that we use are shown in figure 4.14.

Table 4.9. Full SED templates we use in the cases where we have access to IRS templates but not full SED templates.

IRS Template	Substitute Full SED Template	Description
PG 1211+143	Infrared QSO	Template from Polletta et al. (2007)
Centaurus A Nucleus	Mrk 231, $A_K = 2.0$	Template from Berta (2005); Polletta et al. (2007)
IRAS FSC 00183-7111	Mrk 231	Template from Berta (2005); Polletta et al. (2007)
IRAS FSC 14348-1447	NGC 6090	Local starburst galaxy, template from Polletta et al. (2007)
I Zw 1	Red Quasar	Template from Polletta et al. (2007)

Fitting Technique

We wish to find the best fit redshift for each of these IRS templates. Since no continuum is detected for any object in the lower wavelength order, LL2 is not used for fitting purposes. We convert the template from the rest-frame to the observed frame for redshift bins in the range $0 - 4$ with a bin width of 0.001. We then bin the observed LL1 spectrum into 0.6μm wavelength bins and do the same to the template IRS spectra. For the observed spectrum we calculate the mean flux weighted by the errors in each wavelength bin. For the template we calculate the mean flux in each wavelength bin with no weighting. We then calculate the χ^2 for each redshift using the following equation

$$\chi^2 = \sum_i \frac{(f_i^o - b f_i^t)^2}{\sigma_i^2} \tag{4.1}$$

where f_i^o and f_i^t are the observed and template fluxes in wavelength bin i. b is a normalisation factor which is calculated as the mean ratio between the binned observed spectrum and the binned template spectrum, weighted by the observed errors of the bin propagated in quadrature, σ_i. The summation is over all wavelength bins. We then calculate the reduced χ^2, $\chi^2_\nu = \chi^2/\nu$, where ν is the number of degrees of freedom, given by $N - 1$, where N is the number of wavelength bins used in the calculation. We calculate this χ^2_ν at each redshift for each template for each object. We remove redshift bins where the overlap between the observed spectrum and template IRS spectrum mean that fewer than 10 bins are used in the calculation (the primary effect of this was to remove low redshift bins for F10214+4724 as this object is at $z = 2.286$). Usually, the best fit template is selected as that with a minimum in χ^2. However, the noisy nature of our spectra means that spikes in the χ^2 distribution are likely due to chance coincidence between features and possible noise spikes. Therefore, we look at the full χ^2_ν distribution for each template for each object in figure 4.15. The figure shows firstly, that the values of χ^2_ν that we find are large, with only a very few points < 10. This suggests that the templates do not fit the observations well, as expected given the large variations in each spectrum. Secondly, different templates produce (relatively) good fits to the data at various redshifts, and in some cases there are (relatively) good fits to the data for the same template at different redshifts. In order to investigate these results further we look in more depth at the 'good' fits and utilise the limits from the data at other wavelengths to attempt to exclude some possible scenarios for each object. For the purposes of this analysis we define a scenario as a specific template at a specific redshift.

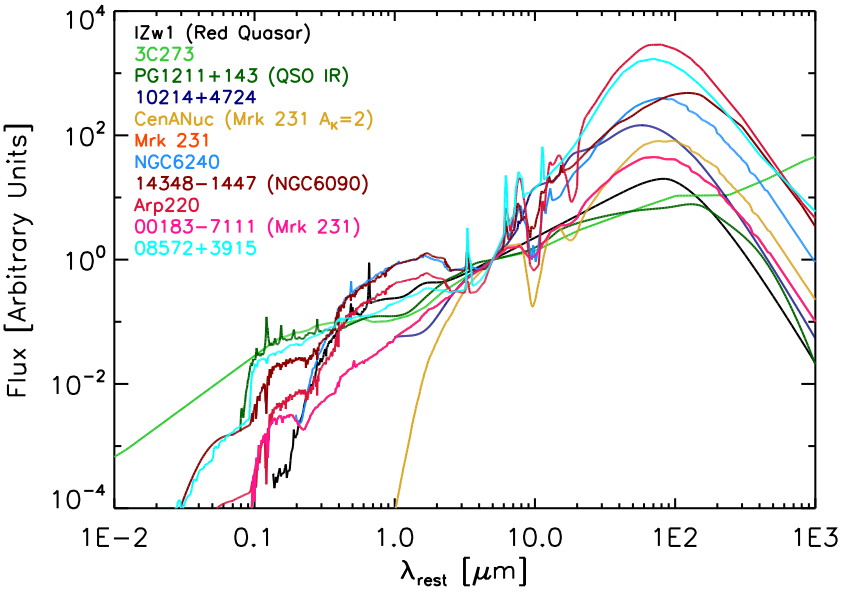

Figure 4.14: The final full SED templates used for comparing the broad-band photometry of the 4 red objects with the results of fits of the observed IRS spectra to template IRS spectra. In the cases where we do not have access to full SEDs the alternative SED used is shown and labeled in brackets. Colour coding is as figure 4.12.

Object 1

For this object we see 17 possible scenarios, shown in table 4.10. For each scenario we apply the dust-extinction law of Chiar & Tielens (2006) to the full template SED. We increase the magnitude of extinction and re-calculate the normalisation until the template is consistent with the IRAC fluxes/limits, up to a maximum of $A_K = 15$ (this corresponds to an A_V of over 100, such obscuration is extreme and is hence chosen as an upper limit). We reject scenarios which require larger extinction than this. This removes 11 scenarios as indicated in table 4.10. The fit of the observed IRS spectrum to the IRS template spectra along with the SED templates with the required extinction for the remaining scenarios are shown in figure 4.16. Of these scenarios several are rejected because they are inconsistent with the MAMBO limit from a visual inspection. These are 3C273 at a redshift of 1.72; Mrk 231 at a redshift of 3.61; Cen A at a redshift of 2.85 and PG1211+143 at a redshift of 3.19. This leaves I Zw1 at $z = 2.82$ with $A_K = 3.0$ and $z = 3.68$ with $A_K = 2.0$. The χ^2_ν of these fits are 12.47 and 9.51 respectively, although in the case of IZw1 at $z = 3.68$ the template IRS spectrum does not span the entire wavelength range of the observed spectrum.

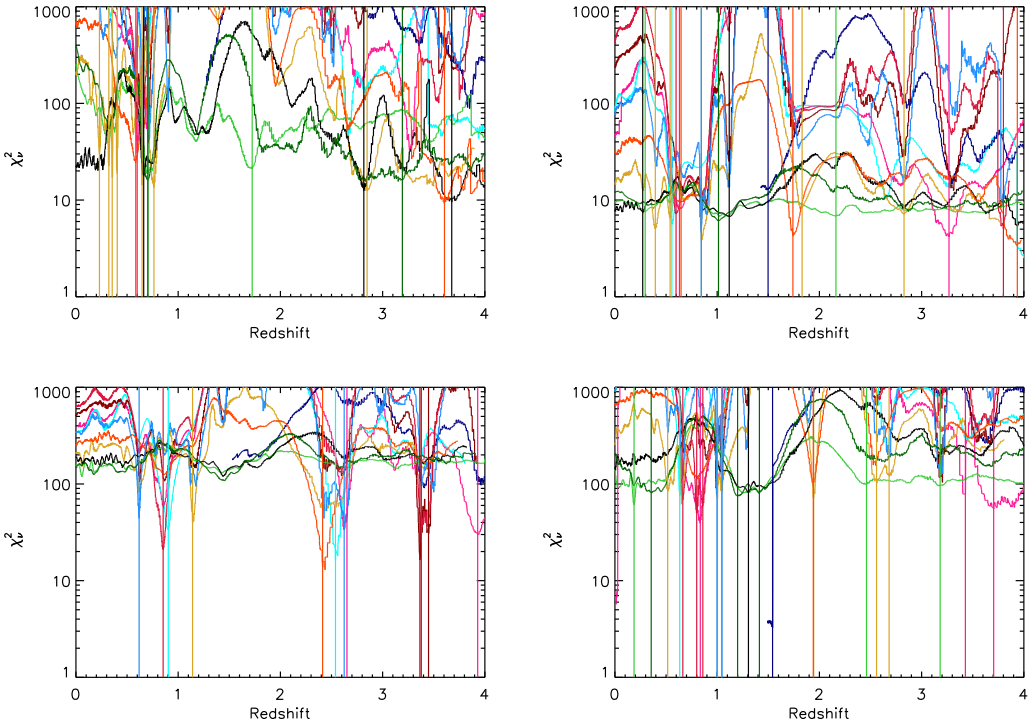

Figure 4.15: The distribution as a function of redshift of χ^2_ν for each template. Objects $1-4$ are shown in the panels going from left to right and top to bottom. The colours are as figure 4.12. Vertical lines represent the template and redshift combinations that we investigate further (see text).

Table 4.10. Possible scenarios for Object 1. Rows in bold are the scenarios that are not removed by the broad-band photometry.

Template	Redshift	χ^2_ν
00183-7111	0.60	30.51*
3C273	0.70	18.77*
3C273	1.72	21.11†
CenANuc	0.23	29.73*
CenANuc	0.32	22.46*
CenANuc	0.36	17.15*
CenANuc	0.40	18.74*
CenANuc	0.65	14.28*
CenANuc	0.76	13.46*
CenANuc	2.85	12.51†
IZw1	0.66	17.91*
IZw1	**2.82**	**12.47**
IZw1	**3.68**	**9.51**
Mrk231	0.59	24.36*
Mrk231	3.61	9.15†
PG1211+143	0.70	16.01*
PG1211+143	3.19	16.07†

*Scenario requires $A_K > 15$ to be consistent with the IRAC fluxes/limits.

†Scenario inconsistent with broad-band photometry.

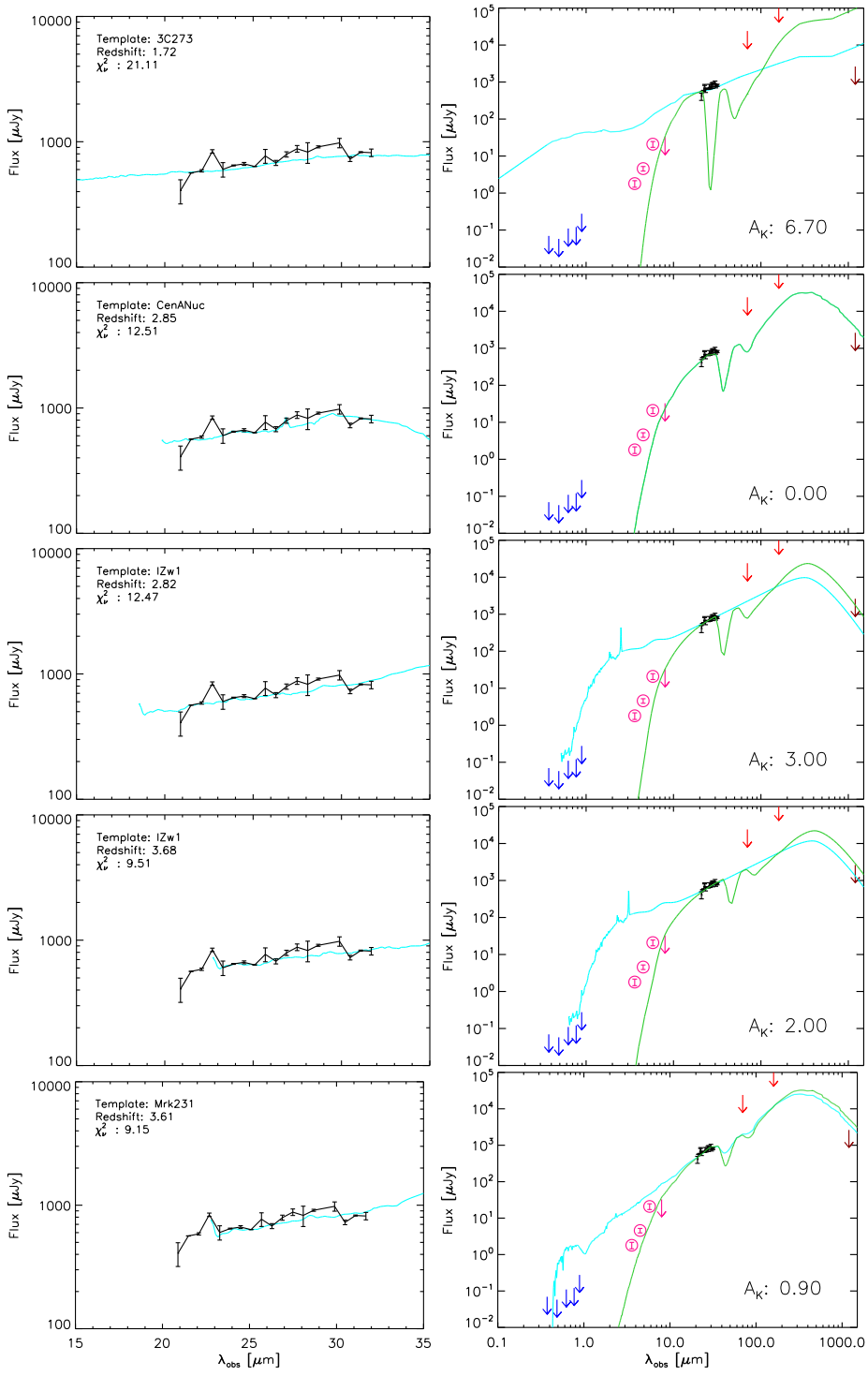

Figure 4.16: SED plots of object 1 for those scenarios shown in table 4.10 where $A_K < 15$. Each row represents a different template and redshift combination. In each case the left hand panel shows the IRS template (cyan) fit to the IRS spectrum (black) and the right hand panel shows the full template SED (cyan) along with the CFHTLS limits in blue, the IRAC fluxes/limits in pink, the MIPS 70 and 160μm limits in red and the MAMBO limit in Burgundy. In the right hand panel we also show the full template SED with the added extinction required for it to be consistent with the IRAC fluxes (green line). All plots are in the observed frame.

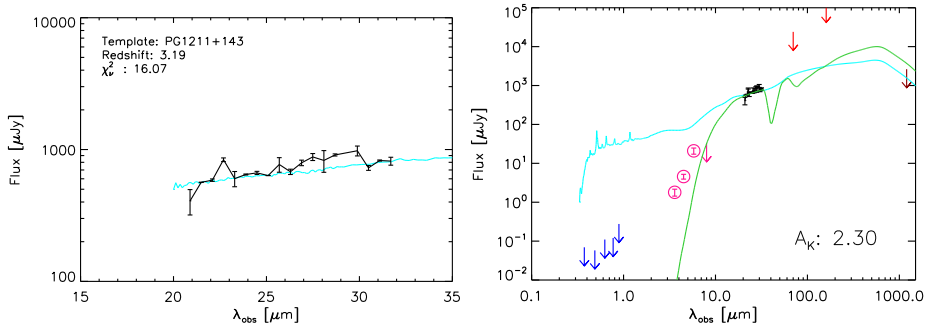

figure 4.16 continued

Object 2

For this object we see 21 possible scenarios which are shown in table 4.11. In all cases the χ^2_ν of the fit is surprisingly reasonable. We again remove templates which require more than $A_K = 15$. The remaining scenarios are shown in figure 4.17. We again remove those scenarios which are inconsistent with the broad-band photometry, the i-band detection in particular removes most scenarios. The only approximately consistent scenario is that of IRAS FSC 10214+4724 at a redshift of 1.5 without any additional extinction, although the SED does not extend to short enough wavelengths to compare to the CFHTLS detection and the IRAC channels 3 and 4 are larger than the template.

Table 4.11. Possible scenarios for Object 2. Rows in bold are the scenarios that are not removed by the broad-band photometry.

Template	Redshift	χ^2_ν
00183-7111	0.63	8.09*
00183-7111	3.27	4.16†
08572+3915	0.56	5.61*
10214+4724	**1.50**	**12.73**
3C273	0.30	7.56*
3C273	2.16	6.82†
Arp220	0.60	7.18†
Arp220	3.80	5.05†
CenANuc	0.40	5.05*
CenANuc	0.54	6.46*
CenANuc	0.85	3.78*
CenANuc	1.83	8.45†
CenANuc	2.83	7.12†
IZw1	0.27	7.32*
IZw1	1.12	6.72*
Mrk231	0.65	9.49*
Mrk231	1.74	4.23†
Mrk231	3.94	3.41†
NGC6240	0.84	4.75†
PG1211+143	1.01	6.08*

*Scenario requires $A_K > 15$ to be consistent with the IRAC fluxes/limits

†Scenario inconsistent with broad-band photometry.

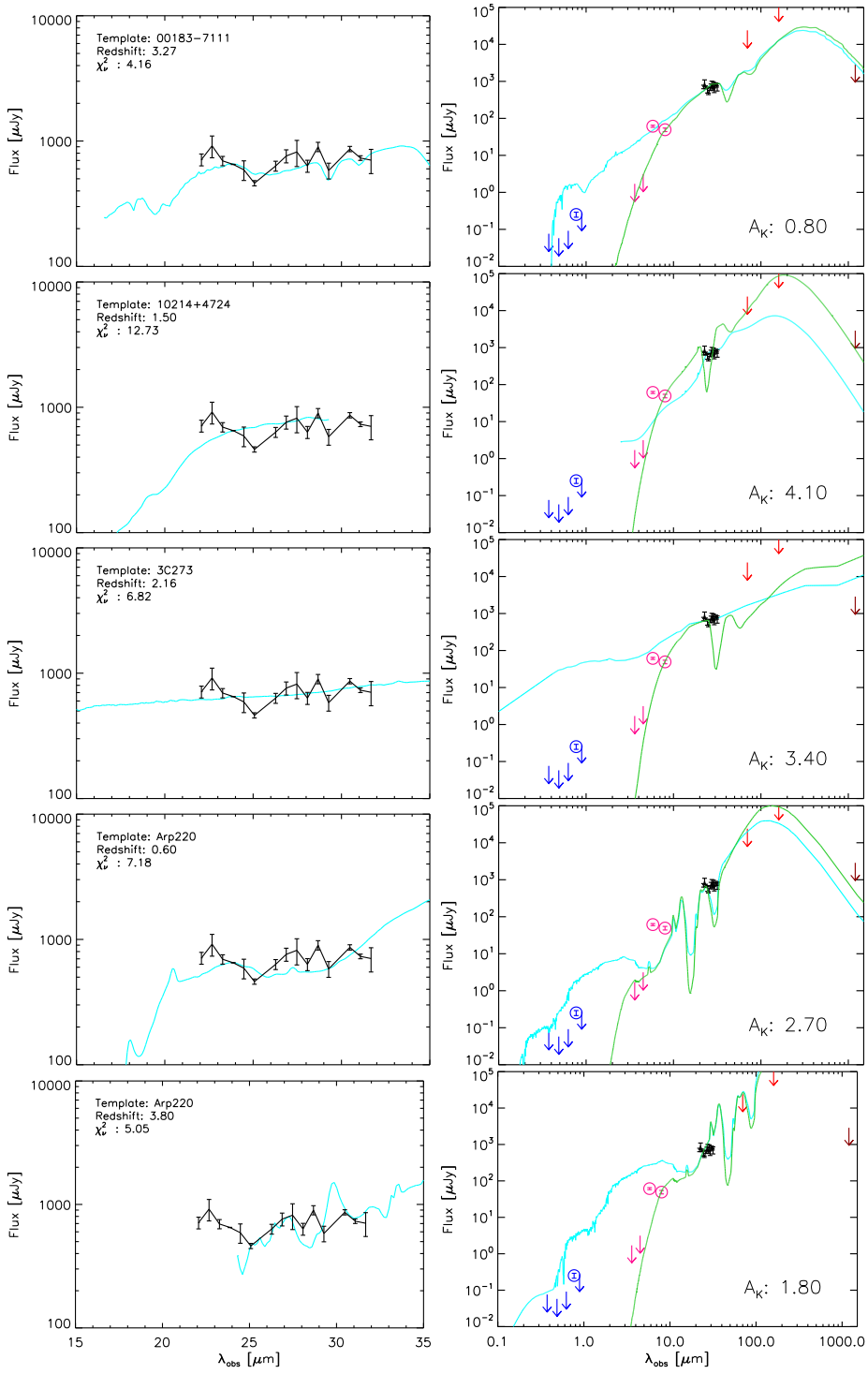

Figure 4.17: As figure 4.16 but object 2. In this case the i band from the CFHTLS is a detection rather than an upper limit.

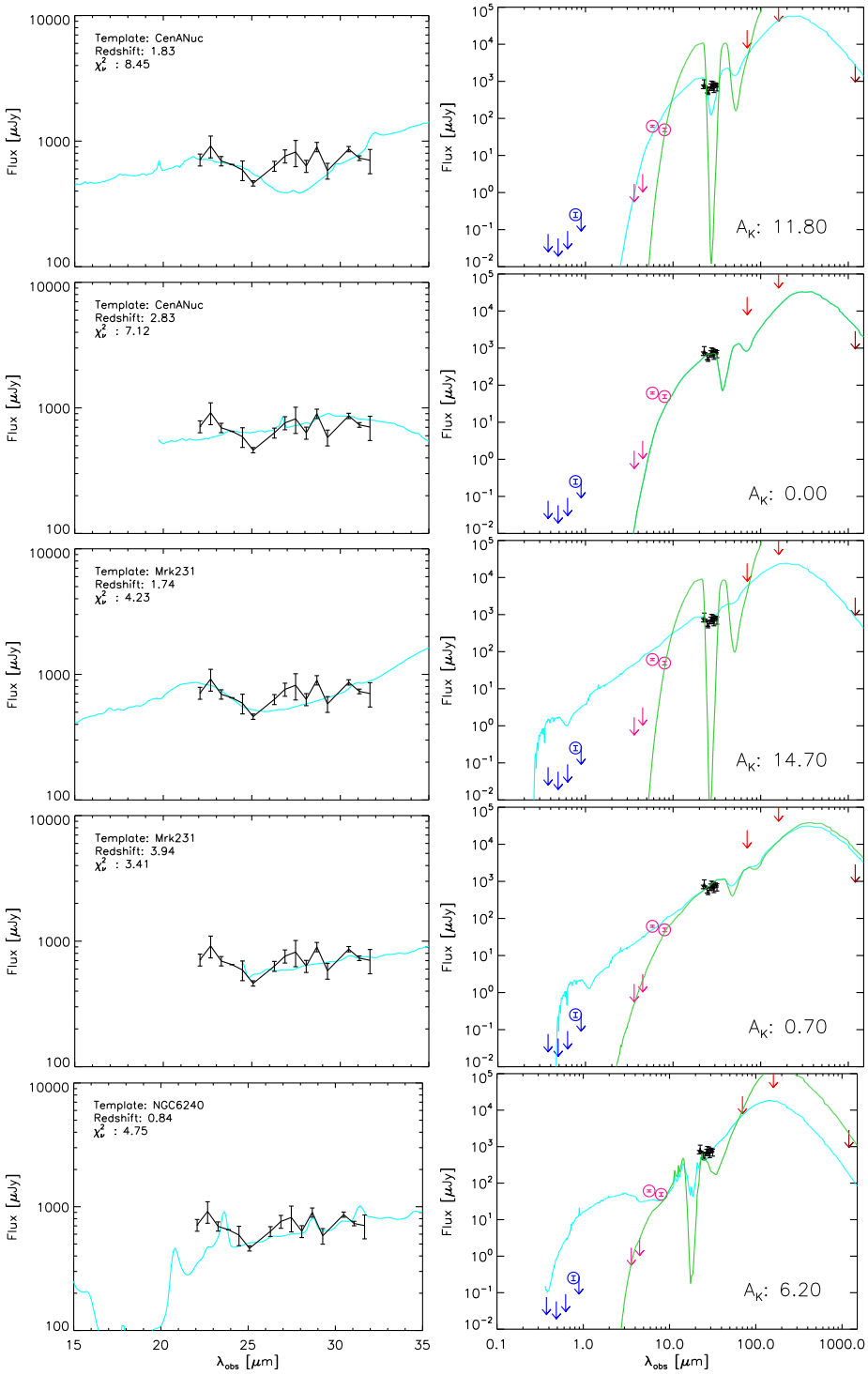

figure 4.17 continued

Table 4.12. Possible scenarios for Object 3. Rows in bold are the scenarios that are not removed by the broad-band photometry.

Template	Redshift	χ^2_ν
00183-7111	2.65	44.89†
00183-7111	3.93	30.64†
08572+3915	**0.90**	**33.40**
08572+3915	2.54	16.26†
14348-1447	3.37	16.35†
14348-1447	3.45	30.70†
Arp220	0.85	20.94†
Arp220	3.38	28.37†
CenANuc	1.14	39.76*
Mrk231	2.41	13.76†
NGC6240	0.62	44.04*
NGC6240	2.62	33.57†

*Scenario requires $A_K > 15$ to be consistent with the IRAC fluxes/limits.

†Scenario inconsistent with broad-band photometry.

Object 3

For this object we see 12 possible scenarios which are shown in table 4.12. The scenarios which remain after removing those which require $A_K > 15$ are shown in figure 4.18. Removing objects which are not consistent with the broad-band photometry leaves only IRAS FSC 08572+3915 at $z = 0.9$ with $A_K = 2.2$ and $\chi^2_\nu = 33.1$. At this redshift the IRAC 5.8μm flux is boosted by a rest-frame 3.3μm PAH feature.

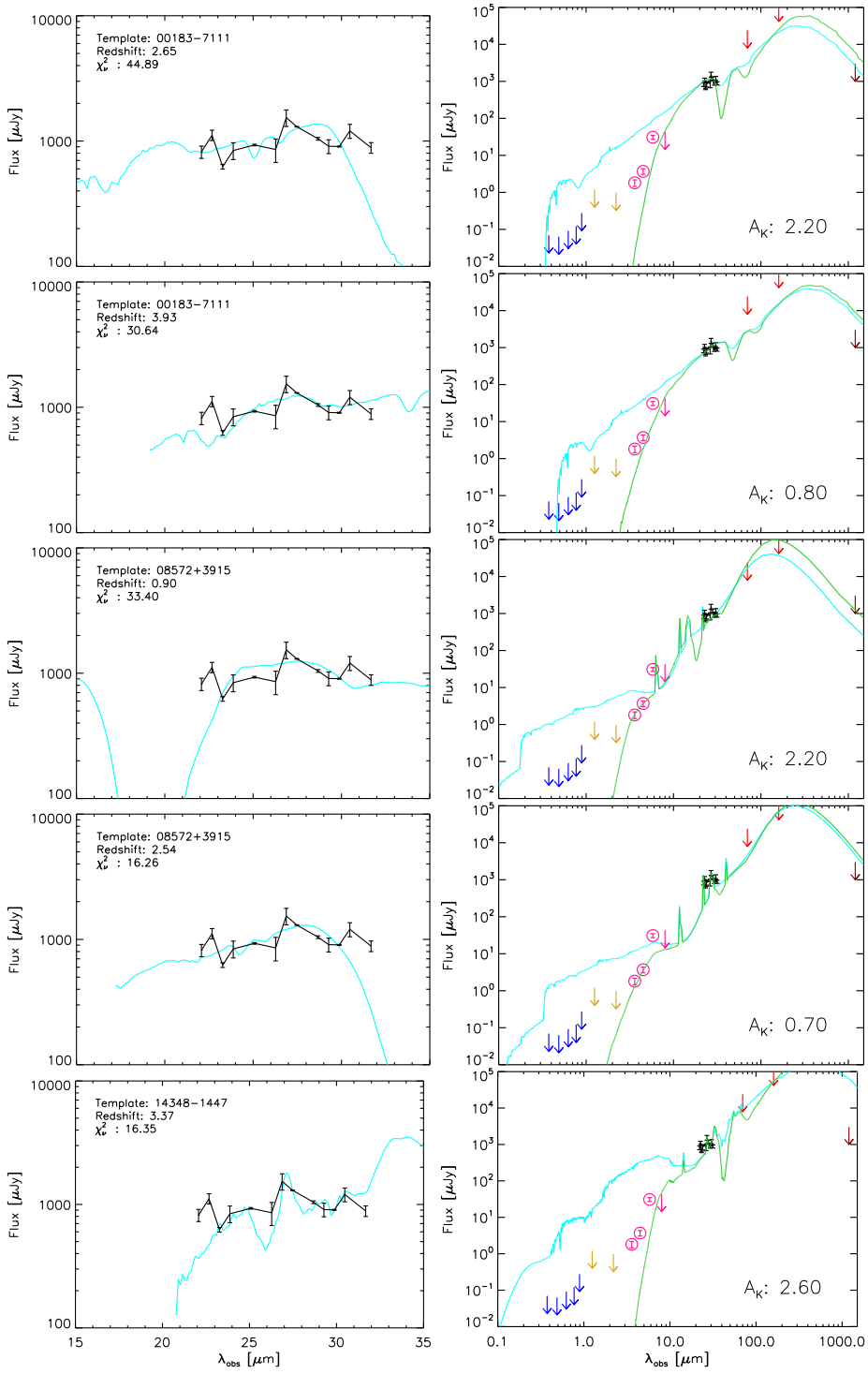

Figure 4.18: As figure 4.16 but object 3. In addition DXS J and K band limits are shown in gold.

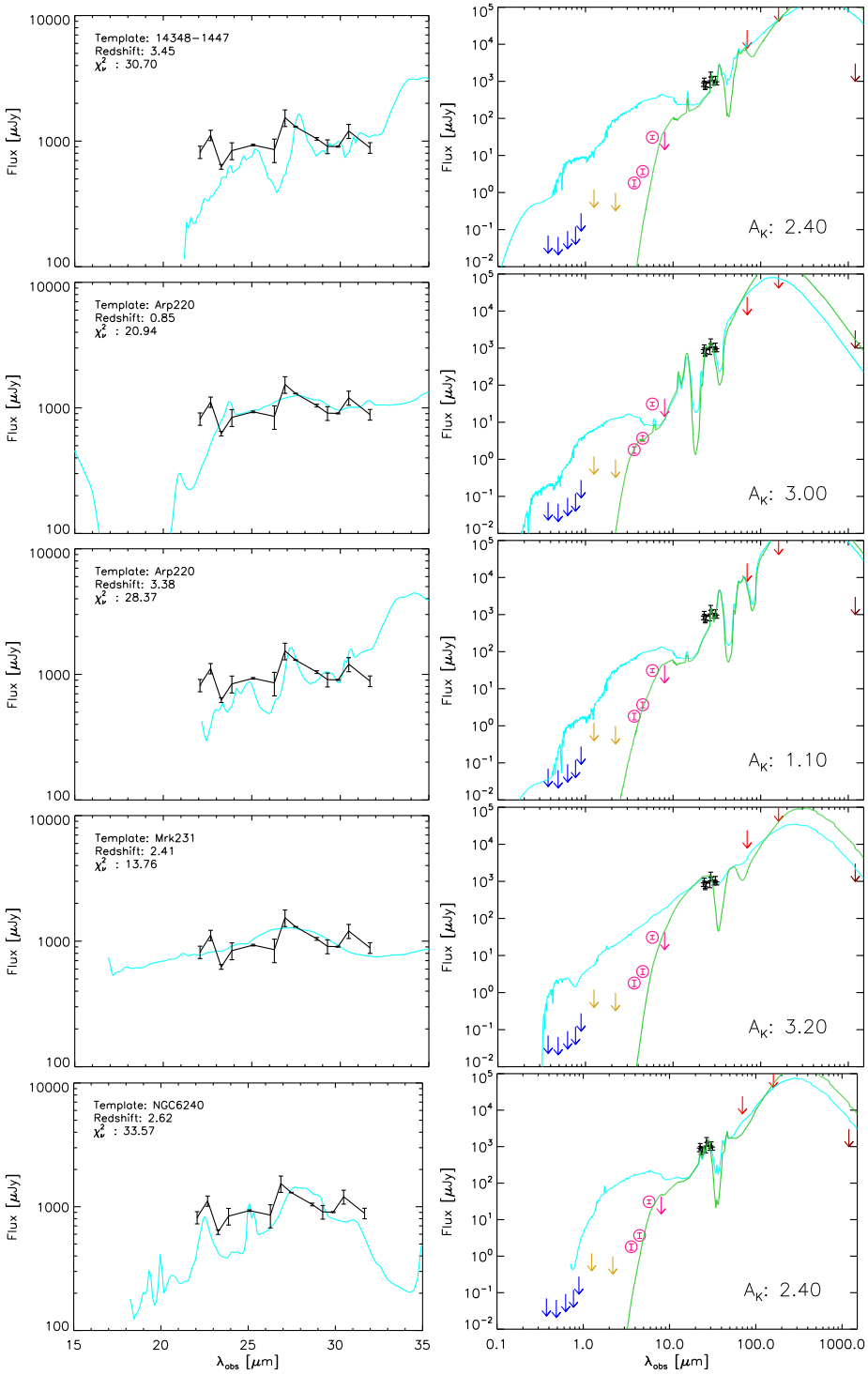

figure 4.18 continued

Object 4

For this object we see 24 possible scenarios shown in table 4.13. Figure 4.19 show the SEDs of the scenarios remaining after removing those requiring more than 15 magnitudes of extinction. Following the procedure we have used above we remove scenarios which are inconsistent with the various limits. We are then left with IRAS FSC 10214+4724 at a redshift of 1.54 with $A_K = 0.5$ and $\chi^2_\nu = 3.28$.

Table 4.13. Possible scenarios for Object 4. Rows in bold are the scenarios that are not removed by the broad-band photometry.

Template	Redshift	χ^2_ν
00183-7111	0.84	39.07*
00183-7111	3.43	78.37†
00183-7111	3.71	55.19†
08572+3915	0.63	76.05*
10214+4724	**1.54**	**3.26**
3C273	0.19	60.98*
3C273	2.46	98.23 †
3C273	3.18	96.19†
Arp220	0.66	68.52*
Arp220	0.80	50.22†
Arp220	0.86	59.29†
CenANuc	0.52	83.42*
CenANuc	1.00	71.09*
CenANuc	1.04	81.76*
CenANuc	1.94	71.61†
CenANuc	2.56	101.81†
CenANuc	2.68	120.55 †
IZw1	1.31	81.78*
Mrk231	1.94	102.57†
NGC6240	1.00	78.05*
NGC6240	1.05	100.90*
PG1211+143	0.36	80.95*
PG1211+143	1.20	75.00*
PG1211+143	1.41	79.14*

*Scenario requires $A_K > 15$ to be consistent with the IRAC fluxes/limits

†Scenario inconsistent with broad-band photometry.

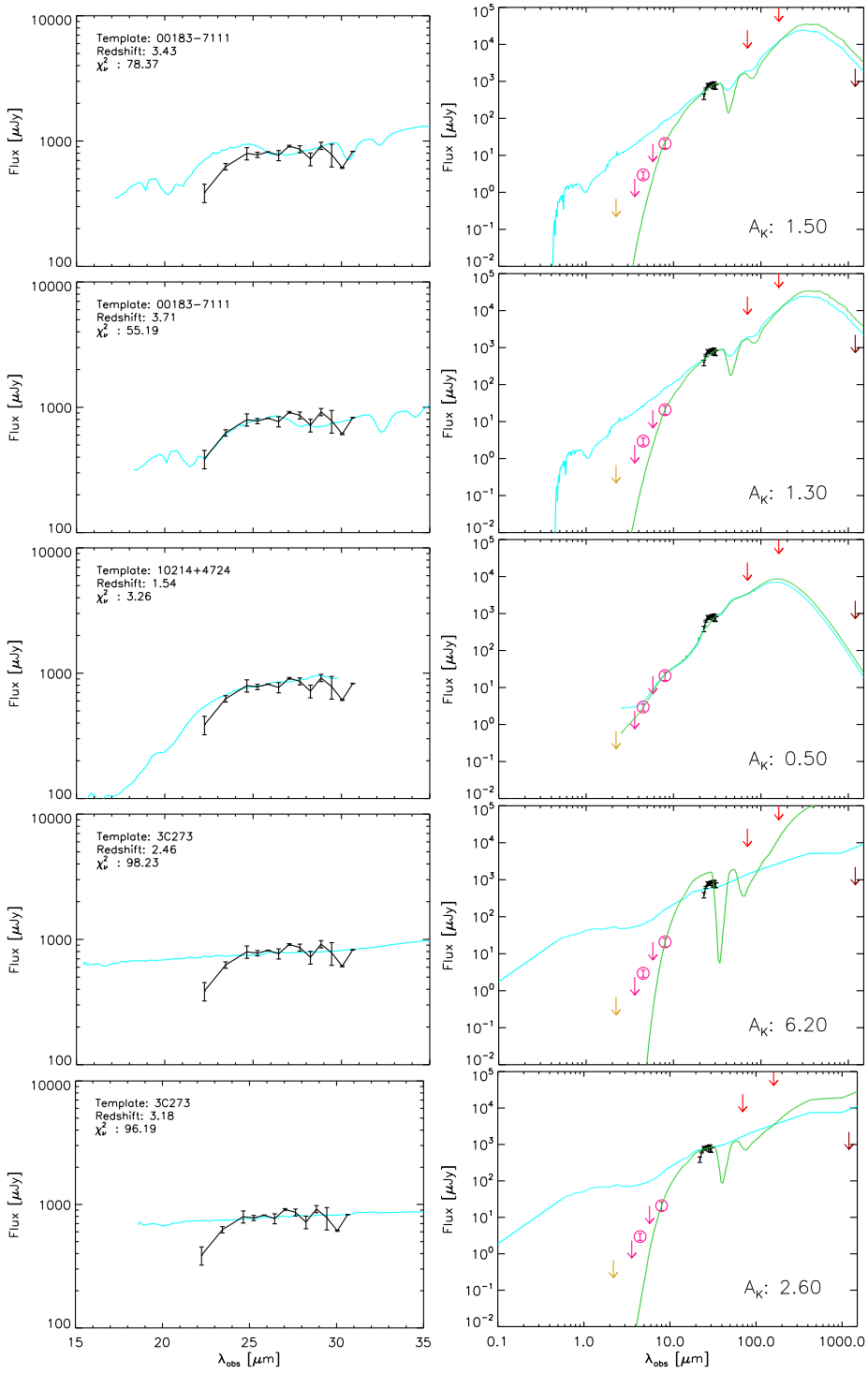

Figure 4.19: As figure 4.16 but object 4. In addition the DXS K band limit is shown in pink.

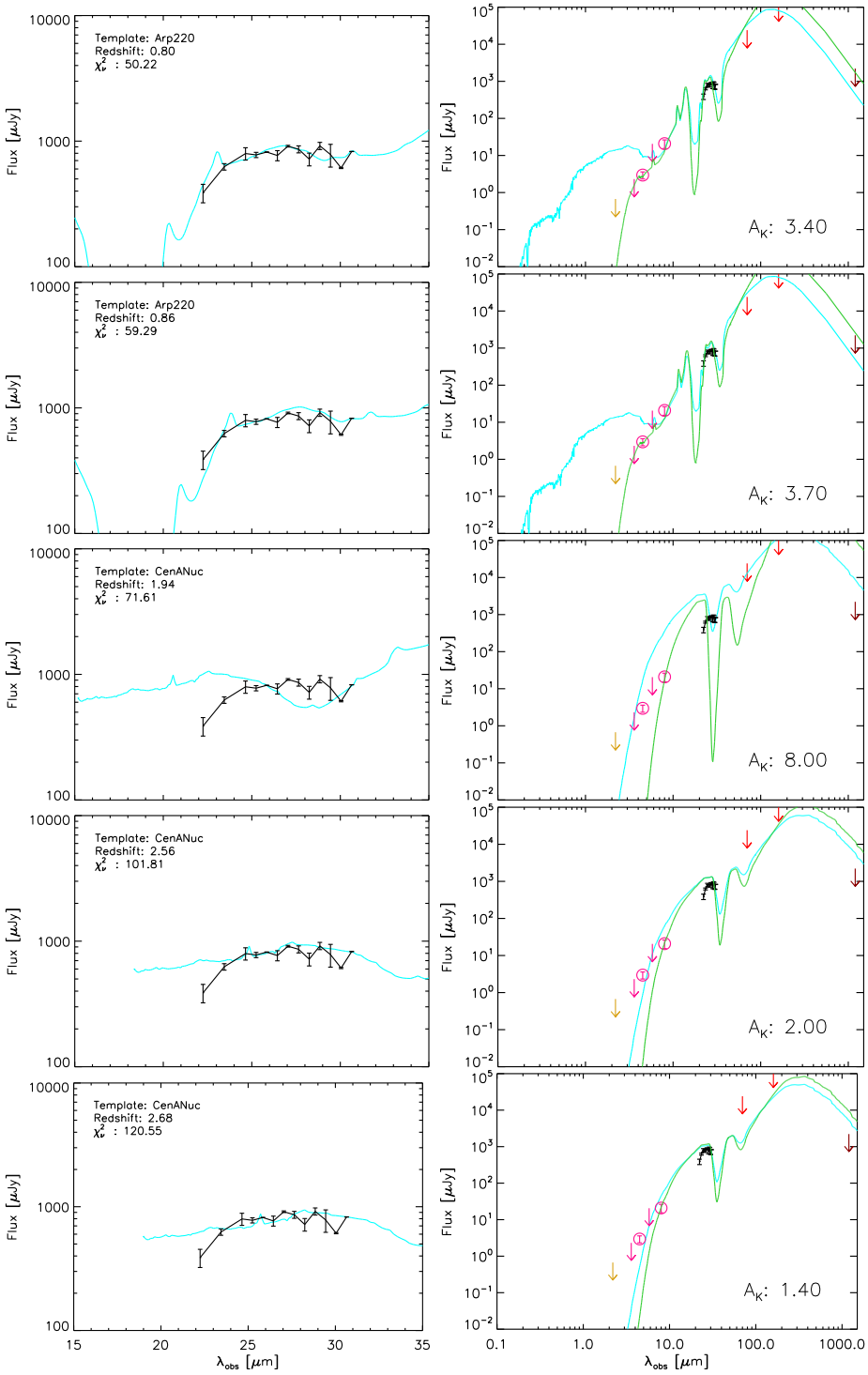

figure 4.19 continued

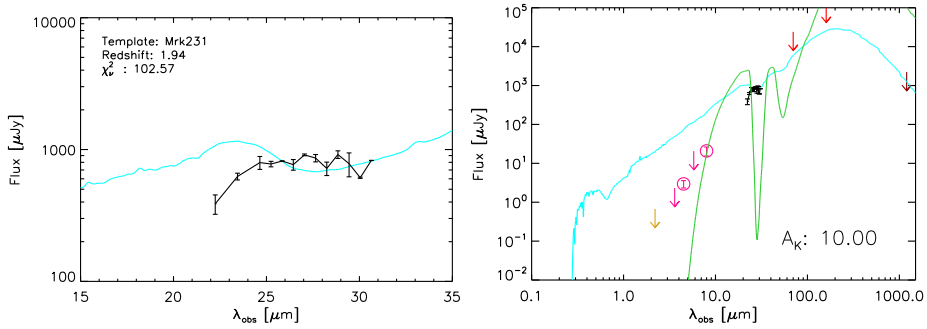

figure 4.19 continued

4.5.3 Summary

A summary of the above discussion is shown in table 4.14. The two techniques that we have employed do not appear to give consistent results, and this likely reflects the large uncertainties involved. However, for object 1 there is some agreement, with both methods suggesting highly obscured, high redshift objects. We note, however, that the spectrum fitting finds higher redshifts. Each of the fits appear very similar from a visual inspection, however, to be conservative we prefer the lower redshift, lower extinction match of Mrk 231 with $A_K = 1.2$ at $z = 2.65$. For object 2 there is no agreement between the two methods. From a visual inspection of the two possible scenarios the F10214+4724 template at a redshift of 1.50 seems to give the best match to the photometry, although this is highly speculative and no template gives a particularly good fit. In the case of object 3 the feature matching method suggests a Mrk 231 template with $A_K = 0.5$ at $z = 3.4$. The spectrum fitting suggests an F08572+3915 template at $z = 0.9$. From a visual inspection of the SEDs the template most consistent with the data is that of F08572+3915 at a redshift of 0.9 with $A_K = 2.2$. Finally, in the case of object 4 there is, again, no agreement. The feature matching method suggests a redshift of 2.38 whereas the spectrum fitting suggests 1.54. Again, from a visual inspection of the fits the template of F10214+4724 at a redshift of 1.54 with $A_K = 0.5$ seems to be the best match to the data. This suggests that these objects represent a wide range of redshifts, from $0.9 - 2.65$, although there is clearly a large degeneracy between redshift and dust extinction, and we again note the uncertainty in the spectra.

Table 4.14. Summary of the interpretation of the IRS spectra through two methods. Note that in the feature matching case the only full SED template considered is Mrk 231.

Object	Feature Matching			Template Fitting		
	z	Template	A_K	z	Template	A_K
1	2.65	Mrk 231	1.2	2.82	IZw1	3.0
				3.68	IZw1	2.0
2	3.1	Mrk 231	0.2	1.5	F10214+4724	0
3	3.40	Mrk 231	0.4	0.9	F08572+3915	2.2
4	2.38	Mrk 231	2.0	1.54	F10214+4724	0.5

4.6 Discussion

We have performed a search for the most extreme objects detectable in the SWIRE survey. We have selected objects with extreme 24μm to 3.6μm colours, from 24μm sources detected in two epochs. We have identified a population of galaxies which have been missed in previous searches for highly obscured objects, such as those of Dey et al. (2008). However, selecting a sample purely based on objects detected at 24μm in two epochs but not found in the 5σ IRAC catalogue results in large contamination from objects where the 24μm detection is due to a PRF artifact from a nearby bright source. From a visual inspection of postage stamps at both IRAC and 24μm we were able to produce a sample of four objects which genuinely satisfy the selection criteria.

We obtained IRS spectra in the LL1 and LL2 modules for each of these objects. No continuum was detected in LL2, but all objects were detected with LL1, albeit with low signal-to-noise. In addition, we obtained upper limits from MAMBO photometry and from the CFHTLS and DXS. There is one object which is detected in the CFHTLS i-band. It is clear from the above analysis that we have not been able to conclusively determine either the redshifts of these objects nor their power source. Due to the faintness of our objects the IRS spectra we have obtained are very noisy allowing only speculation for the presence of emission features. Despite these caveats, we have established plausible redshift determinations for each object. Object 1 is plausibly at a redshift of 2.65; object 2 at 1.5; object 3 at 0.9 and object 4 at 1.54, but we note that all have redshift aliases. Interestingly, we do not find that they are all high redshift, highly obscured versions of the $z \sim 2$ DOGs that we expected. Object 1 does satisfy this hypothesis, but objects 2, 3 and 4 are at the lower end of the DOG redshift selection. These objects are rare, the XMM data that we use covers $\sim$ 8.2 sq. degs. giving a source density of $\sim$ 0.5 per sq. deg.

Using the above redshift determinations, we calculate the far-infrared luminosity (LIR) by integrating the template with the required dust extinction over the wavelength $8 - 1000\mu$m. The results are shown in table 4.15. Objects 1, 3 and 4 are classed as ULIRGs, with infrared luminosities $10^{12} < L_{IR} < 10^{13} \mathrm{L}_{\odot}$ whereas object 2 is slightly less luminous and is classed as a LIRG. We also use the X-ray flux upper limits to estimate upper limits to the X-ray luminosity, shown in table 4.15. Since the objects are not detected in the X-ray observations we cannot calculate a column density and thus assess whether they are Compton Thick. However, the lower limit of the monochromatic mid-infrared to X-ray luminosity ratio ($\log_{10}(L_{6\mu\mathrm{m}}/L_{2-12\mathrm{keV}})$) is 2.62, 3.13, 2.6 and 2.46 for objects 1, 2, 3

and 4 respectively. This is well within the range observed for classical AGN of 0.13-13 (Polletta et al., 2007, 2008a).

Table 4.15. Estimates of the far-infrared luminosity (LIR) and X-Ray Luminosity (XRL) for each object at the estimated redshift. Columns are Object, redshift of the best fit and the corresponding template and dust extinction required, infrared luminosity, soft (0.2-2keV) X-ray luminosity upper limit and hard (2-12 keV) X-ray luminosity upper limit.

Object	Redshift	Template	Extinction [A_K]	$\log_{10}$LIR [$L_\odot$]	Soft XRL [erg s^{-1}]	Hard XRL [erg s^{-1}]
1	2.65	Mrk 231	1.2	12.60	$< 1.1 \times 10^{42}$	$< 1.8 \times 10^{42}$
2	1.50	F10214+4724	0.0	11.67	$< 3.8 \times 10^{41}$	$< 9.4 \times 10^{41}$
3	0.90	F08572+3915	2.2	12.43	$< 1.6 \times 10^{41}$	$< 3.5 \times 10^{41}$
4	1.54	F10214+4724	0.5	12.11	$< 4.6 \times 10^{41}$	$< 8.6 \times 10^{41}$

It is unclear what is the mechanism behind the power source of these objects. The speculative PAH emission in objects 1, 3 and 4 suggests starburst activity. However, for our tentative preferred scenarios, the template objects are powered by both starburst and AGN. In any case, all the objects require significant dust obscuration - the template of F10214+4724 requires no additional extinction to be approximately consistent with the photometry of object 2, however, F10214+4724 is a highly obscured object and is a candidate Compton Thick AGN.

Complementary to this analysis, Shupe et al. (2009) obtained IRS spectra of a similar set of objects. Their sample consisted of 3 objects. Since their objects are bright 24μm sources they obtained spectra with better SNR than those presented here. They find that their objects have redshifts $\gtrsim 2.2$ and evidence that they are powered in part by highly extinguished AGN. It is, however, likely that star-formation also plays a large role.

Similar selections have been used previously, for example that of Dust Obscured Galaxies (DOGs; Dey et al., 2008). DOGs are selected on the basis of high 24μm to optical flux ratios. DOGs have been suggested as being the sought after high redshift, luminous, Compton Thick AGN often invoked to explain the cosmic X-ray background (see e.g. Fiore et al., 2008). However, in samples of DOGs there is a significant fraction which are powered by starbursts rather than AGN (Sajina et al., 2008; Murphy et al., 2009; Georgakakis et al., 2010). This could mean that, while there are some DOGs which are Compton Thick (see e.g. Georgakakis et al., 2009), there is a large fraction which are consistent with Compton thin AGN with lower luminosities or pure starbursts (Donley et al., 2008; Georgakakis et al., 2010). The SED fitting of Georgakakis et al. (2010) further suggests that $z \sim 1$ analogues of the $z \sim 2$ DOGs which are not detected at X-ray wavelengths are dominated by starbursts in the mid-IR. While we cannot say anything definitive about the objects presented here, the extreme mid-infrared colours and the SED fits suggest large dust obscuration that could plausibly be Compton Thick AGN. We note, however, that these objects are too rare to form the whole population of Compton Thick AGN to explain the Cosmic X-ray Background discussed in section 1.6, but they could be some of the most extreme of these objects.

Chapter 5

Spectral Energy Distribution of $z \gtrsim 1$ Type Ia Supernovae Hosts in GOODS: Constraints on Evolutionary Delay

5.1 Introduction

We now turn our attention to much smaller scales. In chapter 2 we saw that by studying the local environment of galaxies we could learn about galaxy evolution. We now apply a similar idea to Type Ia Supernovae (SNe Ia) by studying the host galaxies in which these explosions arise. By making use of a deep, narrow *Spitzer* survey with coverage with the *Hubble Space Telescope* we are able to fit spectral energy distributions to the host galaxies of SNe Ia.

This work was done with supervision from R. Chary and has been submitted for publication in the *Astrophysical Journal*.

5.1.1 Type Ia Supernova Delay Times

It has been shown that SNe Ia are standardisable candles in that there is a very tight relation between the peak luminosity and the width of the light-curve (Phillips, 1993). For this reason SNe Ia have been used to measure the cosmic distance scale and to probe the expansion properties of the universe, leading to the discovery that its expansion rate is accelerating due to the existence of a repulsive force, given the name Dark Energy (Riess et al.,

1998; Perlmutter et al., 1999). It is important to fully understand how SNe Ia are produced in order to minimise the systematic uncertainties associated with these measurements and enable the properties of Dark Energy to be investigated as a function of cosmic time.

It is widely believed that SNe Ia are the explosion of a White Dwarf (WD) star that has reached a critical mass (the Chandrasekhar mass, Chandrasekhar, 1931). The physical mechanism leading to the WD reaching this mass is still highly debated. Broadly, there are two leading ideas for SN Ia progenitors. The first is that the WD star gains mass via accretion of material from a normal companion star which has filled its Roche Lobe, referred to as the Single Degenerate (SD) scenario. The second, the Double Degenerate (DD) scenario involves the merger of two WD stars after formation and ejection of a common envelope in a binary system (see Livio, 2001; Podsiadlowski et al., 2008, for a review).

In order to try to differentiate between these possible scenarios it is important to constrain the SN Ia delay time, i.e. the time between the formation of the stellar system and the supernova explosion. Evidence for a range of delay times has existed for some time. For example, observations show that SNe Ia are preferentially found in late type rather than early type galaxies, suggesting they are associated with young stellar populations with ages of ~ 50 Myrs (van den Bergh, 1990; Mannucci et al., 2005). Wang et al. (1997) showed that SNe Ia are more likely to be found in the disk of a galaxy rather than the bulge, indicating an association with recent star formation and short delay times. Studies which calculate the delay time by convolving an assumed star formation history (SFH) with a delay time distribution (DTD) have suggested longer delay times of a few Gyrs (Gal-Yam & Maoz, 2004; Strolger et al., 2004; Dahlen et al., 2004; Barris & Tonry, 2006; Dahlen et al., 2008; Strolger et al., 2010). However, Förster et al. (2006) show that these analyses depend strongly on the assumed SFH, giving large systematic errors, prompting Oda et al. (2008) to fit both the SFH and the DTD. However, those authors were only able to place weak constraints on the DTD. From a spectroscopic study of the star-formation histories of local SN Ia hosts Gallagher et al. (2005) put a lower limit on the delay time of 2 Gyrs.

Mannucci et al. (2006) have shown that a combination of observations at high and low redshift cannot be matched by a DTD with a single delay time, but that they are best matched by a bi-modal DTD. This hypothesis is developed further by various groups (Scannapieco & Bildsten, 2005; Sullivan et al., 2006; Neill et al., 2006, 2007) who model the SN Ia rate as a two-component distribution with a delayed component dependent on the

host galaxy stellar mass and a prompt component dependent on the host galaxy star formation rate. Several authors have used this model to reproduce the observed SN Ia rates at $z \sim 1$ (Aubourg et al., 2008; Neill et al., 2007; Dahlen et al., 2004; Botticella et al., 2008), although again these results depend on the assumed SFH. In order to avoid such an assumption, Totani et al. (2008) used an SED fitting technique to determine the ages of the host galaxy stellar populations to derive a DTD which is a power-law in the range 0.1 - 10 Gyrs. From a spectroscopic study, Howell (2001) showed that sub-luminous SNe Ia tend to come from old populations whereas over-luminous SNe Ia are from young populations, suggesting different progenitor scenarios for the two populations. Furthermore, Pritchet et al. (2008) showed that the single degenerate scenario alone is not sufficient to explain the observed DTD. By studying the local environment of SNe Ia (rather than the properties of the whole of the host galaxy) Raskin et al. (2009) found that the average delay time of nearby prompt SNe was $\sim 0.3-0.5$ Gyrs, although their model allows $\sim 30\%$ of prompt SNe Ia to have delay times shorter than 0.1 Gyrs.

From a study of the X-ray properties of nearby ellipticals, Gilfanov & Bogdan (2010) suggest that the X-ray flux from these galaxies is consistent with only $\sim$5% of SNe Ia arising from accreting white dwarfs in elliptical galaxies - such systems are expected to produce X-ray emission for a significant time, whereas in the white dwarf merger (i.e. double degenerate) scenario, the X-ray emission is only present shortly before the explosion. They do not constrain the progenitors of SNe Ia in late-type galaxies where the contribution from the single degenerate scenario could be significant. Using a maximum-likelihood inversion procedure, Maoz et al. (2010) recover the DTD for a sample of local SNe Ia utilising the SFH of each individual galaxy, finding evidence for both prompt (with delay times < 0.42 Gyrs) and delayed (with delay times > 2.4 Gyrs) SNe, where the DTD has a peak at short delay times but a broad distribution to longer delay times. Similar conclusions are reached by Brandt et al. (2010).

Greggio (2010) build on the parameterisation of Greggio (2005) of the evolution of binary systems to calculate some features of the DTD of single-degenerate, double degenerate and mixed model progenitor scenarios. All models are consistent with both prompt and delayed SNe, although the distributions are continuous (suggesting that the distinction is arbitrary). They do explore scenarios where there is a mix of SD and DD and where the SD contributes more prompt SNe than the DD channel, however, they see no theoretical basis for this and comparisons to the observed SN Ia rates of Greggio & Cappellaro (2009) and Sullivan et al. (2006) do not favour the mixed scenarios.

5.1.2 GOODS Type Ia Supernovae

The Great Observatories Origins Deep Survey (GOODS; Dickinson et al., 2003) is a multi-wavelength survey covering ~ 330 arcmin^2 over two fields. In conjunction with the GOODS survey a supernova search was conducted, surveying both fields at several different epochs with HST ACS (Giavalisco et al., 2004) resulting in a catalogue of 22 SNe Ia at $z \geq 0.95$ with spectroscopic redshifts, (Riess et al., 2004, 2007). We add a further 3 SNe: 1997fg, 1997ff and 2002dd from past SN searches in these fields (Gilliland et al., 1999; Riess et al., 2001; Blakeslee et al., 2003).

In the present work, we compile optical/near-infrared photometry from ACS and NICMOS on HST, *Spitzer* $3.6-24\,\mu$m data as well as supplementary ground-based data where available for the host galaxies of these SNe Ia. We then fit the multi-wavelength photometry of the hosts to the Single Stellar Population (SSP) models of Charlot and Bruzual (priv. com.) in order to find the ages of the stellar populations in the SN host galaxies, thus allowing us to study the delay times of SNe Ia.

Furthermore, by calculating the ages of the stellar populations we can constrain the first epoch of low mass star formation (the progenitors of SNe Ia have masses $\lesssim 8\mathrm{M}_{\odot}$, see e.g. Blanc & Greggio, 2008, and references therein), i.e. the time after the Big Bang that stars must have formed in order to yield the stellar populations we find. This allows us to constrain models which suggest that only stars with $\gtrsim 10\mathrm{M}_{\odot}$ might have formed at $z \sim 6$ (Tumlinson et al., 2004).

5.2 Host Galaxy Identification

We use the supernova sample of Riess et al. (2007) with additional SNe Ia from Gilliland et al. (1999) and Blakeslee et al. (2003), giving us 25 SNe Ia at $z \geq 0.95$. We cross-matched these SNe Ia with the GOODS ACS v2.0 catalogue in both the Northern and Southern Fields using the software *topcat* (Taylor, 2003) and a cross-matching radius of $1''$. This resulted in a catalogue of 22 SNe Ia host galaxies. We then match the ACS host galaxy positions to the ground-based and IRAC positions with a radius of $0\farcs5$, after correcting the IRAC and ground-based catalogues for the well-known $0\farcs38$ offset in the GOODS North catalogues. The SN positions are also corrected for this offset where necessary. The large radius used for our initial cross-match ensures that all possible SNe Ia with detected ACS host galaxies are identified, however, it could lead to false identifications with other galaxies. Therefore we visually inspected the ACS images for each SN Ia, but all appeared to be good iden-

tifications. The three SNe with no matches are 2002dd, HST04Sas and HST04Gre. In the cases of 2002dd and HST04Sas, the host is not found in the catalogue due to confusion with nearby bright galaxies. HST04Gre appears to be a hostless SN Ia, the V-band postage stamp is shown in figure 5.1 along with the host for SN 1997ff in the same band, where the host is well identified. The co-ordinates of the SNe Ia and their host galaxies are given in Table 5.1 (SNe Ia with ambiguous host identifications are shown with only the SN coordinates given).

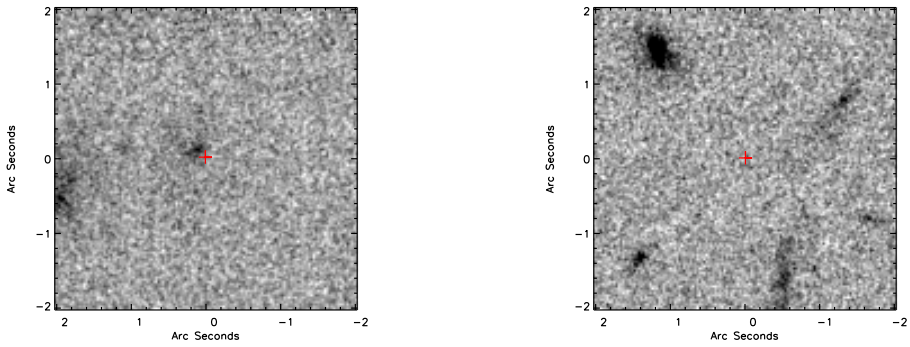

Figure 5.1: HST V band images centred around two SNe Ia, the positions of which are indicated by the red cross. The left hand panel shows the host galaxy for 1997ff is well identified whereas the right hand panel shows that the host for HST04Gre has not been identified. It is therefore removed from the sample of host galaxies which are analysed in this work.

In order to break the well-known degeneracy that exists between age and extinction in fitting model spectral energy distributions to optical/NIR photometry, we use the MIPS 24μm photometry to place constraints on the fraction of energy that is absorbed by dust and re-emitted at longer wavelengths. This results in upper limits on the amount of extinction applied to the model SED.

For each host we then have HST ACS $BViz$, *Spitzer* IRAC ch$1-4$[1] and MIPS 24μm[1] data as well as ground based[2] $UJHK$. We also have some HST NICMOS JH coverage from Buitrago et al. (2008). We reject photometry with statistical errors larger than 0.3 mag which are indicative of marginal detections. We then add a systematic error in quadrature to the photometric errors given in the catalogue of 5% for HST ACS and NICMOS (Pavlovsky et al., 2004; Thatte et al., 2009), 10% for IRAC ch$1-3$ and ground-

[1]With the exception of SNe HST04Pat, which was off the edge of the complete *Spitzer* survey, and 2002ki which had an uncertain IRAC counterpart due to confusion.

[2]Ground-based data is from the Very Large Telescope, Keck Telescope, Kitt Peak National Observatory and the Cerro Tololo Inter-American Observatory.

Table 5.1. J2000 coordinates of the SNe Ia and the offset to the host galaxies along with the spectroscopic redshift of the SNe Ia (either spectroscopy directly of the SN Ia or from spectroscopy of the host). SNe Ia where the host galaxy offset is missing have a confused or undetected host and are therefore dropped from the sample.

SN Name	SN RA	SN Dec	Host Offset [″]	redshift
1997ff	189.18379	62.21244	0.15	1.75[3]
2003es	189.23079	62.21987	0.48	0.95[1]
2003az	189.33196	62.31031	0.16	1.26[1]
2003dy	189.28817	62.19128	0.29	1.34[1]
2002ki	189.36813	62.34434	0.33	1.14[2]
HST04Pat	189.53750	62.31312	0.41	0.97[1]
HST05Fer	189.10458	62.25662	0.66	1.02[1]
HST05Koe	189.09550	62.30644	0.39	1.23[1]
HST05Red	189.25708	62.20666	0.39	1.19[3]
HST05Lan	189.23633	62.21481	0.74	1.23[2]
HST04Tha	189.22987	62.21779	0.39	0.95[1]
HST04Eag[4]	189.33705	62.22799	0.46	1.02[2]
HST05Gab	189.05763	62.20210	0.40	1.12[1]
HST05Str	189.08596	62.18072	0.05	1.01[1]
1997fg	189.24029	62.22092	0.39	0.95[3]
2003aj	53.18471	-27.91844	0.20	1.31[3]
2002fx	53.02833	-27.74289	0.26	1.40[3]
2003ak	53.19542	-27.91372	0.36	1.55[3]
2002hp	53.10329	-27.77161	0.19	1.30[3]
2002fw	53.15633	-27.77961	0.51	1.30[1]
HST04Mcg[4]	53.04250	-27.83055	0.57	1.37[2]
HST04Omb	53.10558	-27.75084	0.22	0.98[1]
HST04Sas	189.22546	62.13966	-	1.39[1]
2002dd	189.23067	62.21281	-	0.95[1]
HST04Gre	53.08954	-27.78286	-	1.14[1]

[1]Spectroscopic redshift from supernova, high confidence sample.

[2]Spectroscopic redshift from supernova and host galaxy, high confidence sample.

[3]Spectroscopic redshift from host galaxy alone, supernova considered type Ia based on photometry and/or presence within a red, Early-type host. Not part of the high confidence sample.

[4]Typographical error in the co-ordinates given in Riess et al. (2007) discovered by comparison to their postage stamps. Original co-ordinates are HST04Eag 189.33646, 62.22820; HST04Mcg 53.04175, -27.83055, corrected co-ordinates are those presented here.

based photometry and 15% for IRAC ch4 (Reach et al., 2005). We remove the southern U band data from the analysis due to inhomogeneous variations across the field.

The process of mosaicing the ACS data includes the flux from the SNe in the Riess et al. (2007) sample. We have estimated and subtracted out the SN contribution to the host galaxy photometry in the catalogue using the following process. We use the SN photometry given in Riess et al. (2004, 2007). In each band we add up the total SN flux and divide by the number of epochs of observations going into the ACS stack and subtract this from the host flux. This effect is present in the i and z bands, with a small contribution in the V-band (partly due to the SN colour and partly because the later Riess et al. (2007) SN search did not include V-band re-imaging of the GOODS fields). The B-band data was taken at an earlier time to the Viz data and is thus not affected. In several cases Riess et al. (2004) give i and z band SN photometry but not the V-band photometry. In these cases, we estimate the contribution to the $V-$band by extrapolating a simple power-law spectrum fit to the nearest two bands. In a very few cases, only $z-$band photometry is given; in these cases we fit the power-law to the observed colours of Type Ia SNe as presented in Jha et al. (2007) to measure the contribution of the SN in the $i-$band and the $V-$band. In all cases the correction to the host photometry in the V-band is small (there are only 3 cases where the correction is larger than 0.01μJy with the largest being 0.076μJy). In the i and z-bands the correction is small in most cases, the correction is larger than $\sim$ 10% of the host flux in only 4 and 5 cases respectively. In the cases of HST05Gab and 2002fw the SN contamination is very large, giving unreliable photometry in the i and z bands. Removing these bands leaves us with good photometry only in the BV, IRAC ch1 and ch2 in the case of HST05Gab and only BV and K in the case of 2002fw. Since we are unlikely to be able to constrain the host SED with only 3 or 4 bands we remove these SNe from the analysis. In the remaining cases a visual inspection further suggests that the contamination is small. Therefore, although the details of the stack process could affect the precise correction that is required, this effect is likely to be small.

The final photometry used, including the systematic errors added in quadrature is given in tables 5.2 (HST ACS, ground-based) and 5.3 (*Spitzer* IRAC and MIPS). The photometry used in the present work for the host galaxy of SN 1997ff differs from that given in Riess et al. (2001). In particular, Riess et al. (2001) give B-band photometry of 26.67 ± 0.16 mag, whereas we do not find an accurate detection for the host-galaxy in this band (the catalogue value is 28.23 ± 1.26 mag so it is removed from our analysis due to the

large error). Further investigation revealed that the host is given in Williams et al. (1996) as B-band magnitude of 29.18 with a signal-to-noise of 3.5. A similar pattern is seen in the iz bands suggesting that perhaps there is a variable Active Galactic Nucleus (AGN) in this host, although further investigation beyond the scope of this work is required to confirm this.

Table 5.2: HST ACS and ground-based photometry of the host galaxies used in the fits, the errors given include additional systematic errors (see text). All magnitudes are in AB magnitudes.

SN Name	U [mag]	B [mag]	V [mag]	i [mag]	z [mag]	J [mag]	H [mag]	K [mag]
1997ff	-	-	26.11± 0.16	25.06± 0.10	23.97± 0.06	22.59± 0.05[1]	21.60± 0.05[1]	-
2003es	-	25.86± 0.17	24.12± 0.06	22.54± 0.05	21.65± 0.05	21.11± 0.05[1]	20.44± 0.05[1]	19.66± 0.11
2003az	-	26.26± 0.17	26.74± 0.21	25.14± 0.08	24.30± 0.06	-	-	-
2003dy	23.75± 0.11	23.56± 0.06	23.49± 0.05	23.28± 0.06	22.76± 0.05	-	-	21.96± 0.24
2002ki	24.31± 0.11	24.37± 0.07	24.26± 0.06	23.88± 0.06	23.45± 0.06	-	-	21.97± 0.28
HST04Pat	22.49± 0.10	-	21.58± 0.06	20.80± 0.05	20.39± 0.05	20.24± 0.14	-	19.94± 0.14
HST05Fer	25.89± 0.17	25.97± 0.07	25.84± 0.07	25.05± 0.06	24.52± 0.06	-	-	-
HST05Koe	26.33± 0.23	-	25.02± 0.12	24.09± 0.09	23.45± 0.07	-	-	21.80± 0.28
HST05Red	24.76± 0.11	24.62± 0.06	24.61± 0.06	24.34± 0.06	24.14± 0.06	23.87± 0.05[1]	23.72± 0.05[1]	-
HST05Lan	-	26.45± 0.19	25.31± 0.07	24.25± 0.06	23.30± 0.05	22.59± 0.05[1]	21.84± 0.05[1]	-
HST04Tha	-	26.99± 0.22	25.24± 0.06	23.94± 0.05	23.04± 0.05	22.60± 0.05[1]	21.99± 0.05[1]	21.48± 0.14
HST04Eag	24.05± 0.11	23.93± 0.06	23.56± 0.06	22.91± 0.05	22.57± 0.05	21.96± 0.23	-	21.19± 0.15
HST05Gab	-	26.78± 0.19	26.76± 0.14	-	-	-	-	-
HST05Str	24.77± 0.11	24.33± 0.07	24.04± 0.06	23.50± 0.06	23.12± 0.06	-	-	-
1997fg	24.31± 0.11	23.99± 0.06	23.56± 0.06	22.90± 0.06	22.59± 0.05	22.12± 0.25	-	21.90± 0.23
2003aj	-	25.09± 0.07	24.99± 0.06	24.85± 0.07	24.23± 0.06	23.96± 0.15	-	23.67± 0.17

continued on next page

Table 5.2: *continued*

SN Name	U [mag]	B [mag]	V [mag]	i [mag]	sz [mag]	J [mag]	H [mag]	K [mag]
2002fx	-	25.59± 0.08	25.90± 0.09	25.62± 0.10	25.50± 0.09	25.28± 0.22	25.28± 0.29	24.92± 0.28
2003ak	-	23.66± 0.06	23.57± 0.06	23.39± 0.06	23.14± 0.06	22.57± 0.11	-	22.45± 0.12
2002hp	-	-	25.86± 0.11	24.04± 0.06	23.15± 0.06	21.80± 0.11	21.25± 0.11	20.71± 0.10
HST04Mcg	-	25.09± 0.11	24.54± 0.08	23.74± 0.07	23.06± 0.06	22.16± 0.11	21.63± 0.11	21.21± 0.11
HST04Omb	-	23.17± 0.05	23.16± 0.05	22.86± 0.05	22.69± 0.05	22.56± 0.11	22.85± 0.12	22.49± 0.12

[1]NICMOS photometry

Table 5.3: *Spitzer* IRAC and MIPS photometry of the host galaxies used in the fits, the errors given include additional systematic errors (see text).

SN Name	3.6 [μJy]	4.5μm [μJy]	5.8μm [μJy]	8.0μm [μJy]	24.0μm [μJy]
1997ff	30.1± 3.0	33.3± 3.3	29.4± 3.0	20.0± 3.0	27.5± 4.8
2003es	56.6± 5.7	39.3± 3.9	29.6± 3.0	20.4± 3.1	< 25
2003az	20.1± 2.0	20.3± 2.0	15.4± 1.6	10.4± 1.6	< 25
2003dy	7.6± 0.8	6.7± 0.7	5.0± 0.6	4.4± 0.7	< 25
2002ki	< 0.5	< 0.5	< 1.5	< 1.5	< 25
HST04Pat	-	-	-	-	< 25
HST05Fer	2.1± 0.2	1.3± 0.1	1.3± 0.4	-	< 25
HST05Koe	16.3± 1.6	13.2± 1.3	11.7± 1.3	8.2± 1.4	63.1± 6.6
HST05Red	2.5± 0.2	1.9± 0.2	-	1.2± 0.4	< 25
HST05Lan	21.9± 2.2	18.6± 1.9	12.2± 1.3	8.8± 1.4	< 25
HST04Tha	13.4± 1.3	9.0± 0.9	6.4± 0.7	3.4± 0.6	< 25
HST04Eag	10.3± 1.0	7.6± 0.8	5.8± 0.7	5.7± 0.9	50.9± 5.1
HST05Gab	0.6± 0.1	0.3± 0.1	< 1.5	< 1.5	< 25
HST05Str	5.4± 0.5	3.8± 0.4	2.8± 0.5	2.3± 0.6	< 25
1997fg	7.8± 0.8	5.6± 0.6	4.5± 0.5	3.7± 0.6	< 25
2003aj	1.6± 0.2	1.3± 0.1	-	< 1.5	< 25
2002fx	0.4± 0.1	0.4± 0.1	< 1.5	-	< 25

continued on next page

Table 5.3: *continued*

SN Name	3.6 [μJy]	4.5μm [μJy]	5.8μm [μJy]	8.0μm [μJy]	24.0μm [μJy]
2003ak	5.0± 0.5	5.1± 0.5	3.3± 0.5	2.2± 0.6	< 25
2002hp	35.4± 3.5	31.9± 3.2	22.2± 2.2	15.4± 2.3	< 25
HST04Mcg	20.8± 2.1	20.1± 2.0	14.7± 1.5	13.1± 2.0	59.5± 6.0
HST04Omb	4.3± 0.4	3.0± 0.3	1.8± 0.4	-	< 25

5.3 Model Fitting

We use the population synthesis models of Charlot and Bruzual (CB07, priv. com.) which are generated from an updated version of the Bruzual & Charlot (2003) GALAXEV code to produce models which include a new prescription for Thermally Pulsating AGB stars. The code calculates the spectral evolution of a stellar population based on a library of observed stellar spectra (see Bruzual & Charlot (2003) and references therein). We generated a suite of models with varying metallicity, Initial Mass Function (IMF; i.e. the distribution of stellar masses for the starburst), stellar population age and star formation history (SFH, either a constant SFR or an exponentially declining SFR with e-folding time τ). For each model we apply a dust extinction correction of varying A_V with a Calzetti et al. (2000) dust extinction law, giving a total of $\sim 5 \times 10^5$ models. Table 5.4 shows the parameter values used to generate the models. Finally, we ensure that the age of the stellar population never exceeds the age of the Universe at the redshift of the SN Ia.

Table 5.4. Input parameters used to generate the model SEDs

Parameter	Allowed Values
Metallicity	0.005, 0.020, 0.200, 0.400, 1.000, 2.500 $Z_\odot$
IMF	Salpeter: $\frac{dn}{dM} = M^{-1.35}$ $\quad 0.1M_\odot < M < 100M_\odot$
	Chabrier: $\frac{dn}{dM} = \exp(-(\log_{10}(M) - \log_{10}(0.08))^2/0.9522)$ $\quad 0.1M_\odot < M < 1M_\odot$
	$= M^{-1.3}$ $\quad 0.1M_\odot < M < 100M_\odot$
SFH	$\psi(t) = \tau^{-1}\exp(-t/\tau)$, $\quad \tau = 0.01$, 0.03, 0.1, 0.3 1 Gyrs and $\tau = \infty$ i.e. constant SFR
Stellar population age	unevenly spaced in the range 0.001 - 6 Gyrs
Dust, A_V	0 - 5 mag, step size of 0.1 mag, starburst extinction law (Calzetti et al., 2000)

Each model is then converted to the observed frame using the spectroscopic redshift of the SN Ia and convolved with the response/filter functions of the instruments in order to generate the equivalent observed photometry for each model in each band. We then calculate the χ^2 of each model compared to the data, according to the equation

$$\chi^2 = \sum \frac{(f_i^o - b f_i^m)^2}{\sigma_i^2} \tag{5.1}$$

where f^o is the observed flux in each band, f^m is the model flux in each band, σ is the observed error (including the additional systematic error), b is a normalization factor (calculated as the mean ratio of the observed flux to the model flux, weighted by the errors) and the summation is over all bands. We then find the model with the minimum χ^2 for each host galaxy.

In order to break the degeneracy between young models with large extinction and old models with low extinction we use the 24μm photometry since it is a reliable proxy for the fraction of light that is absorbed by dust and reprocessed at longer wavelengths. By using the Chary & Elbaz (2001) templates, the 24μm photometry can be translated to a total far-infrared (FIR) luminosity. This provides an upper limit to the fraction of optical/near-infrared light that is absorbed by dust. We then compare this to the FIR luminosity of each model, calculated thus

$$I = \int l_\lambda (1 - \exp(-A_V \kappa / 1.086)) \mathrm{d}\lambda \tag{5.2}$$

where l_λ is the flux of the model at each wavelength λ and κ is the extinction correction given by the extinction law of Calzetti et al. (2000). Any models which have an FIR luminosity that is in excess of the FIR luminosity calculated from the 24μm photometry/limits are rejected. We use upper limits to reject any models that exceed the photometric limit in a given band if the host is not detected in that band. The limits we use are 28.6, 28.6, 27.9, 27.4 AB mag for the ACS $BViz$ bands (5σ limits), 0.5, 0.5, 1.5, 1.5μJy for the IRAC ch1-4 and 25μJy for the MIPS 24μm data (80% completeness limits).

Each SED in the CB07 models is the combination of the SEDs from all the various stars that have formed (and evolved) over the lifetime of the model galaxy. All but one of our star-formation histories is exponential, in these cases most of the stars are formed at the redshift of formation. The final time-step from the models is the upper limit to the age of a star in the population. While most of the stars in the population are old, most of the luminosity comes from younger stars. In order to account for this we calculate a mean age weighted by the fractional contribution to the V-band luminosity from the stars of each age, i.e. a 'luminosity-weighted' age.

5.4 Results

We have found the best-fit stellar population model for each host using a minimum χ^2 technique. The set of best fitting parameters for each host along with the χ^2_ν of the fit is shown in Table 5.5. Since we have calculated the χ^2 for each model, we calculate the errors by finding those bins with $\chi^2 < \chi^2_{min} + \chi^2_{gauss}$, where χ^2_{min} is the minimum χ^2 of the fit and χ^2_{gauss} is the χ^2 value for a 68% and 95% confidence level for a normal χ^2 distribution with the same number of degrees of freedom as used in the fit (given by the number of photometric points less the number of parameters). The best-fitting SEDs along with the observed photometry used in the fit are shown in figure 5.2. It is also worth noting the effect of using the 24μm limit at this stage. Figure 5.3 is an enlarged version of the SED plot for 1997fg but also shown is the best-fitting SED found if the FIR luminosity limit is not used. The figure shows that both SEDs are reasonable fits to the data (with χ^2 of 11.1 when the limit is included and 3.6 when it is not), however by including the limit, the best-fit luminosity-weighted age changes from ~ 0.02 Gyrs to ~ 0.09 Gyrs.

Table 5.5: Best-fit parameters for each SN host (labeled by SN). Errors are calculated by finding the parameter value which raises the measured χ^2 (marginalised over all other parameters) above the 68% confidence threshold. In cases where the best-fit is at the extreme end of parameter space, or if the marginalised χ^2 never reaches larger than the threshold, no error is given (the latter only occurs for the metallicity, Z, and SFH parameter, τ, as they are not well sampled). Age, $\langle$Age$\rangle$, Z and M are the final time-step age, luminosity weighted age, metallicity and stellar mass respectively.

SN Ia	Age [Gyrs]	$\langle$Age$\rangle$ [Gyrs]	A_V[mags]	Z[Z$_\odot$]	τ[Gyrs]	IMF	χ^2	M [log$_{10}$(M$_\odot$)]
1997ff	$0.571^{+0.444}_{-0.062}$	$0.561^{+0.341}_{-0.090}$	$0.5^{+0.4}_{-0.3}$	$2.500_{-1.500}$	$0.01^{+0.09}$	salpeter	3.05	$11.06^{+0.150}_{-0.297}$
2003es	$2.300^{+0.700}_{-1.161}$	$1.999^{+0.700}_{-0.898}$	$0.3^{+4.7}_{-0.3}$	$1.000^{+1.500}_{-0.995}$	$0.30_{-0.29}$	chabrier	1.95	$10.80^{+0.330}_{-0.328}$
2003az	$4.750_{-3.316}$	$3.897^{+0.001}_{-2.763}$	$0.7^{+0.6}_{-0.1}$	$2.500_{-2.100}$	$1.00_{-0.70}$	salpeter	4.71	$11.12^{+0.301}_{-0.673}$
2003dy	$0.286^{+4.214}_{-0.172}$	$0.180^{+1.568}_{-0.102}$	$0.4^{+0.2}_{-0.4}$	$0.400^{+2.100}_{-0.395}$	$0.10_{-0.09}$	chabrier	0.65	$9.84^{+0.731}_{-0.287}$
2002ki	$0.005^{+4.995}$	$0.002^{+1.961}$	$1.6^{+3.4}_{-1.2}$	$0.005^{+2.495}$	$0.01^{+0.09}$	chabrier	3.40	$8.93^{+1.291}_{-0.070}$
HST04Pat	$0.064^{+0.017}_{-0.014}$	$0.054^{+0.017}_{-0.014}$	$1.8^{+0.2}_{-0.2}$	$0.005^{+2.495}$	$0.01^{+0.09}$	chabrier	5.22	$10.79^{+0.288}_{-0.071}$
HST05Fer	$2.500^{+3.000}_{-2.214}$	$1.708^{+0.484}_{-1.528}$	$0.0^{+0.7}$	$0.400^{+2.100}_{-0.200}$	$1.00_{-0.90}$	chabrier	1.83	$9.23^{+0.354}_{-0.381}$
HST05Koe	$0.072^{+0.089}_{-0.008}$	$0.062^{+0.062}_{-0.008}$	$1.8^{+3.2}_{-0.2}$	$2.500_{-1.500}$	$0.01^{+0.02}$	salpeter	2.02	$10.23^{+0.145}_{-0.332}$
HST05Red	$0.055^{+0.586}_{-0.023}$	$0.031^{+0.205}_{-0.009}$	$0.8^{+4.2}_{-0.4}$	$1.000^{+1.500}_{-0.995}$	$0.03_{-0.02}$	chabrier	2.55	$8.84^{+0.482}_{-0.111}$
HST05Lan	$1.700^{+0.200}_{-0.091}$	$1.400^{+0.200}_{-0.091}$	$0.3^{+0.2}_{-0.3}$	$1.000^{+1.500}_{-0.600}$	$0.30_{-0.29}$	salpeter	1.66	$10.66^{+0.043}_{-0.298}$
HST04Tha	$2.200^{+3.550}_{-1.061}$	$1.899^{+2.997}_{-0.798}$	$0.0^{+0.5}$	$1.000^{+1.500}_{-0.800}$	$0.30^{+0.70}_{-0.29}$	chabrier	2.02	$10.07^{+0.548}_{-0.275}$
HST04Eag	$5.500_{-5.436}$	$2.192^{+3.298}_{-2.138}$	$0.6^{+0.2}_{-0.3}$	$0.005^{+2.495}$	Constant SFR	salpeter	2.49	$10.48^{+0.476}_{-0.997}$
HST05Str	$0.072^{+0.072}_{-0.008}$	$0.062^{+0.045}_{-0.008}$	$0.6^{+4.4}_{-0.1}$	$2.500_{-1.500}$	$0.01^{+0.02}$	chabrier	1.53	$9.25^{+0.353}_{-0.064}$

continued on next page

Table 5.5: *continued*

SN Ia	Age [Gyrs]	⟨Age⟩ [Gyrs]	A_V[mags]	Z[$Z_\odot$]	τ[Gyrs]	IMF	χ^2	M [$\log_{10}(M_\odot)$]
1997fg	$0.102^{+2.898}_{-0.102}$	$0.092^{+2.088}_{-0.092}$	$0.4^{+0.1}_{-0.3}$	$2.500_{-2.495}$	$0.01^{+0.99}$	chabrier	1.86	$9.43^{+0.860}_{-0.086}$
2003aj	$0.161^{+4.339}_{-0.108}$	$0.124^{+1.624}_{-0.082}$	$0.1^{+0.9}_{-0.1}$	$1.000^{+1.500}_{-0.995}$	$0.03_{-0.02}$	salpeter	0.77	$9.25^{+0.611}_{-0.335}$
2002fx	$2.750^{+1.500}_{-2.746}$	$1.225^{+0.419}_{-1.224}$	$0.0^{+1.2}$	$0.005^{+2.495}$	Constant SFR	chabrier	1.63	$8.94^{+0.373}_{-0.875}$
2003ak	$0.128^{+0.127}_{-0.078}$	$0.118^{+0.035}_{-0.078}$	$0.0^{+0.6}$	$1.000^{+1.500}_{-0.995}$	$0.01^{+0.09}$	chabrier	0.53	$9.70^{+0.435}_{-0.160}$
2002hp	$1.700^{+2.800}_{-0.795}$	$1.587^{+2.903}_{-0.720}$	$0.3^{+0.5}_{-0.3}$	$1.000^{+1.500}_{-0.800}$	$0.10^{+0.20}_{-0.09}$	salpeter	0.45	$11.00^{+0.379}_{-0.459}$
HST04Mcg	$0.128^{+3.122}_{-0.047}$	$0.118^{+2.300}_{-0.047}$	$1.5^{+0.1}_{-1.5}$	$1.000^{+1.500}_{-0.995}$	$0.01^{+0.99}$	salpeter	0.56	$10.61^{+0.508}_{-0.372}$
HST04Omb	$0.203^{+0.516}_{-0.153}$	$0.108^{+0.158}_{-0.068}$	$0.0^{+0.2}$	$1.000^{+1.500}_{-0.600}$	$0.10_{-0.09}$	chabrier	1.27	$9.14^{+0.345}_{-0.157}$

Since we are only fitting one population to the photometry of the host galaxies it is possible that the SN Ia progenitors were born in a more recent starburst which only contributes a fraction to the total emission of the galaxy which is dominated by an older population. In this case we would overestimate the ages as we would fit to the dominant, older population but the SN Ia in fact comes from a younger population. In order to test this possibility we perform a two-component fit. We use the best-fitting parameters for metallicity, SFH and IMF and take a model which is as old as the universe at the host redshift and a model which is 10 Myrs old. We then add the two models together allowing the fractional contribution from the young population to vary between 0 - 1 in steps of 0.1. We also allow the extinction to vary and to be different in the two populations. In all cases the resulting fit is worse than the original best-fit using only one population. This suggests that our assumption that the SNe Ia most likely come from the one population model we are fitting is valid.

We also assessed the Charlot & Fall (2000) prescription for the dust extinction. We find that the ages using the Charlot & Fall (2000) recipe differ from those using the Calzetti et al. (2000) recipe by more than a factor of 2, in only 3 cases. In two of these cases these ages are larger than those using the Calzetti et al. (2000) recipe, however, in all 3 cases the χ^2 of the best-fit is lower using a Calzetti et al. (2000) recipe compared to the Charlot & Fall (2000) recipe. We conclude that our derived ages are robust with respect to the fitting technique.

Figure 5.4 shows contour plots of the χ^2 distribution in the luminosity-weighted age - A_V plane for the SNe host galaxies, showing 68% and 95% confidence intervals. The figure shows that in some cases there is a fairly smooth distribution of the degeneracy between the luminosity-weighted age of the stellar population and the dust extinction, in that good fits can be achieved with younger populations with a higher dust extinction, as expected. This degeneracy remains despite our removing any models which give a FIR luminosity that is inconsistent with the MIPS 24μm data, although it is much reduced. Many panels of figure 5.4, however, do not show a smooth distribution. While they generally show the same degeneracy, it is clear that the age parameter is not sampled sufficiently, in particular at older ages, to give a smooth distribution. Unfortunately, we are unable to alter the ages of the output of the stellar population models. However, the uncertainties in table 5.5 and figures 5.6 and 5.10 spans the entire range of ages that give consistent fits.

Figure 5.5 shows the luminosity weighted stellar population ages of the host galaxies. This age is plotted for each SN Ia host with the reduced χ^2 ($\chi^2_\nu = \chi^2/\nu$, where ν is the

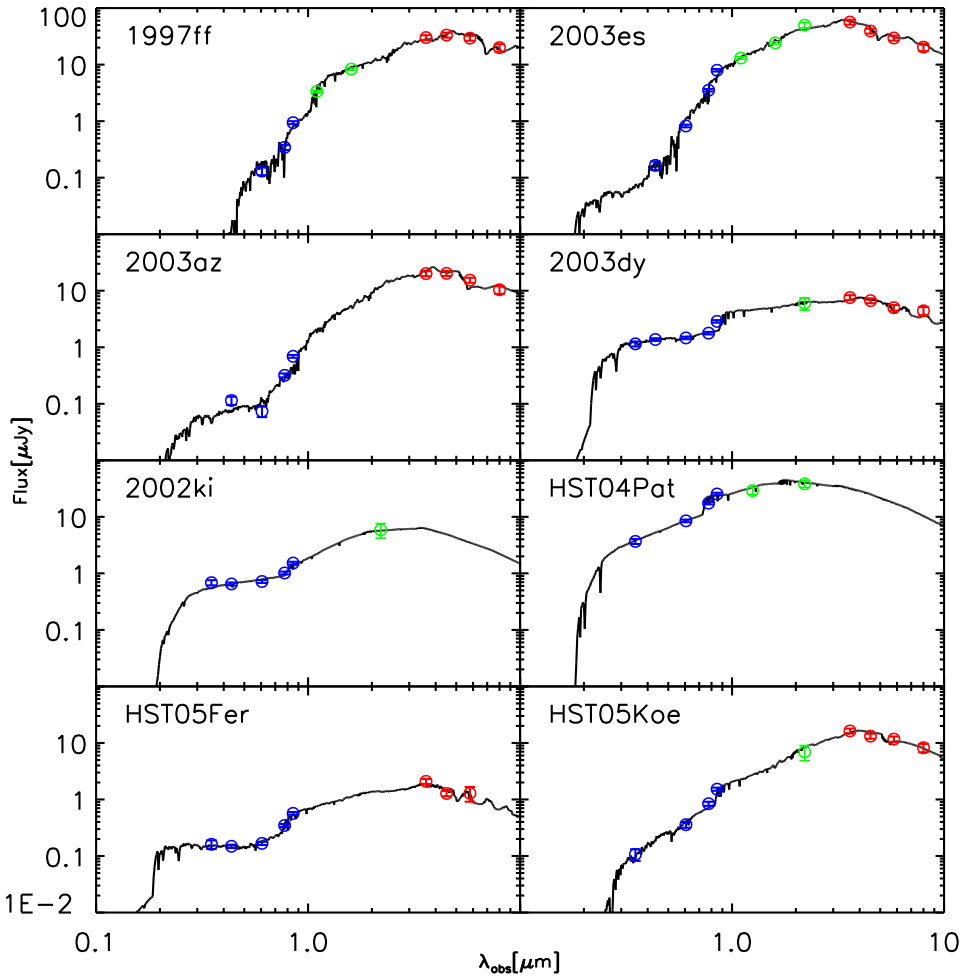

Figure 5.2: SED plots for the best fit model for the SNe host galaxies, blue points are optical data, green points are near-infrared and red points are IRAC ch1 − 4.

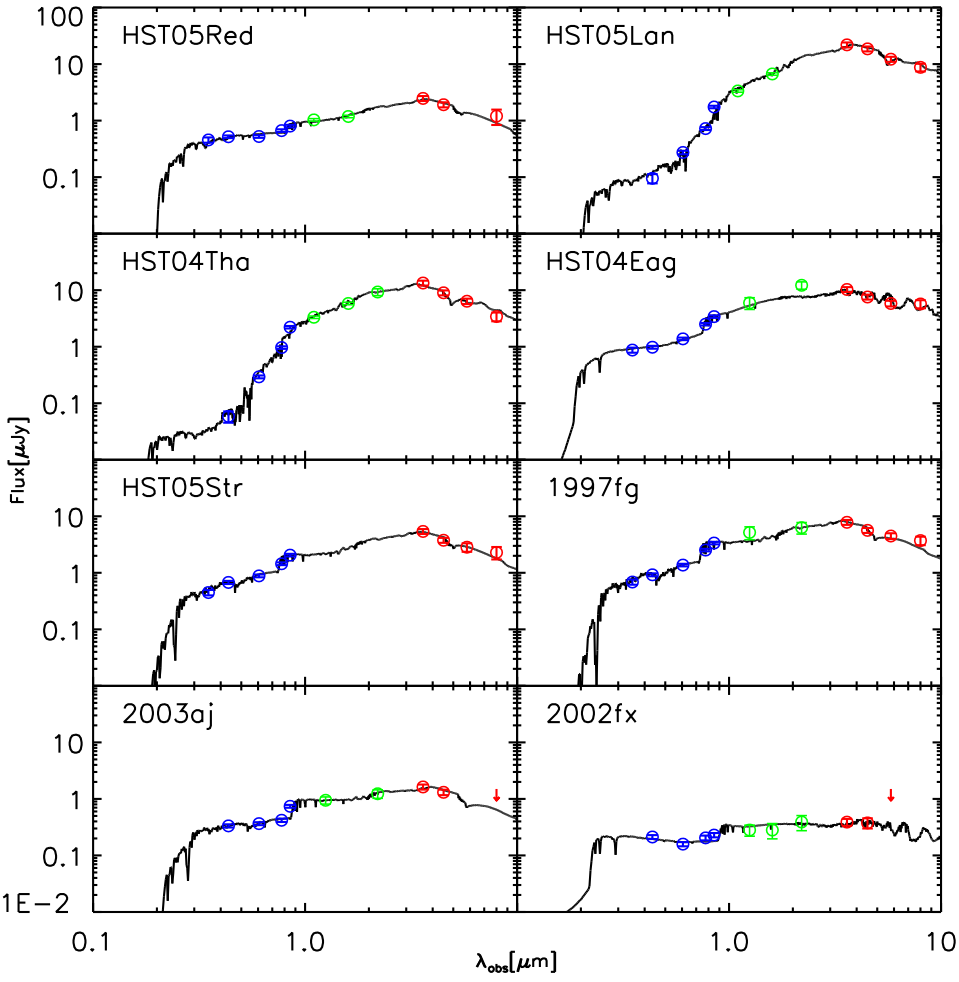

figure 5.2 continued

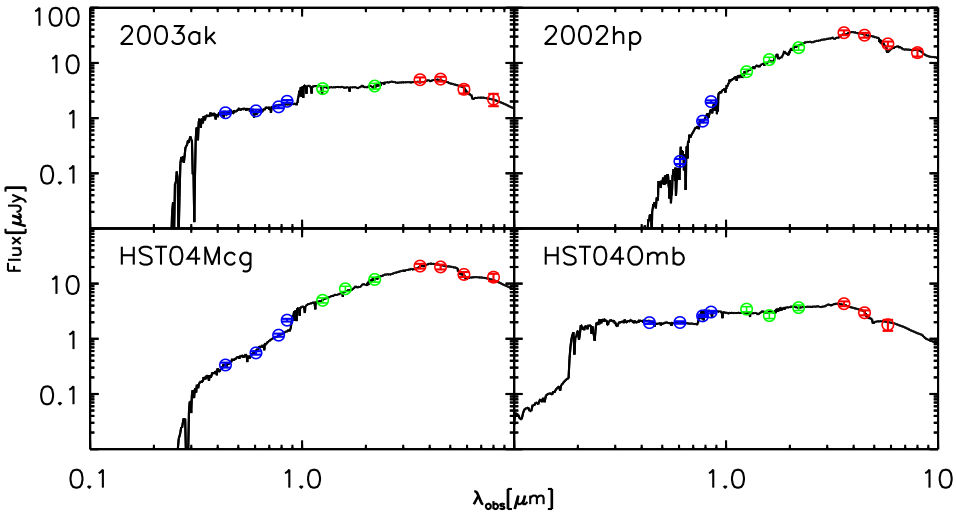

figure 5.2 continued

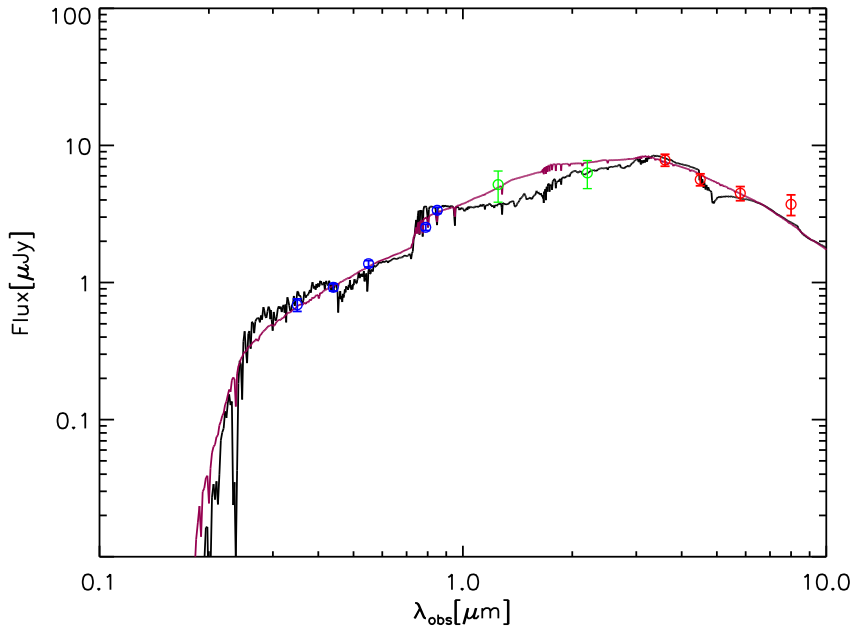

Figure 5.3: SED plot for the best fit model for the host galaxy of SN Ia 1997fg, blue points are optical data, green points are near infrared and red points are IRAC ch1 – 4. The black line shows the best-fit model SED, the magenta line shows the best-fit model SED when the FIR luminosity limit is not included. The best-fit luminosity-weighted age, A_V combination changes from (0.02 Gyr, 2.1 mag) to (0.09 Gyr, 0.4 mag) when the limit is included.

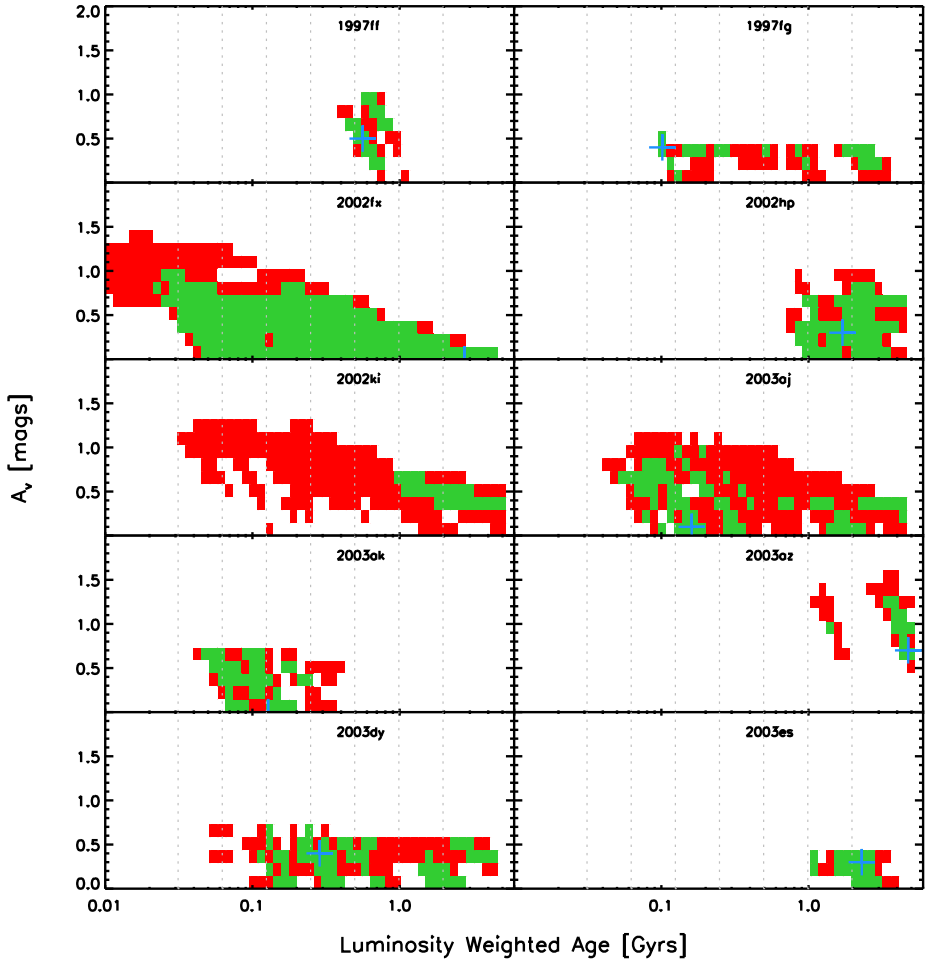

Figure 5.4: Contour plots of the χ^2 distribution for the SNe Ia host galaxies. The contours were calculated by collapsing over the remaining axes, i.e. for a fixed pair of luminosity-weighted age-A_V values the minimum χ^2 allowing all other parameters to vary was found. This was then binned together. The green area is the 68% confidence level and the red area is the 95% confidence level. The confidence levels were found by finding those bins with $\chi^2 < \chi^2_{min} + \chi^2_{gauss}$, where χ^2_{min} is the minimum χ^2 across the whole parameter range (i.e. the χ^2 of the best-fit) and χ^2_{gauss} is the χ^2 value which gives the 68% or 95% confidence level for a normal χ^2 distribution with the same number of degrees of freedom as used in the fit. The blue cross gives the position of the best fit. Note however that the best fit luminosity weighted age of the host galaxy of 2002ki is off the end of the plot, with an age of 0.005Gyrs. This is not shown for clarity with the remainder of the host galaxies, 2002ki is in any case removed from the sample due to the large errors. Also note that 5Myrs is an unrealistically short lifetime. The grey dotted lines show the position of the bins used in figure 5.7.

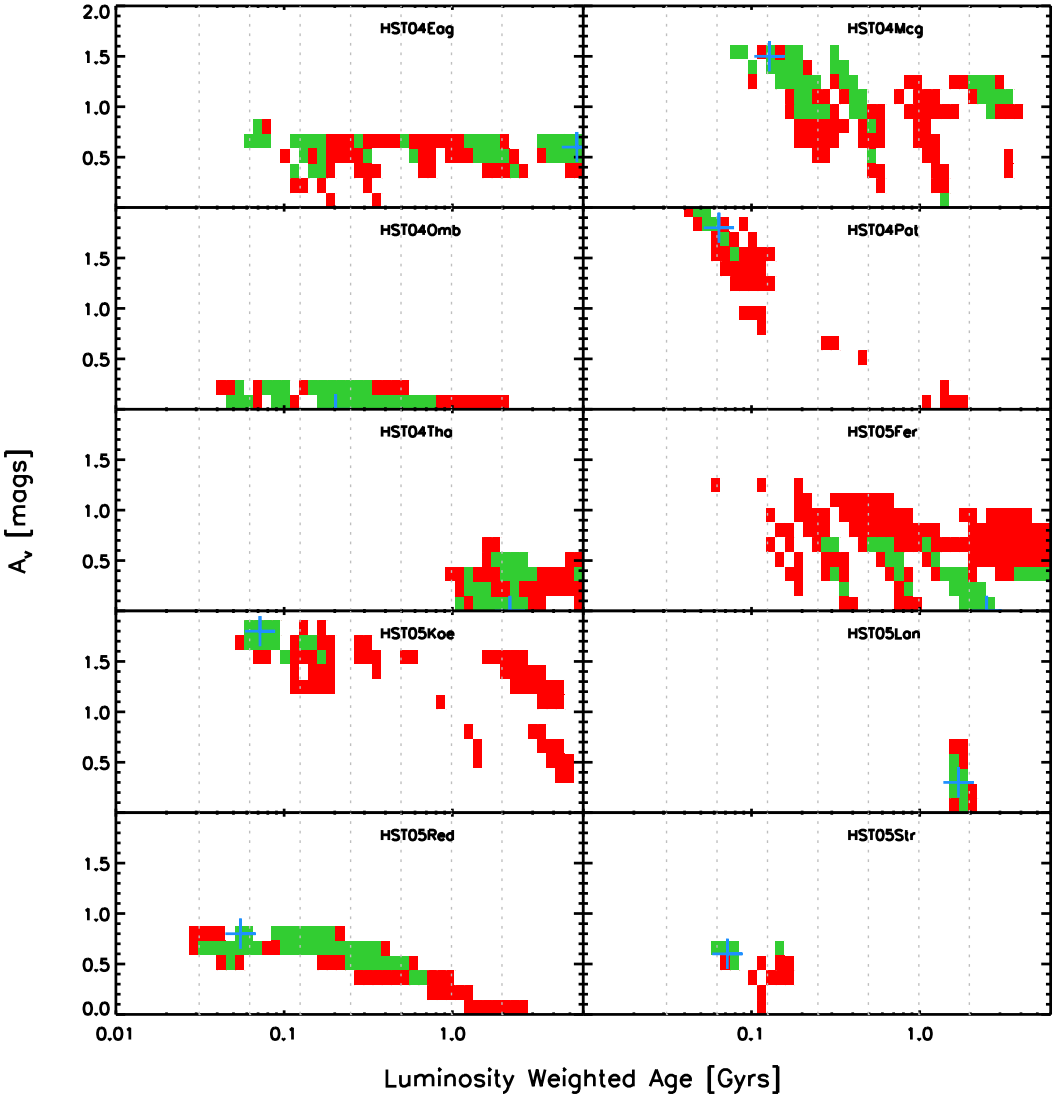

figure 5.4 continued

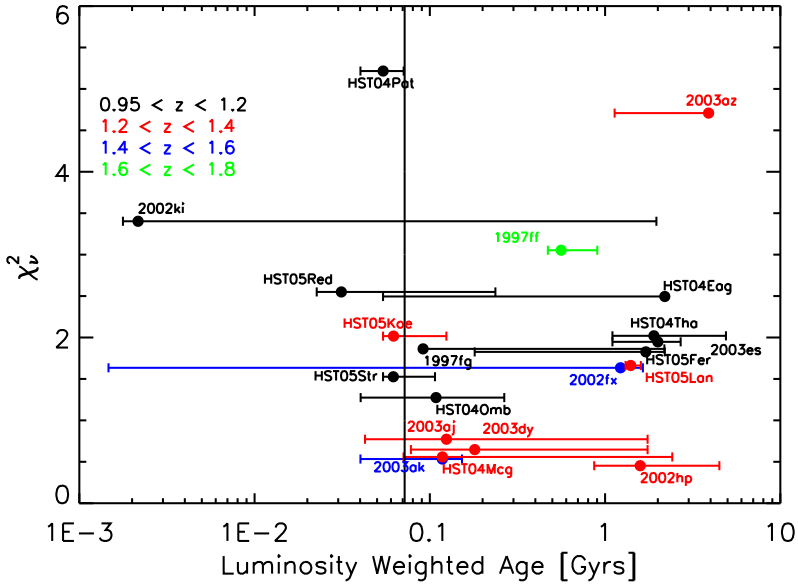

Figure 5.5: The plot shows the luminosity-weighted ages of the stellar populations in the hosts with the associated χ^2_ν. There are some SNe Ia which originate from very young hosts (< 0.1Gyr). The vertical line is the weighted mean age of 0.07 Gyrs.

number of degrees of freedom) of the best-fit model. The error bars are calculated from the grid of χ^2, whereby we find the luminosity-weighted age at which the χ^2 rises above the 68% confidence level, collapsing over all other parameters. The plot shows that there are two hosts with exceptionally large error bars, namely the host galaxies of 2002fx and 2002ki. In the latter case this is most likely due to the lack of IRAC photometry, in the former case this is most likely due to large photometric uncertainties. In any case we remove these hosts from the analysis (including the calculations based on this plot). The plot shows a large range of luminosity weighted ages from 0.03 - 3.90 Gyrs, with both prompt and delayed SNe Ia. As we wish to constrain the maximum delay time, we show the plot again but when the upper-age limit (i.e. the final time-step of the CB07 models) rather than the luminosity-weighted mean age is used in figure 5.6. The plot shows that the young ages remain.

The distribution of the best-fit luminosity-weighted stellar population ages are shown in figure 5.7. The black solid line represents all SNe and includes 'Silver' SNe and 'Gold' SNe without spectra. The red dashed line gives the histogram when only high confidence SNe Ia are included, these are SNe which are classed as 'Gold' in Riess et al. (2007) and also have good spectra of the SNe. 'Bronze' SNe are not included in any of this analysis. The figure suggests a bi-modal distribution with median ages of 0.11 and 1.9 Gyrs for the

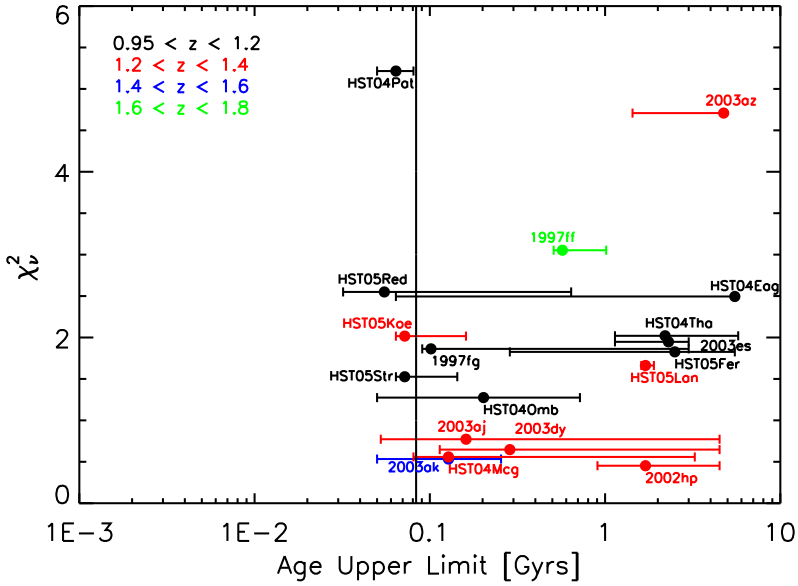

Figure 5.6: The plot shows figure 5.5 but when using the age upper-limits rather than luminosity-weighted ages. The vertical line is the weighted mean age of 0.08 Gyrs.

two populations (both the whole sample and when only considering the high-confidence SNe Ia). We arbitrarily consider a host luminosity-weighted age < 0.4 Gyrs to be young, as this is the minimum in the distribution and since there is no precise definition in the literature.

We perform a KS-test to determine whether a bi-modal distribution is a good description of the data. Comparing to a distribution comprised of two gaussian distributions centered at the young and old median ages (allowing the standard deviation of each gaussian and the ratio between their amplitudes to vary) gives a KS-statistic of 0.99 for the high confidence SNe Ia and 0.97 for the whole sample.

Due to the large error bars for the ages of the stellar populations we perform a monte carlo simulation to test the strength of any bi-modality. For each simulation, we calculate an age for each SN from the probability distribution calculated from the χ^2 distribution of the error bars shown in figure 5.5. We then repeat the KS-test. We perform this simulation 1000 times. We find that a bi-modal distribution as compared to a single gaussian distribution or a constant distribution is preferred 95% and 97% of the time for the whole sample and for the high confidence sample respectively. Finally, we use the simulation to test the existence of prompt SNe given the large error bars of figure 5.5. The mean number of young hosts in the simulation is 9.5 ± 0.05 and of old hosts is 10.5 ± 0.05 for the full sample. When considering only the high confidence SNe Ia the average number

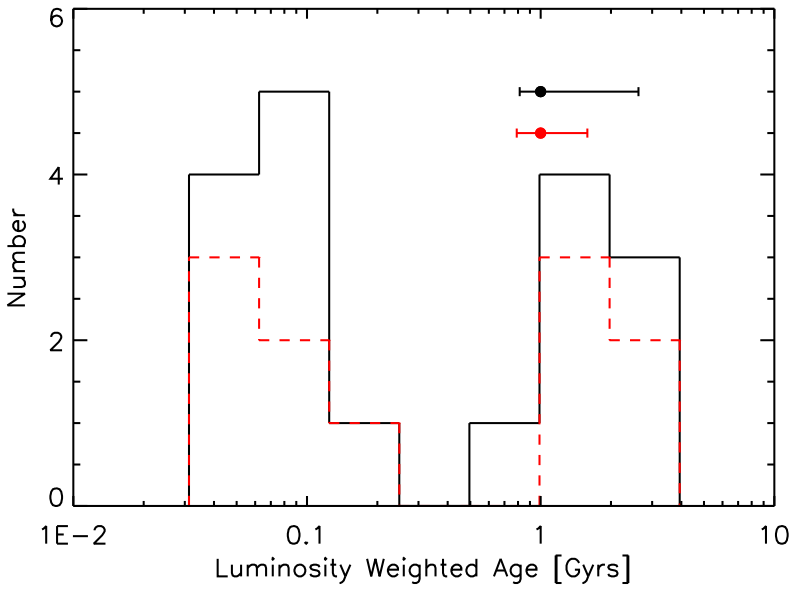

Figure 5.7: A histogram of the luminosity weighted ages of the stellar populations in $z \geq 0.95$ Type Ia SN host galaxies. The ages appear to show a bi-modal distribution with the younger population having a median age of 0.11 Gyrs and the older population having a median age of 1.9 Gyrs. The black solid line shows the distribution for all SNe and the red dashed line shows the distribution when only high confidence SNe Ia are included. The red and black points show the median error bars of the two samples.

of young and old hosts is 4.6 ± 0.03 and 6.4 ± 0.03. These results suggest that we can be fairly confident of the existence of prompt SNe at $z \gtrsim 1$. We see a slight preference for a bi-modal delay time distribution, but this is not highly significant.

Finally, we wish to calculate the delay time distribution (DTD). In order to do this we must account for the selection efficiency of the supernova search. Typically, this is achieved in the form of a 'control time' calculation (which is the total time that a SN could have been detected). We use the control time calculation for this SN search of Dahlen et al. (2008) as an estimate of the probability of detecting a supernova as a function of redshift. Dahlen et al. (2008) give supernova rates and the number of supernovae in four redshift bins between 0.2 and 1.8. We use the three highest redshift bins to interpolate the control time at each of the redshifts of our SNe using the equation

$$R = \frac{N}{t_c \Delta V} \tag{5.3}$$

where R is the SN Ia rate, N is the number of SNe observed in a redshift bin, t_c is the control time and ΔV is the volume of the redshift bin (Strolger et al., 2010). We then divide the best-fit luminosity-weighted stellar population ages by this control time. In order to calculate the DTD we then calculate a histogram of this distribution and divide the histogram by the equivalent distribution of a sample of the field population in the GOODS survey with spectroscopic redshifts and $z \geq 0.95$. The field sample we use consists of 1507 galaxies across the northern and southern fields (R. Chary, priv. com.). Figure 5.8 shows a histogram of the best-fit luminosity-weighted ages of the field sample and figure 5.9 shows the resulting DTD. We again perform a monte carlo simulation of the distribution of the DTD. We find that a bi-modal distribution is preferred 80% of the time for the whole sample and 74% of the time when considering only the high confidence SNe Ia. For the whole sample an exponential distribution is preferred 11% of the time and a single gaussian distribution 8.7%. For the high-confidence sample a single gaussian is prefered in 14% of the simulations and an exponential distribution 7% of the time. In figure 5.9 we also plot the DTD obtained by Totani et al. (2008). For most bins the two measurements are consistent, however, between 0.4 and 2 Gyrs the Totani et al. (2008) result has a larger SN rate than that found here and their results do not appear to be bi-modal. The Totani et al. (2008) result was obtained over a lower redshift window, extending between $0.4 < z < 1.2$ and it is possible the difference reflects a change in the dominant SN Ia progenitor.

Since SNe Ia are believed to be the explosions of White Dwarfs (WD) which have reached the Chandrasekhar mass, the stars eventually giving rise to these explosions are

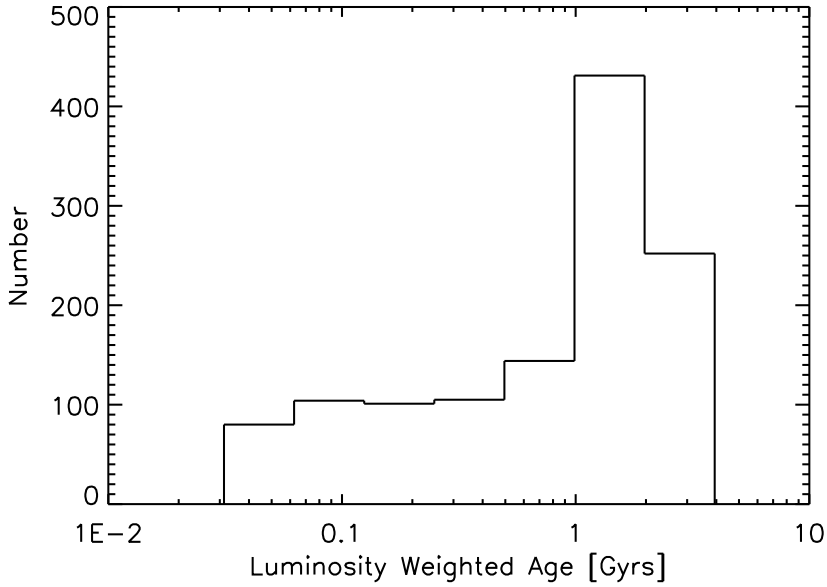

Figure 5.8: Histogram of the luminosity weighted ages of the field sample used in the DTD calculation.

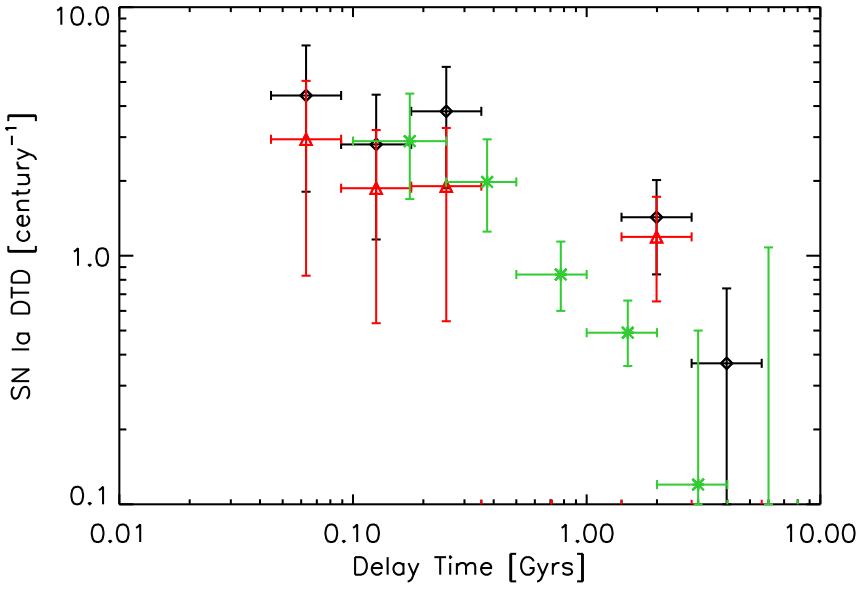

Figure 5.9: Type Ia Supernova Delay Time Distribution (DTD) for $z \gtrsim 1$ SNe. The black points are that obtained for the whole sample, the red points are that obtained for the high confidence SNe only. Also shown is the DTD obtained by Totani et al. (2008) in green.

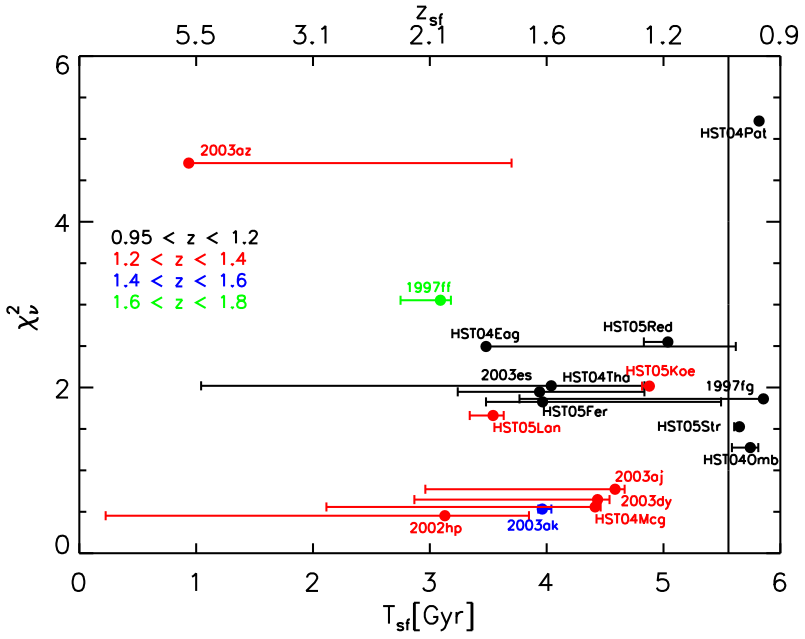

Figure 5.10: The plot shows the first epoch of low mass star formation for each host with the associated χ^2_ν. The vertical line is the weighted mean epoch of low mass star formation of 5.6 Gyrs. The $\lesssim 8 M_\odot$ progenitor stars of SNe Ia are certainly in place by $z \sim 2$ and possibly by $z \sim 5$.

low mass stars. A star of $\gtrsim 8\, M_\odot$ will explode as a core-collapse supernova instead of forming a WD (Blanc & Greggio, 2008). Therefore, with the ages of the underlying stellar populations which produce the SNe Ia we can constrain the first epoch of low mass star formation, T_{sf}

$$T_{sf} = T_z - T_{stellar} \tag{5.4}$$

where T_z is the age of the universe at the redshift of the host galaxy and $T_{stellar}$ is the best-fit luminosity-weighted stellar population age. T_{sf} is the time since the Big Bang when the stellar population formed. The results are shown in figure 5.10 where the error bars are calculated as above. The figure suggests that $\lesssim 8 M_\odot$ stars formed within 3 Gyrs of the Big Bang and possibly by $z \sim 5$. If these results are confirmed they are in contrast to the proposal by Tumlinson et al. (2004) who suggest that instead of requiring the first stars to be very massive stars ($M > 140 M_\odot$) the primordial IMF may be truncated at $\sim 10 - 20 M_\odot$ at $z \gtrsim 6$. This suggestion was primarily based on the Fe-peak and $r-$process elemental abundance patterns of extremely metal poor stars in the Galactic halo.

5.5 Discussion

We have utilised the multi-wavelength spectral energy distribution of the host galaxies of Type Ia SNe at $z \gtrsim 1$ to identify a possible bi-modal distribution of luminosity-weighted stellar ages and thereby delay times between the burst of star-formation and the time at which the SN explodes. We find evidence for both prompt (i.e. short delay times, $\lesssim 0.4$ Gyrs) and delayed (i.e. long delay times) SNe Ia, with some extremely young ($\lesssim 0.1$Gyrs) luminosity weighted ages. We discuss our results in the context of past measurements at low and high redshift.

5.5.1 Low Redshift

In the low redshift universe there is evidence for both prompt and delayed SNe Ia. Aubourg et al. (2008) find significant evidence for a population of SNe Ia with progenitor lifetimes of <0.18 Gyrs. Mannucci et al. (2005) find that SNe Ia are more common in blue rather than red galaxies and Della Valle et al. (2005) find that the SN Ia rate is 4 times higher in radio-loud rather than radio-quiet galaxies, suggesting that SNe Ia are associated with younger stellar populations and therefore shorter delay times. Schawinski (2009) fit SDSS and GALEX photometry of the host galaxies of 21 local SNe Ia in early type galaxies to a two-component Stellar Population model, with an old component (of age varying 1 - 15 Gyrs) to represent the older, underlying population and a young starburst component with varying age and mass fraction. They find no SNe Ia with delay times < 0.1 Gyrs, and a range of minimum delay times of 0.275 - 1.25 Gyrs. This is perhaps to be expected as only SNe Ia in early type galaxies are studied. Furthermore, measurements of the SN Ia rate at different redshifts have suggested that the delayed SNe Ia give a more significant contribution to the total rate at low redshift (Sullivan et al., 2006; Neill et al., 2006, 2007).

Gallagher et al. (2005) perform a spectroscopic study of the host galaxies of 57 local SNe Ia to deduce the SFR and SFH of the host galaxy. By measuring the Scalo-b parameter they see evidence for a bi-modal distribution which further suggests two progenitor classes for the SNe. However, they put a lower limit on the delay time of 2 Gyrs. It is hard to see how to reconcile these two results, although again these are local galaxies when we would expect more delayed SNe than prompt SNe.

Neill et al. (2009) perform an SED fitting analysis of UV and optical photometry of the host galaxies of a sample of local SNe Ia. They confirm the results of Sullivan et al. (2006) who showed that brighter SNe occur in galaxies with higher specific SFR. Gallagher et al. (2008) obtained optical spectra for the host galaxies of 29 SNe Ia selected to be local

early type galaxies. From comparisons to stellar population synthesis models they find a correlation between age or metallicity with peak SN Ia $V-$band absolute magnitude, preferring a trend with age (based on the trend of SN Ia rate with specific SFR) such that SNe Ia from older populations are fainter. Howell et al. (2009) find a very weak correlation between luminosity-weighted age of the host and ^{56}Ni mass derived from the integrated luminosity of the SN also suggesting that older, low mass progenitors produce fainter SNe Ia.

5.5.2 High Redshift

Many authors have attempted to constrain the delay time distribution (DTD) of SNe Ia by comparing the observed SN Ia rate to that predicted by a convolution of the DTD with an assumed SFH, (Gal-Yam & Maoz, 2004; Strolger et al., 2004; Dahlen et al., 2004; Barris & Tonry, 2006; Dahlen et al., 2008; Strolger et al., 2010). These studies have argued for a range of characteristic delay times, spanning 1 - 4 Gyrs.

This seems at odds with our results which show a large proportion of SNe Ia with delay times < 0.1 Gyrs. Indeed, the Strolger et al. (2004, 2010) result, finding a characteristic delay time of $3-4$ Gyrs, is based on an analysis of the same set of SNe used in the present work. Dahlen et al. (2004, 2008) use the models of Strolger et al. (2004) with a measurement of the GOODS SN Ia rate to show that the best fit DTD is a Gaussian with a mean delay time of 3.4 Gyrs. However, Förster et al. (2006); Blanc & Greggio (2008) have shown that the results of such analyses are strongly dependent on the assumed SFH, introducing systematic errors, and as such our results are not necessarily at odds with those authors. Results from Oda et al. (2008), who attempt to fit both the SFH and DTD simultaneously, are only able to put weak constraints on the DTD. Furthermore, Poznanski et al. (2007) measure the SN Ia rate at a similar redshift range using a dataset from the Subaru Deep Field and find a more constant rate which could suggest shorter delay times. In a companion paper to Gal-Yam & Maoz (2004), Maoz & Gal-Yam (2004) show that iron abundances in clusters require delay times of < 2 Gyrs.

These seemingly contradictory results, with evidence for both prompt and delayed SNe Ia at high and low redshift have led to the suggestion of a two-component DTD (Mannucci et al., 2005). For example, Mannucci et al. (2006) use several datasets to show that the observations cannot be simultaneously matched by a single delay-time. Several authors have developed this further, suggesting a model with a prompt component dependent on the specific SFR (SFR per unit stellar mass) of the host galaxy and a delayed

component dependent on the stellar mass of the host galaxy (Scannapieco & Bildsten, 2005; Sullivan et al., 2006; Neill et al., 2006, 2007; Aubourg et al., 2008). These DTDs are then matched to the observed SN Ia rate to fit the model parameters, tending to find a best-fit DTD dominated by the prompt component, especially at high-redshift. Furthermore, in many of these models the contribution of the prompt component is expected to increase with redshift (Sullivan et al., 2006). The average SN Ia light curve width appears to increase with redshift, supporting these models (prompt SNe Ia are more luminous and have a broader light curve Howell et al., 2007; Sullivan et al., 2009). However, some studies have shown that SN Ia rate measurements are unable to differentiate between DTD models to any significance (Neill et al., 2006, 2007; Blanc & Greggio, 2008; Botticella et al., 2008; Oda et al., 2008) and that these results are still highly dependent on the choice of SFH. Kuznetsova et al. (2008) re-computed the results of Dahlen et al. (2004) using a more sophisticated technique and additional data to find that they could not discriminate between a two-component model and a gaussian single delay time DTD.

Totani et al. (2008) perform an analysis similar to that presented here using SN Ia host galaxies in the Subaru/XMM-Newton Deep Survey (SXDS) in the redshift range $0.4-1.2$. They find a DTD in the range $0.1-8$ Gyrs (extending to 10 Gyrs from the SN Ia rate in local ellipticals). This analysis selects old, passively evolving galaxies and therefore does not probe the shortest delay times. However, they do not find a bi-modal distribution as we find here.

There are a number of implications of this result for cosmological studies. That there is a large population of SNe Ia which have short delay times means that these objects could be used as cosmological probes to very high redshift ($z \gtrsim 3$). Furthermore, if prompt and delayed SNe Ia have different light-curve shape/luminosity relations the host galaxy will need to be taken into account when using SNe Ia to determine the equation of state parameter of dark energy, w, especially when considering possible evolution of this parameter. Using a large dataset of SNe Ia spanning a wide redshift range Sullivan et al. (2010) showed that SN Ia light-curve widths depend on host galaxy specific star formation rate (SSFR) and stellar mass, with narrow light curve SNe Ia found preferentially in lower SSFR and/or more massive host galaxies. Such effects must be accounted for when using SNe Ia as cosmological probes; for example, Sullivan et al. (2010) suggests the inclusion of an additional parameter in cosmological analyses to remove the host dependence.

5.5.3 IMF Evolution

By comparing the luminosity-weighted ages of the stellar population in the host galaxies with the age of the Universe at the redshift of the SNe, we can identify the first epoch at which star-formation occurred in the host galaxies. This provides an upper limit to the formation of stars which might be the progenitors of the Type Ia SNe. Since it is generally thought that $\lesssim 8\,M_\odot$ stars are the progenitors of Type Ia SNe we have used the host galaxy SED analysis to show that these low mass stars were in place 3 Gyrs after the Big Bang and possibly as early as $z \sim 5$ albeit with significant uncertainties that are related to the uncertainties associated with measuring stellar population ages (Figure 5.10). Tumlinson et al. (2004) argue that the nucleosynthesis yields as estimated from the metal abundances in halo stars and the electron scattering optical depths from the cosmic microwave background are well matched by requiring an IMF at $z \sim 6$ which is truncated at $10 - 20\ M_\odot$ rather than the requirement that the first stars are very massive ($> 140 M_\odot$). However, if our results are confirmed and low mass stars are found at redshifts as high as 5, this would rule out such a truncated IMF.

Chapter 6

Conclusion

In this thesis we have made extensive use of large area, infrared galaxy surveys to explore several aspects of galaxy evolution. In the first instance we were particularly interested in the role that environment plays in galaxy evolution. This phenomenon is well demonstrated in the literature, especially at low redshift, and as such we conducted a high-redshift cluster search. However, we find that environment does not seem to affect the objects in our selection. This work was based on the SWIRE/DXS survey. We then assessed the possibility of using the AKARI all-sky survey to extend this work in both survey area and wavelength range. However, we found that the survey sensitivity is no greater than that of IRAS (although it has much improved spatial resolution). We have also used the large scale SWIRE survey to identify a sample of extreme objects for which we undertook further observations. Finally, we study the local environment of SNe Ia . We calculate the delay time distribution of these objects from the ages of the stellar populations in which they reside. We now go through the conclusions from each chapter in turn.

6.1 High Redshift Cluster Candidates

We have identified a list of 118 clusters at a redshift of ~ 1.0 and 40 clusters at a redshift of ~ 1.5 with 95% and 55% reliability respectively, giving reliability corrected number densities of 11.7 and 2.3 clusters per square degree. These clusters have been identified over a large area ~ 9.6 sq. degs. in the SWIRE/DXS surveys using the 1.6μm spectral bump feature to select galaxies in two redshift ranges. We calculate the reliability using simulations and an analysis of the selection function. We use the 3.6μm flux to calculate the stellar mass of both cluster and field bump selected galaxies. We are complete for masses $> 10^{11}\mathrm{M}_{\odot}$ due to a conservative K-band limit on the DXS data due to uncertain

completeness calculations. Above this mass we find that there is no difference between the mass of bump-selected galaxies as a function of environment. Similarly, the ratio of the *Spitzer* MIPS 24μm to IRAC 3.6μm flux (a proxy for specific star formation rate) shows no difference between cluster and field environments. If confirmed this would mean that galaxies which show a bump build up their stellar mass independent of environment. Furthermore, such galaxies exhibit star formation which is not affected by environment. This conclusion is subject to several caveats, not least that the calculation of mass is extremely uncertain. Furthermore, our conservative cluster identification could mean that the field mass function is being diluted by objects in group environments. Finally, these results could suggest that the bumps-selection selects galaxies that are strongly clustered, i.e. galaxies that reside within high density environments, thus we do not see the field mass function in our sample.

6.1.1 Future Work

To be confident in our cluster sample we need spectroscopic follow-up to confirm the redshifts of the cluster galaxies, such as from a targeted study of a subsample of the bumps cluster candidates. This would also allow more accurate mass and star-formation rate determinations of the cluster galaxies to confirm our results that suggest specific star-formation is independent of environment at $z \sim 1$. A further spectroscopic program observing the field would allow a more accurate comparison between the field and cluster environments. In addition, X-ray observations of the cluster candidates would be interesting. This would allow an estimation of the cluster mass; we have given an attempt to measure the cluster stellar mass, but this accounts for only $\sim 2-5\%$ of the total mass (including dark matter) of the cluster (see e.g. Rosati et al., 2002, and references therein). This would allow us to explore whether this lack of variation with environment persists. Confirmation of the Bump-2 clusters would allow us to study the star-formation in different environments at $z \sim 1.5$. Previous work based on individual clusters has suggested that at this redshift clusters harbour a greater fraction of star-forming galaxies (Hilton et al., 2010; Tran et al., 2010). With our Bump-2 cluster sample we would be able to greatly increase the sample size.

It would also be interesting to extend the cluster sample to a wider area. The DXS survey currently only covers $\sim$ 10 sq. degs. of the $\sim$50 sq. deg. SWIRE survey. K-band observations of the full SWIRE area would produce a significantly larger cluster sample. Part of this will be achieved in future releases of the DXS survey data which will

eventually cover $\sim$ 35 sq. degs., along with the VISTA Deep Extragalactic Observations Survey (VIDEO).

Finally, it would be interesting to push the Bump-3 detection further. Previous authors have shown that the Bump-3 selection can produce high-redshift samples when additional constraints are included. For example, Farrah et al. (2008) include an additional constraint on the 24μm flux since at the Bump-3 redshift the rest-frame 7.7μm PAH feature appears in this band. This does, however, restrict the selection primarily to ULIRGs. Perhaps including this constraint along with a calculation of the 24μm selection function would allow detection of galaxy over-densities at $z \sim 2.5$, although the selection would be biased towards star-forming galaxies. Alternatively, a spectroscopic redshift program of our Bump-3 selected objects, expanding on those obtained by Berta et al. (2007); Farrah et al. (2008), would show whether it is the RR08 photo-z's that are incorrect rather than the Bumps selection.

6.2 Completeness and Reliability of the AKARI All-Sky Survey

We have calculated the completeness and reliability of the AKARI all-sky survey. We calculate completeness from injection of synthetic sources into the data-stream and we calculate reliability from comparisons to the deep 70μm *Spitzer* catalogue in the EN1 region. We focus on the WIDE-S band as this is the source detection band, the N60, N160 and WIDE-L band catalogues will be based on photometry of the positions of WIDE-S sources. We find that the WIDE-S band is complete to $\sim$3Jy and the 50% completeness limit (which is approximately the flux limit of the survey) is $\sim$1Jy when confirmation is included. This requires that sources are detected in two independent scans. We calculate that the reliability of the WIDE-S survey is $\sim$60% at the 50% completeness limit. These detection limits are comparable to that of IRAS, however the improved spatial resolution of the AKARI FIS allows a significantly improved all-sky catalogue to be produced.

6.2.1 Future Work

Recently an updated version of the Green Box software has been used to re-reduce the data and the completeness and reliability of this data are likely improved, as suggested by complimentary analyses to that presented here. It would therefore be interesting to re-calculate these two quantities.

6.3 IRS Observations of Four Extremely Red Objects in the SWIRE Survey

We have identified 4 objects in the XMM field of the SWIRE survey which have extreme 24μm to IRAC wavelength colours. We have found that a simple selection of 24μm sources detected in two different epochs which are not found in the 5σ IRAC catalogue is contaminated by a large number of objects for which the 24μm detection is a PRF artifact from a nearby, bright extended object. However, from a visual inspection, a genuine sample of objects can be identified. Objects selected in this manner have a number density of $\sim$0.5 per sq. deg. We have attempted to suggest plausible redshifts for the 4 objects we found in the XMM field based on analysis of 10 hrs of *Spitzer* IRS spectroscopy. We find that one of the objects is likely an obscured AGN at high redshift ($z \gtrsim 2$), although star-formation is likely to contribute as well. The remaining objects are likely at lower redshifts, $\sim$ 1.5 and $\sim$ 1.0. Three of the objects are classed as ULIRGs and all show evidence that they are highly obscured. While these scenarios are plausible, the noisy nature of the spectra mean that these conclusions cannot be certain and further data is required to be conclusive; all objects have redshift aliases. We have been unable to determine whether or not they are Compton Thick, however, the high dust extinction required for consistency with the MIR colours makes this a plausible hypothesis.

6.3.1 Future Work

Since this analysis was performed an improvement in the data-reduction methodology has been identified, the first piece of analysis to follow-up these objects would be to re-analyse the data. Once this has been completed, the most obvious further future work is to extend the selection to include the other 5 SWIRE fields. Recently, two-epoch images have become available in the SWIRE-ES1 field, however, a sample across all *Spitzer* surveys would be interesting. In particular, exploring the other SWIRE fields would explore the maximum possible area and hence give the largest sample. Alternatives include looking in the GOODS field to see whether or not a similar set of objects have in fact been detected in those deeper IRAC images, although the small field means the chances of there being an object at all are low. Finally, it is clear that the data we have obtained is not sufficient to fully characterise these objects. Further, deeper spectra, perhaps with the Herschel Space Telescope or the Atacama Large Millimeter/sub-millimeter Array (ALMA), should illuminate the redshift and possible power sources of these objects.

6.4 Host Galaxies of Type Ia Supernovae in GOODS

We have studied the host galaxies of a sample of 22 Type Ia Supernovae (SNe Ia) at $z \geq 0.95$ from Gilliland et al. (1999); Blakeslee et al. (2003); Strolger et al. (2004); Riess et al. (2004, 2007). We use the broadband photometry from HST ACS *BViz*, *Spitzer* IRAC as well as *UJHK* ground-based and some HST NICMOS *JH* data from the GOODS survey. We fit the photometry to the single stellar population models of Charlot & Bruzual (priv. com.) which are generated from the latest version of the GALAXEV code (Bruzual & Charlot, 2003). We use *Spitzer* MIPS 24μm data to place upper limits on the far-infrared luminosity of the hosts to break the well-known age-extinction degeneracy associated with SED fitting. We find the best-fit model for each host using a minimum χ^2 technique to estimate the luminosity-weighted age of the stellar population of the SN Ia progenitors and hence place upper limits on the possible SN Ia delay times. We find evidence for both prompt and delayed SNe Ia and that the SN Ia delay times possibly have a bi-modal distribution. We also show that the $\lesssim 8 M_{\odot}$ SN Ia progenitor stars are in place by $z \sim 2$ and possibly by $z \sim 5$ (although with significant uncertainty) arguing against a truncated IMF in the first Gyr after the Big Bang.

6.4.1 Future Work

While it seems clear from our results that there is evidence for high redshift SNe Ia with prompt delay times the sample size is still small (20). A larger sample is required to confirm our results of bi-modality. Furthermore, the results of Strolger et al. (2010) which used the same sample of SNe Ia as used here suggested a single gaussian delay time with little evidence for prompt SNe Ia. Obtaining larger samples is, of course, an observational challenge due to the need for repeated observations of a large area to high depth. However, currently most of the effort is going into finding SNe Ia at lower redshifts for use in cosmology, such as the Panoramic Survey Telescope & Rapid Response System (Pan-STARRS) survey and Dark Energy Survey.

Bibliography

Abell, G. O. 1958, ApJS, 3, 211 14, 27

Adami, C., et al. 2010, A&A, 509, A81+ 29

Alexander, D. M., Chartas, G., Bauer, F. E., Brandt, W. N., Simpson, C., & Vignali, C. 2005, MNRAS, 357, L16 119

Allamandola, L. J., Tielens, A. G. G. M., & Barker, J. R. 1985, ApJ, 290, L25 102

—. 1989, ApJS, 71, 733 102

Andreon, S. 2006, A&A, 448, 447 76

Andreon, S., Maughan, B., Trinchieri, G., & Kurk, J. 2009, A&A, 507, 147 27, 75

Andreon, S., Valtchanov, I., Jones, L. R., Altieri, B., Bremer, M., Willis, J., Pierre, M., & Quintana, H. 2005, MNRAS, 359, 1250 25, 27

Andriesse, C. D., & de Vries, J. 1978, A&A, 68, 123 102

Annis, J., et al. 1999, in Bulletin of the American Astronomical Society, Vol. 31, Bulletin of the American Astronomical Society, 1391–+ 28

Armus, L., et al. 2004, ApJS, 154, 178 102, 113, 116

—. 2006, ApJ, 640, 204 116, 119

—. 2007, ApJ, 656, 148 116

Arnouts, S., et al. 2007, A&A, 476, 137 11

Arp, H. 1966, ApJS, 14, 1 120

Aubourg, É., Tojeiro, R., Jimenez, R., Heavens, A., Strauss, M. A., & Spergel, D. N. 2008, A&A, 492, 631 149, 177, 179

Babbedge, T. S. R., et al. 2004, MNRAS, 353, 654 38

—. 2006, MNRAS, 370, 1159 76

Bahcall, N. A., et al. 2003, ApJS, 148, 243 28, 29

Baldry, I. K., Glazebrook, K., Brinkmann, J., Ivezić, Ž., Lupton, R. H., Nichol, R. C., & Szalay, A. S. 2004, ApJ, 600, 681 9

Baldry, I. K., Glazebrook, K., & Driver, S. P. 2008, MNRAS, 388, 945 15, 75

Baldry, I. K., et al. 2005, MNRAS, 358, 441 10

Balogh, M., et al. 2004a, MNRAS, 348, 1355 15

Balogh, M. L., Baldry, I. K., Nichol, R., Miller, C., Bower, R., & Glazebrook, K. 2004b, ApJ, 615, L101 9, 15

Balogh, M. L., Christlein, D., Zabludoff, A. I., & Zaritsky, D. 2001, ApJ, 557, 117 17, 69

Balogh, M. L., Navarro, J. F., & Morris, S. L. 2000, ApJ, 540, 113 10, 78

Bamford, S. P., Rojas, A. L., Nichol, R. C., Miller, C. J., Wasserman, L., Genovese, C. R., & Freeman, P. E. 2008, MNRAS, 391, 607 9

Barnes, J., Hernquist, L., & Schweizer, F. 1991, Scientific American, 265, 40 10

Barris, B. J., & Tonry, J. L. 2006, ApJ, 637, 427 148, 178

Barthel, P. D. 1989, ApJ, 336, 606 10

Baugh, C. M. 2006, Astronomy and Geophysics, 47, 020000 8

Baugh, C. M., Lacey, C. G., Frenk, C. S., Granato, G. L., Silva, L., Bressan, A., Benson, A. J., & Cole, S. 2005, MNRAS, 356, 1191 21

Beichmann, C. A. 1985, Infrared Astronomical Satellite (IRAS) catalogs and atlases. Explanatory supplement 13

Bell, E. F., et al. 2004, ApJ, 608, 752 10

Bennett, C. L., et al. 2003, ApJ, 583, 1 3

Bergé, J., et al. 2008, MNRAS, 385, 695 29

Bernard-Salas, J., et al. 2009, ApJS, 184, 230 102

Berta, S. 2005, PhD thesis, Dipartimento di Astronomia, Univ. di Padova, Vicolo dell'Osservatorio 2, I-35122, Padova, Italy 119, 121, 122

Berta, S., et al. 2007, A&A, 467, 565 36, 45, 48, 183

Bertin, E., & Arnouts, S. 1996, A&AS, 117, 393 92

Biviano, A., Durret, F., Gerbal, D., Le Fevre, O., Lobo, C., Mazure, A., & Slezak, E. 1996, A&A, 311, 95 24

Blain, A. W., & Phillips, T. G. 2002, MNRAS, 333, 222 19, 20

Blakeslee, J. P., et al. 2003, ApJ, 589, 693 150, 185

Blanc, G., & Greggio, L. 2008, New Astronomy, 13, 606 150, 176, 178, 179

Blandford, R. D., & Rees, M. J. 1978, Phys. Scr, 17, 265 9

Blanton, M. R., Eisenstein, D., Hogg, D. W., Schlegel, D. J., & Brinkmann, J. 2005, ApJ, 629, 143 15

Blanton, M. R., & Moustakas, J. 2009, ARA&A, 47, 159 14, 15, 75

Blanton, M. R., et al. 2003, ApJ, 592, 819 6

Bolzonella, M., et al. 2009, ArXiv e-prints 76

Bond, J. R., Kofman, L., & Pogosyan, D. 1996, Nature, 380, 603 60

Borch, A., et al. 2006, A&A, 453, 869 76

Borys, C., Chapman, S., Halpern, M., & Scott, D. 2003, MNRAS, 344, 385 19

Boselli, A., & Gavazzi, G. 2006, PASP, 118, 517 15

Botticella, M. T., et al. 2008, A&A, 479, 49 149, 179

Bower, R. G., Benson, A. J., Malbon, R., Helly, J. C., Frenk, C. S., Baugh, C. M., Cole, S., & Lacey, C. G. 2006, MNRAS, 370, 645 8

Bower, R. G., Lucey, J. R., & Ellis, R. S. 1992, MNRAS, 254, 589 8, 27

Brandl, B. R., et al. 2006, ApJ, 653, 1129 102

Brandt, T. D., Tojeiro, R., Aubourg, É., Heavens, A., Jimenez, R., & Strauss, M. A. 2010, ArXiv e-prints 149

Brandt, W. N., & Hasinger, G. 2005, ARA&A, 43, 827 21

Bravo-Alfaro, H., Caretta, C. A., Lobo, C., Durret, F., & Scott, T. 2009, A&A, 495, 379 15

Bremer, M. N., et al. 2006, MNRAS, 371, 1427 65

Brinchmann, J., Charlot, S., White, S. D. M., Tremonti, C., Kauffmann, G., Heckman, T., & Brinkmann, J. 2004, MNRAS, 351, 1151 9

Broadhurst, T., & Lehar, J. 1995, ApJ, 450, L41+ 19, 118

Brodwin, M., et al. 2006, ApJ, 651, 791 29

—. 2008, ApJ, 687, L65 20

Bruzual, G., & Charlot, S. 2003, MNRAS, 344, 1000 159, 185

Buitrago, F., Trujillo, I., Conselice, C. J., Bouwens, R. J., Dickinson, M., & Yan, H. 2008, ApJ, 687, L61 151

Bundy, K., et al. 2006, ApJ, 651, 120 76

Bussmann, R. S., et al. 2009, ApJ, 693, 750 21

Butcher, H., & Oemler, Jr., A. 1978, ApJ, 226, 559 14

—. 1984, ApJ, 285, 426 16

Cabanac, R. A., et al. 2007, A&A, 461, 813 29

Calzetti, D., Armus, L., Bohlin, R. C., Kinney, A. L., Koornneef, J., & Storchi-Bergmann, T. 2000, ApJ, 533, 682 159, 160, 161, 165

Capak, P., Abraham, R. G., Ellis, R. S., Mobasher, B., Scoville, N., Sheth, K., & Koekemoer, A. 2007, ApJS, 172, 284 16

Caputi, K. I., et al. 2009, ApJ, 691, 91 16

Carilli, C. L., Wrobel, J. M., & Ulvestad, J. S. 1998, AJ, 115, 928 119

Casali, M., et al. 2007, A&A, 467, 777 31

Chandrasekhar, S. 1931, ApJ, 74, 81 4, 148

Chapman, S. C., Blain, A. W., Smail, I., & Ivison, R. J. 2005, ApJ, 622, 772 19

Chapman, S. C., Smail, I., Blain, A. W., & Ivison, R. J. 2004, ApJ, 614, 671 19

Charlot, S., & Fall, S. M. 2000, ApJ, 539, 718 165

Chary, R., & Elbaz, D. 2001, ApJ, 556, 562 19, 161

Chiar, J. E., & Tielens, A. G. G. M. 2006, ApJ, 637, 774 113, 121, 124

Cimatti, A., Daddi, E., & Renzini, A. 2006, A&A, 453, L29 8

Cirasuolo, M., et al. 2007, MNRAS, 380, 585 11

Coia, D., et al. 2005, A&A, 431, 433 16

Coil, A. L., Newman, J. A., Cooper, M. C., Davis, M., Faber, S. M., Koo, D. C., & Willmer, C. N. A. 2006, ApJ, 644, 671 16

Coil, A. L., et al. 2008, ApJ, 672, 153 16, 25

Cole, S., Lacey, C. G., Baugh, C. M., & Frenk, C. S. 2000, MNRAS, 319, 168 6, 8

Colless, M., et al. 2001, MNRAS, 328, 1039 6

Comastri, A. 2004, in Astrophysics and Space Science Library, Vol. 308, Supermassive Black Holes in the Distant Universe, ed. A. J. Barger, 245–+ 21

Cooper, M. C., Newman, J. A., Madgwick, D. S., Gerke, B. F., Yan, R., & Davis, M. 2005, ApJ, 634, 833 24

Cooper, M. C., et al. 2006, MNRAS, 370, 198 16

—. 2008, MNRAS, 383, 1058 16

Cowie, L. L., Songaila, A., Hu, E. M., & Cohen, J. G. 1996, AJ, 112, 839 8, 10

Croton, D. J., et al. 2005, MNRAS, 356, 1155 15

—. 2006, MNRAS, 365, 11 8

Cucciati, O., et al. 2006, A&A, 458, 39 16

—. 2009, ArXiv e-prints 26, 75

Cuillandre, J., & Bertin, E. 2006, in SF2A-2006: Semaine de l'Astrophysique Francaise, ed. D. Barret, F. Casoli, G. Lagache, A. Lecavelier, & L. Pagani , 265–+ 11

Cyburt, R. H., Fields, B. D., & Olive, K. A. 2003, Physics Letters B, 567, 227 4

Daddi, E., et al. 2003, ApJ, 588, 50 16

—. 2005, ApJ, 631, L13 19

Dahlen, T., Strolger, L., & Riess, A. G. 2008, ApJ, 681, 462 148, 174, 178

Dahlen, T., et al. 2004, ApJ, 613, 189 148, 149, 178, 179

Dalton, G. B., Maddox, S. J., Sutherland, W. J., & Efstathiou, G. 1997, MNRAS, 289, 263 27

Davis, M., Huchra, J., Latham, D. W., & Tonry, J. 1982, ApJ, 253, 423 26

Davis, M., et al. 2003, in Society of Photo-Optical Instrumentation Engineers (SPIE) Conference Series, Vol. 4834, Society of Photo-Optical Instrumentation Engineers (SPIE) Conference Series, ed. P. Guhathakurta, 161–172 24

De Propris, R., Stanford, S. A., Eisenhardt, P. R., Holden, B. P., & Rosati, P. 2007, AJ, 133, 2209 76

de Vaucouleurs, G., de Vaucouleurs, A., Corwin, Jr., H. G., Buta, R. J., Paturel, G., & Fouqué, P. 1991, Third Reference Catalogue of Bright Galaxies. Volume I: Explanations and references. Volume II: Data for galaxies between 0^h and 12^h. Volume III: Data for galaxies between 12^h and 24^h. 120

Della Valle, M., Panagia, N., Padovani, P., Cappellaro, E., Mannucci, F., & Turatto, M. 2005, ApJ, 629, 750 177

Demarco, R., et al. 2010, ArXiv e-prints 28, 57, 65

Desai, V., et al. 2007a, ApJ, 669, 810 102, 116

—. 2007b, ApJ, 660, 1151 16

Desert, F., Boulanger, F., & Puget, J. L. 1990, A&A, 237, 215 102

Dey, A., et al. 2008, ApJ, 677, 943 20, 101, 143, 146

Dickinson, M., Giavalisco, M., & The Goods Team. 2003, in The Mass of Galaxies at Low and High Redshift, ed. R. Bender & A. Renzini, 324–+ 11, 150

Djorgovski, S., & Davis, M. 1987, ApJ, 313, 59 6

Dole, H., et al. 2001, A&A, 372, 364 19

—. 2006, A&A, 451, 417 12

Donley, J. L., Rieke, G. H., Pérez-González, P. G., & Barro, G. 2008, ApJ, 687, 111 146

Downes, D., Solomon, P. M., & Radford, S. J. E. 1993, ApJ, 414, L13 119

Dressler, A. 1980, ApJ, 236, 351 14, 24

Dressler, A., Lynden-Bell, D., Burstein, D., Davies, R. L., Faber, S. M., Terlevich, R., & Wegner, G. 1987, ApJ, 313, 42 6

Dressler, A., Rigby, J., Oemler, A., Fritz, J., Poggianti, B. M., Rieke, G., & Bai, L. 2009, ApJ, 693, 140 16

Dressler, A., et al. 1997, ApJ, 490, 577 10, 16

Driver, S. P., et al. 2009, Astronomy and Geophysics, 50, 050000 11

Dye, S., et al. 2006, MNRAS, 372, 1227 32

Eales, S., Lilly, S., Webb, T., Dunne, L., Gear, W., Clements, D., & Yun, M. 2000, AJ, 120, 2244 19

Ebeling, H., & Wiedenmann, G. 1993, Phys. Rev. E, 47, 704 24

Efstathiou, G., Ellis, R. S., & Peterson, B. A. 1988, MNRAS, 232, 431 69

Einasto, J., Einasto, M., & Gramann, M. 1989, MNRAS, 238, 155 60

Einasto, J., Hütsi, G., Einasto, M., Saar, E., Tucker, D. L., Müller, V., Heinämäki, P., & Allam, S. S. 2003, A&A, 405, 425 60

Einasto, J., Tago, E., Einasto, M., Saar, E., Suhhonenko, I., Heinämäki, P., Hütsi, G., & Tucker, D. L. 2005, A&A, 439, 45 60

Eisenhardt, P. R. M., et al. 2008, ApJ, 684, 905 29, 75

Eisenstein, D. J. 2003, ApJ, 586, 718 24

Elbaz, D., Cesarsky, C. J., Chanial, P., Aussel, H., Franceschini, A., Fadda, D., & Chary, R. R. 2002, A&A, 384, 848 19

Elbaz, D., et al. 2007, A&A, 468, 33 16, 78

Ellis, R. S., Smail, I., Dressler, A., Couch, W. J., Oemler, Jr., A., Butcher, H., & Sharples, R. M. 1997, ApJ, 483, 582 17, 27

Emerson, J., McPherson, A., & Sutherland, W. 2006, The Messenger, 126, 41 12

Fadda, D., Elbaz, D., Duc, P., Flores, H., Franceschini, A., Cesarsky, C. J., & Moorwood, A. F. M. 2000, A&A, 361, 827 16

Farrah, D., Afonso, J., Efstathiou, A., Rowan-Robinson, M., Fox, M., & Clements, D. 2003, MNRAS, 343, 585 19, 102, 119

Farrah, D., Geach, J., Fox, M., Serjeant, S., Oliver, S., Verma, A., Kaviani, A., & Rowan-Robinson, M. 2004, MNRAS, 349, 518 16, 78

Farrah, D., et al. 2001, MNRAS, 326, 1333 19

—. 2006, ApJ, 641, L17 16, 36, 76, 78

—. 2007, ApJ, 667, 149 102

—. 2008, ApJ, 677, 957 36, 38, 40, 45, 102, 183

—. 2009, ApJ, 700, 395 20, 102

Fazio, G. G., et al. 2004, ApJS, 154, 10 29, 30

Finoguenov, A., et al. 2007, ApJS, 172, 182 25

—. 2009, ArXiv e-prints 25

Fiore, F., et al. 2008, ApJ, 672, 94 21, 146

Fisher, K. B., Huchra, J. P., Strauss, M. A., Davis, M., Yahil, A., & Schlegel, D. 1995, ApJS, 100, 69 120

Fontana, A., et al. 2004, A&A, 424, 23 8, 76

—. 2006, A&A, 459, 745 8, 76

Förster, F., Wolf, C., Podsiadlowski, P., & Han, Z. 2006, MNRAS, 368, 1893 148, 178

Franceschini, A., Aussel, H., Cesarsky, C. J., Elbaz, D., & Fadda, D. 2001, A&A, 378, 1 19

Frayer, D. T., et al. 2006, AJ, 131, 250 28

Frost, M., Oliver, S., Farrah, D., Lencz, C., Baugh, C., & Almeida, C. 2010, in preparation 16, 25, 38, 50

Furusawa, H., et al. 2008, ApJS, 176, 1 38

Gal-Yam, A., & Maoz, D. 2004, MNRAS, 347, 942 148, 178

Gallagher, J. S., Garnavich, P. M., Berlind, P., Challis, P., Jha, S., & Kirshner, R. P. 2005, ApJ, 634, 210 148, 177

Gallagher, J. S., Garnavich, P. M., Caldwell, N., Kirshner, R. P., Jha, S. W., Li, W., Ganeshalingam, M., & Filippenko, A. V. 2008, ApJ, 685, 752 177

García López, R. J., Randich, S., Zapatero Osorio, M. R., & Pallavicini, R. 2000, A&A, 363, 958 27

Gavazzi, R., & Soucail, G. 2007, A&A, 462, 459 29

Geach, J. E., et al. 2006, ApJ, 649, 661 16

Genzel, R., et al. 1998, ApJ, 498, 579 19, 102

Georgakakis, A., Rowan-Robinson, M., Nandra, K., Digby-North, J., Perez-Gonzalez, P. G., & Barro, G. 2010, ArXiv e-prints 146

Georgakakis, A., et al. 2009, MNRAS, 397, 623 146

Georgantopoulos, I., Georgakakis, A., Rowan-Robinson, M., & Rovilos, E. 2008, A&A, 484, 671 21

Gerke, B. F., et al. 2005, ApJ, 625, 6 26, 27, 52, 75

Gerken, B., Ziegler, B., Balogh, M., Gilbank, D., Fritz, A., & Jäger, K. 2004, A&A, 421, 59 15

Giavalisco, M., et al. 2004, ApJ, 600, L93 11, 150

Gilfanov, M., & Bogdan, A. 2010, ArXiv e-prints 149

Gillett, F. C., Forrest, W. J., & Merrill, K. M. 1973, ApJ, 183, 87 102

Gilliland, R. L., Nugent, P. E., & Phillips, M. M. 1999, ApJ, 521, 30 150, 185

Gioia, I. M., Maccacaro, T., Schild, R. E., Wolter, A., Stocke, J. T., Morris, S. L., & Henry, J. P. 1990, ApJS, 72, 567 25

Giovanelli, R., & Haynes, M. P. 1985, ApJ, 292, 404 15

Gladders, M. D., Lopez-Cruz, O., Yee, H. K. C., & Kodama, T. 1998, ApJ, 501, 571 17, 27

Gladders, M. D., & Yee, H. K. C. 2000, AJ, 120, 2148 28

—. 2005, ApJS, 157, 1 28, 75

Gnedin, O. Y., Brown, W. R., Geller, M. J., & Kenyon, S. J. 2010, ApJ, 720, L108 69

Gómez, P. L., et al. 2003, ApJ, 584, 210 15

Goto, T., Yamauchi, C., Fujita, Y., Okamura, S., Sekiguchi, M., Smail, I., Bernardi, M., & Gomez, P. L. 2003, MNRAS, 346, 601 14

Goto, T., et al. 2002, AJ, 123, 1807 29

Graham, J. A. 1978, PASP, 90, 237 119

Grazian, A., et al. 2006, A&A, 453, 507 16

Greggio, L. 2005, A&A, 441, 1055 149

—. 2010, MNRAS, 406, 22 149

Greggio, L., & Cappellaro, E. 2009, in American Institute of Physics Conference Series, Vol. 1111, American Institute of Physics Conference Series, ed. G. Giobbi, A. Tornambe, G. Raimondo, M. Limongi, L. A. Antonelli, N. Menci, & E. Brocato, 477–484 149

Grove, L. F., Benoist, C., & Martel, F. 2009, A&A, 494, 845 27, 75

Gulkis, S., Lubin, P. M., Meyer, S. S., & Silverberg, R. F. 1990, Scientific American, 262, 132 2

Gunn, J. E., & Gott, III, J. R. 1972, ApJ, 176, 1 10, 78

Guth, A. H. 1981, Phys. Rev. D, 23, 347 4

Hacking, P., & Houck, J. R. 1987, ApJS, 63, 311 19

Hambly, N. C., et al. 2008, MNRAS, 384, 637 31

Hao, L., et al. 2005, ApJ, 625, L75 102, 116, 118

Hartley, W. G., et al. 2008, MNRAS, 391, 1301 36

Hashimoto, Y., Barcons, X., Böhringer, H., Fabian, A. C., Hasinger, G., Mainieri, V., & Brunner, H. 2004, A&A, 417, 819 65

Henry, J. P., et al. 2010, ArXiv e-prints 26

Hewett, P. C., Warren, S. J., Leggett, S. K., & Hodgkin, S. T. 2006, MNRAS, 367, 454 31

Higdon, S. J. U., Armus, L., Higdon, J. L., Soifer, B. T., & Spoon, H. W. W. 2006, ApJ, 648, 323 102

Higdon, S. J. U., et al. 2004, PASP, 116, 975 103

Hilton, M., et al. 2010, ArXiv e-prints 79, 182

Hogg, D. W., et al. 2004, ApJ, 601, L29 15

Holden, B. P., et al. 2005, ApJ, 626, 809 17

Hopkins, A. M., & Beacom, J. F. 2006, ApJ, 651, 142 10

Hopkins, P. F., Bundy, K., Hernquist, L., & Ellis, R. S. 2007, ApJ, 659, 976 10

Horne, K. 1986, PASP, 98, 609 104

Horner, D. J., Perlman, E. S., Ebeling, H., Jones, L. R., Scharf, C. A., Wegner, G., Malkan, M., & Maughan, B. 2008, ApJS, 176, 374 25

Houck, J. R., Schneider, D. P., Danielson, G. E., Neugebauer, G., Soifer, B. T., Beichman, C. A., & Lonsdale, C. J. 1985, ApJ, 290, L5 18

Houck, J. R., et al. 2004, ApJS, 154, 18 22, 92, 101, 102

—. 2005, ApJ, 622, L105 20

Howell, D. A. 2001, ApJ, 554, L193 149

Howell, D. A., Sullivan, M., Conley, A., & Carlberg, R. 2007, ApJ, 667, L37 179

Howell, D. A., et al. 2009, ApJ, 691, 661 178

Hubble, E. 1929, Proceedings of the National Academy of Science, 15, 168 1

Hubble, E. P. 1922, ApJ, 56, 162 8

—. 1925, Popular Astronomy, 33, 252 1

—. 1926, ApJ, 64, 321 8

Huchra, J., Davis, M., Latham, D., & Tonry, J. 1983, ApJS, 52, 89 26

Huchra, J. P., & Geller, M. J. 1982, ApJ, 257, 423 24, 26

Hughes, D. H., et al. 1998, ArXiv Astrophysics e-prints 19

Icke, V. 1985, A&A, 144, 115 16

Ilbert, O., et al. 2004, MNRAS, 351, 541 69

—. 2010, ApJ, 709, 644 76

Irwin, J. M. e. a. 2008, in preparation 31

Jansen, F., et al. 2001, A&A, 365, L1 21, 26

Jha, S., Riess, A. G., & Kirshner, R. P. 2007, ApJ, 659, 122 153

John, T. L. 1988, A&A, 193, 189 36

Just, D. W., Zaritsky, D., Sand, D. J., Desai, V., & Rudnick, G. 2010, ApJ, 711, 192 16

Kauffmann, G., White, S. D. M., Heckman, T. M., Ménard, B., Brinchmann, J., Charlot, S., Tremonti, C., & Brinkmann, J. 2004, MNRAS, 353, 713 15, 75, 78

Kauffmann, G., et al. 2003, MNRAS, 341, 54 9

Kawada, M., et al. 2007, PASJ, 59, 389 80, 81, 82

Kennicutt, Jr., R. C. 1998, ARA&A, 36, 189 66

Kepner, J., Fan, X., Bahcall, N., Gunn, J., Lupton, R., & Xu, G. 1999, ApJ, 517, 78 29

Kessler, M. F., et al. 1996, A&A, 315, L27 13

Kim, R. S. J., et al. 2002, AJ, 123, 20 24, 29

Kleinmann, S. G., Brecher, K., & Ingham, W. H. 1976, ApJ, 207, 532 102

Knobel, C., et al. 2009, ApJ, 697, 1842 26

Kodama, T., & Bower, R. G. 2001, MNRAS, 321, 18 16

Koester, B. P., et al. 2007a, ApJ, 660, 239 28

—. 2007b, ApJ, 660, 221 28

Komatsu, E., et al. 2010, ArXiv e-prints 5

Kowalski, M., et al. 2008, ApJ, 686, 749 5

Kreysa, E., et al. 1998, in Society of Photo-Optical Instrumentation Engineers (SPIE) Conference Series, Vol. 3357, Society of Photo-Optical Instrumentation Engineers (SPIE) Conference Series, ed. T. G. Phillips, 319–325 22, 108

Krick, J. E., Surace, J. A., Thompson, D., Ashby, M. L. N., Hora, J. L., Gorjian, V., & Yan, L. 2009, ApJ, 700, 123 78

Kriek, M., van der Wel, A., van Dokkum, P. G., Franx, M., & Illingworth, G. D. 2008, ApJ, 682, 896 10

Krivonos, R., Vikhlinin, A., Churazov, E., Lutovinov, A., Molkov, S., & Sunyaev, R. 2005, ApJ, 625, 89 21

Kuznetsova, N., et al. 2008, ApJ, 673, 981 179

Lacy, M., et al. 2005, ApJS, 161, 41 28

Lagache, G., Dole, H., & Puget, J. 2003, MNRAS, 338, 555 19

Lanzuisi, G., Piconcelli, E., Fiore, F., Feruglio, C., Vignali, C., Salvato, M., & Gruppioni, C. 2009, A&A, 498, 67 21

Larson, R. B., Tinsley, B. M., & Caldwell, C. N. 1980, ApJ, 237, 692 78

Laurent, O., Mirabel, I. F., Charmandaris, V., Gallais, P., Madden, S. C., Sauvage, M., Vigroux, L., & Cesarsky, C. 2000, A&A, 359, 887 102

Lawrence, A., et al. 1999, MNRAS, 308, 897 19

—. 2007, MNRAS, 379, 1599 12, 30, 31

Lazzati, D., Campana, S., Rosati, P., Panzera, M. R., & Tagliaferri, G. 1999, ApJ, 524, 414 25

Le Fèvre, O., et al. 2004, A&A, 417, 839 38

—. 2005, A&A, 439, 845 26, 38, 45

Le Floc'h, E., et al. 2005, ApJ, 632, 169 10, 11, 19

Lebouteiller, V., Bernard-Salas, J., Sloan, G. C., & Barry, D. J. 2010, PASP, 122, 231 103

Leger, A., D'Hendecourt, L., & Defourneau, D. 1989, A&A, 216, 148 102

Leger, A., & Puget, J. L. 1984, A&A, 137, L5 102

Lehmann, I., et al. 2001, A&A, 371, 833 65

Lemaître, G. 1927, Annales de la Societe Scietifique de Bruxelles, 47, 49 1

Lewis, I., et al. 2002, MNRAS, 334, 673 15

Li, C., Kauffmann, G., Jing, Y. P., White, S. D. M., Börner, G., & Cheng, F. Z. 2006, MNRAS, 368, 21 15, 75

Lilly, S. J., Le Fevre, O., Hammer, F., & Crampton, D. 1996, ApJ, 460, L1+ 10

Lilly, S. J., Tresse, L., Hammer, F., Crampton, D., & Le Fevre, O. 1995, ApJ, 455, 108 10

Limousin, M., et al. 2009, A&A, 502, 445 29

Lin, Y., Mohr, J. J., & Stanford, S. A. 2004, ApJ, 610, 745 76

Lindner, U., et al. 1996, A&A, 314, 1 60

Livio, M. 2001, in Supernovae and Gamma-Ray Bursts: the Greatest Explosions since the Big Bang, ed. M. Livio, N. Panagia, & K. Sahu, 334–355 4, 148

Łokas, E. L., Bode, P., & Hoffman, Y. 2004, MNRAS, 349, 595 59

Lonsdale, C. J., Farrah, D., & Smith, H. E. 2006, Ultraluminous Infrared Galaxies (Springer Verlag), 285–+ 18, 19

Lonsdale, C. J., Hacking, P. B., Conrow, T. P., & Rowan-Robinson, M. 1990, ApJ, 358, 60 19

Lonsdale, C. J., et al. 2003, PASP, 115, 897 13, 30, 91

Lopes, P. A. A., de Carvalho, R. R., Gal, R. R., Djorgovski, S. G., Odewahn, S. C., Mahabal, A. A., & Brunner, R. J. 2004, AJ, 128, 1017 29

Lumsden, S. L., Nichol, R. C., Collins, C. A., & Guzzo, L. 1992, MNRAS, 258, 1 27

Lynden-Bell, D. 1971, MNRAS, 155, 95 69

Madau, P., Ferguson, H. C., Dickinson, M. E., Giavalisco, M., Steidel, C. C., & Fruchter, A. 1996, MNRAS, 283, 1388 10

Madgwick, D. S., et al. 2002, MNRAS, 333, 133 15

Magnelli, B., Elbaz, D., Chary, R. R., Dickinson, M., Le Borgne, D., Frayer, D. T., & Willmer, C. N. A. 2009, A&A, 496, 57 19, 84

Makovoz, D., & Marleau, F. R. 2005, PASP, 117, 1113 92

Mann, R. G., et al. 2002, MNRAS, 332, 549 19

Mannucci, F., Della Valle, M., & Panagia, N. 2006, MNRAS, 370, 773 148, 178

Mannucci, F., Della Valle, M., Panagia, N., Cappellaro, E., Cresci, G., Maiolino, R., Petrosian, A., & Turatto, M. 2005, A&A, 433, 807 148, 177, 178

Maoz, D., & Gal-Yam, A. 2004, MNRAS, 347, 951 178

Maoz, D., Mannucci, F., Li, W., Filippenko, A. V., Della Valle, M., & Panagia, N. 2010, ArXiv e-prints 149

Marcillac, D., et al. 2008, ApJ, 675, 1156 16, 78

Marinoni, C., Davis, M., Newman, J. A., & Coil, A. L. 2002, ApJ, 580, 122 24

Marleau, F. R., et al. 2004, ApJS, 154, 66 28

Marley, M. S., Saumon, D., Guillot, T., Freedman, R. S., Hubbard, W. B., Burrows, A., & Lunine, J. I. 1996, Science, 272, 1919 4

Marziani, P., Sulentic, J. W., Dultzin-Hacyan, D., Calvani, M., & Moles, M. 1996, ApJS, 104, 37 118

Mather, J. C. 1982, Optical Engineering, 21, 769 2

Maughan, B. J., Jones, C., Jones, L. R., & Van Speybroeck, L. 2007, ApJ, 659, 1125 65

Mazure, A., et al. 2007, A&A, 467, 49 29, 30

McCracken, H. J., Ilbert, O., Mellier, Y., Bertin, E., Guzzo, L., Arnouts, S., Le Fèvre, O., & Zamorani, G. 2008, A&A, 479, 321 16, 25

McCracken, H. J., et al. 2003, A&A, 410, 17 38

McMahon, R. G., Walton, N. A., Irwin, M. J., Lewis, J. R., Bunclark, P. S., & Jones, D. H. 2001, New Astronomy Reviews, 45, 97 38

Melbourne, J., et al. 2009, AJ, 137, 4854 21

Meneux, B., et al. 2006, A&A, 452, 387 16

Mihos, J. C., & Hernquist, L. 1994, ApJ, 431, L9 10, 19

Milgrom, M. 1983, ApJ, 270, 365 5

Miller, C. J., et al. 2005, AJ, 130, 968 28

Moore, B., Lake, G., Quinn, T., & Stadel, J. 1999, MNRAS, 304, 465 10, 78

Mortier, A. M. J., et al. 2005, MNRAS, 363, 563 19

Moshir, M., Kopman, G., & Conrow, T. A. O. 1992, IRAS Faint Source Survey, Explanatory supplement version 2 13, 34, 81, 89

Murakami, H., et al. 2007, PASJ, 59, 369 13, 80

Murphy, E. J., Chary, R., Alexander, D. M., Dickinson, M., Magnelli, B., Morrison, G., Pope, A., & Teplitz, H. I. 2009, ApJ, 698, 1380 146

Murphy, Jr., T. W., Soifer, B. T., Matthews, K., Armus, L., & Kiger, J. R. 2001, AJ, 121, 97 120

Muzzin, A., Wilson, G., Lacy, M., Yee, H. K. C., & Stanford, S. A. 2008, ApJ, 686, 966 16, 17, 28, 76

Muzzin, A., Yee, H. K. C., Hall, P. B., Ellingson, E., & Lin, H. 2007, ApJ, 659, 1106 76

Muzzin, A., et al. 2009, ApJ, 698, 1934 28

Nakagawa, T., et al. 2007, PASJ, 59, 377 81

Neill, J. D., et al. 2006, AJ, 132, 1126 148, 177, 179

Neill, J. D., et al. 2007, in American Institute of Physics Conference Series, Vol. 924, The Multicolored Landscape of Compact Objects and Their Explosive Origins, ed. T. di Salvo, G. L. Israel, L. Piersant, L. Burderi, G. Matt, A. Tornambe, & M. T. Menna, 421–424 148, 149, 177, 179

—. 2009, ApJ, 707, 1449 177

Netzer, H., Lemze, D., Kaspi, S., George, I. M., Turner, T. J., Lutz, D., Boller, T., & Chelouche, D. 2005, ApJ, 629, 739 119

Neugebauer, G., & Leighton, R. B. 1969, Two-micron sky survey. A preliminary catalogue 12

Neugebauer, G., et al. 1984, ApJ, 278, L1 13

Norberg, P., Eke, V., & the 2dFGRS Team. 2003, Ap&SS, 285, 205 26

Norberg, P., et al. 2002, MNRAS, 336, 907 6, 14

Oda, T., Totani, T., Yasuda, N., Sumi, T., Morokuma, T., Doi, M., & Kosugi, G. 2008, PASJ, 60, 169 148, 178, 179

Oliver, S., et al. 2000, MNRAS, 316, 749 13

—. 2010, MNRAS, 588 78

Olsen, L. F., et al. 1999, A&A, 345, 681 27

—. 2007, A&A, 461, 81 27

Orr, M. J. L., & Browne, I. W. A. 1982, MNRAS, 200, 1067 9

Ouchi, M., & SXDS. 2007, in Bulletin of the American Astronomical Society, Vol. 38, Bulletin of the American Astronomical Society, 226–+ 26

Overzier, R. A., et al. 2006, ApJ, 637, 58 26

Pacaud, F., et al. 2006, MNRAS, 372, 578 65

—. 2007, MNRAS, 382, 1289 65

Papovich, C., et al. 2004, ApJS, 154, 70 84

—. 2010, ArXiv e-prints 38, 75

Pavlovsky, C., et al. 2004, ACS Data Handbook 151

Peacock, J. A. 1987, in NATO ASIC Proc. 208: Astrophysical Jets and their Engines, ed. W. Kundt, 185–196 9

Peebles, P. J. E. 1980, The large-scale structure of the universe 25, 60

Pentericci, L., et al. 2000, A&A, 361, L25 26

Penzias, A. A., & Wilson, R. W. 1965, ApJ, 142, 419 1

Pérez-González, P. G., et al. 2008, ApJ, 675, 234 76

Perlman, E. S., Horner, D. J., Jones, L. R., Scharf, C. A., Ebeling, H., Wegner, G., & Malkan, M. 2002, ApJS, 140, 265 25

Perlmutter, S., et al. 1999, ApJ, 517, 565 4, 148

Pfeffermann, E., et al. 1999, in Society of Photo-Optical Instrumentation Engineers (SPIE) Conference Series, Vol. 3765, Society of Photo-Optical Instrumentation Engineers (SPIE) Conference Series, ed. O. H. Siegmund & K. A. Flanagan, 184–191 109

Phillips, M. M. 1993, ApJ, 413, L105 4, 147

Pierre, M., et al. 2004, Journal of Cosmology and Astro-Particle Physics, 9, 11 108

—. 2007, MNRAS, 382, 279 65

Podsiadlowski, P., Mazzali, P., Lesaffre, P., Han, Z., & Förster, F. 2008, New Astronomy Review, 52, 381 4, 148

Poggianti, B. M., Bridges, T. J., Komiyama, Y., Yagi, M., Carter, D., Mobasher, B., Okamura, S., & Kashikawa, N. 2004, ApJ, 601, 197 17

Poggianti, B. M., Smail, I., Dressler, A., Couch, W. J., Barger, A. J., Butcher, H., Ellis, R. S., & Oemler, Jr., A. 1999, ApJ, 518, 576 17

Poggianti, B. M., et al. 2008, ApJ, 684, 888 16, 17

—. 2009a, ApJ, 693, 112 17

—. 2009b, ApJ, 697, L137 16

Pointecouteau, E., Arnaud, M., & Pratt, G. W. 2005, A&A, 435, 1 52

Polletta, M., Weedman, D., Hönig, S., Lonsdale, C. J., Smith, H. E., & Houck, J. 2008a, ApJ, 675, 960 20, 144

Polletta, M., et al. 2007, ApJ, 663, 81 39, 113, 119, 120, 121, 122, 144

—. 2008b, A&A, 492, 81 100

Pope, A., et al. 2008, ApJ, 689, 127 20

Popesso, P., Böhringer, H., Romaniello, M., & Voges, W. 2005, A&A, 433, 415 15

Postman, M., & Geller, M. J. 1984, ApJ, 281, 95 14

Postman, M., Lauer, T. R., Oegerle, W., & Donahue, M. 2002, ApJ, 579, 93 27

Postman, M., Lubin, L. M., Gunn, J. E., Oke, J. B., Hoessel, J. G., Schneider, D. P., & Christensen, J. A. 1996, AJ, 111, 615 27, 29

Postman, M., et al. 2005, ApJ, 623, 721 16

Poznanski, D., et al. 2007, MNRAS, 382, 1169 178

Pozzetti, L., et al. 2007, A&A, 474, 443 8, 76

Pritchet, C. J., Howell, D. A., & Sullivan, M. 2008, ApJ, 683, L25 149

Puget, J. L., & Leger, A. 1989, ARA&A, 27, 161 102

Quadri, R., et al. 2007, ApJ, 654, 138 16

Ramella, M., Boschin, W., Fadda, D., & Nonino, M. 2001, A&A, 368, 776 24

Ramos Almeida, C., et al. 2009, ApJ, 702, 1127 120

Raskin, C., Scannapieco, E., Rhoads, J., & Della Valle, M. 2009, ApJ, 707, 74 149

Reach, W. T., et al. 2005, PASP, 117, 978 153

Rees, M. J. 1984, ARA&A, 22, 471 19

Rieke, G. H., Lebofsky, M. J., Thompson, R. I., Low, F. J., & Tokunaga, A. T. 1980, ApJ, 238, 24 9

Rieke, G. H., & Low, F. J. 1972, ApJ, 176, L95+ 18

—. 1975, ApJ, 200, L67 102

Rieke, G. H., et al. 2004, ApJS, 154, 25 22, 30

Riess, A. G., et al. 1998, AJ, 116, 1009 4, 147

—. 2001, ApJ, 560, 49 150, 153

—. 2004, ApJ, 607, 665 150, 153, 185

—. 2007, ApJ, 659, 98 150, 152, 153, 171, 185

Rines, K., Geller, M. J., Diaferio, A., Kurtz, M. J., & Jarrett, T. H. 2004, AJ, 128, 1078 17, 76

Romer, A. K., Viana, P. T. P., Liddle, A. R., & Mann, R. G. 2001, ApJ, 547, 594 26

Romer, A. K., et al. 2000, ApJS, 126, 209 25

Rood, H. J. 1988, ARA&A, 26, 245 60

Rosati, P., Borgani, S., & Norman, C. 2002, ARA&A, 40, 539 25, 182

Rosati, P., Della Ceca, R., Burg, R., Norman, C., & Giacconi, R. 1995, ApJ, 445, L11 25

Roseboom, I. G., Oliver, S., & Farrah, D. 2009, ApJ, 699, L1 17

Rowan-Robinson, M. 2001, ApJ, 549, 745 120, 121

—. 2003, MNRAS, 345, 819 38

Rowan-Robinson, M., et al. 1991, Nature, 351, 719 18, 19, 118

—. 1997, MNRAS, 289, 490 19

—. 2004, MNRAS, 351, 1290 38

—. 2005, AJ, 129, 1183 38

—. 2008, MNRAS, 386, 697 38

Rubin, V. C., Ford, W. K. J., & . Thonnard, N. 1980, ApJ, 238, 471 4

Sajina, A., Yan, L., Armus, L., Choi, P., Fadda, D., Helou, G., & Spoon, H. 2007, ApJ, 664, 713 19

Sajina, A., et al. 2008, ApJ, 683, 659 146

Sandage, A. 1965, ApJ, 141, 1560 118

Sandage, A., Tammann, G. A., & Yahil, A. 1979, ApJ, 232, 352 69

Sanders, D. B., Mazzarella, J. M., Kim, D., Surace, J. A., & Soifer, B. T. 2003, AJ, 126, 1607 19

Sanders, D. B., & Mirabel, I. F. 1996, ARA&A, 34, 749 19, 120

Sanders, D. B., Phinney, E. S., Neugebauer, G., Soifer, B. T., & Matthews, K. 1989, ApJ, 347, 29 118

Sanders, D. B., Soifer, B. T., Elias, J. H., Madore, B. F., Matthews, K., Neugebauer, G., & Scoville, N. Z. 1988, ApJ, 325, 74 9, 10

Sarazin, C. L. 1986, Reviews of Modern Physics, 58, 1 25

Saunders, W., Frenk, C., Rowan-Robinson, M., Lawrence, A., & Efstathiou, G. 1991, Nature, 349, 32 60

Saunders, W., Rowan-Robinson, M., Lawrence, A., Efstathiou, G., Kaiser, N., Ellis, R. S., & Frenk, C. S. 1990, MNRAS, 242, 318 19

Savage, R. S., & Oliver, S. 2007, ApJ, 661, 1339 83

Sawicki, M. 2002, AJ, 124, 3050 36

Scannapieco, E., & Bildsten, L. 2005, ApJ, 629, L85 148, 179

Scharf, C. A., Jones, L. R., Ebeling, H., Perlman, E., Malkan, M., & Wegner, G. 1997, ApJ, 477, 79 25

Schawinski, K. 2009, MNRAS, 397, 717 177

Schawinski, K., et al. 2007, ApJS, 173, 512 24, 26

Schechter, P. 1976, ApJ, 203, 297 69

Scheuer, P. A. G. 1987, in Superluminal Radio Sources, ed. J. A. Zensus & T. J. Pearson, 104–113 9

Schmidt, M. 1963, Nature, 197, 1040 9

—. 1968, ApJ, 151, 393 69

—. 1970, ApJ, 162, 371 113, 118

Scodeggio, M., et al. 1999, A&AS, 137, 83 27

—. 2009, A&A, 501, 21 76

Scott, S. E., et al. 2002, MNRAS, 331, 817 19

Scoville, N., et al. 2007a, ApJS, 172, 150 16

—. 2007b, ApJS, 172, 1 11

Sekiguchi, K., et al. 2004, Subaru/XMM-Newton Deep Survey, 40–+ 38

Sellgren, K. 1984, ApJ, 277, 623 102

Serjeant, S., et al. 2008, MNRAS, 386, 1907 16

Seyfert, C. K. 1943, ApJ, 97, 28 113, 119

Shupe, D. L., et al. 2008, AJ, 135, 1050 92, 93

Shupe, D. L., et al. 2009, in American Astronomical Society Meeting Abstracts, Vol. 214, American Astronomical Society Meeting Abstracts, 417.04 146

Simpson, C., & Eisenhardt, P. 1999, PASP, 111, 691 36

Skrutskie, M. F., et al. 2006, AJ, 131, 1163 12

Smail, I., Edge, A. C., Ellis, R. S., & Blandford, R. D. 1998, MNRAS, 293, 124 16

Smail, I., Ivison, R. J., Blain, A. W., & Kneib, J. 2002, MNRAS, 331, 495 19

Smith, G. P., Treu, T., Ellis, R. S., Moran, S. M., & Dressler, A. 2005, ApJ, 620, 78 16

Soifer, B. T., Sanders, D. B., Madore, B. F., Neugebauer, G., Danielson, G. E., Elias, J. H., Lonsdale, C. J., & Rice, W. L. 1987, ApJ, 320, 238 19

Soifer, B. T., et al. 1984, ApJ, 278, L71 13, 19

Solomon, P. M., Downes, D., & Radford, S. J. E. 1992, ApJ, 387, L55 119

Solomon, P. M., Downes, D., Radford, S. J. E., & Barrett, J. W. 1997, ApJ, 478, 144 118

Spoon, H. W. W., Marshall, J. A., Houck, J. R., Elitzur, M., Hao, L., Armus, L., Brandl, B. R., & Charmandaris, V. 2007, ApJ, 654, L49 116

Spoon, H. W. W., et al. 2004, ApJS, 154, 184 102, 116, 120

—. 2006, ApJ, 638, 759 102, 116

Springel, V., Frenk, C. S., & White, S. D. M. 2006, Nature, 440, 1137 6, 7

Springel, V., et al. 2005, Nature, 435, 629 6, 60

Stanford, S. A., Eisenhardt, P. R., & Dickinson, M. 1998, ApJ, 492, 461 27

Stanford, S. A., et al. 2006, ApJ, 646, L13 27, 75

Steidel, C. C., Adelberger, K. L., Shapley, A. E., Erb, D. K., Reddy, N. A., & Pettini, M. 2005, ApJ, 626, 44 28

Steidel, C. C., Giavalisco, M., Dickinson, M., & Adelberger, K. L. 1996, AJ, 112, 352 38

Strateva, I., et al. 2001, AJ, 122, 1861 9

Strauss, M. A., Huchra, J. P., Davis, M., Yahil, A., Fisher, K. B., & Tonry, J. 1992, ApJS, 83, 29 118

Strolger, L., Dahlen, T., & Riess, A. G. 2010, ApJ, 713, 32 148, 174, 178, 185

Strolger, L., et al. 2004, ApJ, 613, 200 148, 178, 185

Strüder, L., et al. 2001, A&A, 365, L18 109

Sturm, E., Lutz, D., Verma, A., Netzer, H., Sternberg, A., Moorwood, A. F. M., Oliva, E., & Genzel, R. 2002, A&A, 393, 821 102

Sullivan, M., Ellis, R. S., Howell, D. A., Riess, A., Nugent, P. E., & Gal-Yam, A. 2009, ApJ, 693, L76 179

Sullivan, M., et al. 2006, ApJ, 648, 868 148, 149, 177, 179

—. 2010, MNRAS, 406, 782 179

Surace, J. A., et al. 2005, Spitzer Science Center 31, 93

Swinbank, A. M., et al. 2007, MNRAS, 379, 1343 30, 64, 65

—. 2008, MNRAS, 391, 420 21

Tacconi, L. J., Genzel, R., Lutz, D., Rigopoulou, D., Baker, A. J., Iserlohe, C., & Tecza, M. 2002, ApJ, 580, 73 19

Takeuchi, T. T., Yoshikawa, K., & Ishii, T. T. 2000, ApJS, 129, 1 69

Tanaka, M., Finoguenov, A., & Ueda, Y. 2010, ArXiv e-prints 39

Taylor, M. B. 2003, Topcat, http://www.starlink.ac.uk/topcat/ 38, 150

Teplitz, H. I., et al. 2006, ApJ, 638, L1 116, 118, 119, 121

Thatte, D., Dahlen, T., & al., e. 2009, NICMOS Data Handbook 151

Thompson, D., et al. 2001, A&A, 377, 778 65

Toomre, A. 1977, ARA&A, 15, 437 10

Toomre, A., & Toomre, J. 1972, ApJ, 178, 623 10, 78

Totani, T., Morokuma, T., Oda, T., Doi, M., & Yasuda, N. 2008, PASJ, 60, 1327 149, 174, 175, 179

Tran, K., Franx, M., Illingworth, G., Kelson, D. D., & van Dokkum, P. 2003, ApJ, 599, 865 17

Tran, K., et al. 2010, ArXiv e-prints 79, 182

Tumlinson, J., Venkatesan, A., & Shull, J. M. 2004, ApJ, 612, 602 150, 176, 180

Valtchanov, I., et al. 2004, A&A, 423, 75 26, 65

van Breukelen, C., et al. 2006, MNRAS, 373, L26 29, 75

van de Weygaert, R., Aragon-Calvo, M. A., Jones, B. J. T., & Platen, E. 2009, ArXiv e-prints 60

van den Bergh, S. 1990, PASP, 102, 1318 148

van Dokkum, P. G., Franx, M., Kelson, D. D., & Illingworth, G. D. 1998, ApJ, 504, L17+ 17

Venemans, B. P., et al. 2002, ApJ, 569, L11 26

—. 2005, A&A, 431, 793 26

Vergani, D., et al. 2010, A&A, 509, A260000+ 17

Verma, A., Charmandaris, V., Klaas, U., Lutz, D., & Haas, M. 2005, Space Science Reviews, 119, 355 19

von Benda-Beckmann, A. M., & Müller, V. 2008, MNRAS, 384, 1189 60

Vulcani, B., Poggianti, B. M., Finn, R. A., Rudnick, G., Desai, V., & Bamford, S. 2010, ApJ, 710, L1 17

Waddington, I., et al. 2007, MNRAS, 381, 1437 34

Wagoner, R. V., Fowler, W. A., & Hoyle, F. 1967, ApJ, 148, 3 4

Wang, L., Hoeflich, P., & Wheeler, J. C. 1997, ApJ, 483, L29+ 148

Wang, L., et al. 2008, MNRAS, 387, 601 80

Warren, S. J., et al. 2007a, ArXiv Astrophysics e-prints 32

—. 2007b, MNRAS, 375, 213 32

Watson, M. G., et al. 2001, A&A, 365, L51 109

Weedman, D., et al. 2006a, ApJ, 653, 101 20

Weedman, D. W., Le Floc'h, E., Higdon, S. J. U., Higdon, J. L., & Houck, J. R. 2006b, ApJ, 638, 613 20, 104

Weedman, D. W., et al. 2005, ApJ, 633, 706 102, 113, 116, 118, 119

—. 2006c, ApJ, 651, 101 20, 109

Weinmann, S. M., van den Bosch, F. C., Yang, X., & Mo, H. J. 2006, MNRAS, 366, 2 15

Weisskopf, M. 2000, APS Meeting Abstracts, J8001+ 26

Weisskopf, M. C., Tananbaum, H. D., Van Speybroeck, L. P., & O'Dell, S. L. 2000, in Society of Photo-Optical Instrumentation Engineers (SPIE) Conference Series, Vol. 4012, Society of Photo-Optical Instrumentation Engineers (SPIE) Conference Series, ed. J. E. Truemper & B. Aschenbach, 2–16 21

Werner, M. W., et al. 2004, ApJS, 154, 1 13

White, S. D. M., & Frenk, C. S. 1991, ApJ, 379, 52 6

White, S. D. M., & Rees, M. J. 1978, MNRAS, 183, 341 6

Wilkins, S. M., Bunker, A. J., Ellis, R. S., Stark, D., Stanway, E. R., Chiu, K., Lorenzoni, S., & Jarvis, M. J. 2010, MNRAS, 176 38

Williams, R. E., et al. 1996, AJ, 112, 1335 11, 154

Willis, J. P., et al. 2005, MNRAS, 363, 675 65

Willmer, C. N. A. 1997, AJ, 114, 898 69

Wilson, G., Muzzin, A., & Lacy, M. 2006, in Astronomical Society of the Pacific Conference Series, Vol. 357, Astronomical Society of the Pacific Conference Series, ed. L. Armus & W. T. Reach, 238–+ 28

Wilson, G., et al. 2005, in Bulletin of the American Astronomical Society, Vol. 37, Bulletin of the American Astronomical Society, 1485–+ 28

Wilson, G., et al. 2009, ApJ, 698, 1943 27, 28

Wolf, C., et al. 2004, A&A, 421, 913 11

—. 2009, MNRAS, 393, 1302 16

Worsley, M. A., Fabian, A. C., Barcons, X., Mateos, S., Hasinger, G., & Brunner, H. 2004, MNRAS, 352, L28 21

Worsley, M. A., et al. 2005, MNRAS, 357, 1281 21

Wright, E. L., Eisenhardt, P., & Fazio, G. 1994, in Bulletin of the American Astronomical Society, Vol. 26, Bulletin of the American Astronomical Society, 893–+ 36

Yagi, M., et al. 2010, AJ, 140, 1814 15

Yamamura, I., et al. 2009, in American Institute of Physics Conference Series, Vol. 1158, American Institute of Physics Conference Series, ed. T. Usuda, M. Tamura, & M. Ishii, 169–170 80, 81, 83, 85, 89, 90

Yan, L., et al. 2005, ApJ, 628, 604 19, 109

—. 2007, ApJ, 658, 778 19, 20

Yee, H. K. C., Gladders, M. D., Gilbank, D. G., Majumdar, S., Hoekstra, H., & Ellingson, E. 2007, in Astronomical Society of the Pacific Conference Series, Vol. 379, Cosmic Frontiers, ed. N. Metcalfe & T. Shanks, 103–+ 28

Yoon, J. H., Schawinski, K., Sheen, Y., Ree, C. H., & Yi, S. K. 2008, ApJS, 176, 414 26

York, D. G., et al. 2000, AJ, 120, 1579 6

Zatloukal, M., Röser, H., Wolf, C., Hippelein, H., & Falter, S. 2007, A&A, 474, L5 29, 75

Zehavi, I., et al. 2002, ApJ, 571, 172 15

Zwicky, F. 1937, ApJ, 86, 217 4